Novel Drug Carriers for

Pulmonary Administration

Utilising a Template-Assisted Approach

Dissertation

zur

Erlangung des Doktorgrades

der Naturwissenschaften

(Dr. rer. nat.)

dem

Fachbereich Pharmazie der

Philipps-Universität Marburg

vorgelegt von

Clemens Rudolf Josef Tscheka

aus **Gera**

Marburg/Lahn **2016**

Erstgutachter: **Prof. Dr. Marc Schneider**

Zweitgutachter: **Prof. Dr. Udo Bakowsky**

Eingereicht am **18.12.2015**

Tag der mündlichen Prüfung am **29.01.2016**

Hochschulkennziffer: 1180

E R K L Ä R U N G

Ich versichere, dass ich meine Dissertation

„Novel Drug Carriers for Pulmonary Administration Utilising a Template-Assisted Approach"

selbständig ohne unerlaubte Hilfe angefertigt und mich dabei keiner anderen als der von mir ausdrücklich bezeichneten Quellen bedient habe. Alle vollständig oder sinngemäß übernommenen Zitate als solche gekennzeichnet.

Die Dissertation wurde in der jetzigen oder einer ähnlichen Form noch bei keiner anderen Hochschule eingereicht und hat noch keinen sonstigen Prüfungszwecken gedient.

Marburg, den 18.12.2015

....

Clemens Tscheka

Niemand ist weiter von der Wahrheit entfernt

als derjenige, der alle Antworten weiß.

Zhuangzi

Table of Contents

Table of Contents

Table of Contents

1 Lists of Abbreviations and Symbols, Equations, Figures and Tables

1.1 List of Abbreviations and Symbols

A549	Human adenocarcinoma alveolar epithelial cell line [1]
AFM	Atomic force microscopy
API	Active pharmaceutical ingredient
AuNP	Gold nanoparticle
bEND 3	mouse brain endothelial cell line [2]
BSA	Bovine serum albumin
Caco2	Heterogeneous human epithelial colorectal adeno-carcinoma cell line [3]
CAM	Cell adhesion molecule
CLEM	Correlative light and electron microscopy
CLSM	Confocal laser scanning microscope
CNT	Carbon nanotube
CREKA	Targeting peptide for tumours, the sequence is CREKA [4]
CTAB	Cetyltrimethylammonium bromide
d_{aer}	Aerodynamic diameter
d_{geo}	Geometric diameter
DLS	Dynamic light scattering
DMEM	Dulbecco's modified eagle medium
DNA	Deoxyribonucleic acid
DPBS	Dulbecco's phosphate buffered saline
DPI	Dry powder inhaler
DUSA	Dosage unit sampling apparatus
ECD	Effective cut-off diameter
ECM	Extracellular matrix
EDTA	Ethylenediaminetetraacetic acid
EM	Electron microscopy
ESEM	Environmental scanning electron microscope
F3	Targeting peptide for tumours, 31-residue peptide [4]
FCS	Fetal calf serum

Lists

FDA	Food and Drug Administration
FITC	Fluorescein isothiocyanate
FLM	Fluorescence light microscopy
FPF	Fine particle fraction
G	α-L-guluronic acid
GM-CSF	Granulocyte macrophage colony stimulating factor
GTA	Glutaraldehyde
HeLa	Immortalized human cell line [5]
HEPES	4-(2-hydroxyethyl)-1-piperazineethanesulfonic acid
HMDS	Hexamethyldisilazane
hTERT	Immortalized human fibroblasts cell line [6]
HUVEC	Human umbilical vein endothelial cells [7]
ICAM	Intercellular adhesion molecule 1 [7]
IgG	Immunoglobulin G
IL-1	Interleukin-1
INN	International nonproprietary name
L929	Murine alveolar fibroblast cell line
LbL	Layer-by-layer
LM	Light microscopy
m	(Molecular) mass
M	β-L-mannuronic acid
MDA-MB-435	Tumour cell line [8]
MHS	Murine alveolar macrophages
MOC	Micro-orifice collector
MPS	Mononuclear phagocyte system
MSN	Mesoporous silica particles
MWCNT	Multi-walled carbon nanotube
NGI	Next generation pharmaceutical impactor
NP	Nanoparticle
PAH	Polyallylamine hydrochloride
PBS	Phosphate buffered saline
PC	Polycarbonate

PC-3	Human prostate cancer cell line [9]
PCL	Polycaprolactone
PCS	Photon correlation spectroscopy
PDLLA	Poly(DL-lactide)
PDMS	Polydimethylsiloxane
PEG	Polyethylene glycol
PFPE	Perfluoropolyether
Ph.Eur.	European Pharmacopoeia
PLA	Poly(D-lactic acid)
PLGA	Poly(lactic-co-glycolic acid)
pLL	Poly(L-lysine)
PMMA	Polymethylmethacrylate
PP	Polypropylene
PRINT	Particles replication in non-wetting templates
PS	Polystyrene
PSS	Polystyrene sulfonate
PTFE	Polytetrafluoroethylene/Teflon
PVP	Polyvinylpyrollidone
RAW 264.7	Primary murine macrophages [1]
rcf	Relative centrifugal force
RES	Reticuloendothelial system
ROI	Region of interest
RSD	Relative standard deviation
SD	Standard deviation
SE	Secondary electron
SEM	Scanning electron microscopy
S-FIL	Step and flash imprint lithography
SNB19	Brain tumour cell line [10]
SPM	Scanning probe microscopy
STED	Stimulated emission depletion microscopy
STO	Mouse fibroblast cell line [10]
STORM	Stochastic optical reconstruction microscopy

Lists

SWCNT	Single-walled carbon nanotube
TC	Tissue culture treated polystyrene
TEM	Transmission electron microscopy
THF	Tetrahydrofuran
THP1	Activated human macrophages
TLR-2	Toll-like receptor 2
USAN	United States adopted name
USP	United States Pharmacopoeia
UV	Ultraviolet
V	Volume
VIS	Visible
WHO	World Health Organisation
θ	Contact angle
λ_{em}	Emission wavelength
λ_{ex}	Excitation wavelength
ρ	Density
χ	Correction factor for the shape of airborne particles for the calculation of d_{aer}

1.2 List of Equations

IV

1.3   List of Figures

1.4   List of Tables

2 General Introduction

2.1 Non-Spherical Particles for Drug Delivery

In the advent of nanotechnology the shape of generated colloidal particles has been predominantly spherical simply because they are in many cases easier to make [11]. Spheres form automatically, given appropriate conditions. Spheres exhibit the optimal ratio between volume and surface and thus minimize the surface tension. Advances in visualization techniques (4.2.1.2) and the development of techniques for the tailoring of geometry (2.1.2) have advanced basic research, revealing numerous and fundamental implications of shape for interactions with biological systems (2.1.3). The potential is being discovered and shape can be regarded as an essential design parameter for progressive drug delivery systems [12-15]. Studies performed by many different groups show that it influences the biodistribution and targeting (2.1.3.3), the immune response and toxicity (2.1.3.4), as well as the longevity of circulation, or the control of the residence time (2.1.3.3.2). One of the most studied subjects are internalization processes (2.1.3.1); substantial differences have been discovered for adhesion (2.1.3.2), the speed and extend of internalization with variations as a function of the cell line, even the phenotype matters [1]. Differing orientation of non-spherical particles can entail uptake through different uptake mechanisms, even dictating the fate of the particle intracellularly [1], or intracellular trafficking (2.1.3.1.3).

Effects of shape have been discovered for systemic as well as for local administration, such as inhalation. More basic research is being conducted in this lively field, contributing to a thorough understanding of the interactions of therapeutics with biological systems, thereby helping to decipher the dominant parameters. Shape as an essential design parameter may allow to advance the field of drug delivery, by offering even more effective therapeutics.

2.1.1 Non-Spherical Particles for Pulmonary Administration

In the course of the harmonization of toxicological studies about the potential hazards of fibre exposition, the term fibre was defined by the World Health Organisation (WHO) [16, 17]. Accordingly, a fibre is an object, exceeding a length of 5 µm and a width smaller than 3 µm; the aspect ratio is larger than 3. The aspect ratio is defined as the length to width ratio. Objects within these limitations fulfil the requirements to proceed to the deep lung upon inhalation, one important argument for the definition of the dimensions.

Elongated particles exhibit properties that can be utilized in order to improve pulmonary drug delivery. The non-spherical shape changes the aerodynamic properties upon inhalation. Fibres and cylinders show a higher probability to deposit in the peripheral lung in comparison to spheres of identical volume. The aerodynamic behaviour is mainly governed by the diameter of the object, the length only has a minor influence due to alignment of the fibres with the airstream [18]. This alignment was also observed for other fluids, the circulation time was drastically increased for flexible fibres. Hydrodynamic considerations indicate that shorter particles interact less with the flow and more with surfaces or cells [19]. Therefore the mass per particle that can be delivered to the target region is increased. Furthermore, fibres show less deposition in the nasal and oral region in comparison to spheres with the same aerodynamic diameter (see 2.3.2), increasing the target efficiency for pulmonary application [20]. The threshold regarding the size of particles being able to proceed to the peripheral lung, the fine particle fraction (FPF), is 5 µm for conventional spherical particles; larger particles predominately deposit in the upper airways (2.3.2).

In addition, fibres are expected to be less prone to form aggregates because the contact area is decreased for an erratic or random distribution in comparison to spheres. Nevertheless, this does not hold true for more ordered contacts between fibres. Supposing a parallel orientation

of fibres, the contact area is increased in comparison to spherical particles. The large surface area of small particles can result in cohesion between single particles which can cause severe aggregation [21]. The aggregates behave differently in the airstream, thus depositing in different regions of the inhalation tract. Besides prevention of aggregation, monodispersity is a vital factor for controlled deposition in the target region since the site of deposition is bound to the geometrical (size and shape) properties of the particle during the inhalation process. Alveolar macrophages clear the respiratory region from foreign objects, including pathogens and senescent cells. Phagocytosis, essential for homeostasis of healthy tissue and clearance, was found to be strongly influenced by the shape and orientation of the object [15, 22]. Modifications of the geometry change time and mechanism required for uptake [1, 23]. As a consequence, certain non-spherical particles have the potential to control clearance processes, a core prerequisite for a sustained release system for therapeutics [15, 23]. The shape of a long cylinder, or a fibre can reduce phagocytosis drastically [23]. Only at one of the two ends macrophages are able to initiate internalization of the particle. This predominantly prolongs the time required for uptake, but can also reduce the extend of uptake. Toxicological studies about the mineral fibre asbestos, which is not biodegradable, confirm that phagocytosis of fibres and as a consequence the clearance from the lungs is inefficient [24]. Longer asbestos fibres have been observed to be more harmful [25]. It has been reported that in particular asbestos fibres longer than 16 microns exhibit retarded clearance [26]. The reduction of uptake opens up the opportunity to extend the residence time, which is one of the main objectives a sustained release system should fulfil.

2.1.2 Preparation Strategies for Non-Spherical Particles

The formation of micron- and nano-sized objects in different shapes has already been mastered for a longer time. At the beginning of the last decade, several methods were available, ranging from lithographic to chemical synthesis approaches [27, 28]. The potential for drug delivery has not been realized for long time, but more and more studies and techniques are being published [12, 14]. The toolbox of techniques has been extended to techniques specifically designed for drug delivery purposes [13, 15]. These new techniques have paved the way for the elucidation of the implication of shape on interactions with biological systems (2.1.3). The efforts for shape specific formation encompass many fundamentally different approaches, each being suitable for certain materials and sizes. Depending on the approach the freedom of tailoring and the minimal particle size that can be reached differs fundamentally. Looking at the literature, inorganic and elemental carbon-based particles were found to be generated in smaller dimensions than tailored, complex polymeric objects. However, the latter exhibit a higher freedom of design with respect to adapting the form. As a consequence the potential utility for drug delivery and hence medical applications is increased.

As the formation of non-spherical particles is a crucial aspect for application, relevant procedures will be summarized in the chapters below. For more detailed information, the following review articles are recommended for the inclined reader [15, 27-30]. A focus is laid on several approaches that might be suited for drug delivery, but there are more methods available which are not discussed in this work.
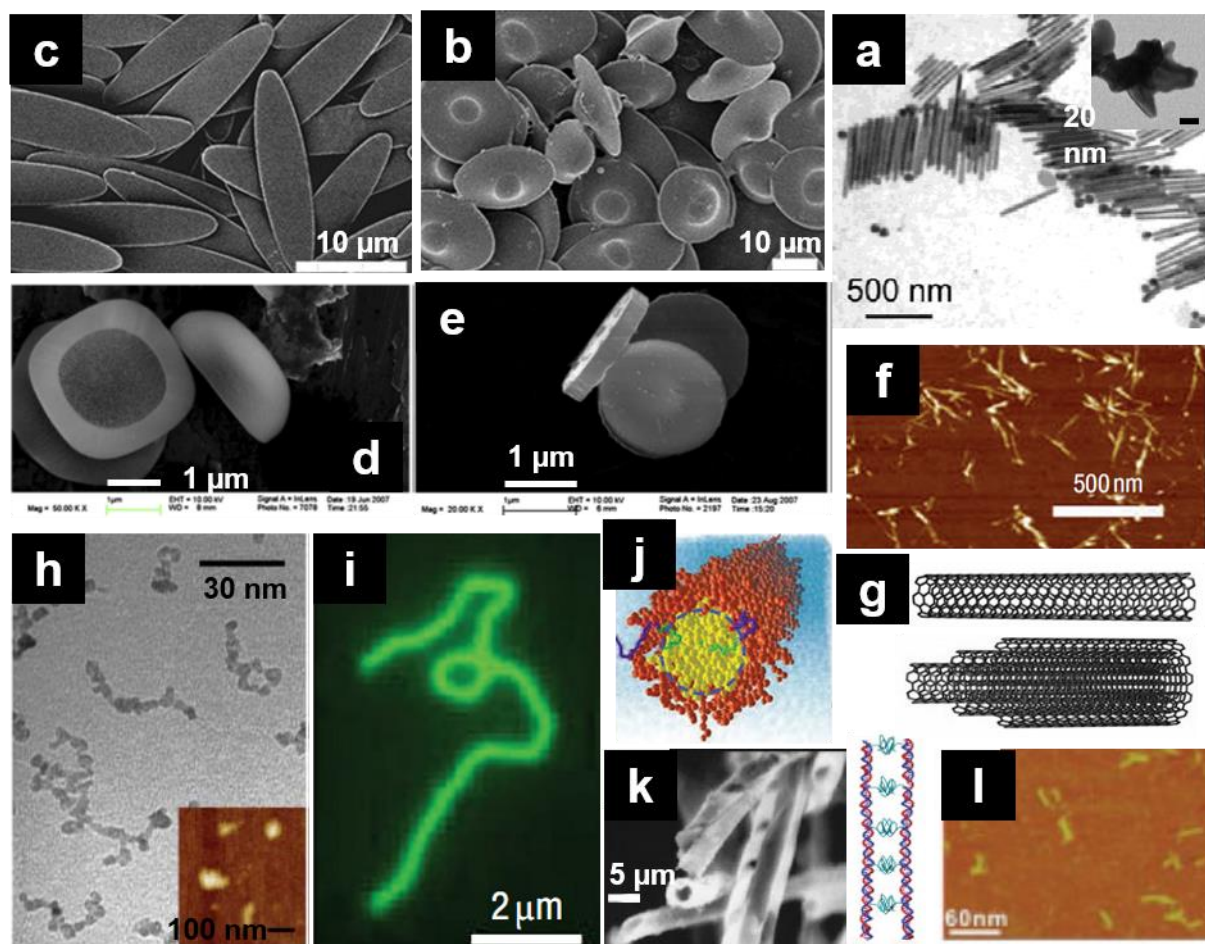
Figure 1 – Selection of non-spherical particles formed with various strategies.

(a) TEM micrographs of rod-like [31] gold nanoparticles (AuNP). The inset shows an urchin-shaped AuNP [32]. (b), (c) SEM micrographs of non-spherical polystyrene (PS) particles created by a stretching technique in the form of (b) UFOs and (c) elliptical discs [22]. (d), (e) SEM images of (d) quasi-hemispherical and (e) discoidal silicon-based microparticles [33]. (f) AFM image of hydrophilic single-walled carbon nanotubes (SWCNTs) on a silicon substrate [75]. (g) Schematic of molecular structure of (top) SWCNT and (bottom) multi-walled CNT (MWCNT). (h) TEM image of worm-like nanostructure of iron oxide particles coated with dextran. The inset shows an AFM image of elongated iron oxide particles [8]. (i) Fluorescence microscopy shows an isolated filamentous block copolymer associate (filomicelle) [19]. (j) Schematic of the filomicelle structure: yellow/green indicates hydrophobic polymer, orange/blue is hydrophilic [19]. (k) SEM micrograph of copper-coated self-assembly tubules from chiral lipids. The tubules are hollow and the helical wrappings evident in some tubules are all right-handed [34]. (l) (left) Schematic of structure of rod-like DNA block copolymer micelles, consisting of two parallel double helices and (right) corresponding AFM picture of the resulting nanoobjects [3]. Images reproduced with permission [3, 8, 19, 22, 31-34, 75].

2.1.2.1   Formation of Non-Spherical Particles by Chemical Synthesis

2.1.2.1.1   Gold Nanoparticles (AuNPs)

A straightforward and classical bottom-up approach is the synthesis of particles. Gold nanoparticles (AuNP) have attracted considerable attention and are suitable for drug delivery [35, 36]. They can also be prepared in non-spherical form by selection of appropriate reaction conditions. Rods with variable length-to-width ratios below 10 can be created smaller than 100 nm [5, 31, 37], even complex forms like "urchins" are possible [32, 38] (Figure 1 c). Drug loading of these systems can be performed e.g., by the layer-by-layer technique (LbL) incorporating the active agent in the coating. Advantages of gold nanoparticles encompass ease of synthesis of monodisperse nanoparticles with different sizes (1 - 100 nm), surface functionalization, and detection based on the optical properties [36]. Nevertheless, these biocompatible particles cannot be degraded in the body and the long term toxicity is still widely unknown.

2.1.2.1.2   Silicon Derivatives

Silica nanoparticles can be prepared by two general synthetic routes: the Stöber [39] and microemulsion process [40]. These methods allow a controlled generation of spherical silica particles with uniform sizes, ranging from 50 nm to 2 μm in diameter. Mesoporous silica particles (MSN) have a well-defined and controllable morphology, as well as porosity and can be synthesized as described by Di Renzo *et al.* [41]. A modified Stöber synthesis allows for the preparation of differently shaped MSN (e.g., nanoworms, nanocylinders) by altering the molar ratios of different chemicals during synthesis [42, 43].

Another technique, yielding anisometric silicon objects, is based on the conversion of spherical beads into oblate ellipsoids by means of ion beam irradiation. This technique has been successfully applied on spheres with a diameter in the interval 125 nm – 1 μm [44].

Silicon derivatives can be fabricated in various shapes using different techniques. For cylindrical particles one fabrication method utilizes membranes. Monodisperse objects with potentially very high aspect ratios and a diameter smaller than 50 nm can be generated [45, 46]. Decuzzi *et al.* used a microfabrication approach, encompassing different etching techniques for the generation of quasi-hemispherical (Figure 1 d), discoidal (Figure 1 e), or cylindrical silicon particles with a size below 10 μm [33].

2.1.2.2   Non-Spherical Particles, Formed by Self-Assembly Methods

2.1.2.2.1   Micellar Systems

Classical self-assembly of surfactants allows adjustment of the form (lamellae, cylinders, or vesicles) of the assembled objects limited within these thermodynamically stable mesophases. The chemical composition as well as the ratio and dimension of the polar and the non-polar segment result in different macrostructures [34, 47]. Moreover, the technique is not limited to amphiphilic fatty acid derivatives, but also allows for the use of amphiphilic polymers. Block copolymers can be utilized and fundamental parameters such as stability, release properties and size can be tailored [48]. These filamentous micelles made from block copolymers can be produced with diameters below 25 nm and a length of more than 10 μm (Figure 1 i, j) [19]; even Janus cylinder architectures are feasible [49]. However, the mechanical stiffness of non-cross-linked objects is low and the structure of the non-covalent associates depends on external factors (surrounding media, temperature, etc.) in addition to the structural parameters of the monomers [47], restricting a straightforward design of the

desired geometry [34]. In this context, amphiphilic DNA block copolymers, single-stranded-oligonucleotides covalently bound to a hydrophobic core segment of biocompatible polymer, were found to form rod-like micelles through hybridization with longer DNA sequences. The rods consist of two parallel aligned double helices and have the dimension 3 - 4 × 30 nm (Figure 1 l) [3]. These micelles have been reported to exhibit various shapes, including ellipsoidal [50], rod- or thread-like micelles [51], ribbons [47], and hollow cylinders (Figure 1 k) [34], among others.

Micellar systems have already been loaded with active substances and can serve as carriers for hydrophilic and hydrophobic molecules due to their amphiphilic nature. Loading of amphiphilic compounds and lipids can be performed following different protocols, depending on the characteristics of the active pharmaceutical ingredient (API). Hydrophilic drugs can interact with the hydrophilic moiety of the amphiphilic compound. Hydrophobic drugs on the contrary can be enclosed in micelles, interacting with the lipophilic moieties.

2.1.2.2.2 Other Self-Assembly Methods for Non-Spherical Particles

The production strategy for iron oxide nanoworms below 100 nm in length (Figure 1 h) [8] is based on the linear assembly of magnetic nanoparticles, including iron oxide, along strands of high molecular-weight dextrans [52]. These segmented nanopearl chains can also be formed from different biotemplates [53], however, cannot be generated in perfect accuracy in terms of homogeneity with this method.

2.1.2.3   Template-Assisted Formation of Particles

The most prominent approach resulting in the largest variety of particles, including fibre formation, is the template-assisted approach. For the template method two general approaches are used: the coating of a core material [54], or the coating of inner surfaces of moulds in a multitude of setups, which are removed after the casting process.

Biocompatible particles mimicking key aspects of red blood cells, including the shape, could be formed with a layer-by-layer approach, by coating of a core material (Figure 2 j) [55]. Spherical and discoidal polymeric objects were used as a template for the sequential deposition of protein and polyelectrolytes. After the built-up of the coating, the core was dissolved and the characteristic shape of erythrocytes formed upon collapse of the shell. Additionally, active agents can be incorporated in the layers, or can be used as layer material itself.

Template-assisted methods are mainly based on polymeric materials. Filling of membranes serving as a moulds also allows the formation of cylindrical objects, such as rods and fibres, with high fidelity (Figure 2 a-e). It is the most versatile approach, allowing to produce a vast variety of shapes depending on the geometry of the template (Figure 2). Generally, size is accompanied by a more elaborate shape and therefore ranges primarily in micron dimension. The morphology is highly tailorable, except for the open side not facing the mould. In general, one should be aware that the presence of polymerization initiators and limitations in the scaling up may restrict the applicability of template-assisted approaches in the biomedical field.
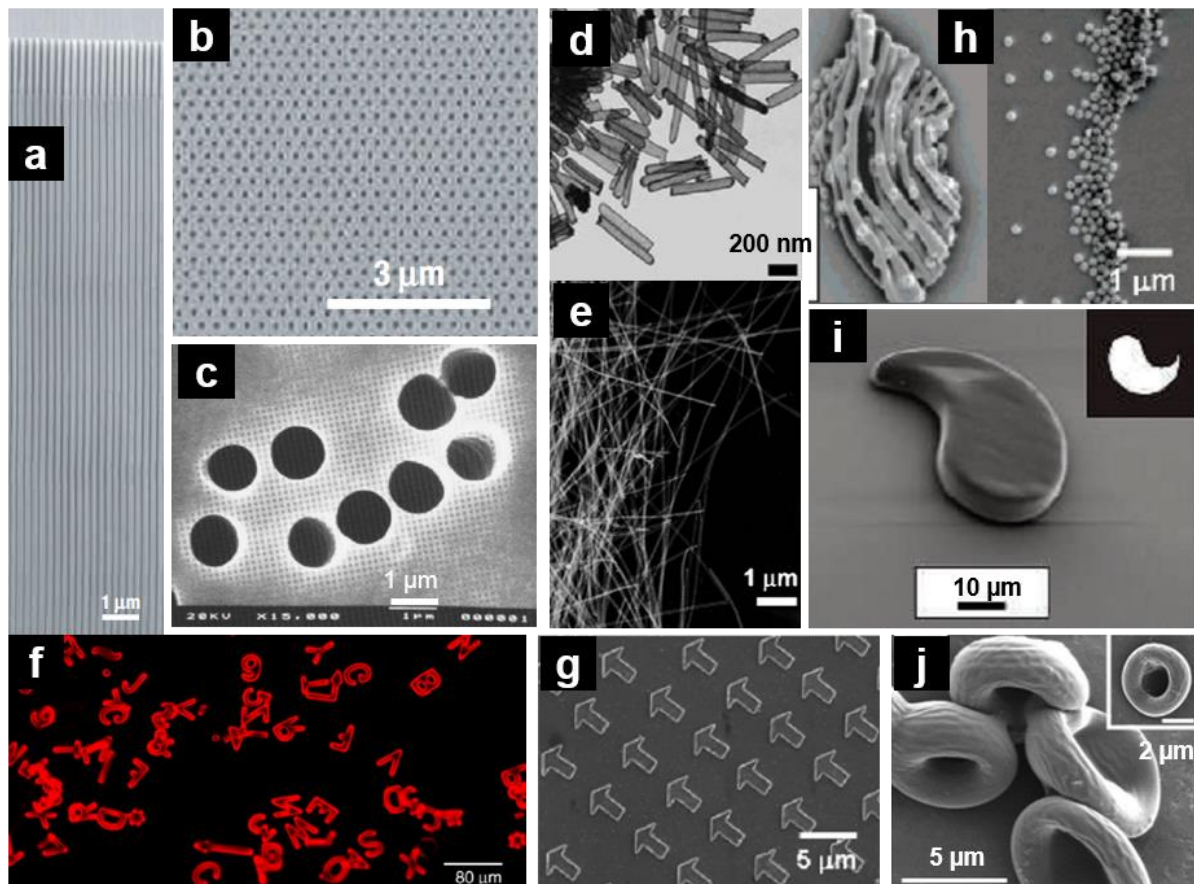
Figure 2 – Membranes used for the formation of cylindrical particles and non-spherical particles formed with template-assisted techniques.

(a) SEM micrograph of a cross-section of an alumina membrane (internal diameter = 210 nm) with an extremely high aspect ratio (>1,000) of uniform nanopores [56]. (b) SEM image showing the (top) surface of the alumina membrane with a perfect hexagonal arrangement of the nanopores [56]. (c) SEM image of a track-etched polycarbonate membrane (PC) with a pore diameter of 1 µm [57]. (d), (e) TEM micrographs of silica nanotubes with (d) 60 nm diameter and (e) length of 12.4 µm [45]. (f) Fluorescence image of PLGA particles created with a hydrogel template, representing symbols of a computer keyboard [58]. (g), (h) Polymeric particles fabricated using the PRINT process. SEM images of (g) 3 µm arrow-shaped PEG particles and of (h) 200 nm trapezoidal-shaped particles being isolated (right), or aggregated through an interlinking layer (left) [59]. (i) SEM image of a polymeric particle that was made in a microfluidic device polymerized by light. The inset shows the transparency mask feature that was used to make the corresponding particle [60]. (j) SEM micrograph of artificial red blood cells which were formed using the layer-by-layer technique [55]. Images reproduced with permission [45, 55-60].

2.1.2.3.1 Membrane Aided Formation

The well-established template-assisted method was pioneered by Martin [61]. In the approach a membrane with uniform pores is utilized, enabling the formation of cylindrical objects within the confined space. After filling of this confined space, the template is dissolved, releasing the desired cylindrical particles. Porous alumina membranes (Figure 2 a, b) and track-etched membranes (Figure 2 c) are the two most common templates for this approach [58]. They can be regarded as complementary regarding their physico-chemical properties, inorganic oxide on the one hand and organic polymer on the other hand. For this reason, is it possible to choose an appropriate solvent not dissolving the deposited substance for most scenarios [62]. The internal geometry and structure of the membrane template dictates the resulting geometry (track-etched membranes ~ > 10 nm and alumina membranes ~ > 5 nm [57]), while both can be produced in a thickness of a few microns. Both types have parallel, straight, uniform pores [63], allowing the formation of fibres with very high aspect ratios with high precision and abundance (Figure 2 e) [56]. The variety of feasible materials for this approach is enormous, ranging from inorganic nanostructures, such as gold nanorods [64], or nanotubes (Figure 2 d) [65], silica tubes [45, 46] and objects made from semiconductors [61, 62] to organic compounds, including hydrophobic, hydrophilic, biocompatible and biodegradable polymers [62, 66]. Active agents can either be loaded in the material forming the cylinder, or bound to the surface.

2.1.2.3.2 Particles Replication in Non-Wetting Templates (PRINT)

Inspired by soft lithography [67], which is regarded as a promising technique for technical applications, efforts have been undertaken to translate this technology to the biomedical field. Classical soft lithography techniques have the potential to form complex structures in

the submicron dimension. The bottleneck of this method for drug delivery purposes used to be the interlinking layer that prevented the formation of separate particles (Figure 2 h, left image). The PRINT technique (particles replication in non-wetting templates) is a promising and prominent approach that uses a PFPE (perfluoropolyether)-mould which is non-wetting to both organic and inorganic compounds [28, 59, 68]. The liquid precursors in each cavity are less likely to form any connecting layer to their neighbours over the surface of the mould [59] which is a widespread problem. The PRINT technique is applicable for several materials, including proteins (albumin [69]) and biocompatible and biodegradable polymers (Figure 2 g) (e.g., poly(ethylene glycol (PEG)) [59, 70]; poly(D-lactic acid (PLA)) [59]), that can be solidified by polymerization. With this approach a resolution as low as 20 nm can be achieved with a composite mould [71]. The PRINT technique was extended and refined for the formation of high aspect ratio objects (> 50) due to a stretching step, implemented during sequential production of the flexible soft lithographic mould [72].

2.1.2.3.3 Step and Flash Imprint Lithography (S-FIL)

Continuing with lithographic techniques, Glangchai *et al.* [73] demonstrated the potential of Step and Flash Imprint Lithography (S-FIL). This nanomoulding process is applicable to biocompatible polymers (for instance PEG of different chainlength) and can form complex shapes in sub 100 nm dimension. As a proof of concept, the potential for drug delivery of susceptible payloads was assessed by loading the particles with proteins (streptavidin [73], avidin [59]). For both molecules the complex with biotin could be formed and was interpreted as an indicator for a gentle loading process, maintaining the biological functionality of the proteins.

2.1.2.3.4 Hydrogel Template Method

In this context, the use of other mould materials has also been described in literature.

Acharya *et al.* [58] report about a hydrogel (gelatin) template for the fabrication of complex

particles down to size of 200 nm. The template is prepared by pouring an aqueous solution of

gelatin onto a master, which has protruding geometries. After solidification and removal, the

gelatin mould is filled with an hydrophobic polymer, e.g., poly(lactic-co-glycolic acid) (PLGA)

(Figure 2 f) forming the particles.

2.1.2.3.5 Continuous Flow Lithography

Dendukuri *et al.* described a photolithography-based microfluidic technique, allowing the

production of complex shapes (Figure 2 i) [60]. An oligomer stream (PEG-diacrylate),

containing a photosensitive initiator, flows through a microfluidic device and is cured by

pulsatile light irradiation. Hereby, particle geometry is controlled by the mask and the cross-

section of the channel in the microfluidic device. This technique allows for the formation of

objects ≥ 1 µm (Figure 2 i). Since this is a continuous technique, with low polymerization times

of below 0.1 s, the yield is high and should therefore be well suited for large scale production.

Nevertheless, the presence of polymerization initiators and limitations in scaling up might

restrict the applicability of the presented approaches in the biomedical field.

2.1.2.4 Various Approaches to Form Non-Spherical Particles

2.1.2.4.1 Carbon Nanotubes (CNTs)

Carbon nanotubes (CNTs) [74] are considered as promising materials even for biomedical

applications [75, 76]. CNTs can exhibit diameters as low as a few nanometres and a length of

up to centimetres [77]. These potentially extremely high aspect ratio fibres form upon

addition of energy, either in the form of light (laser ablation), electricity (arc discharge), or heat (chemical vapour deposition) to a carbon source. These tubes can be divided into two classes (Figure 1 g) [24], single-walled CNTs (SWCNTs) (Figure 1 f) [75, 78] and multi-walled CNTs (MWCNTs), concentric single-walled tubes stacked into each-other. They have been intensively studied ever since their discovery 1991 [74]. In general, these particles are hydrophobic but can be rendered water soluble by surface modifications. In addition, allowing for drug loading [78] and reducing the pronounced tendency to agglomerate. Even though being a promising approach, safety issues still need to be investigated thoroughly. This is of special interest regarding the structural analogy to asbestos in particular for longer tubes [24].

2.1.2.4.2 Stretching of Spheres

Mitragotri and co-workers have utilized a mechanical stretching method based on the work of Ho *et al.* [79] to form polymer particles consisting of polystyrene (PS) [22, 80], or PLGA [2, 81]. The spherical objects, used as precursors are immobilized in a polymeric film. Thereafter, they are liquefied either by dissolution in a solvent for the precursor, or heating above the glass transition temperature and subsequently stretched. Modifications of this protocol yield shapes in great variety [80], including complex shapes in great diversity with diameters well below 1 μm (Figure 1 a, b) whereas size depends on the primary particles. Furthermore, the particles can be loaded with active compounds.

2.1.2.4.3 Electrospinning

Electrospinning is a technique used widely in tissue engineering [82-85]. It allows for the generation of fibres from a multitude of polymers, ranging from synthetic to natural, including biodegradable polymers and blends, in the micron and nanometer size range. It is a

continuous process, which is ideal for the generation of meshes having a random distribution of fibres.

The standard electrospinning setup consists of a round nozzle, being one electrode and a plain collecting plate, representing the other electrode. An electrical potential is applied between the drop at the nozzle and the collector. A jet is emitted from the drop and approaches the oppositely charged collecting plate. Repulsive forces between the charges, accumulated within the jet, cause a continuous elongation of the jet over time. The jet does not elongate in a straight line until the solvent is utterly evaporated and the polymer has solidified. The jet changes its direct trajectory toward the opposite electrode in the range of milliseconds and approaches in spiralling loops. Depending on the experimental setup this phenomenon can be observed several times. The morphology of the fibres result from both, the evaporation of the solvent and the elongation of the thread during the formation [82]. This mechanism holds true for solutions, classically being applied for electrospinning.

In General, electrospinning yields smooth wires with a homogenous diameter over the entire length. Variants of fibres, including tubes and core-shell fibres have been described. Objects such as particles can be incorporated into the fibres. The technique is not limited to solid and resistant inorganic particles. Literature gives examples for successful incorporation of small molecules, macromolecules, such as DNA, proteins, enzymes, and even sound cells.

The bottleneck of this technique is the alignment and ordering of the filaments, which is not described for unordered meshes. The alignment is a prerequisite for the production of fibres with a defined length. This step could extend the applicability beyond tissue engineering and wound healing, which are locally applied, for the broader field of drug delivery, using nanofibres with a length of choice. Different approaches have been described, most

commonly using a rotating cylindrical collector electrode [82] in order to align the fibres. Subsequently, the fibres can be cut mechanically or using a laser.

2.1.2.5 Stimulus Triggered Transition of Shape

The shift of morphology of non-spherical particles in response to an external trigger with relevance for drug delivery has been reported [81]. Based on the observation that geometry modulates internalization processes, the transition of shape could be utilized to precisely control the kinetics and success of ingestion. Elliptical disc microparticles made from varying PLGA morphed into spheres of equivalent volume. In all cases the driving force for the morphological switch has been the minimization of interfacial tension, opposed by the viscosity of the PLGA. Stimuli have been altering this balance and therefore could accelerate the conversion. Firstly, the elevation of temperature leads to a decrease of viscosity of PLGA. Secondly, PLGA, being a weak acid, exhibits a varying degree of dissociation depending on the surrounding media; its charged groups possess a higher polarity and alter the interfacial tension. Consequently, the reduction of the pH causes a decreased polarization due to protonation of the acid functions, which itself gives rise to a higher interfacial tension. This thermodynamic unfavourable state is circumvented by downsizing of the interface forming spheres. The last stimulus examined was the binding of amphiphilic chemicals. A positively charged compound with a non-polar residue could bind to the negatively charged PLGA particles in physiological pH (~ 7.4) and increased the interfacial tension. This is analogue to the effect of the reduction of the pH.

A clinical application is conceivable, may it be the elevation of temperature through ultrasound exposure, the acidic environment in tumours or the administration of an amphiphilic compound.

2.1.3 Effects of Non-Spherical Shape of Drug Carriers on Processes *in Vivo*

The production of micro- and nanostructures with high homogeneity and precise control of the geometry has paved the way for the elucidation of the implications of shape for biological processes. The various production techniques for micro- and nanoparticles (2.1.2) of desired shape have rendered it possible to discover fundamental mechanisms that are relevant for many disciplines, including drug delivery.

Nonetheless, factors influencing the outcome of the studies besides the shape are plentiful and their interplay is complex. In some cases, the effect cannot be fully attributed to shape. Parameters such as elasticity [19, 70], size and volumes [4, 8, 10, 32, 33, 86], material composition [33], surface charge and chemistry [9, 10] are favouring certain pathways and impeding others. The whole set of properties of a particle is responsible for the behaviour under the respective experimental conditions and may serve as an explanation for the contradictory outcomes of some studies.

2.1.3.1 Internalization Processes and Trafficking

The dependency of size on internalization mechanisms has been studied widely [87, 88]. Smaller objects are known to be taken up more rapidly and the internalization mechanism differs with respect to the size. Having the chance to create specific bindings, receptor mediated internalization is favoured.

Endocytosis can be subdivided into four main pathways [89], namely phagocytosis, macropinocytosis, clathrin- and calveolae-mediated endocytosis. Phagocytosis is the mechanism through which specialized cells usually internalize objects larger than 0.5 - 0.75 μm in diameter [90]. It involves the formation of highly ordered actin structures in form of cup-like or toroidal arrangements, which are specific for phagocytosis; polymerization in different

arrangements are also observed during other endocytosis pathways. Drawing the line to a size of 500 nm for receptor mediated endocytosis, particles below this threshold are predominantly internalized by a calveolae-mediated mechanism (< 120 nm), whereas the internalization of objects < 200 nm involve clathrin-coated pits [1, 87]. Macropinocytosis is of major relevance for endocytosis above the limitation of 500 nm, not showing the actin polymerization in a ring-like fashion, which is specific for phagocytosis. The engulfment of smaller particles requires a minor rearrangement of the cytoskeleton, whereas this becomes more pronounced with the formation of protruding actin filaments for larger particles. In parts, the results of the study presented in the following subchapters might seem contradictory at first sight. In order to describe the whole picture, the conditions of the studies are presented in detail.

The geometry of an object impacts many mechanism of internalization, not only relevant for pulmonary drug delivery. The most important clearance mechanism for the clearance of foreign material in the deep lung is phagocytosis [22]. The mechanism of internalization differs substantially, depending on the target region, the cell species within the target region and the characteristics of the particle (including the size, the shape, the surface chemistry, etc.)[15].

2.1.3.1.1 Phagocytosis

Phagocytosis is one of four pathways of endocytosis, which are used for internalization processes into cells. It describes the physiological process of clearing, amongst others, foreign objects of dimension 500 -750 nm and above, which is performed by specialized cells [90]. It is of particular importance for pulmonary drug delivery, because it is the dominant mechanism for clearance in the respiratory region. Mitragotri and co-workers report in their seminal paper about the implications of differently shaped polystyrene objects on phagocytosis, studied with

rat alveolar macrophages (Figure 3) [22]. Being phagocytes and part of the innate immune system, the macrophages internalized these non-spherical particles, recognizing it as "contamination". The success of the engulfment is depending on two factors. Firstly, the initiation of the ingestions is substantially influenced by the local shape at the place of first-contact with the particle, spherical particles only exhibiting one, in contrast to non-spherical particles having at least two. Roughly, the limitation for internalization is the geometrical shape of a sphere, being more oblate the macrophage will only spread on the object. On the other hand, a more conical local morphology leads to a synchronized polymerization of cytoskeleton component actin, a toroid is formed around the object as the membrane is pushed further over the object. Importantly, this finding entails various phagocytosis scenarios for identical non-spherical particles, depending on the initial orientation of the particle towards the macrophage during the initiation of phagocytosis. The completion of phagocytosis is limited by the volume of the object; particles with volumes exceeding the dimension of the phagocyte are not being ingested. The experiments were performed with objects (spherical and non-spherical) with equivalent volumes of 1 - 12.5 µm PS spheres with and without decoration with the immunoglobulin G (IgG). Notably, the decoration with IgG antibodies did not alter the behaviour of the macrophages with respect to initiation of phagocytosis.
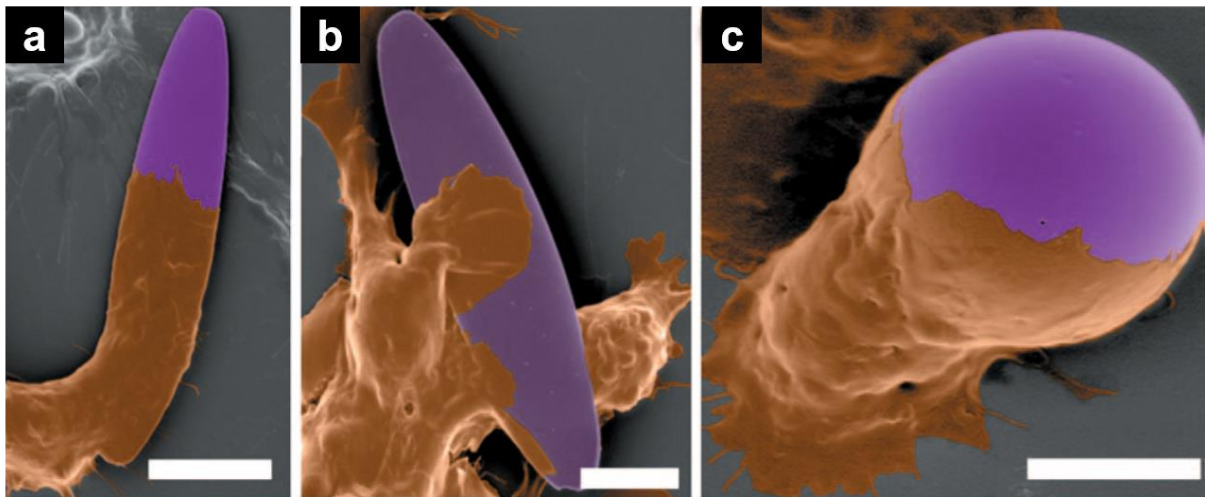
Figure 3 – Colourised SEM micrographs of alveolar macrophages internalizing non-spherical particles.

The macrophages (brown) interact with polystyrene particles (purple) of different shapes and in different orientations [22]. (a) The cell body can be seen at the end of an elliptical disc and the membrane has progressed down the length of the particle. (b) A cell has attached to the flat side of an elliptical disc and has spread on the particle. (c) A spherical particle has attached to the top of a cell and the membrane has progressed over approximately half the particle. Images reproduced with permission [22].

Applying the paradigm to the shape of a disc for instance, phagocytosis is only initiated if macrophages approach from the narrow ends of the object. If the initial point of contact is on the flat side of the disc, meaning that the curvature is low, phagocytosis will not take place. Similarly, stiff worm-like objects made from PS could only become internalized if the point of initial contact happen to be the ends [23].

This shape and orientation dependant uptake allows for the explanation of phagocytosis on flexible filamentous micelles, the so-called filomicelles and the longevity of circulation [19]. *In vitro* examination of phagocytosis (with and without flow) with activated human macrophages THP1 revealed that filamentous micelles were internalized less often than spherical micelles. The exceptional circulation time of over 1 week in mice could be explained with the alignment of the flexible micelles with the blood flow, giving rise to fewer collisions of the micelles with

the vascular walls and contact with RES. The reticuloendothelial system (RES) or mononuclear phagocyte system (MPS) is tissue rich of phagocytotic cells, such as the spleen and the liver, responsible for the clearance of the blood stream. Additionally, being flexible the filomicelles could extricate from the phagocytes and were dragged away by the strong hydrodynamic force of the blood flow. The particles sacrificed the part that was captured by the phagocytes, and thereby were successively shortened. It must be noted that the capturing was only observed to take place from the ends of the filaments, supporting the paradigm, that the particles can only be phagocytosed, when approaching with a high curvature region [22]. Eventually, smaller objects were entirely taken up by the phagocytes of the reticuloendothelial system like their spherical counterparts.

2.1.3.1.2 Endocytosis

Shape of some of the most infectious pathogens have been discovered to be non-spherical, such as the rod-shaped Gram-negative bacteria *Salomonella*, *Shigella* and *Yersinia* [91], the filamentous Ebola and Marburg Virus [19], or the complex shape of the bacteria virus lambda phage [92]. In the internalization of those pathogens receptor-mediated endocytosis plays a major role. It is typically the mechanism of uptake for various small objects, such as those infectious particles (virions) or nanoparticles [15], in contrast to phagocytosis, which is restricted to specialized cells proficient to internalize larger objects [90]. The effects of shape on endocytosis were studied with nanoparticles exhibiting different geometries, such as gold nanoparticles (AuNPs)[5, 9, 10, 32, 93], or larger polymeric [2, 7, 70], or silica particles [1, 94].

2.1.3.1.2.1 Computer Simulation of Endocytosis

Decuzzi *et al.* compared various shapes regarding their internalization in an *in silico* study [95]. It was computed that elongated or flattened particles, lying parallel to the cell membrane may evade, or slow down endocytosis, depending on further conditions. This in particular holds true for disc-like shapes; it is less pronounced for ovoid objects, oriented with their high curvature region towards the cell, for instance (Figure 4) [29]. Therefore, objects presenting higher curvature regions to the cell, such as discs not lying parallel towards the surface, are increasingly taken up. Spheres, being isometric, always present high curvature regions and are therefore taken up more easily.
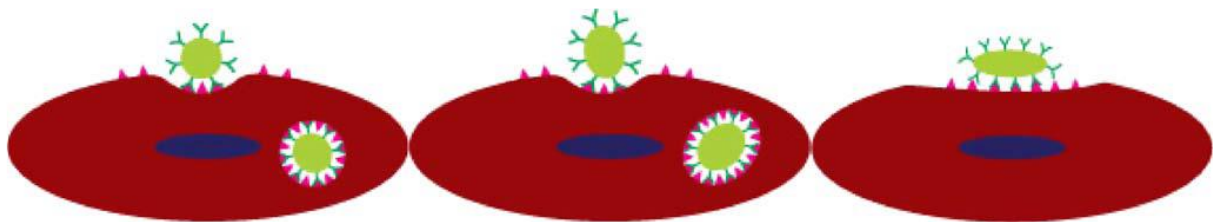
Figure 4 – Adhesion and uptake of particles with different shape and orientation to the cell membrane.
Spherical and ovoid particles are more easily internalized in comparison to the elongated particles with parallel orientation. Nonetheless, the adhesion of the elongated particle in this orientation is increased because of the elevated contact area, increasing the number of specific interactions. Illustration reproduced with permission [29].

Experimental examination and confirmation of the above mentioned hypothesis was performed by various groups. The results are summarized in detail in the following passages.

2.1.3.1.2.2 Gold Nanoparticles (AuNP)

Gold NPs (AuNP) are among the materials used most frequently for the assessment of the biological response of cells towards nanoparticles, because their shape and surface chemistry can be tailored [93] [36], neither are they immunosuppressive, or inflammatory [96].

The studies conducted with gold nanoparticles revealed that non-spherical shape reduced internalization in comparison to spheres. Since various shapes and cells were compared the details of the single studies need to be considered.

Chithrani *et al.* compared the endocytosis of rod-shaped AuNP and AuNP of a size below 100 nm. More precisely, the dimensions of the objects were 14 nm and 74 nm for the spheres and rods with aspect ratios of 3 (14 × 40 nm) and 5 (14 × 74 nm). HeLa cells (immortalised human cell line) were used for the *in vitro* experiments. It was found that the number of ingested particles per cell for both aspect ratios lies below both spheres. Longer cylinders were engulfed to a lower extent than their shorter counterparts.

The uptake mechanism was studied in more detail and quantified comparing AuNP spheres (14 and 50 nm) and rods (20 × 30 nm, 14 × 50 nm, 7 × 42 nm) coated with the protein transferrin [10]. It was confirmed that spheres were predominantly taken up. Depending on the cell line (fibroblasts (STO cells) HeLa cells and brain tumour cells (SNB19 cells)) more than 5-fold 50 nm spheres were internalized compared to the highest aspect ratio rods. The higher the aspect ratio, the less was taken up into the cells.

It should be mentioned that there is reliable evidence that transferrin was only bound to the ends of the rods. The surfactant Cetyltrimethylammonium bromide (CTAB), which is obligatory for the formation of the rods, but not the spheres, was most likely still bound to the longitudinal surface and was thereby preventing the adsorption of protein.

Besides the shape, the varying decoration with proteins might play an essential role for the uptake behaviour. In addition to deliberately modified surfaces, upon injection the particle surface is covered with plasma proteins. This protein corona substantially differs depending on the surface properties and thus the material of the system with respect to amount, pattern and type [10, 97].

Interestingly, opsonisation can also be affected by the particle shape, leading to different types and orientations of the adsorbed opsonins [33].

Hutter *et al.* [32] found differences in the distribution for the uptake into brain tissue (hippocampal neurons and microglia cells). It was concluded that this can be attributed to a differing mode of internalization favouring a certain geometry. In the study, spherical (23 nm), rod- (43 × 12 nm) and urchin-shaped (77 nm) AuNPs (Figure 1 c) with the same surface chemistry were examined. The particles were either coated with PEG, or the presence of the salt CTAB rendered the particles positively charged. It was found that urchins were predominately taken up by microglia and rods were only imbibed by neurons. Microglia cells are the resident macrophages of the brain and spine contributing to preserve the homeostasis through clearance processes, internalizing the irregularly shaped urchins that exhibit many high curvature spikes. Neurons typically internalize proteins through endocytotic pathways.

The internalization of AuNP spheres (30, 50 and 90 nm diameter) and rods (10 × 35 and 10 × 45 nm) was quantified on the human prostate cancer cell line PC-3 [9]. Plain AuNP spheres (negative zeta potential ~ -34 mV) were compared with the identical spheres after PEGylation, rendering the zeta potential more positive (~ -20 mV) and PEGylated rods with positive zeta potential (~ +20 mV), due to the formation process. The plain AuNP were internalized partially to a 1000-fold higher extent compared to the PEGylated (spheres + rods) counterparts. PEGylation is an established modification, increasing the surface hydrophilicity,

thereby reducing uptake substantially [98]. A higher quantity of 45 nm long rods was internalized than the other PEGylated shorter 35 nm cylinders. Comparing the spheres, the 50 nm particles were taken up to the highest extent, however, exceeded by the larger rods.

In the studies by Chithrani *et al.* [5, 10] the uptake was observed to be lower and slower for gold nanorods in comparison to spherical AuNPs. It was speculated that this could be attributed to differences in curvature between spheres and rods [5] and thereby confirmed the biophysical hypothesis of the theoretical model [95]. Additionally, it was speculated that cylindrical particles having adsorbed longitudinally, can have a higher contact area with the membrane in comparison to spheres, which can block further receptors that would not be available for the ingestion of other particles.

Being contradictory results in comparison to the other studies by Hutter *et al.* [32] and Arnida *et al.* [9] (on first sight), one ought not to forget that the surface charge differed fundamentally and influences cannot be neglected for the interpretation. The steric hindrance due to PEGylation prevents the binding to the cell and it was speculated that the positive surface charge enhances interactions. The surface of cells exhibits a negative charge, favouring cationic surface charge of carrier systems over neutral or positive surface chemistry [99, 100]. Elongated objects exhibit an increased contact surface, causing more uptake in contrast to the paradigm of reduced uptake for elongated objects (2.1.3.1.1).

2.1.3.1.2.3 Particles with Features in the Micron Range

Herd *et al.* examined the impact of geometry of silica particles on the mode of internalization in a variety of cell lines, including the immortalized cell line A549 epithelial lung cells and the primary cells: murine macrophages RAW 264.7, human alveolar, tissue macrophages and epithelia cells [1]. The silica particles had spherical (~ 200 nm), cylindrical (~ 400 × 200 nm)

and worm-like (~ 1300 × 300 nm) shape [86]. In a prior study, the group did not find significant differences for the uptake in A549 and RAW 264.7 cells for the tested particles [86], neither were significant differences found for the toxicity. A threshold for the toxicity of the silica nanomaterial, regardless of the tested shapes, was discovered. In the recent study, the group elaborated on the differences of the uptake mechanisms, utilizing specific pharmacological inhibitors, as well as TEM analysis, the pattern of actin polymerization (phalloidin staining) and gene expression [1]. Phenotypical differences between the macrophage cell lines (alveolar and tissue macrophages) regarding the degree of uptake, were confirmed by the pharmacological studies. More spheres were taken up by alveolar macrophages in comparison to tissue macrophages. Furthermore, pharmacological inhibitors showed a different effect on the species of macrophages, proofing that cell function is relevant for the outcome. In brief, spherical particles were internalized predominately through clathrin-mediated endocytosis, whereas the larger worm-like silica particles were either internalized through micropinocytosis, or phagocytosis. Gene expression studies were not specific for the discrimination. One dimension of the worms is still within the limit of 200 nm for clathrin-mediated endocytosis, which seemed to be activated for particles approaching with their transversal side. Not all experiments were performed with the cylindrical particles, because of the high similarity with the worm-like particles.

In another study, silica particles with varying aspect ratio were compared regarding their uptake into HeLa and A549 cells [94]. The mesoporous silica nanoparticles had diameters of 50 - 90 nm and length of 110 - 300 nm, the three groups had aspect ratios of ~ 1.5, ~ 2.5 and ~ 4.5. The aspect ratio determined the quantities of uptake, with a maximum for the aspect ratio of 2.5 taken up through macropinocytosis. For these particles, the maximal number of filopodia, actin polymerization and the correspondent protein expression was induced. The

particles were loaded with the chemotherapeutic drugs camptothecin and paclitaxel and showed the highest cytotoxicity in HeLa cells for this aspect ratio. It was concluded that the cells are capable of sensing the differences of the aspect ratio.

Larger polymeric non-spherical particles in the micron size range formed by a stretching technique [80] were used for other studies [2, 7]. Muro *et al.* [7] also exposed HUVEC cells to elliptical discs (0.1 × 1 × 3 μm) and spheres (0.1, 1, 5, 10 μm) that were both decorated with ICAM ligands (intercellular adhesion molecule 1) in order to selectively target the endothelium.

The uptake kinetics for discs were slower than for spheres. This observation lead to the speculation that this might be attributed to a novel uptake mechanism and the group discovered that internalization happened via CAM-mediated endocytosis (cell adhesion molecule-mediated endocytosis), since clathrin- and calveolae-mediated pathways usually are restricted to much smaller dimensions [15]. Systematic biochemical inhibitor studies reveal that particles of all examined geometries were taken up through the same process. Differences were observed for the kinetics and the relative orientation towards the actin-stress fibres, which are rearranged during endocytosis.

Yoo *et al.* [2] compared the uptake of spherical particles (PS 1 μm or PLGA 1.8 μm diameter) with the uptake of elliptical discs of identical volume (either PS or PLGA). The volume was kept constant through stretching of the respective beads (2.1.2.4.2). The elliptical discs exhibited aspect ratios of ~ 5 and had dimensions of 0.2 × 0.7 × 3.5 μm³ for PS and a length of ~ 7 μm for the larger PLGA discs, respectively. The discs were conjugated with poly(L-lysine) (pLL) on the surface, rendering the zeta potential positive. The experiments were conducted with different cell lines; bEND 3, a mouse brain endothelial cell line for PS and HUVEC, human umbilical vein endothelial cells for PLGA. Both morphologies were taken up by both cell lines

for both materials. Significant differences for the uptake kinetics comparing spheres and discs were observed

In accordance with Muro *et al.* [7] discs were taken up more slowly than spheres. More precisely, PLGA discs were internalized to much lower extend (4-fold) within the first hour, over the course of the experiment levelled off after 4 h, with only a mild excess of ~ 30 %. Discs exhibited predominately tangential orientation during uptake. The slower kinetics for uptake of discs in both studies can be explained with the higher surface-to-volume ratio in comparison to spheres, giving rise to an elevated deformation of the plasma membrane in order to adapt to the varying curvature of the disc.

Gratton *et al.* [70] examined the internalization of polymeric cubes and cylinders (aspect ratio of 3 or below) with pronounced differences in size and shape in HeLa cells. Particles made from cationic, cross-linked PEG hydrogels, formed with the PRINT technique [59, 68], were observed to show a significantly different ingestion with respect to the kinetics and the amount. Cubic particles of 3 µm and 5 µm side length were internalized to a much lower extend (< 20 %) than smaller 2 µm cubic particles (45 % uptake); all other geometrical objects, being smaller and cylinders with variable aspect ratio were engulfed to at least ~ 75 %. Substantial difference were observed for the speed of endocytosis. Having comparable volumes, the longer rods with an aspect ratio of 3 (150 × 450 nm) were internalized four times faster than the rods with aspect ratio 1 (200 nm). The internalization efficiency in both cases was above 75 %, with a higher value for the prolonged particles. Comparing the rates of internalization for rods with an aspect ratio of 3, the objects with a diameter of 100 nm exhibited a slower uptake in comparison to a diameter of 150 nm. The extend of uptake could not be increased through smaller size. Furthermore, the study indicates differences in the mode of uptake with respect to shape and size. The 150 nm diameter particles with aspect

ratio 3 use multiple uptake mechanisms, explaining their amplified internalization (faster and more), involving clathrin- and calveolae-mediated and others mechanisms, whereas it was speculated that the other particles mainly utilize non-clathrin and non-calveolae-mediated pathways (200 nm and 1 µm cylinders with aspect ratio 1).

In a nutshell, the observed behaviour could not be traced back to a single variable, considering the differences of the particles regarding size, volume, aspect ratio, volume and charge effects. It was speculated that the increased contact area of particles with higher aspect ratio allows for more cationic interactions with the cell membrane; particles with negative zeta potential exhibited slower uptake, which is in accordance with other studies [9, 32]. The increased contact area resulted in slower uptake in other studies, which was explained with the unfavourable deformation of the cell membrane, in contrast [2, 7].

A multitude of factors have to be considered for a complete elucidation of uptake. Physical properties [12], such as flexibility, should also be taken into account. The particles prepared with the PRINT process show a certain flexibility [70]. Dennis Discher and co-workers report about the relevance of elasticity and shape for the uptake of so-called filomicelles (Figure 1 i, j) [19]. These are flexible, filamentous micelles with a diameter of ~ 50 nm and a length of more than 10 µm and are decorated with PEG that show an exceptional longevity in circulation, in contrast to their spherical counterparts. Phagocytosis in macrophages was examined under flow, as well as endocytosis into epithelial cells (human lung-derived epithelium) under static incubation conditions. In contrast to phagocytosis, for which an internalization of particles below 3 µm was observed, only filomicelles with a length of 2.5 µm were recovered after incubation, implying a different mechanism. It was speculated that after longitudinal adhesion, motor mechanisms pinch off smaller endolysosomal vesicles, fragmenting the micelles.

It should also be mentioned that contradictory observations have also been made regarding the uptake behaviour of non-spherical microparticles. In a study using filamentous DNA block copolymers the uptake into the epithelium was examined. The internalization of rods (~ 3 – 4 × 30 nm) was 12-fold more efficient compared with spheres (~ 5.5 nm) observed after lysis of the Caco2 cells [3]. This again shows that the impact of design parameters for drug delivery systems is not yet fully understood and more systematic studies are required.

2.1.3.1.3 Intracellular Trafficking

Some studies focused on the effects of shape on intracellular trafficking and localisation after uptake, which is of vital importance for effective drug delivery. Certain agents need to interact with the DNA, therefore spatial proximity is a desirable feature for vectors designed for DNA delivery. The diffusion coefficient of macromolecules like DNA is comparably low and likelihood of reaching the target is substantially higher if the vector is able to deliver the cargo close to the target region.

Gratton *et al.* [70] found that cylindrical polymeric particles with aspect ratio 3 (150 × 450 nm) were traversed substantially further towards the nucleus than their counterparts with aspect ratio 1 for both larger (1 µm) and for smaller (0.2 µm) cylinders.

Whereas other studies, examining filamentous micellar cylinders with diameters below 100 nm and a length of several microns [19], or hundreds of nm [3] did not report about preferential subcellular accumulation.

Furthermore, it was found that the fraction of rod-shaped AuNPs, which were exocytosed, was higher than for gold spheres in the nanometer range (spheres: 14 and 50 nm and rods: 20 × 30 nm, 14 × 50 nm and 7 × 42 nm) [10]. Increased exocytosis of non-spherical particles was also observed for polymeric microparticles (elliptical discs, aspect ratio ~ 5, made from

PS, length ~ 7 μm and PLGA, 0.2 × 0.7 × 3.5 μm³ compared to spheres of equivalent volume, PS 1 μm and PLGA 1.8 μm diameter) [2].

The same elliptical discs made from PS and PLGA show a strong preference for tangential orientation around the nucleus, being random at the beginning and aligning more and more as a function of time. Further distinctions were found for the kinetics of the approach towards the nucleus, spheres approached significantly faster than elliptical discs.

2.1.3.2 Impact on Adhesion

Another fundamental implication of non-spherical shape is the increased surface area, allowing specific and unspecific interactions. Possessing equivalent volumes particulate systems with prolonged geometry exhibit a larger surface, which can result in a firmer binding. Either polyvalent specific binding, or more area for non-specific interactions, or a combination of both warrants a strong adsorption (Figure 4). Assessing the impact, a theoretical model about the avidity of the binding in linear flow between tissue and non-spherical objects was created [101]. The model allows the calculation of an ideal volume for spheres, having the highest adhesive strength (physiological values for shear stress and receptor density with sphere diameters between 100 - 500 nm were assumed). It could be inferred that oblate objects with equal volume adhere more firmly to the tissue than the spherical counterparts (Figure 4). This means that the volume for equivalent avidity is increased and more payload can be transported; the curvature of a sphere hinders multiple formations of these "anchors", in contrast to a more oblate shape. Applying these parameters to an ellipsoidal oblate particle with an aspect ratio of two results in a roughly 50-fold higher volume for equivalent adhesive strength. Principally, adhesion will only take place if the counteracting force of binding exceeds the dislodging, driven by hydrodynamic forces. The avidity increases

with the number of specific interactions and gives rise to a firm adhesion on the surface [4, 8, 29, 30, 102].

Iron oxide nanoparticles (~ 5 nm in diameter) were interconnected with high-molecular-weight dextran in order to form chain-like structures with a length of 50 - 80 nm (Figure 1 h). The particles were functionalized with the internalizing peptides F3 in one study [8] and with either of the two targeting ligands CREKA, or F3 in the later study [4] in order to provide multiple specific binding sites. The nanochains and the single beads were studied in mice and MDA-MB-435 tumour cell line [8] and in xenograft models of human carcinoma (MDA-MB-435) and fibrosarcoma (HT1080) [4]. It was observed that receptor mediated uptake of rods (5 - 10 iron oxide cores) was increased compared to spheres, composed of one to two iron oxide cores with dextran coating (~ 25 - 35 nm diameter) and a constant ratio of ligands per iron atom, due to their larger surface area and multiple attachment points.

A synthetic microvascular model with bifurcation was used in order to elucidate the adhesion of spheres in comparison to non-spherical objects, such as elongated objects (rods), flattened objects (circular discs) and the combination of both, elongated discs [103]. The particles were formed with the stretching technique (2.1.2.4.2) from spheres with a diameter of 1, 3 and 6 μm made from PS and were coated with an anti-BSA antibody. The microfluidic device was modified with bovine serum albumin (BSA), providing the complementary entity for binding. Both elongated and flattened particles showed a higher propensity for adhesion than the spheres. The elongated objects consistently showed higher adhesion, with a maximum of more than 5-fold, which was depending on the aspect ratio. Adhesion was increased in the junction of the bifurcation because of the complex flow for all tested geometries in comparison to adhesion at the inlet.

2.1.3.3   Circulation and Biodistribution

2.1.3.3.1   Spatial Distribution in Flow – Margination

Margination is the term describing the lateral migration of particles over time. Being administered intravenously, particles are instantly exposed to the hydrodynamic forces exerted from the blood flow. Decuzzi *et al.* reported that fluid dynamic effects and the structure of the vasculature give rise to a spatial distribution of the particulate components of the blood with the accumulation of the cellular components in the centre, surrounded by a "cell free layer" [29]. Theoretical models supposing laminar flow showed that (neutrally buoyant) spherical particles do not drift laterally, unless external forces are applied, such as gravitation, van der Waals, or electrostatic interactions. Non-spherical particles act differently and show more complicated motions, such as tumbling, rolling, rotation and translation. The forces exerted on the particle by the bloodstream depend on the dimension, the orientation and the geometry and result in differing margination profiles and kinetics. According to an *in silico* model, non-spherical particles tend to marginate spontaneously [104]. It was computed that prolate spheroidal particles, described and modulated by the aspect ratio, always drift laterally towards the endothelium and leave the laminar flow.

Verifying this *in vitro*, silica microspheres, quasi-hemispherical, and discoidal silicon particles with equivalent weight were injected into a laminar flow chamber. It was observed that induced by gravitational forces, discoidal particles marginate to the highest extent, followed by the quasi-hemispherical particles and the spheres to the lowest degree. This approximation is valid as long as the particles are sufficiently small and are present in the cell free layer, even though the interaction with the cellular fraction of the blood is neglected [105]. The closer proximity to the endothelium allows for an accelerated distribution to periphery vessels, because off-branching smaller vesicles are more readily entered.

2.1.3.3.2 Longevity in Circulation

Principally, extended circulation in the blood steam is a major criterion for modern drug delivery systems, in particular for cytostatic therapy. Longevity in circulation permits controlled distribution and homing of the drug into the cancer tissue [8] and can be regarded as a key parameter for the specific targeting *in vivo* [106].

Not only elongated shapes, such as filamentous micelles (filomicelles) (Figure 1 i, j), have proven to exhibit a longer half-life [19], other beneficial geometries, such as discs [107] and elliptical discs [7], have been discovered. Being inspired by nature, red blood cells are known to exhibit a long circulation [108] and methods have been found to generate artificial red blood cells, mimicking key properties (Figure 2 j) [55].

The circulation time of liposomes, in the size range of 100 - 150 nm, could be enhanced by the transformation of the spherical vesicles into a disk-like shape. Polymerization of monomeric actin into a filamentous state was utilized for this morphological transition, rats were used as the model system [107].

Polymeric elliptical discs (0.1 × 1 × 3 µm) made from polystyrene were found to remain longer in circulation in mice in comparison to their spherical counterparts (0.1, 1, 5, 10 µm) [7].

Importantly, the exceptional longevity of circulation of filomicelles cannot exclusively be attributed to geometry [19]. The filamentous micelles showed a more than ten times longer circulation of more than one week in comparison to spherical micelles, examined in rats. Rigidity seems to be an important factor as well. Filomicelles exhibiting different degrees of flexibility, showed only minor variations of the circulation time, whereas truly stiff filamentous micelles, prepared by cross-linking, were cleared within hours. A similar observation was made for iron oxide nanochains, covered with dextran with a diameter in the range of 5 nm and a length of mostly 50 - 80 nm, which did not show an elevated circulation time compared

to spherical iron oxide particles [4]. Furthermore, a fragmentation was not observed during circulation, which means that their original morphology was preserved [8]. Another example are water soluble carbon nanotubes of a length of 30 – 38 nm and a diameter of a few nm which were also excreted within hours [78].

2.1.3.3.3   Biodistribution

Polymeric elliptical discs (0.1 × 1 × 3 µm) made from polystyrene decorated with intercellular adhesion molecule (ICAM) ligands to selectively target endothelium were reported to show lower uptake by the liver and a specific targeting of lung tissue in comparison to their spherical (0.1, 1, 5, 10 µm) counterparts [7].

The effects of geometry (size and shape) on biodistribution after systemic administration in nude mice have been studied with various silica spheres (diameter 0.7, 1.0, 2.5, 3.0 µm) and non-spherical objects all having comparable volumes [33]. Spheres with diameter of 1 µm, volume 0.52 µm³ (non-porous) were compared with cylindrical (diameter 1 × 1 µm, volume ~ 0.8 µm³, non-porous), discoidal (diameter 1.6 × 0.3 µm, volume ~ 0.6 µm³, non-porous) and quasi-hemispherical (diameter 1.6 µm, volume ~ 0.6 µm³, porosity 50 - 60 %) all having a negative zeta potential (-32 to -45 mV) due to the identical preparation protocol. The biodistribution was derived from the silicon content of each organ of the tumour bearing mouse. The organs and tissues observed were heart, brain, kidney, lung, liver, spleen and tumour (MDA-MB-231 breast cancer cell line). The most pronounced differences were found for discoidal shape. Among the other non-spherical objects, cylinder with aspect ratio 1 and the quasi-hemispherical object, discs are able to circumvent sequestration by phagocytes best, such as the Kupffer cells in the liver. Therefore, discs show the least accumulation in the liver. The larger fraction that was found in other organs was explained by the higher contact

area of the discs, increasing the adherence at the interface in comparison to spheres. More specific, the highest difference (> 4-fold) was observed for lung, confirming the findings of Muro *et al.* [7], and heart tissue in comparison to the shapes having an aspect ratio close to unity. In brain, kidney and tumour tissue only minute uptake and no statistically significant difference was observed for the tested geometries. It was hypothesized that this could be associated with the relatively large size and could have hindered access to these tissues.

Again in another study, a moderately higher accumulation of non-spherical objects (fibrous filomicelles [19]) was observed. This was leading to the speculation about implications for the localisation of viral infections of the lung with respect to filamentous virions, namely the Ebola and the Influenza Virus H5N1.

Differences in the biodistribution were additionally observed by Sailor and co-workers [8], expressing the accumulation in ratios relative to the amount found in the liver, the accumulation of dextran coated nanochains (length ~ 50 nm) of iron oxide in the spleen (a RES organ) was higher, whereas it was lower in the kidneys.

In addition, these filaments showed differences regarding the retention time after extravasation into tumour tissue in comparison to the beads. Merely the spheres returned into circulation to a high extent, because they were not physically trapped.

2.1.3.4   Immune Response and Toxicity

Infectivity and pathogenicity has been reported to be linked to the shape of pathogens [109] and first toxicological studies regarding the toxicity of man-made non-spherical particles have been undertaken.

Besides varying internalization profiles as examined on brain tissue for sub 100 nm AuNP with spherical, rod and urchin shape (Figure 1 c) the immune response differed substantially [32].

Exclusively urchins and rods induced toll-like receptor 2 (TLR-2) upregulation in microglia, whereas *in vivo* experiments revealed that spherical AuNP did not alter the expression of this TLR-2. Examining the inflammatory cytokine expression pattern more in detail (including interleukin-1 (IL-1) and granulocyte macrophage colony stimulating factor (GM-CSF)), differences for urchin and rods were found, indicating a unique microglia-mediated immune response for each geometry.

First toxicological studies taking into account particle shape were conducted [110]. Nan *et al.* report about an increased toxicity of shorter silica nanorods (50 × 200 nm) in comparison to longer nanorods (50 × 500 nm). This difference can be largely attributed to the increased number of the applied particles, entailing a bigger overall surface. The data in this study was normalized on the mass.

Further particulate vectors have been reported to not be toxic, including PEGylated and plain gold nanorods and -spheres [9] and filomicelles [19].

2.2 Cell Response on Textured Surfaces

The influence of surface structure on cell response is a well-studied subject. Surface texture has shown to be a central parameter for cell communication and activity [111]. It has been discovered that the micro and nano-metric texture of mammalian cells influences basic processes such as cell migration, organization and orientation [83, 112, 113]. Other studies on the effects of artificial micro- and nano-structured surfaces have revealed more effects on cell behaviour, including adhesion, cell morphology, proliferation, and differentiation [114]. A multitude of articles focus on cell response and behaviour on planar (soft and hard) surfaces [115-118], mainly formed with lithographic techniques (such as photolithography and electron beam lithography) extensively used for microchip manufacturing. Yet another method was added to the tool box through the advent of soft lithographic techniques [116, 119, 120], most commonly using the organosilicon compound polydimethylsiloxane (PDMS) [120]. Both the solid silicon wafer and the elastic PDMS master can be utilized to cast many fundamentally different materials, including elastic substrates [118, 121, 122], biodegradable polymers [115], such as the approved PLGA (for pharmaceutical applications) [116, 123], etc. The development of flexible moulds has facilitated the structuring of curved objects that are more adequate for an application *in vivo* in comparison to large planar surfaces, useful for example for implants. Studies with more relevance for the situation *in vivo* could be conducted.

2.2.1 Surrogates for the Extracellular Matrix (ECM)

Finding an adequate surrogate for the extracellular matrix (ECM) is a major objective in the biomedical field [83]. The importance of the geometry of structures also hold true for this biological interface.

The ECM is a hydrophilic material composed of a multitude of macromolecules, lining many types of mammalian cells. It influences essential cell functions, such as the cell communication and activity, and is more than an inert surrounding of the respective cell. The spatial distribution and shape of components is highly important for sound function of the ECM. Mastering the mimic of the composition of the ECM is not sufficient as the localization of the compounds and the geometry are of equal importance [111, 124]. The ECM contains fibrous structures, among which the fibrous glycoproteins from the family of the collagens are the most abundant group [111]. A surrogate ideally would reflect this fibrous geometry, exhibiting a high degree of structural homology with the native ECM.

Electrospinning has been proposed to be a viable technique for the development of a replacement for the native ECM. Electrospinning allows for the production of fibrous meshes made from various polymers (2.1.2.4.3) [82]. Another technique which has not been explored for the generation of fibrous surfaces is the template technique (2.1.2.3.1). This technique can be adapted for a simple and straightforward generation of hairy surfaces. These sheets feature fibres in high abundance originating from this base layer. This combination is an exceptional property of surfaces prepared with the template technique in comparison to lithographic approaches [120] that are principally limited regarding the feature height [125].

2.3 Basics of Inhalation Therapy

2.3.1 Lung Anatomy and Physiology

The human lungs flank the heart in the chest cavity. Despite the similarity the left and right section of the lung are not identical, both are divided into lobes, with two lobes on the left (superior, inferior) and three on the right (superior, middle, inferior), leaving space for the heart. The lobes can further be divided into segments and then into lobules, hexagonal subdivisions of the lungs (the smallest division that is still visible by naked eye) [126, 127]. Physiologically with respect to ventilation, the respiratory tract and the lungs can be divided into two zones. The conducting zone comprising, in direction of inhalation and with decreasing diameter, the mouth or the nose, the pharynx, the trachea, bronchia, bronchioles and terminal bronchioles. These so-called proximal airways comprise the first 16 generations of the respiratory tract. In the peripheral zone, responsible for the gas exchange, the airways branch more until generation 23, comprising the tissues responsible for the gas exchange, ranging from the terminal bronchioles to the terminal end of the respiratory tree, the pulmonary alveoli [128]. The terminal bronchioles divide into alveolar ducts that further divide into alveolar sacs [129].

The composition and structure of the epithelium differs substantially in the respiratory tract. The epithelium in the proximal airways is much thicker and becomes thinner the more the airways branch. This facilitates gas exchange in the respiratory region [130]. In the upper airways, ciliated cells move the mucus, being produced by goblet cells, in distal direction in order to remove debris and foreign material from the respiratory zone (mucociliary clearance) [131]. In the peripheral lungs, the dominant mechanism is phagocytic internalization. In contrast to the mucociliary clearance, representing a physical removal of mucus and debris, in the upper airways the clearance in the alveolar region is cell mediated.

Scavenger cells, the alveolar macrophages, clear senescent cells, pathogens and foreign material in the peripheral lung.

This is a vital defence mechanism, considering the low enzymatic activity and the subtlety of the biological barrier. The large absorption area, the intensive perfusion and the fact that the first pass effect can be circumvented are further convincing arguments for the application of therapeutics via the lung [132]. Not only the systemic administration of small molecules is feasible, also peptides can be administered. The inhalable insulin Exubera (Pfizer Inc.) has been withdrawn from the market, because of an increase of the cancer prevalence; insulin acts as a growth factor. Nonetheless, the inhalable insulin Afrezza (MannKind Corp.) has been approved by the Food and Drug Administration (FDA) in July 2014.

2.3.2   Particle Inhalation

The effectiveness of pulmonary administration depends both on the therapeutic and the inhalation through the patient. Considering physiological inhalation, general requirements have been found for aerosols for inhalation purposes. The aerosol is described by the aerodynamic diameter (d_{aer}) (Equation 1). The d_{aer} of a sample particle is given by the diameter of a sphere with the density of unity that reaches the same terminal velocity [133]. The values for the aerodynamic diameter is influenced by the geometric diameter (d_{geo}), the density ρ and the correction factor χ, which is correcting the influence of shape. χ is 1 for spherical particles and > 1 for non-spherical particles [134]. The equation cannot be applied to all non-spherical shapes, the impact of alignment cannot be accurately described with this approximation.

$$d_{aer} = \chi \times d_{geo} \times \sqrt{\rho}$$

Equation 1 – The aerodynamic diameter (d_{aer})

Based on this value general limits were found. The ideal size for particles, which are intended to proceed to the peripheral lung, is an aerodynamic diameter of 5 – 1 μm. Particles with a d_{aer} between 1 – 0.2 μm are exhaled after inhalation, whereas even smaller particles than 0.2 μm deposit to a great extent [135, 136] (Figure 5). These ultrafine carriers suffer from low payload that can be transported per particle and high surface which can result in aggregation. For these reasons formulation of nanoscopic aerosols is regarded as particularly challenging.
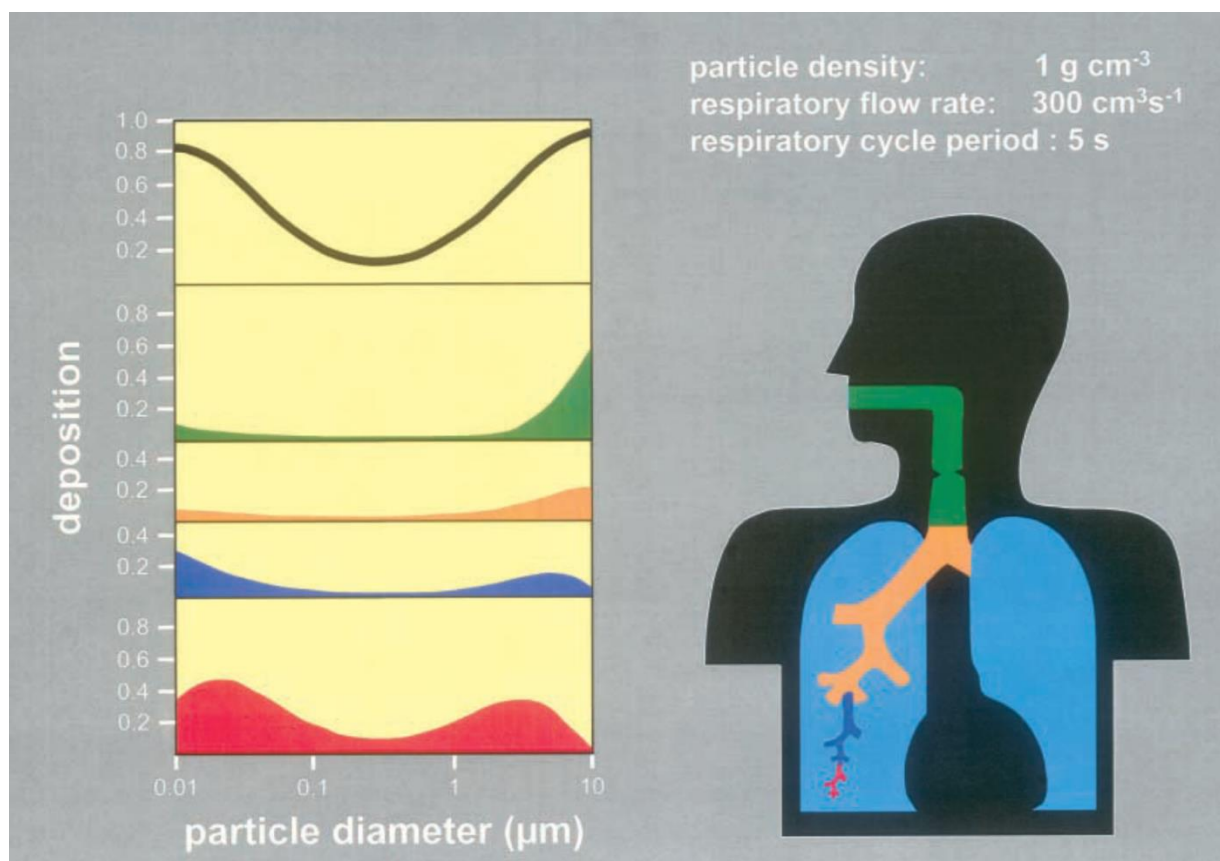
Figure 5 – "Total and regional deposition of unit-density spheres in the human respiratory tract".

The extrathoracic region is depicted in green, the upper bronchial region in orange, the lower bronchial region in blue and the alveolar region in red. Illustration reproduced with permission [136].

The aerodynamic diameter can be assessed with various impactors that are described in the United States Pharmacopoeia (USP) and the European Pharmacopoeia (Ph.Eur.); the state-of-the-art impactor is the next generation pharmaceutical impactor (NGI) (4.2.1.1). Based on the cut-off values of impactors the fine particle fraction (FPF) was introduced. It describes the fraction of an aerosol with a d_{aer} below 4.7 µm [137, 138], whereas this value is rounded to 5 µm in many publications. The FPF describes the particles that can proceed to the peripheral lung, the threshold can be drawn at 5 microns; particles with $d_{aer} > 5$ µm mainly deposit in the upper airways, the oropharyngeal region [139].

The particle deposition inside the lung can be attributed to 3 principals. Impaction is the dominant mechanism for particles with ~ $d_{aer} > 3$ - 1 µm, for smaller particles (~ $d_{aer} > 0.5$ µm) sedimentation becomes increasingly important and Brownian motion which governs the deposition for particles with a ~ $d_{aer} < 1$ - 0.5 µm [136, 140, 141]. The site of deposition depends on the aerodynamic diameter; the bigger the particles are, the more distal the deposition occurs (Figure 5).

General Introduction

3   Aim of this Work

Classical design parameters for drug delivery systems have for a long time been size and surface chemistry, but new features are being increasingly explored. More attention is drawn towards geometrical and morphological properties, such as the texture of the surface, including porosity, flexibility and in particular shape [12, 13]. It has been revealed that the geometry of micro- and nanoparticles alters fundamental properties and the biological response (2.1.3), opening up new options for the design of progressive drug delivery systems [1, 15, 22, 23].

The major benefits of monodisperse non-spherical carrier system for pulmonary administration are:

- Alveolar macrophages clear the respiratory region from foreign materials through phagocytosis. This process was found to be strongly influenced by shape and orientation of the object [15, 22]. Modifications of geometry change time and mechanism required for uptake [1, 23]. As a consequence, certain non-spherical particles have the potential to control clearance processes, a core prerequisite for a sustained release system for therapeutics [15, 23].
  The shape of a long cylinder, or a fibre can reduce phagocytosis drastically [23, 24]. This reduction opens up the opportunity to extend the residence time, which is one of the main objectives for a sustained release system.

- Elongated objects exhibit beneficial aerodynamic properties that can be exploited for pulmonary administration. Fibres and cylinders show a higher probability to deposit in the deep lung in comparison to spheres of identical volume [18] due to alignment of

the fibres with the airstream. Therefore, the mass per particle that can be delivered to the target region is increased.

- Fibres are expected to be less prone to form aggregates, because the contact area is decreased for an erratic distribution. The large surface area of small particles can result in cohesion between single particles, which can cause severe aggregation of particles [21]. Monodispersity is a vital factor for the precise and controlled deposition in the pulmonary target region, since the site of deposition is bound to the geometrical properties of the particle (size and shape) during the inhalation process. The aggregates behave differently in the airstream, thus depositing in other regions of the inhalation tract.

Various techniques have been reported for the formation of cylinder-like particles [15], but monodisperse particle distribution is achieved only by a fraction. The currently available conventional carrier systems for lung administration are not well-defined either. For the sake of simplicity, these particles are commonly denoted spherical, even though the exact geometry is irregular. However, this description is adequate, because the overall shape is sphere-like. Tailor-made, monodisperse and truly cylindrical particles require bottom-up formation within a template, dictating the geometry. These techniques include the fabrication approaches such as PRINT (2.1.2.3.2), polymerization in microfluidic devices (2.1.2.3.5) and the template technique (2.1.2.3.1). Track-etched membranes with their highly homogenous, cylindrical pores in high abundance represent the ideal template for the formation of fibres in the dimension required for deposition in the lung. For conventional spherical particles, the fraction with a diameter below 5 µm is considered to proceed to the lung [133]. Track-etched membranes are available in various pore dimensions below 5 µm.

The pores of track-etched membranes serve as moulds for the generation of fibres. In contrast to the biopersistent asbestos, which cannot be cleared easily [24], substances are favoured that either have been approved for lung administration, or can be degraded in the lungs.

The physiological conditions and the requirements for release of APIs under these conditions must be met by the carrier system. Water soluble solids, as well as biocompatible hydrogels that degrade in aqueous media and do not accumulate represent promising candidates for this carrier system. Dissolution is impeded, because of the scarcity of the alveolar lining fluid acting as the solvent in the peripheral lung. The adequate balance between degradation and persistence has to be found. These requirements were considered for the selection of the compounds utilized for the formation of cylindrical filaments with the template technique. Various hydrogels, solids with high solubility in water (lactose and APIs) and blends of these hydrogels with those solids were examined regarding their applicability for the formation of fibrous particles with the template technique. The stability of these fibres was assessed regarding humidity, as well as the uptake of the filaments through alveolar macrophages, which depends on the orientation of the phagocyte.

Not only can the template technique be used for the formation of fibrous particles [66], it also allows for the formation of textured surfaces; the monodisperse and plentiful fibres are originating from the surface, which is a unique setup [142]. The texture of surfaces has been discovered to be a key parameter for cell communication and activity [111], the impact of shape is not limited to small objects. The micro- and nano-metric texture of mammalian cells influences fundamental processes such as cell migration, organization and orientation [83, 112, 113]. The elucidation of the implications of the surface structure is of utmost interest for the field of tissue engineering. The spatial distribution and shape of components of the ECM is highly important for a sound function, for example. The ECM contains fibrous structures,

among which the collagen fibres are the most abundant proteins [111]. A surrogate ideally would exhibit a nanofibrous geometry, featuring a high degree of structural homology with the native ECM.

The impact of surface structure and the potential utility for the improvement of surrogates for the ECM can be assessed by the adhesion pattern of fibroblasts on the respective surface. Surfaces textured with the template technique, carrying filaments in various dimensions and abundances, were tested in order to elucidate the influence on the adhesion profile of fibroblasts.

Additionally, loading of the textured hydrogel sheets carrying the filaments might proof beneficial, depending on the application. Therefore, the release of model compounds, including macromolecular and small molecules, was quantified.

4 Materials and Methods

4.1 Substances and Devices

4.1.1 List of Substances

Chemical entity or substance	Company
96-well plates Brand pureGrade	Brand GmbH & Co. KG, Wertheim, Germany
200 nm silica particles, plain blue, PSi-B0.2 (λ_{ex} = 354 nm/λ_{em} = 450 nm)	Kisker Biotech GmbH & Co. KG, Steinfurt, Germany
500 nm silica particles, plain blue, PSi-B0.5 (λ_{ex} = 354 nm/λ_{em} = 450 nm)	Kisker Biotech GmbH & Co. KG, Steinfurt, Germany
841 nm silica particles, SiO_2-F-0.85	Micro Particles GmbH, Berlin, Germany
Agarose for electrophoresis	Agarose Sigma, Sigma-Aldrich Chemie GmbH, Steinheim, Germany
Alginat, ultra-high viscosity extracted from brown algae *Lessonia trabeculata* harvested at the Chilean coast [143, 144]	own production, Fraunhofer IBMT, St. Ingbert, Germany
Ammonium hydroxide (NH_4OH) 25 % solution, Suprapur	Merck KGaA, Darmstadt, Germany
B Braun Omnifix 10 ml Luer Lock Solo syringes	B. Braun Melsungen AG, Melsungen, Germany
Brij L23	Sigma-Aldrich Chemie GmbH, Steinheim, Germany
Calcium chloride dihydrate ($CaCl_2 \times H_2O$), ≥ 99.0 %	Sigma-Aldrich Chemie GmbH, Steinheim, Germany

Materials and Methods

CapsuLac 60, alpha-lactose monohydrate	MEGGLE GmbH & Co. KG, BG Excipients & Technology, Wasserburg, Germany
Chitosan, high molecular mass, 470 kDa, DA 6 %	own production, Delair lab, Université Claude-Bernard, Université de Lyon, France
Cover slips (glass) 22 × 22 mm	Paul Marienfeld GmbH, Lauda Königshofen, Germany
D-glucose, ≥ 99.5 %	Sigma-Aldrich Chemie GmbH, Steinheim, Germany
Dichloromethane (CH_2Cl_2) p.a., ≥ 99,9 %	Sigma-Aldrich Chemie GmbH, Steinheim, Germany
Disodium phosphate dihydrate ($Na_2HPO_4 \times H_2O$), p.a.	Merck KGaA, Darmstadt, Germany
Dulbecco's modified eagle medium (DMEM)	Gibco, Life Technologies GmbH, Darmstadt, Germany
Dulbecco's phosphate buffered saline (DPBS)	Gibco, Invitrogen, Life Technologies GmbH, Germany
Eppendorf Safe-Lock Tubes 2.0 mL, polypropylene (PP)	Eppendorf AG, Hamburg, Germany
Ethanol (C_2H_5OH) 96 % vol, Ph.Eur.	VWR International GmbH, Darmstadt, Germany
Ethanol (C_2H_5OH) AnalR NORMAPUR, ≥ 99,8 %	VWR International GmbH, Darmstadt, Germany
Fetal calf serum (FCS)	Lonza Cologne GmbH, Cologne, Germany
Filter holder for 25 mm diameter membranes	Millipore Swinnex 25 mm filter holder PP
FITC (fluorescein isothiocyanate)-dextran, FITC-dextran 2000 0.3 mg/ml	TdB Consultancy AB, Uppsala, Sweden

FITC-pLL, 15 – 30 kDa	Sigma-Aldrich Chemie GmbH, Steinheim, Germany
Fluoresbrite Carboxy YellowGreen polystyrene particles (200 nm)	Polysciences Europe GmbH, Eppelheim, Germany
Fluoresbrite polystyrene particles (50 nm)	Polysciences Europe GmbH, Eppelheim, Germany
Fluorescein-sodium, p.a.	Sigma-Aldrich Chemie GmbH, Steinheim, Germany
Gelatin B bloom 75 from bovine skin	Sigma-Aldrich Chemie GmbH, Steinheim, Germany
Gelatin capsules size 3, transparent	Wepa Apothekenbedarf GmbH, Hillscheid, Germany
Gentamycin	Gibco, Life Technologies GmbH, Darmstadt, Germany
Glass slide 76 × 26 mm	ROTH, Carl Roth GmbH Karlsruhe, Germany
Glutaraldehyde (GTA) aqueous solution 25 %	VWR International GmbH, Darmstadt, Germany
Glycerol, ultra-pure, 99.5 %	VWR International GmbH, Darmstadt, Germany
HEPES Pufferan buffer, ≥ 99.5 %	Carl Roth GmbH, Karlsruhe, Germany
Hexamethyldisilazane (HMDS), reagent grade, ≥ 99 %	Sigma-Aldrich Chemie GmbH, Steinheim, Germany
L-leucine, reagent grade, ≥ 98 %	Sigma-Aldrich Chemie GmbH, Steinheim, Germany

Materials and Methods

Methanol HiPerSolv CHROMANORM for HPLC gradient grade	VWR International GmbH, Darmstadt, Germany
Methylene blue, (USP, BP) pure, pharma grade C	AppliChem GmbH, Darmstadt, Germany
Mica	Plano Planet GmbH, Wetzlar, Germany
Murine alveolar macrophages (MHS)	MHS, ATCC, CRL-2019
Murine L929 fibroblasts	DSMZ, Braunschweig, Germany
Osmium tetroxide (OsO$_4$), ≥ 98.0 %	Sigma-Aldrich Chemie GmbH, Steinheim, Germany
Penicillin/Streptomycin	PAA Laboratories GmbH, Pasching, Austria
Petri dishes, polystyrene (35, 100 mm)	Corning, Lowell, MA, USA and Greiner Bio-One GmbH, Frickenhausen, Germany
Phosphate buffered saline (PBS)	Gibco, Life Technologies GmbH, Darmstadt, Germany
Polyallylamine hydrochloride (PAH), 15.0 kDa	Sigma-Aldrich Chemie GmbH, Steinheim, Germany
Polyethylenimine (PEI), ethylenediamine end-capped, average molecular weight 800 g/mol,	Sigma-Aldrich Chemie GmbH, Steinheim, Germany
Polystyrene (PS) cuvettes	Brand GmbH & Co. KG, Wertheim, Germany
Poly(L-lysine) (pLL), 150-300 kDa, 0.01 %, sterile-filtered, suitable for cell culture	Sigma-Aldrich Chemie GmbH, Steinheim, Germany
PTFE (Polytetrafluoroethylene) membrane filter, pore size 0.2 µm, 25 mm diameter	Whatman GmbH, Dassel, Germany
RPMI 1640-medium	PAA Laboratories GmbH, Pasching, Austria

Salbutamol sulphate/Albuterol sulphate	Boehringer Ingelheim Pharma GmbH & Co. KG, Ingelheim am Rhein, Germany
Sodium cacodylate trihydrate ($(CH_3)_2AsO_2Na \times 3\ H_2O$), purum p.a.	Sigma-Aldrich Chemie GmbH, Steinheim, Germany
Sodium chloride (NaCl), ≥ 99.0 %	Sigma-Aldrich Chemie GmbH, Steinheim, Germany
Sodium hydrogen carbonate/ Sodium bicarbonate ($NaHCO_3$), Ph.Eur.	Merck KGaA, Darmstadt, Germany
Sodium hydroxide (NaOH), ACS,Reag. Ph Eur	Merck KGaA, Darmstadt, Germany
Sodium pyruvate, ≥ 99 %	Sigma-Aldrich Chemie GmbH, Steinheim, Germany
Tannic acid, ACS reagent	Sigma-Aldrich Chemie GmbH, Steinheim, Germany
Tetrahydrofuran (THF) AnalaR NORMAPUR	VWR International GmbH, Darmstadt, Germany
Tissue wipers, KIMTECH SCIENCE* Precision Wipers	KIMBERLY-CLARK PROFESSIONAL*, Kimberly-Clark GmbH, Koblenz-Rheinhafen, Germany
Track-etched membranes; PC; Whatman Nucleopore; 5.0, 3.0, 2.0, 1.0, 0.6, 0.4, 0.2, 0.1 µm pore sizes; 47 and 25 mm diameter	Whatman GmbH, Dassel, Germany
Water (deionized), resistivity higher than 18.0 MΩ cm^{-1} - Millipore Milli-Q purification system	Merck KGaA, Darmstadt, Germany
α-lactose monohydrate MEGGLE CapsuLac 60: < 100 µm: ≤ 10 %, < 250 µm: 40 - 70 %, < 400 µm: ≥ 90 %	MEGGLE Group BG Excipients & Technology GmbH & Co.KG, Wasserburg, Germany

α-lactose monohydrate Sigma, ≥ 99 %	Sigma-Aldrich Chemie GmbH, Steinheim, Germany
β-mercaptoethanol, PharmaGrade	Sigma-Aldrich Chemie GmbH, Steinheim, Germany

4.1.2 List of Devices

Device	Company
Analytical balance Sartorius CPA225D-0CE	Sartorius AG, Göttingen, Germany
Atomic force microscope (AFM)/Scanning probe microscope (SPM) Bioscope with Nanoscope IV controller	DI Digital Instruments, Bruker Corporation Billerica, MA, USA
Confocal laser scanning microscope (CLSM) Carl Zeiss LSM 510 in combination with Carl Zeiss Axiovert 100M, objective C-Apochromat 63x/1.2 water correction	Carl Zeiss Microscopy GmbH, Göttingen, Germany
Dry powder inhaler (DPI) HandiHaler	Boehringer Ingelheim Pharma GmbH & Co. KG, Ingelheim am Rhein, Germany
Dynamic light scattering (DLS)/ Photon correlation spectroscopy (PCS) Malvern Zetasizer nano-ZS	Malvern Instruments GmbH, Herrenberg, Germany
Environmental SEM (ESEM) FEI QUANTA 400 FEG ESEM	FEI Company, Hillsboro, OR, USA

Fluorescence light microscope (FLM) Axio Imager M1m, equipped with the LED system Colibri	Carl Zeiss Microscopy GmbH, Göttingen, Germany
Fluorescence spectrometer FLUOstar OPTIMA	BMG LABTECH GmbH, Offenburg, Germany
Freeze-dryer Edwards Modulyo	Edwards Ltd., Crawley, UK
Heraeus Multifuge X3 centrifuge	Thermo Fisher Scientific Germany BV & Co KG, Braunschweig, Germany
High capacity pump model HCP5	Copley Scientific Ltd., Nottingham, UK
Next generation pharmaceutical impactor (NGI)	Copley Scientific Ltd., Nottingham, UK
NGI dosage unit sampling apparatus (DUSA)	Copley Scientific Ltd., Nottingham, UK
NGI flow meter Copley DFM 2000	Copley Scientific Ltd., Nottingham, UK
NGI pre-separator	Copley Scientific Ltd., Nottingham, UK
pH electrode Mettler Toledo EL20	Mettler-Toledo GmbH, Giessen, Germany
Phase contrast microscopes Nikon Biostation CT and Carl Zeiss Axio Scope.A1 equipped with the camera AxioCam ERc 5s	Nikon Instruments GmbH, Duesseldorf, Germany and Carl Zeiss Microscopy GmbH, Göttingen, Germany
Scanning electron microscopes (SEMs) Carl Zeiss EVO HD15 and JEOL SEM-7000	Carl Zeiss Microscopy GmbH, Oberkochen, Germany and JEOL GmbH, Eching, Gemany
Shaking incubator GFL 3031	GFL Gesellschaft fuer Labortechnik mbH, Burgwedel, Germany
Sonicator BANDELIN SONOREX	BANDELIN electronic GmbH & Co. KG, Berlin, Germany
Sputter coater Quorum Q150R ES	Quorum Technologies Ltd., East Grinstead, UK
UV/VIS spectrometer PerkinElmer Lambda 35	PerkinElmer LAS GmbH, Rodgau, Germany

4.1.3   Chemical Structures
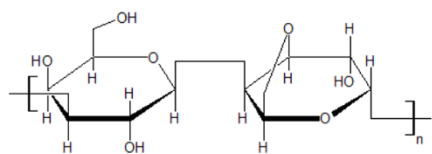
Agarose
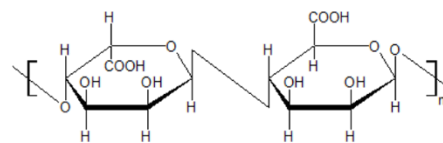
Alginic acid
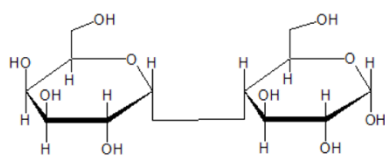
α-lactose
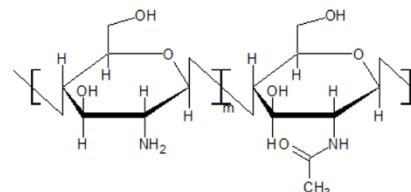
Chitosan
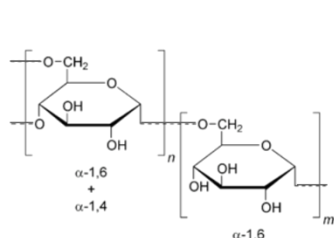
Dextrane
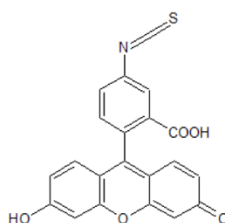
FITC
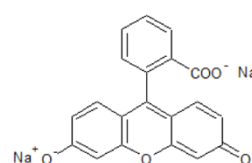
Na-fluorescein
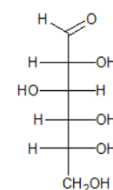
D-glucose
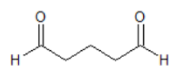
Glutaraldehyde
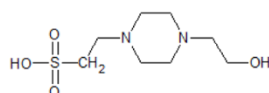
HEPES
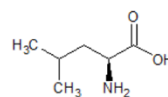
L-leucine
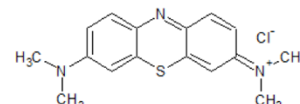
Methylene blue
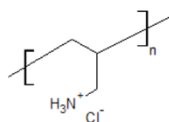
Polyallylamine hydrochloride
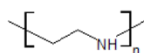
Polyethylenimine
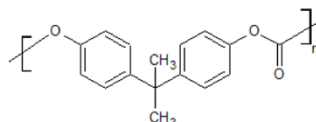
Polycarbonate
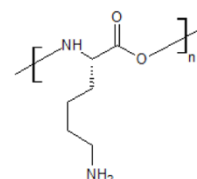
Poly-L-lysine
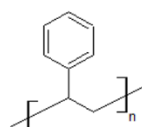
Polystyrene
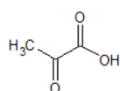
Pyruvic acid
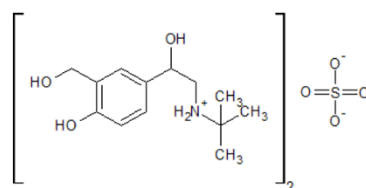
Salbutamol sulfate

Tetrahydrofuran

4.1.4 Agarose

Agarose is a polysaccharide, extracted from seaweed. This polysaccharide is a linear polymer consisting of D-galactose and 3,6-anhydro-L-galactopyranose [145]. It is commonly used in concentrations of 0.7 - 2.0 % in gel electrophoresis for the separation of macromolecules [146]. Agarose forms a gel as a function of the temperature. Under ambient conditions, the linear polymer forms a three-dimensional network through hydrogen bonds. The polymer is not charged, no ionic bonds are required for the formation of the gel network. The pore size of the gel is depending on the concentration, allowing for a tailoring of the separation properties [147]. Agarose gel electrophoresis is the standard technique for the separation and analysis of nucleic acids [148].

4.1.5 Alginate

Hydrogels made from the natural polysaccharide alginate are used in many approaches of regenerative medicine and as immobilization matrix, due to its unique biological, as well as physico-chemical properties [149, 150]. Alginate is synthesized in brown algae as a structural element of the cell wall, as well as in several biofilm producing bacteria [151, 152]. The macromolecule consists of blocks of α-L-guluronic (G) and β-L-mannuronic acid (M). The unbranched polysaccharide forms a gel upon addition of multivalent cations, because the carboxylic groups of mainly adjacent guluronic acid moieties form a complex preferentially with divalent cations [153]. Further studies also revealed that heterogeneous alternating MG moieties are also involved in gelation of alginates [154]. The gelation of alginate can be performed under mild physiological conditions, rendering alginate an ideal candidate for biomedical applications with fragile cargos. The most promising cross-linkers are Ca^{2+} and Ba^{2+}, differing in the long-term stability of the gel, which is higher for Ba^{2+} [155]. In order to

provide a hydrogel suitable for *in vitro,* as well as in *in vivo* applications, a special treatment of raw materials is necessary to receive an ultra-pure and ultra-high viscosity biomaterial [156].

4.1.6   Lactose

Lactose is a disaccharide derived from galactose and glucose found in milk. Crystalline lactose is found in two forms, α- and β-lactose. The isomers differ substantially in solubility; 55 g of β-lactose and 8 g of α-lactose are soluble in 100 g water at 20 °C [157]. In aqueous solution the isomers are in equilibrium, resulting in a solubility of 18.9 g in 100 g water (25 °C) [158]. The change of the ratio between the two stereoisomers has an impact on the optical rotation; the alteration of the optical rotation as a function of the transition to equilibrium is called mutarotation [159]. The rise of solubility of α-lactose over time is attributed to the conversion into the more soluble β-isomer. Through this removal of the α-form, further crystalline α-lactose can be dissolved until the equilibrium between α and β (18.9 g at 25 °C) is reached. The kinetics as well as the quantity of this reaction are influenced by the reaction conditions, such as pH and temperature [157].

Lactose is a widely used excipient for pharmaceutical formulations for multiple applications. It is used in tablets as well as in powders for inhalation. In fact, it is one of the few excipients with FDA-approval for pulmonary administration.

4.2 Methods

4.2.1 Characterization Techniques

4.2.1.1 Next Generation Pharmaceutical Impactor (NGI)

The United States Pharmacopoeia (USP) and European Pharmacopoeia (Ph.Eur.) describe different impactors for the characterization of the aerodynamic properties of aerosols. The next generation pharmaceutical impactor (NGI) is the state-of-the-art impactor [160-162] (Figure 6 a). It is a cascade impactor with 7 stages with a micro-orifice collector (MOC) which is described in both the Ph.Eur. 8.7 (apparatus E) [163] and the USP 39-NF 34 (apparatus 6) [164].
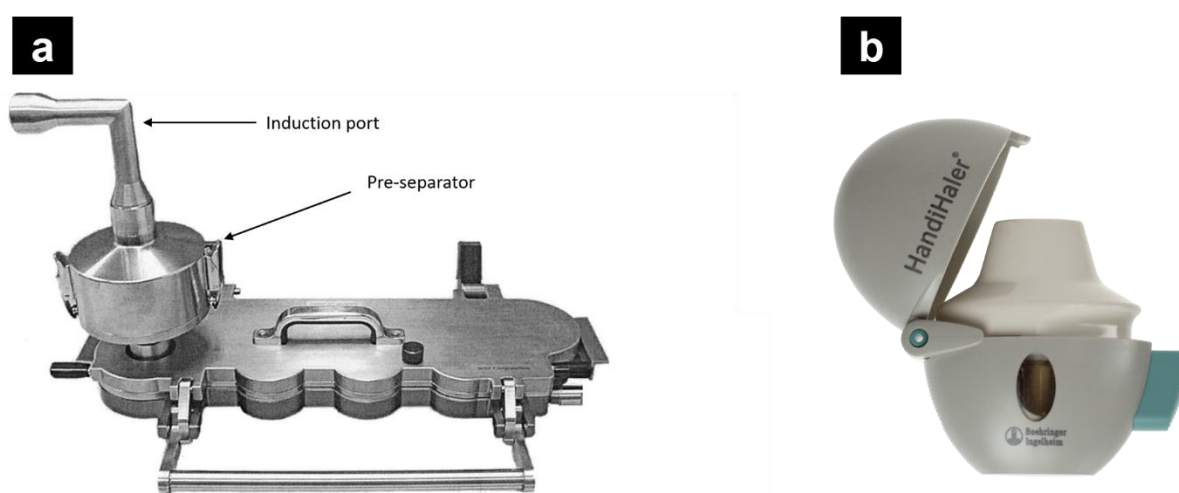
Figure 6 – Next generation pharmaceutical impactor and DPI.
(a) Closed NGI with induction port and pre-separator on the inlet. (b) DPI HandiHaler containing a capsule filled with dry powder. Image (a) adapted from [166].
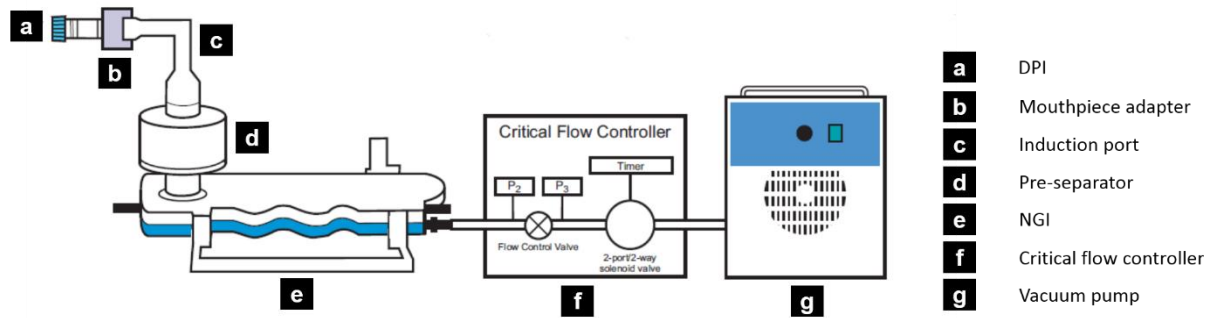
Figure 7 – Experimental setup of NGI experiments.

The NGI (e) is connected to the vacuum pump (g) through the critical flow controller (f). The mouthpiece adapter (b) connects the DPI (a) to the induction port (c) and the pre-separator (d), excluding coarse particles before entering the NGI (e). Illustration adapted from [165].

At the induction port the adapter for the dry powder inhaler is attached. The HandiHaler (Figure 6 b) was exclusively used for the experiments. The vacuum, which is generated through the vacuum pump and adjusted with the critical flow controller, causes the dry powder to be sucked into the NGI (Figure 7). The perpendicular geometry at the induction port causes the air stream to change directions for the first time and first particles are deposited in the induction port. The pre-separator is installed in order to separate the coarse fraction, preventing it from entering the NGI (Figure 8). Following the airstream in the NGI, the air flows through 8 nozzle plates with decreasing nozzle diameters and increasing abundance per stage (Figure 9, Figure 10). The spectrum ranges from one orifice with a diameter of 14.3 mm for stage 1, to 4032 orifices nozzles with diameters of 70 µm for the last stage (MOC). The velocity of the airstream and throughput of air can be adjusted in an interval with physiological relevance. Underneath those nozzle plates the particles impact onto the collection cups, if inertia exceeds the forces dragging the particles with the airstream (Figure 9). The collection cups are coated with a viscous liquid, the stage coating, reducing the deflection from the stages. The aerosol follows the airstream through a cavity in the lid (Figure 9) to the next stage

of the NGI. The nozzles become finer each stage (Figure 10) causing the airstream to accelerate locally and therefore causing more and more impaction per stage. The velocity of the airstream is responsible for the cut-off of the size of the particles at the stages. The threshold is called effective cut-off diameter (ECD) and describes the highest particles diameter that is still deposited on the respective stage on average under the chosen air flow.
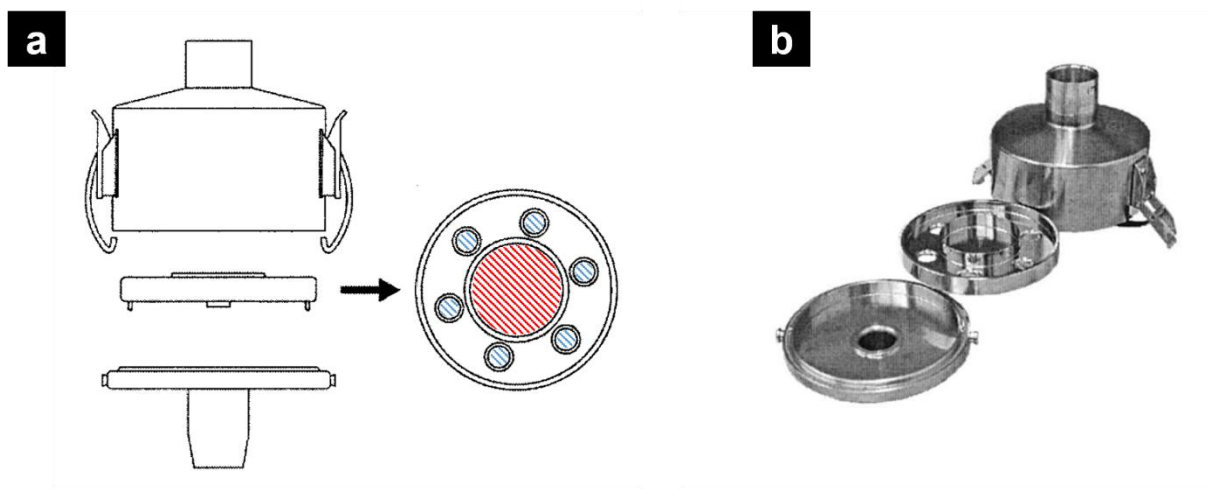
Figure 8 – Disassembled NGI pre-separator.

(a) The illustration displays the components of the pre-separator. The central cup, which is filled with buffer, is marked red, the orifices required for the airflow are marked blue. (b) Photograph of the components of the pre-separator. Image (a) adapted from [163] and image (b) adapted from [165].
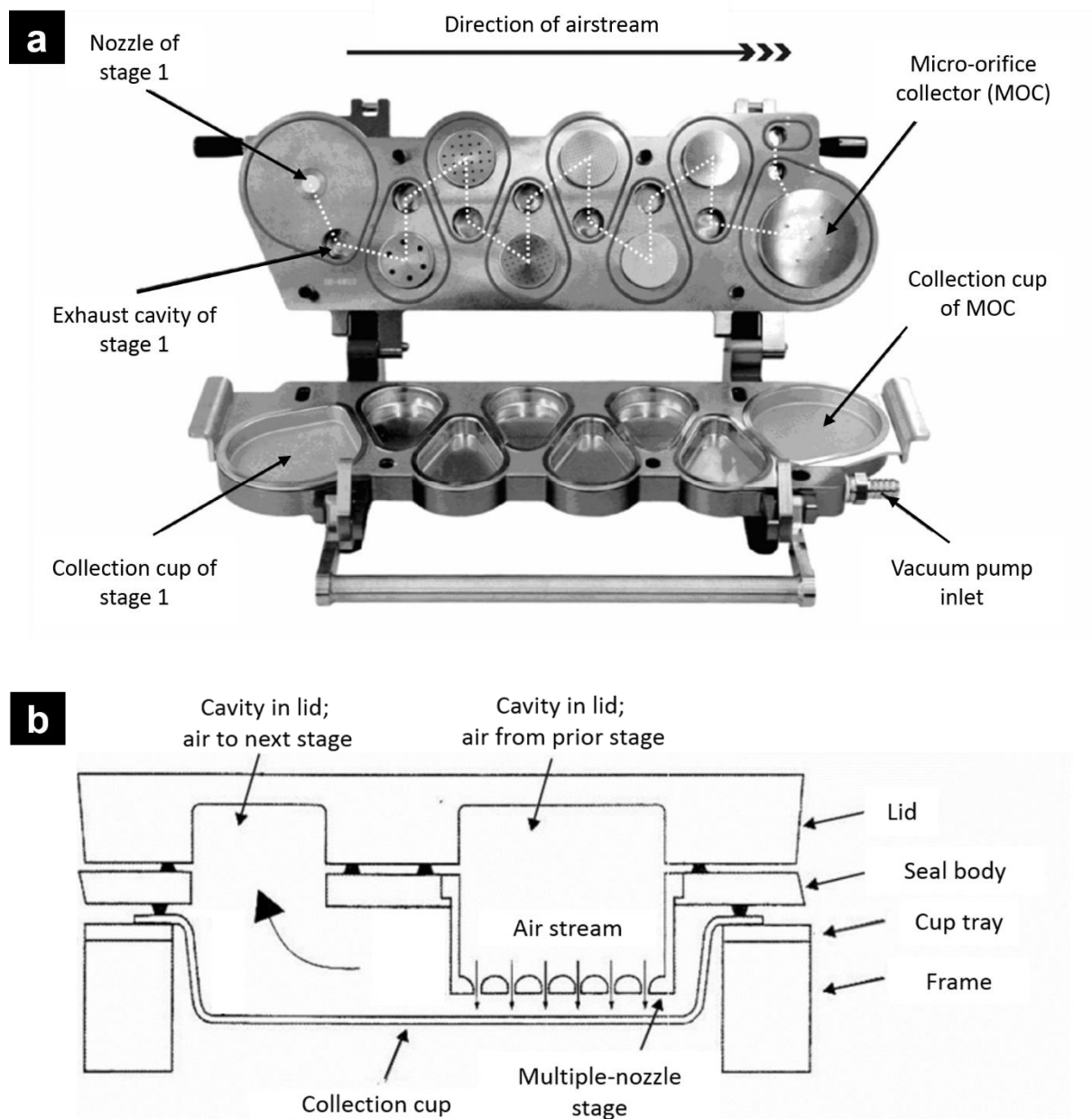
Figure 9 – Illustration of NGI with schematic of air flow.

(a) Opened NGI; the dashed lines indicate the flow of the air through the apparatus.

(b) Illustration of the cross-section of the closed NGI. Images adapted from [166].

Stage 2
6 holes
4.88 mm

Stage 4
52 holes
1.207 mm

Stage 6
396 holes
0.323 mm

MOC
4032 holes
70 µm

Stage 1
1 hole
14.3 mm

Stage 3
24 holes
2.185 mm

Stage 5
152 holes
0.608 mm

Stage 7
630 holes
0.206 mm
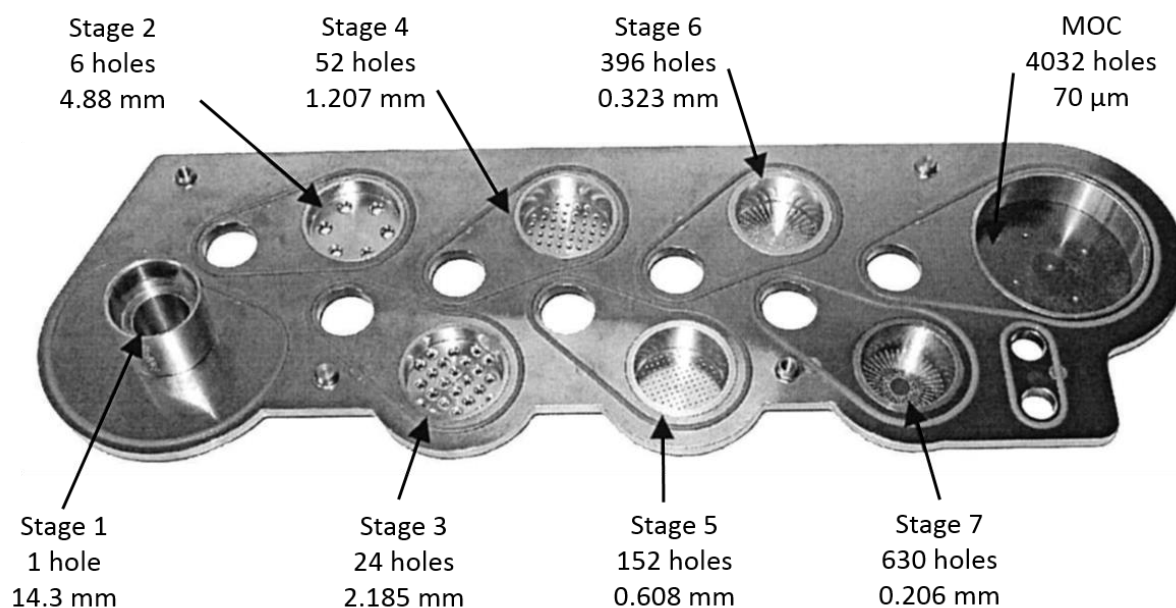
Figure 10 – Apertures of NGI with specification for each stage in top view.

The smaller the nozzles are, the more abundant they are. Image adapted from [165].

4.2.1.1.1 Dosage Unit Sampling Apparatus (DUSA)

The dosage unit sampling apparatus (DUSA) (Figure 11) is used in order to quantify the dose per shot of the dry powder inhaler (DPI) and for the assessment of the adequate air flow for the experiments, which is a function of the air resistance of the DPI (Figure 12). The DUSA is connected via the P1 port and the critical flow controller to the vacuum port. The flow is adjusted until the pressure loss over P1 has reached a value of 4 kPa, in accordance with the requirement of Ph.Eur. If the resistance of the DPI is too low in order to reach this total resistance, a flow of 100 l/min is compulsory. The higher the resistance of the DPI, the lower the flow is in order to reach the mandatory pressure loss. Subsequently, the time of flow has to be adjusted with Equation 2 in order to meet a flow of 4 l per experiment.
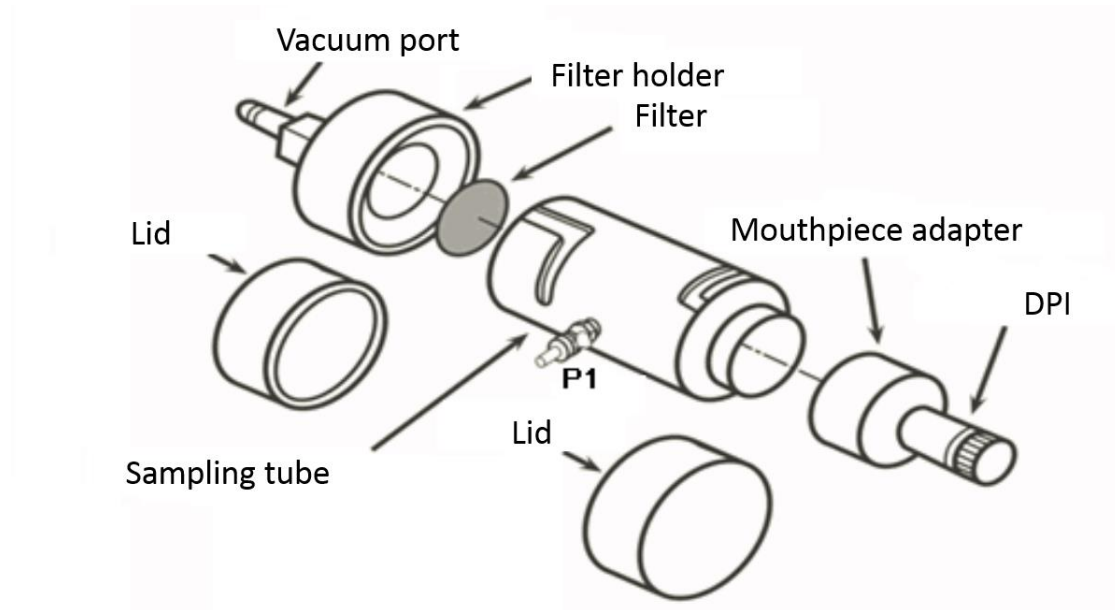
Figure 11 – Dosage unit sampling apparatus (DUSA).

The DPI is connected through a mouthpiece adapter to the sampling tube. The vacuum pump is connected to the vacuum port and the dose is collected in the sampling tube on the surface of the filter and the surface of the sampling tube. The pressure loss caused by the DPI is measured between the P1 port and the vacuum port. Illustration adapted from [165].
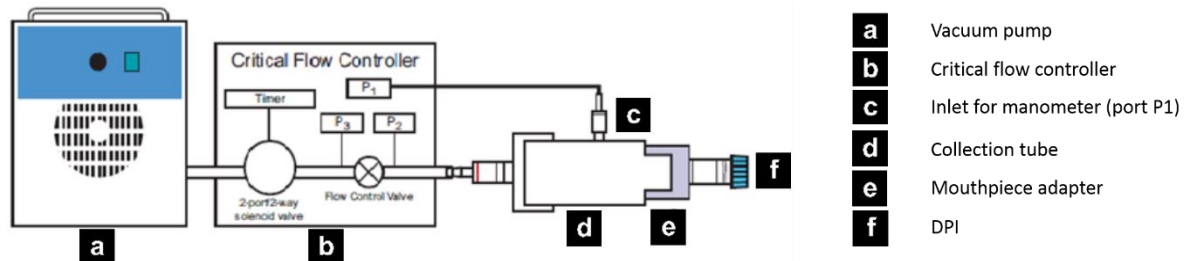
Figure 12 – Schematic of experimental setup with attached DUSA.

The DUSA is connected to the vacuum pump through the critical flow controller. The DPI is connected with an adapter to the DUSA. For the assessment of the flow required for the respective DPI, the port P1 is connected to the critical flow controller as well. Illustration adapted from [165].

$$Time\ of\ flow\ [s] = \frac{4l \times 60s}{flow\ [l]}$$

Equation 2 – Time of ventilation as a function of flow

4.2.1.1.2   Aerodynamic Characterization and Quantification with the NGI

Prior to the experiment, the collection cups (Figure 9 a) are coated with a mixture consisting of glycerol, ethanol and Brij L23 (mass fraction: 0.5 glycerol, 0.35 ethanol, 0.15 Brij) in order to prevent, or reduce the deflection of particles from the collection cups, which corrupts the results. The big collection cups were coated with five drops and the small cups with two drops. The stage coating, which can be obtained commercially, was not used; the mixture used yielded identical results as described before [165]. The central cup of the pre-separator (Figure 8) is filled with 7.5 ml 50 mM HEPES (4-(2-hydroxyethyl)-1-piperazineethanesulfonic acid) buffer.

Before applying the particles, the air throughput was monitored with the flow-meter. A constant value indicated the tightness of all connections.

The HandiHaler shows comparably high resistance of the air flow, meaning that the flow rate of 56 l/min causes the required pressure loss of 4 kPa through the attached DPI and DUSA. For practical reasons the flow was adjusted to 60 l/min and the respective inhalation time of 4 s. After the aerosolization, the powder is collected with buffer. The quantification is described in detail in chapter "Quantification after NGI Experiment" (4.2.2.1.2.1).

4.2.1.2 Visualization Techniques

4.2.1.2.1 Fluorescence Light Microscopy (FLM)

Fluorescence is the phenomenon that specific light is emitted (λ_{em}) after absorption of electromagnetic waves of a certain wavelengths, the so-called excitation wavelength (λ_{ex}). Fluorescence is widely used in life sciences, because it allows the specific detection of various labels in parallel with minimal interference of the system. Fluorescence microscopy does not require extensive sample preparation, except for the introduction of the desired labels and can be performed during incubation with no need for fixation. Fluorescence is shown by various entities, including colloids, such as quantum dots [167] and nanoclusters [168-170], and various small molecules [171]. The various labels vary in many properties, including λ_{em}, λ_{ex}, quantum yield and bleaching. Fluorescence bleaching is the loss of fluorescence due to photochemical degradation of the fluorophores; in particular the molecular dyes degrade as a function of light exposure and the intensity of the fluorescence decreases. From this big pool of substances a label for many applications can be found.

The Abbé diffraction limit restricts the resolution of light microscopic techniques to approximately half the wavelength of the light used [172]. This means that the limitation for conventional light microscopic techniques, such as FLM using visible light, is roughly 200 nm. The development of the super resolution techniques, such as stimulated emission depletion microscopy (STED) [173], or stochastic optical reconstruction microscopy (STORM) [174], which are based upon fluorescence, has been awarded the Noble Prize in 2014. These techniques permit to circumvent the diffraction limit and improve the resolution ~ 5-fold.

4.2.1.2.2 Scanning Electron Microscopy (SEM)

Another important visualization technique has been awarded with the Nobel Prize in physics in 1986. Electron microscopy (EM) allows for an improvement of the resolution through the replacement of light through electrons. For electron microscopic techniques, either electrons permeate the specimen, Transmission Electron Microscopy (TEM), or are used for the scanning of the surface, Scanning Electron Microscopy (SEM). The resolution for electron microscopic techniques can be improved by more than 100-fold with resolutions of roughly 1 nm for SEM and below 1 Å for TEM [175].
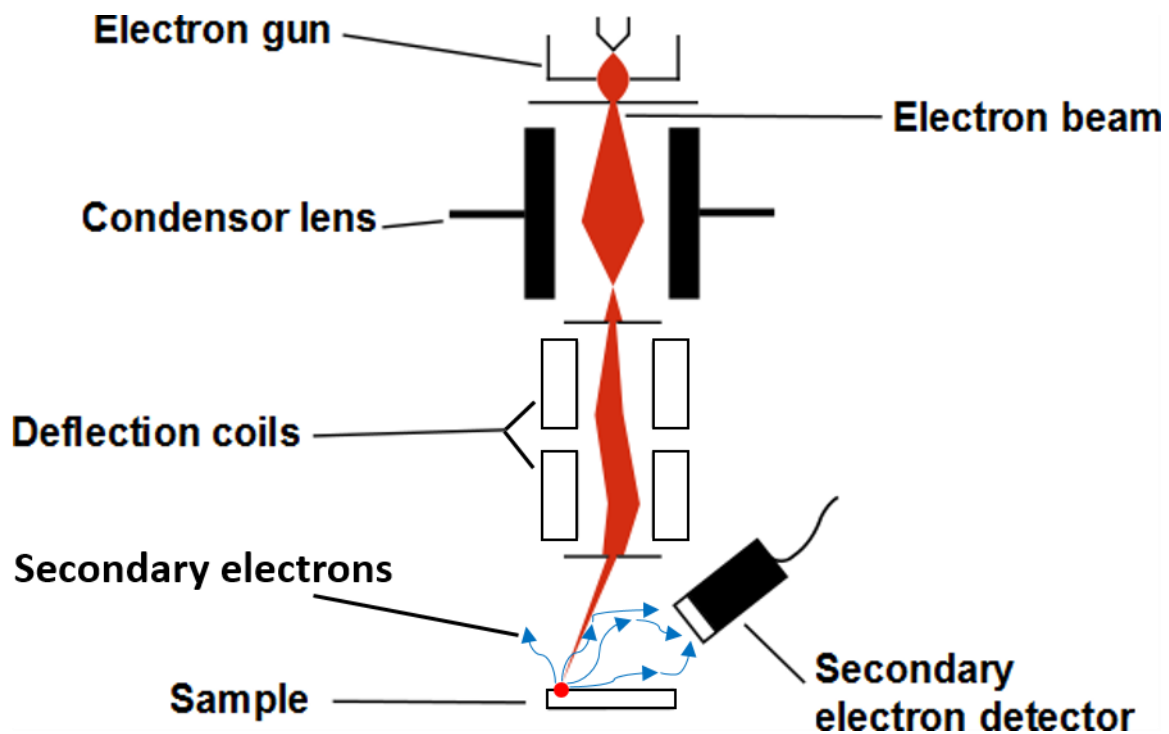
Figure 13 – Illustration of the principle of SEM.
Electrons are emitted from the electron gun, focused by the condenser lens and the deflection coils guide the electron beam in order to scan the specimen. Apertures increase the resolution, only the beam in the centre can pass. The electron beam generates secondary electrons in the surface of the sample that are attracted and quantified by the secondary electron detector.

Materials and Methods

The electrons that are emitted from the electron source are accelerated through an electric field in order to increase the resolution, because it is proportional to the velocity of the electrons. The electron beam is condensed through electromagnetic coils and passes apertures in order to focus the beam on a nanoscopic spot. The image is acquired through the scanning of the specimen in a raster-like fashion in x and y direction. The electron beam (primary electrons), which is guided on the respective raster spot by the deflection coils, causes electrons (secondary and backscattered electrons) and electromagnetic waves (x-rays) to be emitted from this position. Depending on the detector used, different species can be detected. In principal, every SEM is equipped with a secondary electron detector. It collects most of the electrons that are emitted through an electric field and amplifies the signal with a photomultiplier. Step by step the image builds up, reflecting the collected electrons through the brightness of each pixel on the screen (Figure 13), which displays the topology of the surface. Electron microscopy usually requires a high vacuum in the sample chamber, because the electron beam can easily be deflected by gas molecules, decreasing the image quality. Constant refinement and improvement of the operating conditions has led to the development of SEMs which work under a mild vacuum of only 3000 Pa (~ 3 % of atmospheric pressure) and can be used under a vapour atmosphere. In these environmental SEMs (ESEM) the specimen can be preserved at a more natural hydrated state. Nevertheless, the resolution that is reached under these conditions is several orders of magnitude lower than in high vacuum. Specimen that are visualized under high vacuum conditions usually need to be conductive, or coated with a thin conductive layer, often noble metals such as gold or platinum. The coating is called sputtering and has a thickness in the order of 10 nm. The conductive material allows for a dissipation of access electrons that could otherwise accumulate in the specimen and are randomly released deteriorating the image quality. The

gas molecules that are present in the lower vacuum for ESEMs prevent charging of the specimen, sputtering is not required.

4.2.1.2.2.1 Operating Conditions for Scanning Electron Microscopy (SEM)

In general, SEM imaging (EVO HD15) was carried out using 5 kV as acceleration voltage and the secondary electron (SE) detector. If resolution was not sufficient, the acceleration voltage was increased to 10 kV. Prior to imaging, the samples were sputtered (sputter current of 20 mA for 50 s) and coated with a gold layer of approximately 15 nm thickness in order to reduce charging effects and to improve the image quality.

4.2.1.2.3 Correlative Microscopy and Correlative Light and Electron Microscopy (CLEM)

The term correlative microscopy describes approaches that combine fundamentally different visualization techniques on identical samples and positions [176, 177]. Images acquired with different techniques are usually overlaid, expanding the information in comparison to the single techniques. A large variety of visualization techniques, including atomic force microscopy (AFM)/scanning probe microscopy (SPM) [176, 178-181] and electron microscopic techniques (EM) such as TEM [176, 179, 182-185], SEM [176, 184], have been correlated with light microscopy techniques (LM), including super resolution techniques STED [173] and STORM [174]) and more are being extensively explored [176, 185].

Correlative light and electron microscopy (CLEM) is the combination of any EM and LM.

4.2.1.2.3.1 Carl Zeiss Shuttle & Find

The Shuttle & Find system is a basic and straightforward tool combining fluorescence light microscopy (FLM) with SEM in a modular system of standardized hardware and software [186, 187]. The setup allows the combination of the inherent advantages of FLM and SEM. Scanning electron microscopy makes it possible to visualize surfaces with a magnification several orders of magnitude higher than with conventional optical microscopy. Fluorescence microscopy permits labelling of specific compartments of cells, highlighting objects, or the region of interest (ROI) with high biochemical specificity [185]. For correlative microscopy, the labelling can be used as a secure relocation point of the ROI.

For imaging in the sense of correlative microscopy, images gained by FLM and SEM need to be superimposed. Therefore, the same area of the specimen has to be imaged, which is facilitated by the standardized sample holder fitting both setups (Figure 14).

Figure 14 – Shuttle & Find sample holder.
The holder (a) exhibits three L-shaped markers that allow a distinct relocation of any region of interest (ROI). The marks are recognized by the software and are required for a three point calibration (b). Image (a) was modified from a schematic image in the software AxioVision 4.8.

For the correlation of optical and electron microscopy images the sample is placed onto a special holder, enabling unambiguous definition of points on the specimen. The sample holder has three marks required for calibration with the software. The coordinates of the three L-

shaped markers allow precise (≤ 25 µm given by the manufacturer, in practice a few microns) relocation of any ROI of the sample [186, 187]. Usually FLM is performed as first analysis, because the electron beam can destroy the fluorophores [188]. After calibration, the microscope is ready for imaging. Images of ROIs can be captured and their positions are stored in parallel. Subsequently, the sample holder is transferred to the other microscope, followed by a calibration step; the software automatically locates the imaged ROIs. For fluorescence imaging the rods were excited with λ_{ex} = 365 nm and an emission bandpass (BP 445/50) was used for detection. The cells were excited with 470 nm and emission was detected after another bandpass (BP 525/50). SEM imaging was carried out under conditions described in chapter "Operating Conditions for Scanning Electron Microscopy (SEM)" (4.2.1.2.2.1). Subsequently, images of the two microscopes were superimposed in order to display fluorescence and electron signals within one image.

4.2.1.2.4 Operating Conditions for Atomic Force Microscopy (AFM)

For the visualization of microcylinders composed of NPs atomic force microscopy (AFM)/ scanning probe microscopy (SPM) was also performed. Since the suspension of the cylinders interconnected with agarose does not require stabilizers in order to remain stable, no purification was needed prior to imaging. A droplet of the dispersion was placed on a freshly cleaved mica sheet and dried overnight. The samples were prepared and the imaged at room temperature; imaging was performed under atmospheric conditions in tapping mode. A cantilever with a spring constant of 40 N/m and a scan rate of 0.5 Hz (256 lines per image) was used for image acquisition. The raw data was processed by a flattening algorithm to remove background slopes and analysed using Nanoscope SPM software to determine size.

4.2.2 Preparation Strategies for Filamentous Particles with the Template Technique

For the preparation of filamentous/cylindrical particles, an adapted procedure derived from the template-assisted polyelectrolyte encapsulation of nanoparticles [66] was applied. The polyelectrolytes PAH (polyallylamine hydrochloride) and PSS (polystyrene sulfonate) were replaced by hydrogels.

4.2.2.1 Cylindrical Particles Formed with the Template Technique
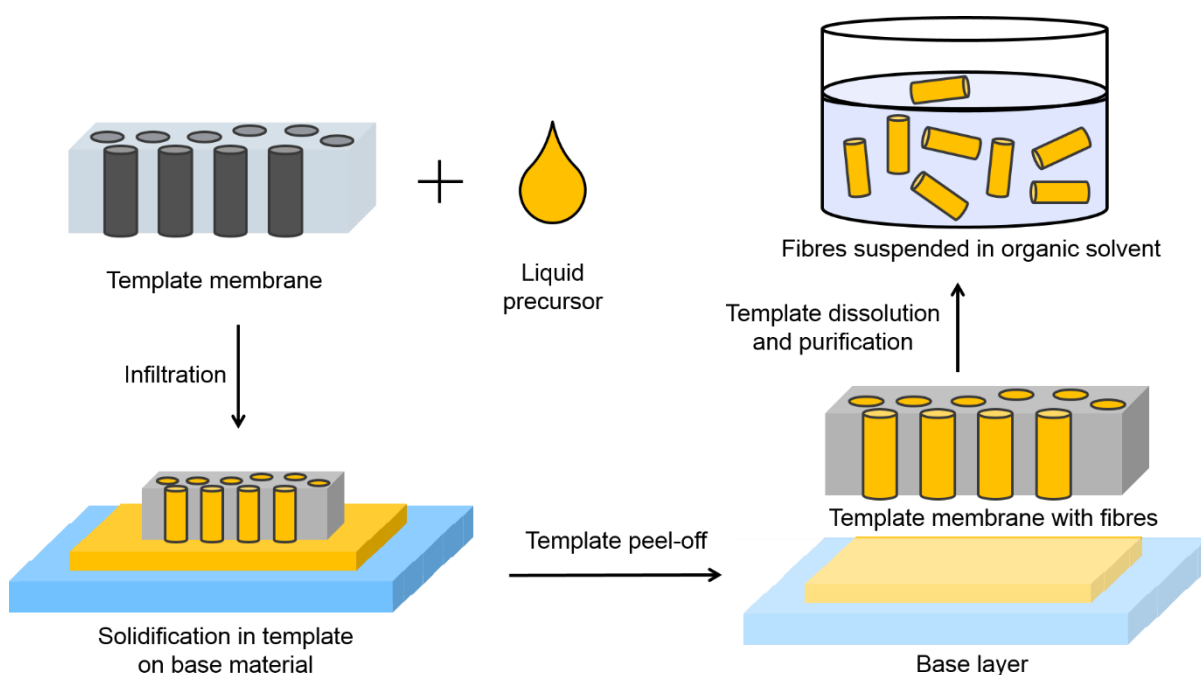
Figure 15 – Illustration of the protocol for the formation of cylindrical particles with the template technique.

The template membrane is applied onto the liquid precursor of the gel forming agent. The pores of the membrane are filled through capillary forces. Following diverse mechanisms the liquid precursor solidifies within the template. After complete solidification, the template membrane is peeled off, separating the template containing the cylinders from the base layer. The template membrane is dissolved in organic solvent, releasing the single particles.

The protocol for the formation of cylindrical particles with the template technique is depicted in Figure 15. In order to rule out any effect of the surface inhomogeneity of the template

membranes (5.1, Figure 23) the membrane was always applied with the shiny side (smooth surface) facing the liquid precursor and the matt side oriented upwards. In order to selectively cleave the fibres at the orifice of the pores and to decrease the likelihood of a layer bridging the single fibres (interlinking layer, Figure 16), the protocol was refined. The strategy is to increase the adhesion between the base material and the base layer, favouring a separation at the intended position. The surface texture and the material of the base material, as well as the volume that is allowed to dry have been observed to have a pronounced impact. The adhesion could be enhanced by scratching of the surface, which significantly increases the surface roughness and the interface, allowing the liquid precursor to bind much stronger to the surface of the base material (Figure 17). Various patterns and intensities of scratching have been tested. The best adhesion was found for scratching of the entire surface, which can be readily achieved with coarse sandpaper. Empirically, it has been assessed that the distribution and abundance of the scratches matters (Figure 17 b). If scratches are more than 1 mm apart, the base layer rather adheres to the template membrane. The hydrophilicity of a surface, which can be described by the contact angle also plays an important role. The polystyrene from standard plastic Petri dishes exhibits a higher contact angle and therefore is more hydrophobic than the glass of glass slides. Literature value for the contact angle (θ) of the relevant surfaces are 83° for PS [189], 72° for polycarbonate (PC) [189] and smaller values for glass surfaces because of the plentiful interactions that can be established between water and the oxygen moieties. The Petri dishes made from PS were replaced by the glass slides, serving as the base material. The last significant factor is the volume that is applied and allowed to dry. The thicker the base layer after drying, the more bridging through the interlinking layer was observed, because the layer becomes less homogenous and crystals composed of lactose are formed (Figure 17 c). The solute content in the aqueous solution was not chosen lower

than 15 % (m/V) for most of the experiments and compositions, including pure lactose and blends with APIs, in order to reduce the likelihood of formation of pores and tubes (5.2.1, Figure 24 e and f). If the solute concentration is lower, more particles with tubular or funnel-shaped cavities are found. In contrast, hydrogels do not form these cavities and were used in lower concentrations than 15 %. Compounds utilized for the generation of cylinders were chosen considering sufficient solubility for the preparation conditions. The ideal volume for this content was 250 – 200 µl for the 25 mm diameter template membrane and approximately 1 ml for the 47 mm template, respectively. The 25 mm template membrane can be replaced by a quarter of a membrane with 47 mm diameter; the 47 mm template is cut with scissors into four equivalent pieces through two perpendicular cuts.
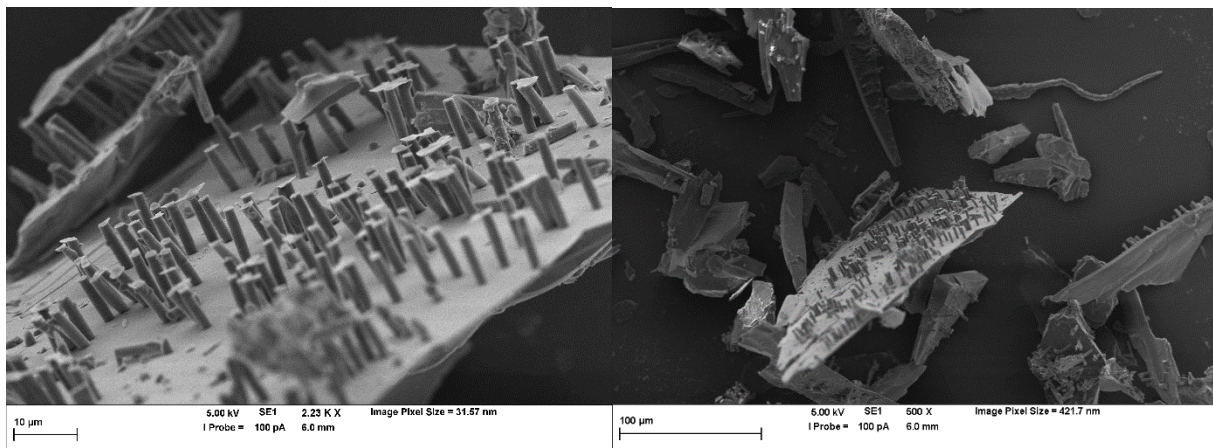
Figure 16 – SEM micrographs of the interlinking layer of alginate-lactose fibres.
The interlinking layer is bridging single fibres. Two micrographs of the same region with varying magnifications were captured.
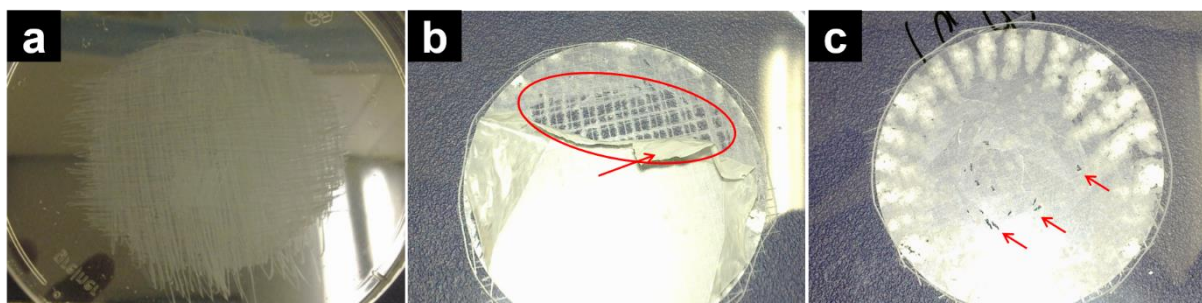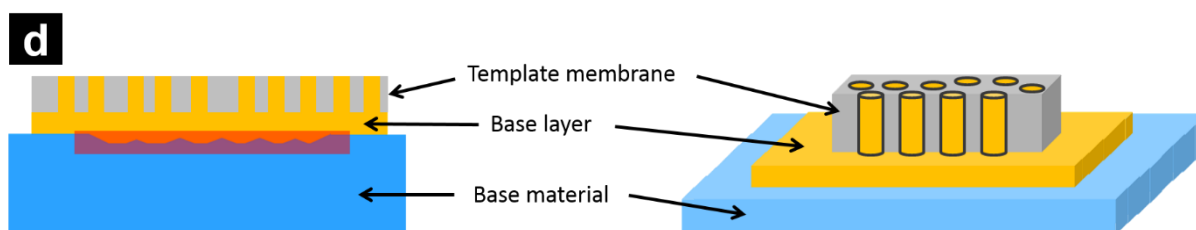
Figure 17 – Impact of increase of surface roughness on the adhesion of the base layer to the base material.

Photographs of the base material (polystyrene from a Petri dish) with different patterns of scratching (a – c) before and after the peel-off of the membrane. (a) The surface in the centre is completely scratched, no gaps in between the scratches; image was taken before the membrane was applied. (b) The centre of the Petri dish is scratched, gaps are visible between the scratches; the membrane has been removed half; (red oval circle) the base layer is adhering to the membrane and not the base material, the clear surface of the Petri dish in between the scratches can be seen; the red arrow indicates a part of the peel-off membrane. (c) The membrane has been completely peeled off and the base layer is fully adhering to the base material, which had been completely scratched without gaps; the red arrows indicate small areas of base layer that have been removed during peel-off. In the lateral part distinct crystals which render the base layer whitish can be seen. (d) Illustration of the experimental setup of the drying step used in the protocols for the formation of cylindrical particles with templates. The left sketch represents a cross-section of the setup which is depicted in the right sketch. The red region of the left illustration depicts the increased surface through scratching.

The membrane has to meet a certain mechanical stability in order to withstand the peeling off. Empirically it was discovered that this goes along with the porosity and the pore diameter, since the thickness of the templates are comparable (10 ± 1 µm, exception 0.4 µm template). The higher the porosity and the smaller the pores, the more problematic the peel-off was, meaning that the template ripped and in some cases could not be removed. Even though the pore diameter of the 0.6 µm template is lower in comparison to the 1.0 µm template, experiments have shown that the tendency to rip is comparable because of the higher

porosity (Table 1). Smaller pore diameters than 0.6 μm were not feasible under the chosen experimental conditions.

4.2.2.1.1 Cylindrical Particles Consisting of APIs and Lactose

Cylindrical particles without hydrogels were prepared from the hydrophilic excipient lactose and the hydrophilic API salbutamol sulphate in variable concentrations.

The solute concentration was kept constant at 15 % (m/V) for blends, as well as for the pure compounds. Salbutamol sulphate is freely soluble in water, with a solubility of 291 mg/ml at room temperature [190], which is higher than for the free base. The solubility limit of fluorescein-Na is 500 mg/ml [191]. The solubility of α-lactose has been reported to be 189.1 mg/ml [158] at room temperature.

After complete dissolution of the solutes, 250 μl of solution was pipetted onto a glass slide with roughened surface. The template membranes (25 mm) were applied with the shiny side facing the solution and allowed to dry under ambient conditions overnight. After peel-off of the template membranes, the membranes were transferred to 2 ml Eppendorf cups (two membranes per cup). CH_2Cl_2 or tetrahydrofuran (THF) (1.6 ml) was used as the solvent for the PC. Centrifugation was utilized for purification from the dissolved templates; time and centrifugation force was adapted to the solvent and the composition of the fibres.

4.2.2.1.2 Cylindrical Particles Made of Alginate, Blended with Lactose

For the preparation of cylindrical particles consisting of alginate, lactose, fluorescein-Na and leucine, exhibiting a solute concentration of 18.2 % (m/V) with a mass faction of 3.3×10^{-2} for agarose, 0.82 for lactose, 0.11 for fluorescein-Na and 3.3×10^{-2} for leucine, the following protocol was used:

Two aqueous solutions, the alginate sol and the gelation liquid containing Ca^{2+}-ions, were prepared separately. The alginate sol contained: 0.6 % (m/V) alginate, 2 % (m/V) fluorescein-Na, 15 % (m/V) lactose, 0.6 % leucine (m/V) and 5 mM HEPES (0.1 %). The gelation liquid contained: 18 mM $CaCl_2$ (0.2 %), 2 % (m/V) fluorescein-Na, 15 % (m/V) lactose and 0.6 % (m/V) leucine in 50 mM HEPES buffer (1.2 %).

The concentration of leucine is critical, it has a pronounced influence on the structure of the cylindrical particles (5.2.2). This change could also be observed macroscopically (Figure 18). The base layer is not homogenous for high L-leucine concentrations, in contrast to its homogenous appearance for concentrations below 0.6 % (m/V). For the highest concentration of 2.0 % (m/V), close to the solubility limit in water for room temperature (24.3 mg/ml [192]) the inhomogeneity is very pronounced; because of the colour, the segregation of the fluorescein-Na can be seen easily.
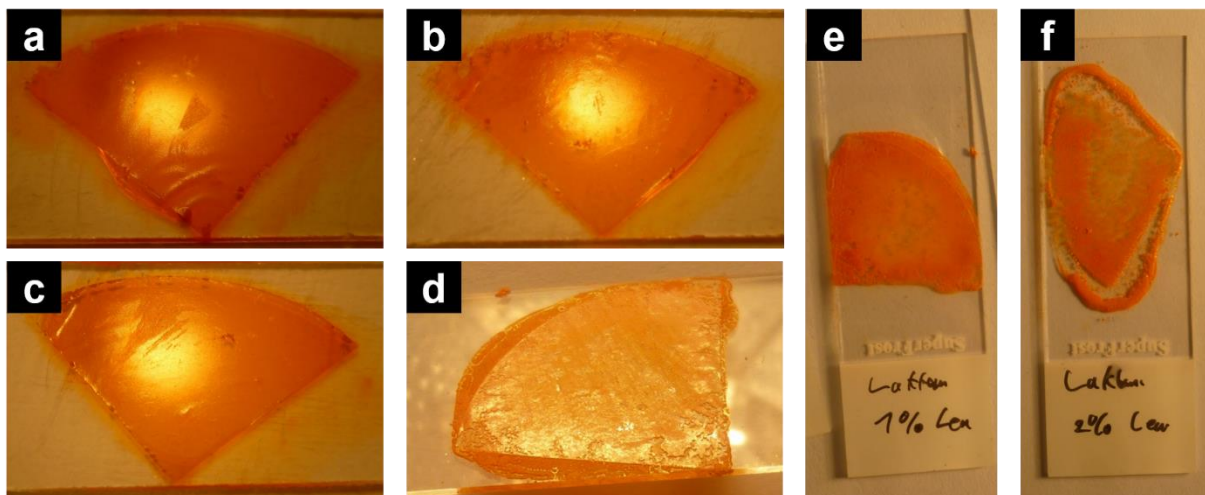
Figure 18 – Photographs of the base layers with varying leucine concentrations after drying of hydrogel and after peel-off of template.

Composition of hydrogel: alginate 0.6 % (m/V), lactose 15 % (m/V), fluorescein-Na 2 % (m/V), leucine 0 – 2 % (m/V); template membrane 2.0 µm. (a) Leucine 0 %, smooth surface; (b) leucine 0.2 %, smooth surface; (c) leucine 0.6 %, smooth surface; (d) leucine 1.0 %, uneven

surface; (e) leucine 1.0 %, top view of glass slide with base layer, showing spotty inhomogeneities; (f) leucine 2.0 %, top view of glass slide with base layer, strong segregation of the compounds, the orange fluorescein has localized inhomogeneously.

The compounds both of the alginate sol and the gelation liquid were mixed and allowed to dissolve overnight before the preparation of the cylindrical particles. Some compounds were diluted from stock solutions.

HEPES buffer (100 mM) was adjusted to pH 7.4 with NaOH. Fluorescein-Na stock solution (20 % (m/V)) was prepared with deionized water. $CaCl_2$ stock solution (50 mM) with 50 mM HEPES buffer. The alginate sol, containing the above mentioned compounds in the given concentrations, was prepared by mixing of the alginate stock solutions (0.7 % (m/V)), fluorescein-Na stock (20 % (m/V)), HEPES buffer (100 mM) and dissolution of the chosen amounts of lactose and leucine. The gelation liquid was prepared by mixing of fluorescein-Na stock with HEPES stock and the dissolution of $CaCl_2$, lactose and leucine. High concentrations of fluorescein were chosen in order to facilitate the detection and quantification even of traces of the marker. High concentrations of lactose were also used in order to avoid the formation of tubes that can form as a function of the concentration used (Figure 24 d). The concentrations of the compounds were kept similar in the gelation liquid and the alginate sol in order to reduce osmotic effects that could alter the distribution of the substances; lactose, fluorescein-Na and leucine concentrations were identical in the alginate sol and the gelation liquid.
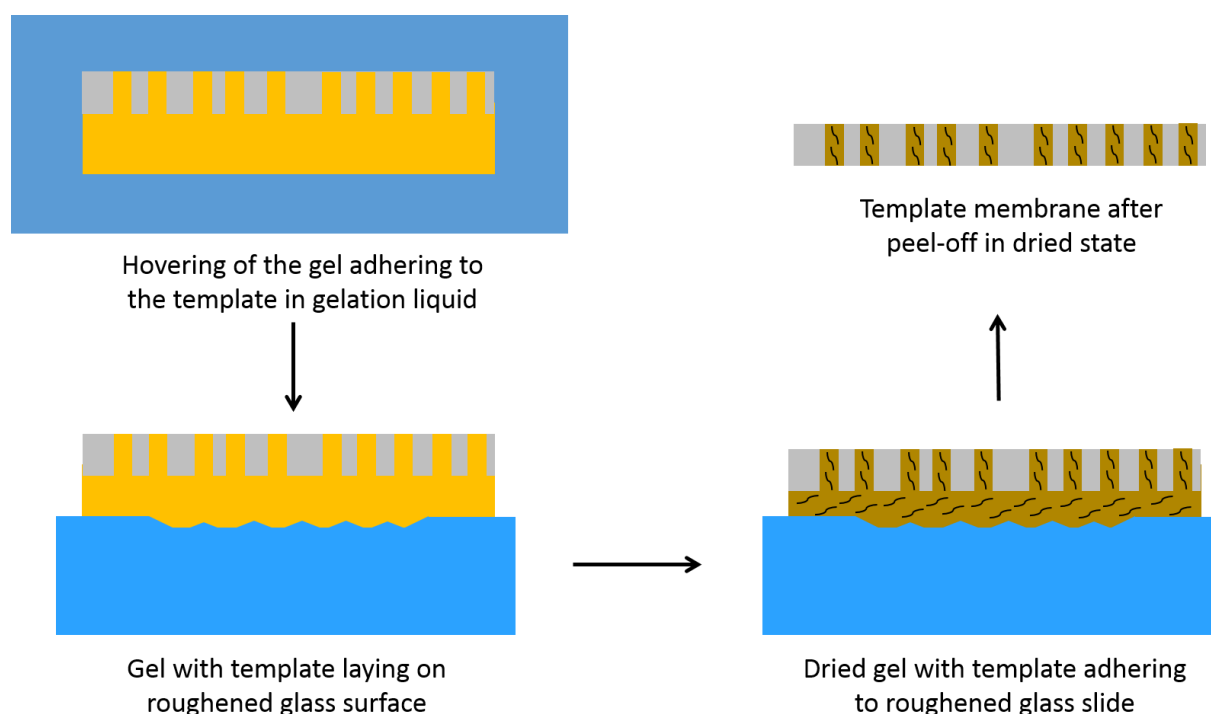
Figure 19 – Schematic of the formation of filaments with the hydrogel alginate.

250 µl of the alginate sol containing the mentioned hydrophilic compounds are pipetted on a PS Petri dish. The template membrane (25 mm) is applied with the shiny side facing the sol, instantaneously wetting the surface of the filter. 1.5 ml of gelation solution is applied covering the entire filter and allowed to form a gel for 15 min; after 10 minutes the gel sheet underneath the membrane is gently lifted if not happened automatically, which guarantees that the Ca^{2+} solution could entirely cross-link the alginate. The Petri dishes consist of PS, which is less hydrophilic than the membrane, consequently the gel adheres to the template rather than the surface of the Petri dish (4.2.2.1). After gelation the filter with the adhering gel is transferred to a glass slide with a roughened surface (4.2.2.1, Figure 17), whereas it is paid attention that the adhering drops of the gelation liquid are removed with tissue wipers. The gel is allowed to dry overnight on the roughened glass slides under exclusion of light. After drying, the membranes are peeled off (Figure 19) with forceps, cleaving the fibres from the base layer selectively. Through the loss of water the material loses flexibility and can be

separated from the base layer. If the membranes are peeled off in wet state, the fibres predominately remain on the base layer (4.2.3.1). Two membranes are transferred to a 2.0 ml Eppendorf cup, 1.6 ml THF is added and vortexed for 15 s for dissolution. The dispersion is allowed to sediment for 30 s after vortexing and the supernatant is transferred to a new Eppendorf cup. This is another measure in order to reduce of remove aggregates, or the interlinking layer (Figure 16); these aggregates sediment much faster than the fibres. The sediment was discarded and the dispersion of the fibres centrifuged at ~ 4300 rcf (relative centrifugal force) for 8 min. The supernatant is removed, the same volume (1.6 ml) is added and vortexed before the next cycle starts. The centrifugation is repeated three times in total in order to remove the PC from the template membrane. After the last cycle, the pellets are redispersed in a few droplets THF for each Eppendorf cup and are combined within one Eppendorf cup. In order to remove aggregates contained in the fibre dispersion, differences in sedimentation are used. The large aggregates sediment (Figure 16) within seconds after vortexing, whereas the fibres largely remain in the supernatant. For this reason the Eppendorf cup is vortexed and the dispersion allowed to sediment for 45 s. The supernatant is removed and processed for drying, containing the purified fibres.

The dispersion of the fibres in THF was filled in a scintillation vial and either dried under N_2 atmosphere or freeze-dried. The drying under N_2 atmosphere was performed in a glass container that was purged with N_2 beforehand in order to remove the air and thus humidity. The N_2 was replaced several times. Prior to freeze-drying, the vial containing the dispersion is immersed into liquid N_2 in order to freeze it and is immediately freeze-dried afterwards. After complete removal of the THF, the fibres are transferred to an empty gelatin capsule with a spatula.

Depending on the template membrane and the corresponding porosity (Table 1) 10 - 16 template membranes had to be used per preparation for a yield of 3 - 6 mg of fibres.

The aerodynamic behaviour was assessed with the next generation pharmaceutical impactor (4.2.1.1). In order to rule out influences of the amount that is applied, the experiments were performed with 3 - 6 mg of powder; in theory the results do not depend on the amount. The gelatin capsule, containing the powder, was applied with the DPI HandiHaler.

4.2.2.1.2.1 Quantification after NGI Experiment

After the aerosolization experiment in the NGI (4.2.1.1.2), the powder is collected with HEPES buffer (50 mM) that was adjusted to pH 7.4. The bigger collection cups (stage 1, 8) are filled with 7.5 ml, the smaller collection cups (stages 2 – 7) are filled with 5 ml buffer (Figure 10). The pre-separator, the induction port, the mouthpiece, the HandiHaler (Figure 6) and the capsule are washed with buffer and the liquid is collected. The buffer used for the DPI and capsule was combined and adjusted to 10 ml. The buffer used for the rinsing of the mouthpiece and the induction port are combined, as well and adjusted to 20 ml. The buffer that was used for the rinsing of the pre-separator is adjusted to 20 ml, including the 7.5 ml buffer the pre-separator is filled with (Figure 8).

For quantification, the fluorescence of the fluorophore fluorescein-Na with the excitation wavelength λ_{ex} = 485 nm and the emission wavelength λ_{em} = 520 nm was utilized. The pH was kept constant through use of HEPES buffer, because fluorescence of fluorescein depends on the pH [193]. Quantification was calculated based on a calibration curve. Samples were diluted (up to 1000-fold) in order have adequate fluorescence intensities within the concentration range of the calibration curve.

Fluorescence was quantified for each batch of fibres with a calibration curve. For this purpose the base layer adhering to the glass slide after cleavage from the template membrane was scraped with a blade and flakes of it were collected. Approximately 10 mg were weighed and diluted in order to reach a concentration range in which the correlation between the fluorescence intensity and fluorescein-Na is linear. As the second reference, the remains of the fibres that were not transferred to the gelatin capsule for the aerosolisation experiment were weighed and diluted accordingly. Each of the two references, the base layer having been formed from the identical gel as the fibres and the fibres that could not be transferred to the capsule for the aerosolisation experiment, was used for a calibration curve, additionally allowing to discover differences in the distribution of fluorescein-Na between fibres and the base layer.

4.2.2.1.3 Cylindrical Particles Made of Pure Agarose and Blends with Lactose

Agarose with a concentration of up to 2.5 % (m/V) is suspended in a solution containing 15 % (m/V) lactose, as well as variable concentrations of fluorescein-Na (< 2 % (m/V)); for pure agarose cylinders (concentrations of maximum 5 % (m/V)), lactose is omitted from the preparation protocol. The dispersion is heated to 120 °C for 20 min in a closed vial under constant stirring in order to guarantee complete dissolution, thereafter the temperature is reduced to 90°C for further 10 min. 500 µl of this clear solution are pipetted onto a glass slide and a template membrane (25 mm) is quickly applied with the shiny side facing the sol. The membrane is peeled off after the solidification of the gel and the drying under ambient conditions overnight. Two membranes are transferred to a 2.0 ml Eppendorf cup, 1.6 ml THF is added and vortexed for 15 s for dissolution. The dispersion of the fibres is centrifuged at ~ 4300 rcf for 8 min. The supernatant is removed, the same volume (1.6 ml) is added and

vortexed before the next cycle starts. Centrifugation is repeated three times in total in order to remove the PC from the template membrane.

4.2.2.1.4 Cylindrical Particles Made of Gelatin

Gelatin in concentrations ranging from 1 - 10 % (m/V) is heated under mild stirring in a closed vial in order to prevent evaporation. For labelling, fluorescence dyes such as fluorescein-Na can be added to the aqueous solution. After complete dissolution in deionized water, 250 µl solution is pipetted onto a Petri dish and one membrane (25 mm) is quickly added. The membrane solution fills the pores of the membrane by capillary forces. 5 ml of the crosslinker glutaraldehyde (GTA) (1 % (V/V) in deionized water) is added in two steps. 1 ml is added on the top of the membrane and after 10 minutes further 4 ml are added. The membrane is allowed to hover in the GTA solution for further 10 minutes.

After crosslinking the filter membrane with the adhering hydrogel is transferred to a scratched glass slide (4.2.2.1). After drying overnight, the membrane is peeled off in order to remove the interlinking layer. The membrane is transferred to an Eppendorf cup and dissolved with 1.6 ml THF. The gelatin filaments are purified by centrifugation at 4300 rcf for 10 min, the supernatant is discarded and 1.6 ml THF is added. This purification cycle is repeated three times.

4.2.2.2 Microcylinders Composed of Nanoparticles
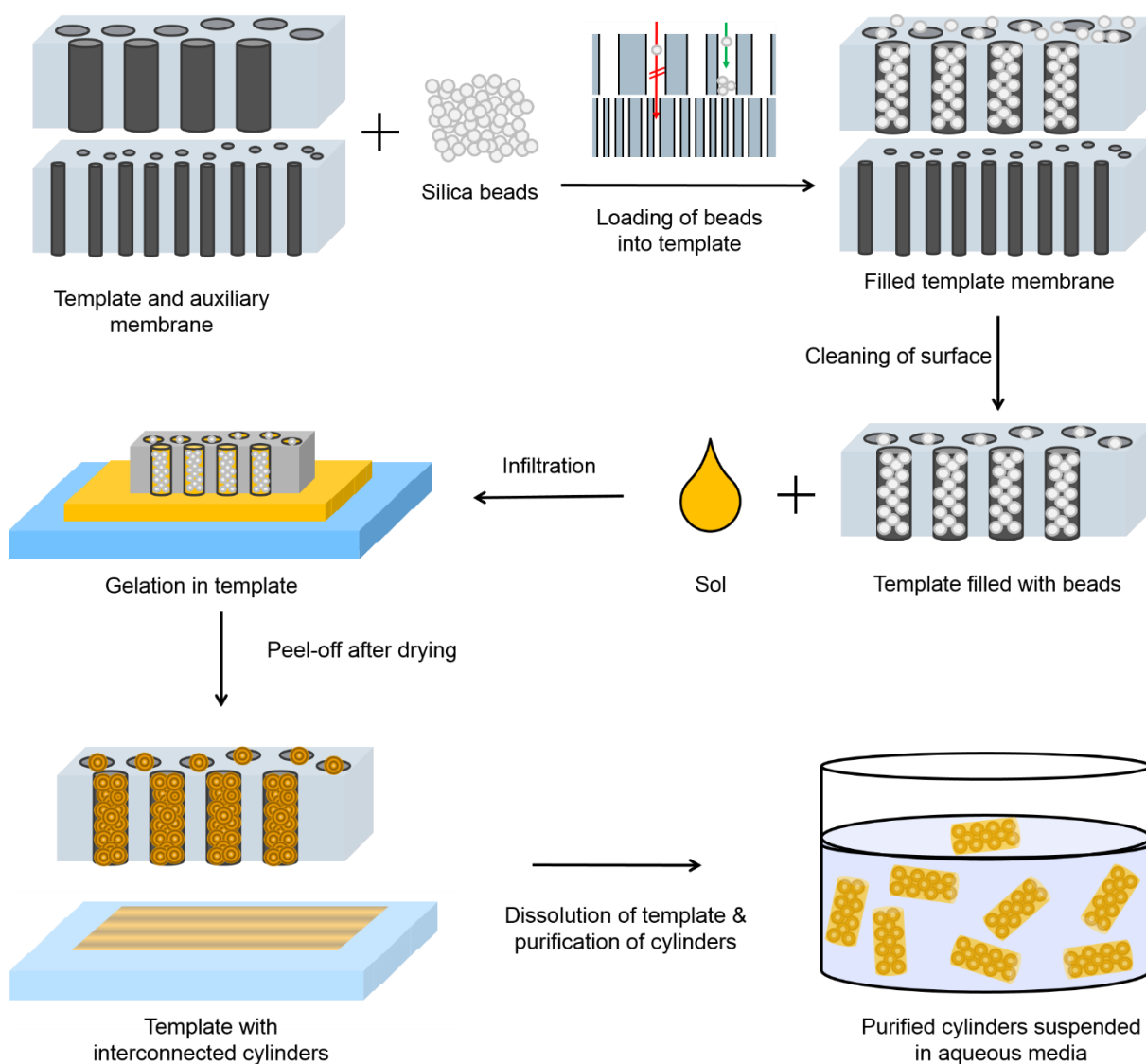
Figure 20 – Illustration of the protocol for the formation of cylindrical microparticles composed of nanoparticles.

The protocol for the formation of microcylinders composed of NPs is illustrated in Figure 20. As the first step, the template membrane with the pore diameter of choice (5.0, 2.0, or 1.0 µm) is filled with silica beads (841, 500, or 200 nm). The template membrane, that is supposed to be filled, is put on top of an auxiliary membrane with lower pore diameter, not permitting the beads to pass through the pores. Both membranes (25 mm) are put on top of each other and are placed in the filter holder. Subsequently, the suspension containing the nanoparticles

(0.1 % (m/V)) is filled in a disposable syringe with Luer lock and filtered through the membranes, thereby trapping the particles in the pores of the membrane with bigger pores. Per membrane, approximately 1 ml is used, regardless of the particle diameter. The amount of particles exceeds the volume of the pores for all templates (Table 1). In principal, the complete filling is guaranteed, supposing a homogenous distribution of the beads into all pores of the template. For all particle sizes an auxiliary membrane (track-etched, PC) with 0.1 µm pore diameter was used. Both membranes were removed from the filter holder and were allowed to dry. The auxiliary membrane was removed and the excess beads, laying on the surface, were carefully wiped away with tissue wipers.

Hydrogels were used for the interconnection of the spherical particles in order to conserve the cylindrical geometry, given by the template. In accordance to the protocol for the generation of cylindrical particles (4.2.2.1), the filled template was only applied to the gel with the shiny side. Being in the liquid state, the sol could enter the pores and interconnect the silica particles. Furthermore, it was payed attention that gel only had contact with one side of the template, preventing the built-up of bridges, or the interlinking layer from both sides of the template. The hydrogel was allowed to form a gel and was stored until the hydrogel was dried. The template membrane was removed from the dried hydrogel base layer and dissolved in THF. Particles were subsequently purified by centrifugation. The pellet was redispersed in deionized water and the suspension was centrifuged again in order to remove the last traces of THF, which is cell toxic. As the last step, the pellet was redispersed in the buffer of choice.

Materials and Methods

4.2.2.2.1 Microcylinders Composed of NPs, Interconnected with Agarose

A solution of 1.5 % (m/V) agarose was used for the interconnection of the silica beads in order to conserve the cylindrical shape. The agarose dispersion was heated up to 130 °C in a closed container (scintillation vial) in order to prevent evaporation on a heating plate under stirring for 30 min. After complete dissolution of the agarose (30 min), the temperature was reduced to 100 °C and stirred for further 15 min. 1 ml of hot agarose solution was removed from the vial and pipetted on a glass slide, quickly the template membrane, containing the silica beads, was applied and the agarose solution could enter the pores and interconnect the silica particles prior to forming a gel. The gel and the template membrane, containing the interconnected silica particles, are allowed to dry under ambient conditions. Excess $CaCl_2$ solution is removed with tissue wipers before the template is applied on the glass slide. Subsequently, the template membranes are peeled off the glass slides and transferred to Eppendorf cups. Two membranes were put into a 2 ml Eppendorf cup and dissolved in 1.6 ml THF. The cups were vortexed for 1 min in order to speed up the dissolution. The dissolved PC was removed by centrifugation, the supernatant, containing the PC of the template membranes, was removed after each cycle and replaced by fresh THF. After three cycles of centrifugation at ~ 4300 rcf for 8 min, the pellet was redispersed in deionized water. Centrifugation was repeated three times at ~ 11000 rcf for 10 min in deionized water in order to completely remove the THF. As the final step particles were redispersed in the buffer of choice.

Alternatively, the particles can be further purified through filtration, separating the microcylinders from the NPs, not having been interconnected. For filtration a track-etched membrane was utilized, having a pore diameter, which allows single beads to pass and the cylinders to be trapped (1.0 µm). A significant fraction of the cylinders was lost though

adhesion on the walls of the filter holder. This could be seen through the fluorescence, stimulated by an UV lamp. The membrane, carrying the cylinders, was directly dissolved in THF after filtration and the filtrate was discarded. Subsequently, the dispersion was centrifuged three times in aqueous media in order to remove the THF. As the last step, the cylinders were redispersed in the buffer of choice.

4.2.2.2.1.1 Microcylinders Composed of NPs, Interconnected with Agarose – Preparation Conditions for Cell Tests

Polycarbonate track-etched membranes with a thickness of approximately 10 µm and a pore size of 2.0 µm (Table 1) were utilized as a template for the formation of the cylindrical particles. Plain blue fluorescing silica beads (λ_{ex} = 354 nm/λ_{em} = 450 nm) with a diameter of 500 nm were filled into the cavities of the membrane. The arrangement of close-packing of equal spheres of the beads gives the submicron texture of the cylinders (Figure 37). The particles were prepared under minimal exposure to light in order to prevent bleaching of the fluorescence dyes. After the last centrifugation cycle the pellet was redispersed in RPMI-medium (5 % FCS, 1 % Penicillin/Streptomycin). The particles redispersed well without aggregation, no stabilizer was added. The particle concentration in the stock solution was determined with a Neubauer chamber and diluted to a final concentration of 100,000 particles/ml in RPMI-medium (5 % FCS, 1 % P/S).

4.2.2.2.2   Microcylinders Composed of NPs, Interconnected with Alginate

Alginate with a concentration of 0.7 % (m/V) was used for the interconnection of the beads, conserving the geometry given by the template membrane. 1 ml of the alginate sol was pipetted onto the surface of a Petri dish. The template membrane (25 mm) containing the silica particles was applied with the shiny side facing the sol, allowing the sol to enter the pores of the track-etched membrane wrapping the silica nanoparticles. 5 ml of gelation liquid (50 mM $CaCl_2$ solution) are applied onto the top of the template membrane covering the entire template membrane; after 10 min the template membrane is gently lifted with forceps, if it has not been automatically lifted up and started to float (Figure 19 and Figure 20). The floating allows for a good exposure of the entire alginate towards the Ca^{2+} solution and a homogenous gelation. After a total gelation time of 15 min the template membrane with the adhering alginate is transferred to a glass slide and dried under ambient conditions. The gel and the template membrane containing the interconnected silica particles are allowed to dry under ambient conditions. Subsequently, the template membranes are peeled off the glass slides and transferred to Eppendorf cups (two membranes into one 2 ml Eppendorf cup) and are dissolved in 1.6 ml CH_2Cl_2 per cup. The cups were vortexed for 1 min in order to speed up the dissolution. The dissolved PC from the template is removed by centrifugation, the supernatant, containing the PC, was removed after each cycle and replaced by fresh solvent. After one further cycle with CH_2Cl_2, THF is used for the purification followed by one cycle with ethanol. Centrifugation is performed at ~ 4300 rcf for 8 min for CH_2Cl_2 and 6 min for THF and EtOH. After the last cycle the pellet is redispersed in deionized water, or the buffer of choice. Between each centrifugation cycle the pellet was vortexed for at least 3 min and sonicated for 10 min.

4.2.3   Preparation Strategies for Hydrogels with Hairy Surface
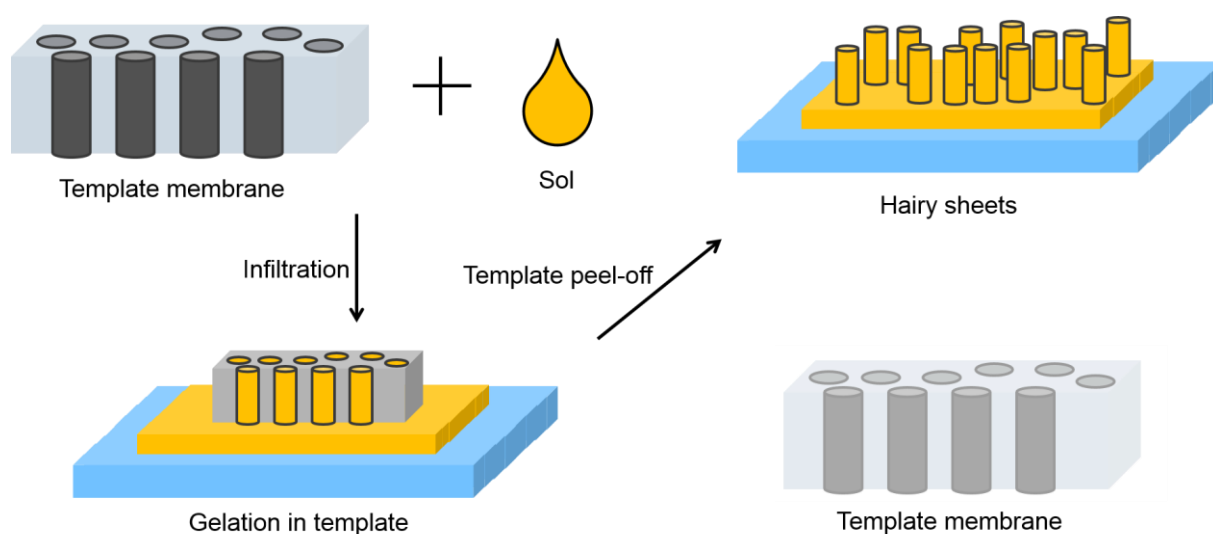
Figure 21 – Illustration of the protocol for the formation of hairy sheets for various hydrogels.

The protocol for the preparation of fibrous sheets, made from hydrogels is depicted in Figure 21. The liquid precursor of the gel (sol) is dropped on a plane surface, such as a glass slide, and the template membrane is applied. The template membrane is filled through the strong capillary forces of the template pores. After infiltration the sol forms a gel within the template, following diverse mechanisms as a function of the gel. After moulding through gelation, the template is peeled off, releasing the hairy sheets.

4.2.3.1   Hairy Surface Made from Alginate

250 µl isotonic 0.9 % NaCl solution containing 0.7 % (m/V) ultra-high viscosity alginate is dropped on a 100 mm Petri dish. The hydrophilic disc-shaped track-etched membrane (25 mm diameter) is applied on the droplet and is allowed to be wetted from the bottom. 1 ml of 50 mM $CaCl_2$ solution is added onto the surface of the wetted filter membrane and allowed to form a gel for 10 min. Further 4 ml of $CaCl_2$ solution are added and the filter is then gently lifted from the Petri dish and allowed to float in the $CaCl_2$ solution droplet with a total volume

of 5 ml for another 15 min. After this gelation step, the filter membrane with the adhering alginate gel is transferred to a Petri dish (diameter 35 mm), which had been coated with a polycation (poly(L-lysine)) before. The electrostatic interaction between the positive surface and the negatively charged alginate layer increases the adhesion to the Petri dish and also facilitates the peel-off of the template membrane. As controls, Petri dishes coated completely with unstructured alginate hydrogels (negative control) as well as standard tissue culture treated surface (positive control) were prepared. For practical reasons, experiments, on which the presented results are based, were carried out mainly with membranes exhibiting diameters of 25 mm; the largest diameter used in the experiments was 47 mm.

4.2.3.1.1 Hairy Surface Made from Alginate – Specific Modification of Filaments

Before peel-off, 1 ml of FITC-pLL (fluorescein isothiocyanate-pLL) is added onto the surface of the template membrane (25 mm diameter), filled with cross-linked alginate, and allowed to interact for 1 min. Subsequently, the FITC-pLL solution is removed and the template with the embedded alginate is washed. Further steps are in accordance with the protocol for the formation of fibrous surfaces made from alginate (4.2.3.1).

4.2.3.1.2 Hairy Surface Made from Alginate – Loading and Release of Model Compounds

Gelation was performed in accordance with the protocol for plain hairy alginate sheets (4.2.3.1). For the loading of the model compound methylene blue equivalent concentrations (0.15 mg/ml) in the alginate sol (0.7 % (m/V)) and the $CaCl_2$ solution (50 mM) were used for gelation, guaranteeing no premature release of drug during the gelation. The solubility of methylene blue in water has been reported to be 40 mg/ml at room temperature [194].

Due to varying diffusion behaviour the loading regime for the macromolecular model compound FITC-dextran was adapted. FITC-dextran (0.3 mg/ml) was solely contained in the alginate sol (0.7 % (m/V)), which formed a gel upon addition of the $CaCl_2$ solution (50 mM). Subsequent steps were identical for both release compounds.

The release experiments were performed in a plastic Petri dish (100 mm). The surface of the Petri dish was treated with a polycation (polyethylenimine (PEI), aqueous solution of 20 mg/ml, coating for 15 minutes) in order to electrostatically adhere the gel to the Petri dish surface and to prevent floating of the gel sheet during release.

After gelation the gel sheet, containing either methylene blue or FITC-dextran, is transferred to the coated Petri dish placed on a shaking incubator (37°C), the release media, either ultra-pure water (adjusted to pH 7.4 with NaOH (1 mol/l)), or Dulbecco's phosphate buffered saline (DPBS) buffer is added and the release started. For quantitative release of the loaded FITC-dextran, phosphate (Na_2HPO_4) is added, forming a complex with the Ca^{2+} ions, being essential for the integrity of the gel. Due to the disintegration, the remaining FITC-dextran is released from the matrix. The final phosphate concentration was 20 mM. All experiments were performed under perfect sink conditions throughout the release phase.

For the quantification either a UV/VIS spectrometer was used at the absorption maximum of methylene blue ($\lambda = 664$ nm) with polystyrene cuvettes, or a fluorescence spectrometer with corresponding 96-well plates using the excitation wavelength 485 nm and the emission at 520 nm for the FITC-labelled dextran. NaOH (1 mol/l) was added prior to quantification in order to adjust the pH to 12.5 ± 0.5 and avoid any pH influence on the measurements.

4.2.3.2   Hairy Surface Made from Agarose

Agarose dispersions of up to 10 % (m/V) are heated to 120 °C for 20 min under constant stirring in a closed vial in order to guarantee complete dissolution, afterwards the temperature is reduced to 90°C for further 10 min. 500 µl of this clear solution are pipetted onto a glass slide and a filter membrane (25 mm) is quickly applied with the shiny side of the membrane facing the sol. The membrane can be peeled off after the solidification due to the temperature drop.

4.2.3.3   Hairy Surface Made from Gelatin

Gelatin in the concentration of choice (1 – 10 % (m/V)) is dissolved in deionized water aided by heating. The gelatin dispersion is heated to a maximal temperature 100 °C and stirred in a closed vial until complete dissolution is reached. Per membrane 250 µl solution is pipetted onto a Petri dish and one membrane (25 mm) is quickly added. The membrane wets the entire surface of the filter. A total of 5 ml of a solution containing 1 % (V/V) of the cross-linker glutaraldehyde (GTA) is added in two steps. 1 ml is added onto the surface of the filter after infiltration of the pores, after 10 min further 4 ml are added and the membrane is allowed to float in the GTA solution for 10 additional minutes. Subsequently the membrane is peeled off the hydrogel.

4.2.3.4   Hairy Surface Made from Chitosan

The chitosan solutions with a concentration of 2 % (m/V) were applied on one side of the track-etched membrane. Due to the high viscosity, the chitosan sol does not automatically distribute evenly at the chosen concentration; it has to be distributed homogenously manually. Per 25 mm template membrane 350 µl solution is applied in order to wet one entire side of the membrane. The membrane is exposed to the fumes of 5 ml of a concentrated

NH$_4$OH (25 %) solution for 15 min in a closed container. Longer exposure times damage the membrane more severely, not allowing a straightforward removal of the membrane through mechanical peeling off.

The gel sheet can be loaded with fluorescein (fluorescein-Na), which does not hinder gelation.

4.2.3.5 Hairy Hybrid Sheet – Differences in the Composition of Hairs and Base Layer
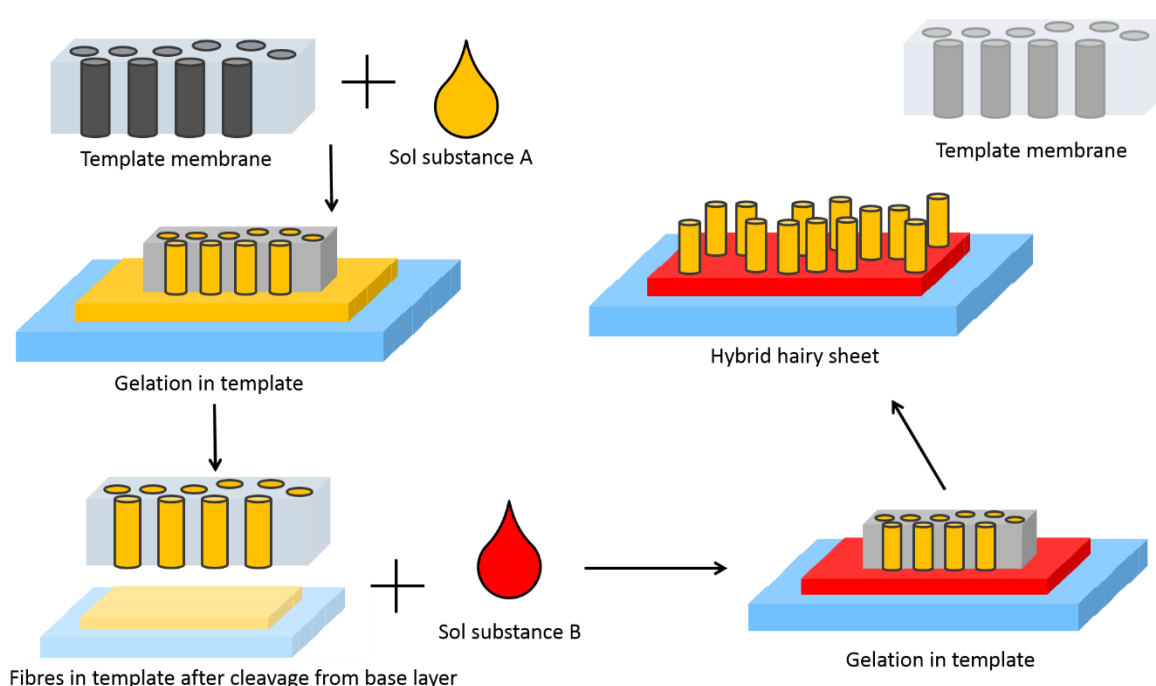
Figure 22 – Schematic of the protocol for the formation of hairy sheets having a different composition of the fibres and the base layer.

The protocol for the formation of hairy surfaces, composed of more than one hydrogel is illustrated in Figure 22.The liquid precursor of the gel (sol substance A) is dropped on a plane surface, such as a glass slide, and the plain template membrane is applied. The template membrane is filled through the strong capillary forces of the template pores. After infiltration, the sol forms a gel within the template, moulding the gel. After drying, the fibres that are trapped in the template membrane are cleaved from the base layer through peel-off. The

protocol is repeated, replacing the plain template membrane with the one filled with the fibres. The liquid precursor of the second gel (sol substance B) is dropped on a glass slide and the filled membrane is added. After gelation, the template membrane is peeled off, releasing the hairy sheets, exhibiting a different composition for the base layer and the hairs.

4.2.3.5.1   Hairy Hybrid Sheet – Differences in Labelling and Concentration between Fibres and Base Layer – Agarose

In adaptation of the protocol for the formation of hairy sheets made from agarose (4.2.3.2), silica particles (200 nm), labelled with a fluorescence dye, were mixed with the heated agarose solution at 90°C just before the filter membrane was applied. In order to guarantee the labelling of all cavities in which the hydrogel progresses, the concentration of the silica labels was chosen very high, with a value of 1/5 (10 mg/ml) of the stock concentration of the solution 50 mg/ml. The dispersion was allowed to homogenize for a few moments through stirring on the rotating plate, before a volume of 500 µl was pipetted onto a glass slide and the template (25 mm) was applied. The silica particle dispersion in agarose was allowed to form a gel. After complete drying, the membrane was peeled off, trapping the labelled hairs within the pores. Subsequently, the protocol for the gelation of agarose was applied (4.2.3.2) with a concentration of 2 % (m/V) and the template containing the labelled fibres, replacing the unprocessed membrane.

4.2.3.5.2 Hairy Hybrid Sheet – Differences in the Type of Hydrogel – Gelatin Hairs on Agarose

Sheets

The protocol was adapted from the formation of hairy surfaces made from gelatin (4.2.3.3).

Additionally, a concentration of 0.6 % (m/V) 50 nm Fluoresbrite polystyrene particles was

added to the gelatin solution in order to label the entire hydrogel. After solidification with

GTA, the hydrogel was allowed to dry on a glass slide, peeled off, thereby trapping the fibres

in the template and cleaving them from the base layer. Subsequently, the protocol for the

gelation of agarose was applied (4.2.3.2) with a concentration of 2 % (m/V). The template

membrane, containing the labelled fibres replaced the unprocessed plain membrane.

Materials and Methods

4.2.4   Cell Experiments

4.2.4.1   Macrophage Uptake of Microcylinders

Murine alveolar macrophages (MHS, ATCC, CRL-2019) were cultured in RPMI 1640-medium containing 10 % FCS, 1 % HEPES, 55 mg sodium pyruvate, 0.75 g sodium hydrogen carbonate, 2.25 g D-glucose, 1 % Penicillin/Streptomycin and 1.95 mg β-mercaptoethanol. 20,000 cells per plate were cultured on glass plates with a size of 22 × 22 mm for one day. Then, the growth medium was changed with medium containing 100,000 cylindrical particles per plate. To analyse the uptake profile, cells were fixed at different time points after addition of particles (0, 1.5, 3, 4.5 and 24 hours). For fixation, cells were incubated in 100 % methanol for 10 minutes and washed three times in phosphate buffered saline. After that, they were incubated in 3 % (V/V) glutaraldehyde for two hours to cross-link the proteins and dried with increasing alcohol concentrations (70 %, 80 %, 95 %, 100 %, 100 %; exchange rate: 1 hour). The samples were sputtered (sputter current of 20 mA for 50 s) and coated with a gold layer of approximately 15 nm thickness. For each sample, several randomly selected frames were captured using FLM until a count of 300 ± 20 macrophages was reached.

4.2.4.2   Cell Interactions with Hairy Surfaces

Cellular response on hairy alginate hydrogels was studied using murine L929 fibroblasts (Figure 66 (d)-(f)). Fibroblasts were cultivated in Dulbecco's modified eagle medium (DMEM) medium, containing 10 % fetal calf serum and 0.1 mg/ml Gentamycin. For passaging, cells were washed with phosphate buffered saline (PBS) and treated with 0.05 %/0.02 % trypsin/EDTA (ethylenediamine-tetraacetic acid). Cell density was adjusted to 5×10^4 cells/ml. A cell suspension of 2 ml was given to the previously prepared samples in 35 mm Petri dishes. Cultivation and observation of samples were performed in an automated microscope

Biostation CT for at least three days. Analysis of image data was performed using NIS-elements software package.

4.2.4.2.1   Characterization of Hairy Surfaces and Visualization of Interactions with Cells

For optical microscopy the illumination was chosen low and exposure time of the camera was increased in order to enhance the visibility of the low optical contrast hairy microstructures. Fluorescence was excited with λ_{ex} = 470 nm and an emission bandpass (BP 525/50) was used for detection. For imaging with the confocal laser scanning microscope (CLSM) the argon laser with λ_{ex} = 488 nm was used, the emission was detected from λ = 505 – 530 nm. The CLSM images were captured and processed with the software Zeiss LSM AIM 4.2.

For the fixation of the samples for SEM imaging, alginate sheets with cells were fixed in sodium cacodylate buffer containing 2 % (V/V) glutaraldehyde for at least 24 h. After that, they were incubated in 2 % (V/V) osmium tetroxide and 1 % (m/V) tannic acid in sodium cacodylate buffer (0.15 M). Samples were dehydrated in increasing ethanol concentrations and finally dried using hexamethyldisilazane (HMDS). The samples were imaged using standard operating settings for the SEM (4.2.1.2.2.1).

Materials and Methods

5 Results and Discussion

5.1 Characterization of Template Membranes

The templates differ greatly regarding the pore abundance and the pore diameter (Table 1). The measured values for porosity, the area of the pores over the template surface area and pore density, correspond to the given values by the manufacturer (porosity < 15 %, pore density 1×10^5 to 6×10^8 pores/cm²) [195].

Pore size of template [µm]	5.0	2.0	1.0	0.6
Thickness of template membrane [µm]	10 ± 1	10 ± 1	10 ± 1	10 ± 1
Pore density/100 µm²	0.38	2.55	18.44	34.75
Pore density/cm²	3.80E+05	2.55E+06	1.84E+07	3.47E+07
Template porosity [%]	7.5	8.0	14.5	9.8
SD of template porosity [%]	0.3	0.3	0.6	0.4
Total volume of pores (25 mm) per membrane [µl]	0.37	0.39	0.71	0.48
Total volume of pores (47 mm) per membrane [µl]	1.30	1.39	2.52	1.70

Table 1 – Specifications of relevant track-etched PC template membranes.
Pore density/100 µm² and pore density/cm² represent the abundance of pores in the template membrane per given area. The template porosity is given by the area of the pores over the filter surface. SD of template porosity represents the standard deviation of the abundance of pores in the template in SEM micrographs of the shiny side of the membrane with more than 250 pores per image (n ≥ 3). The total volume of the pores is calculated on basis of the respective porosity for membranes with 25 and 47 mm diameter.

The template membranes do not possess identical surfaces on the top and bottom surface (Figure 23). The macroscopic appearance indicates differences that were confirmed through

Results and Discussion

SEM analysis. One side exhibits a smooth surface, which appears shiny for the naked eye. The other side appears matt for the naked eye and the SEM images reveal that the surface is entirely covered with irregular indentations besides the homogenous cylindrical pores. An influence of the surface structure on the outcome of the experiments cannot be ruled out, therefore the experiments were all conducted with consideration of the orientation of the membranes.
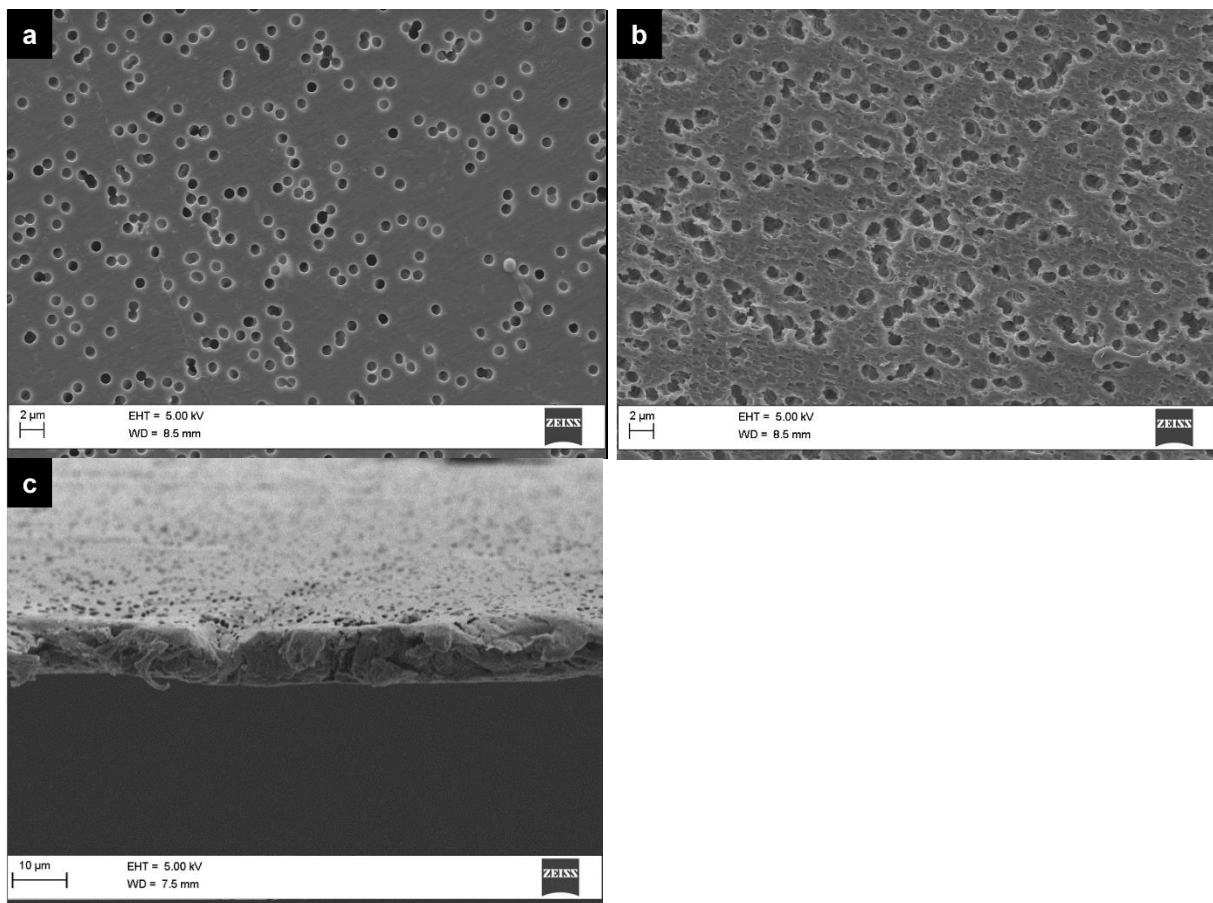
Figure 23 – SEM micrographs of the two surfaces and the cross-section of the identical template membrane.

The template exhibits 1.0 µm pore diameter, images were captured with identical magnification. (a) The surface is smooth. (b) The surface is rough and many indentations besides the pores can be seen. (c) The thickness of the membrane is 10 ± 1 µm, which is in accordance with manufacturer specifications [195]. The cross-section was partially deformed by the blade with which it was cut prior to imaging.

A prerequisite for the utilization of template membranes for moulding purposes is an unhindered filling of the plentiful pores. The hydrophilic fluid precursors are required to fully access the numerous cylindrical pores of the template in order to warrant a high yield and reproducibility of the protocol. Supposing a complete filling of the cavities, the pore volume allows for an estimation of the maximum yield per membrane (Table 1). It can be calculated from the density, since the pore volume is known, ranging from approximately 0.6 to 1.1 mg for the excipient α-lactose monohydrate with a density of 1.525 g/cm³ [196] per membrane (25 mm diameter). In order to guarantee the unhindered filling the wettability of the membrane surface must correspond to the solvents. Most commonly, track-etched membranes are made from polycarbonate (PC), which has a comparatively low surface energy and consequently low wettability. Manufacturers use wetting agents, such as polyvinylpyrollidone (PVP) in order to optimize the wetting behaviour; accordingly treated membranes are denoted by "hydrophilic" [197]. Without exception, hydrophilic template membranes (PC membranes treated with PVP, according to product information sheet [195]) were used for the experiments, enabling a reliable and homogenous wetting of the surface and the pores. Influence of the wetting agent on the outcome of cellular tests can be neglected. Washing prior to the addition of cells quantitatively reduces potential contaminations. Furthermore, PVP is regarded as biodegradable [6, 198] and does not enhance adhesion of fibroblasts. In fact, adhesion of fibroblasts (hTERT cells, immortalized human fibroblasts) on PVP coated surfaces of implants was even diminished in comparison to other coatings [6].

5.2 Filaments Formed with the Template Technique

The various hydrophilic solutions, including hydrogel sols, quickly wet the track-etched membrane and spread well on the surface. Filling of pores with the hydrophilic liquids was observed independent of the pore diameters. The minimum pore diameter was 0.1 µm, used in experiments with the hydrogel agarose (Figure 34, Figure 59). The hydrophilic solution of hydrogel sols, in some cases being viscous (high concentrations of alginate, agarose, gelatin, or chitosan), enters the pores readily, without exception. The strong capillary forces, caused by the large surface to volume ratio of the micron and even more pronounced for the submicron channels, are the driving force for this behaviour. Viscosity, representing the counteracting force for the speed of filling [199], is overcompensated by the narrow diameter of the pores and the low capillary height of 10 ± 1 µm (n = 3, value in accordance with thickness of membranes reported by manufacturer: 6 - 11 µm [195]). The observation of the complete and swift filling of the pores is supported by findings made on channels with comparable geometries [199, 200], giving a filling of the pore in the order of milliseconds even though capillary filling is slowed down in nano-metric channels [199, 200]. Since the pores of the template membrane are being filled completely, the thickness of the membrane dictates the length of the fibres (Figure 23). In some cases the pores are tilted, which leads to moderately longer cylinders.

5.2.1 Cylindrical Particles Consisting of APIs and Lactose

The template technique can be used for the formation of cylindrical particles made of various hydrophilic compounds in a broad concentration range. Cylinders made of hydrophilic APIs, such as fluorescein-Na and salbutamol (INN)/albuterol (USAN) sulphate, as well as blends with the excipient lactose have been prepared in various ratios, allowing to customize the dose of

the inhaled medicine. Cylindrical particles could be formed from 5.0, 2.0, and 1.0 μm template membranes and represented the pore geometry in high fidelity. Salbutamol could be blended with lactose in any ratio at the constant mass concentration of 15 % (Figure 24). In order to guarantee a complete dissolution of the solutes under all experimental conditions, routine experiments were not performed with higher concentrations, because the solubility limit in water for α-lactose has been reported to be 189.1 mg/ml [158]. The solubility of salbutamol sulphate is higher with 291 mg/ml at room temperature [190]. Below a solute content of 15 %, an increasing formation of funnels or tubes was observed (Figure 24 e and f). Nonetheless, single tubular cylinders could also be found at a solute concentration of 15 % (Figure 24 d). The lower the concentration was chosen, the more pronounced the central cavity was (Figure 24 e and f). A high fraction of truncated particles is found for cylinders formed from solutions with low content of lactose (1.5 % m/V)) (Figure 24 f). The tubular shapes that were found after purification from the PC of the template membrane imply that precipitation of the solute begins at the pore walls.
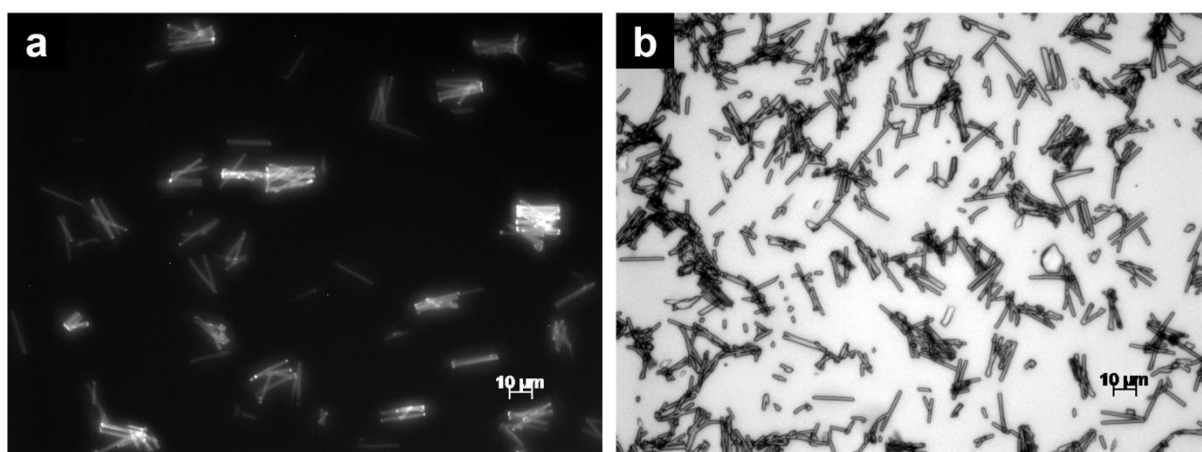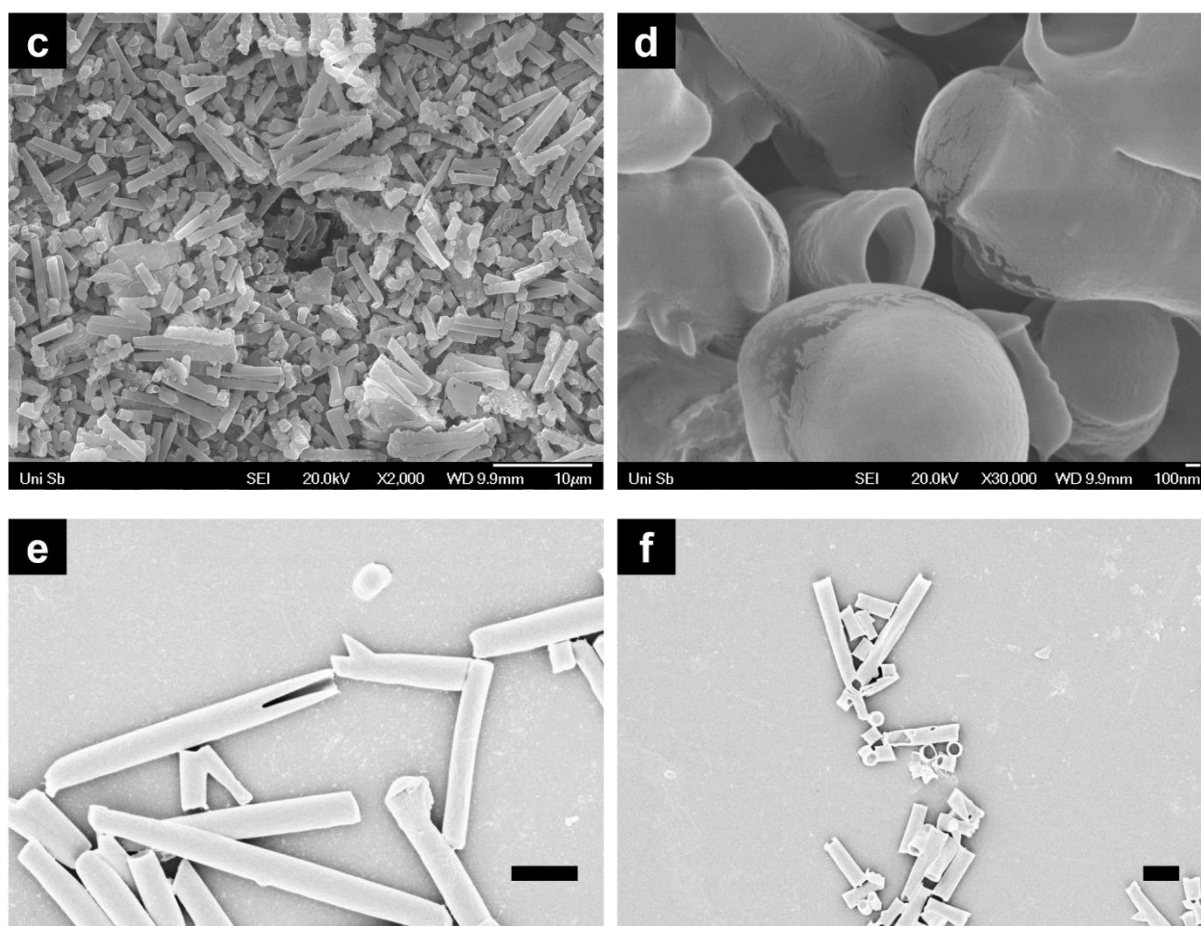
Figure 24 – Light microscopy and SEM images of microcylinders made of lactose and blends with salbutamol.

(a) Fluorescence image of salbutamol-fluorescein-lactose fibres, salbutamol sulphate mass fraction 0.5, fluorescein-Na 0.05, lactose 0.45. (b) Transmission light microscopic images of salbutamol-lactose blended fibres, salbutamol sulphate mass fraction 0.5, lactose 0.5. (c) – (f) SEM micrograph of cylindrical particles after purification from PC; pure lactose. (d) In the centre of the SEM image a tubular particle can be seen. (e), (f) For lower solute concentrations, tubular particles or particles with central funnel are formed. The pore diameter of the template was 1.0 µm, the solute concentration (m/V) was 15 % for (a) – (d) and 1.5 % for (e), (f). The scale bar corresponds to 10 µm (c), 200 nm (d) and 2 µm (e), (f).

The humidity in the deep lung is close to saturation [126]. Harmful long-term accumulation of the cylindrical particles composed of various ratios of lactose, salbutamol and fluorescein-Na can be ruled out, because these particles disintegrated and dissolved after exposure to saturated vapour (Figure 25).
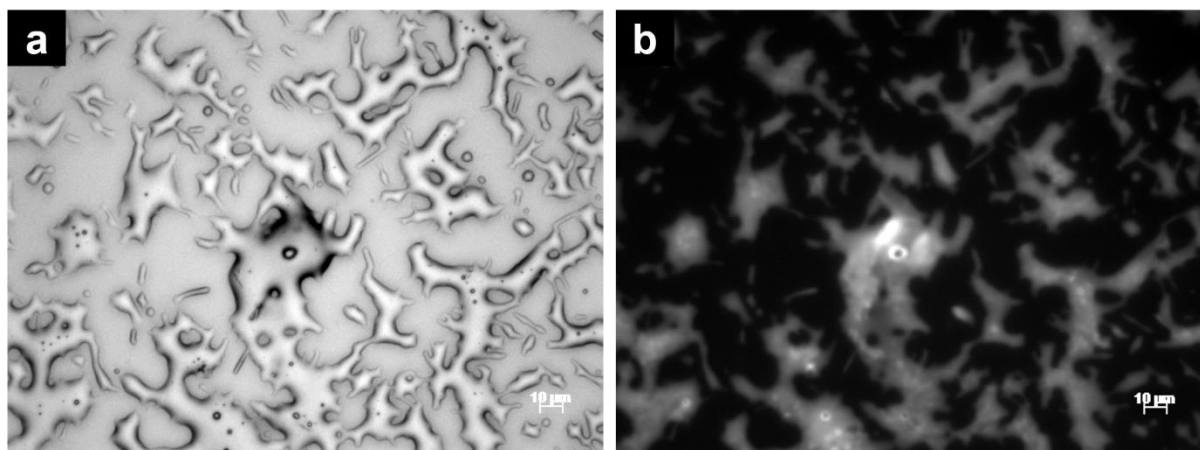
Figure 25 – Light microscopic images of microcylinders made of lactose, salbutamol and fluorescein-Na after exposure to vapour.

(a) The transmission light microscopic image and (b) the fluorescence image were captured at identical position on the specimen. The pore diameter of the template was 1.0 µm, solute concentration 15 % (m/V), consisting of salbutamol sulphate with a mass fraction of 0.5, fluorescein-Na 0.05, lactose 0.45.

5.2.2 Cylindrical Particles Made of Alginate, Blended with Lactose

Mechanisms for clearance are limited in the alveolar region of the lung, the main mechanism is phagocytosis. Enzymatic activity is low in the lungs and the tissue is fragile. This physiology asks for particular precautions for the selection of a carrier system. This explains the fact that the pool of excipients with approval for lung administration from drug agencies is limited. Despite this fact, non-degrading fibres, such as CNTs, are under investigation in order to be used as drug delivery systems for intravenous administration (2.1.2.4.1), but in particular the long CNTs are not appropriate for pulmonary application considering the so-called frustrated phagocytosis, which is known from asbestos [201, 202]. The lining fluid which also serves as solvent for the dissolution of drugs is scarce in the peripheral lung, entailing slower dissolution in comparison to intravenous administration [141].

For these reasons a delivery system that reaches the deep lung to a high extend, does not accumulate and is soluble, or degradable in the scarce fluid present in the lungs is desirable.

Results and Discussion

The filamentous particles consisting of a backbone of alginate and lactose have been designed in order to fulfil these attributes.

The natural polysaccharide alginate is biocompatible and biodegradable and forms gels with divalent cations such as Ca^{2+}. This ion forms complexes with phosphates, which are ubiquitous in the body, degrading the gel in a concentration dependent manner. The dissolution behaviour of the alginate gel is scrutinized in chapter "Drug Loading and Release from Hairy Alginate Surfaces" (5.4.1.1.2). High concentrations of phosphate degrade alginate gels within minutes. Considering the toxicity of asbestos, which can be attributed to long term inflammation because of the so-called frustrated phagocytosis [201, 202], clearance through degradations appears to be particularly important.

Another beneficial property in this context is the high hydrophilicity of alginate gels, reducing the immunologic response which can harm the tissue over time. A prominent exploitation of this phenomenon is the decoration with hydrophilic entities, such as PEG chains in order to hinder the adsorption of proteins [203-206], essential for the activation of the immune system. Among the alginate hydrogels, in particular the gels, which are formed with calcium, inhibit adsorption of serum proteins; in consequence cell attachment and spreading is decreased [207].

Cylindrical particles consisting of alginate and lactose do not completely dissolve after exposure to humidity, in contrast to pure lactose, or blends with APIs (5.2.1), such as salbutamol sulphate, or the fluorescing compound fluorescein-Na (Figure 26 and Figure 27). Despite the low content of alginate in the blend, the hydrogel backbone changes the properties of the fibres drastically. After exposure to humidity, being immersed into water droplets and drying under ambient conditions, the fibrous geometry was retained. The low molecular entities, including lactose and the label (fluorescein-Na), had diffused from the fibre

(Figure 27). The fluorescence of the marker substance fluorescein-Na can be detected beyond the filaments, implying diffusion and release from the cylindrical particles. This alginate hydrogel is stable under these conditions and does not degrade in deionized water. For all evaluated cylinder dimensions (templates 1.0, 2.0, 5.0 µm) the exposed hydrogel gel backbone was found (Figure 26 and Figure 27). The diffusion of chemical entities with hydrodynamic diameters smaller than the pore size of the alginate gel are not hindered (5.4.1.1.2), in contrast to large macromolecules, such as the polysaccharide dextran (2000 kDa), exceeding the mesh size of the gel. These macromolecules are retained within the gel network (Figure 56). The alginate-lactose fibres can be loaded with hydrophilic cargo which is embedded into the alginate-lactose matrix. Alginate releases the load as a function of the hydrodynamic diameter, a measure of the molecular mass. The small molecule methylene blue is released faster than the macromolecule dextran (2000 kDa) under all experimental conditions (5.4.1.1.2, Figure 56).

Furthermore, the alginate gel degrades in presence of the endogenous agent phosphate. Phosphate forms complexes with the Ca^{2+} ions, essential for the formation of the gel (4.1.5) and causes a concentration dependant degradation of the alginate gel (5.4.1.1.2, Figure 56).
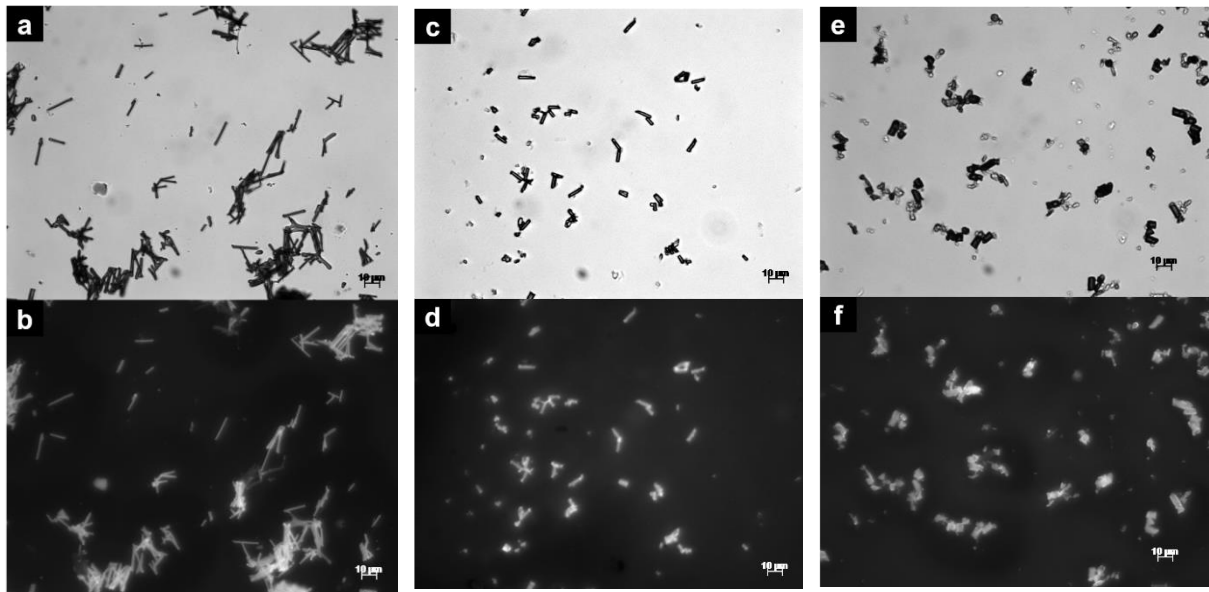
Figure 26 – Light microscopy and fluorescence images of cylindrical alginate-lactose particles, labelled with fluorescein-Na, after purification from PC template.

(a), (b) Fibre diameter is 1 µm; (b) fluorescence image of the identical position. (c), (d) Fibre diameter is 2 µm; (d) fluorescence image of the identical position. (e), (f) Cylinder diameter is 5 µm; (f) fluorescence image of the identical position.
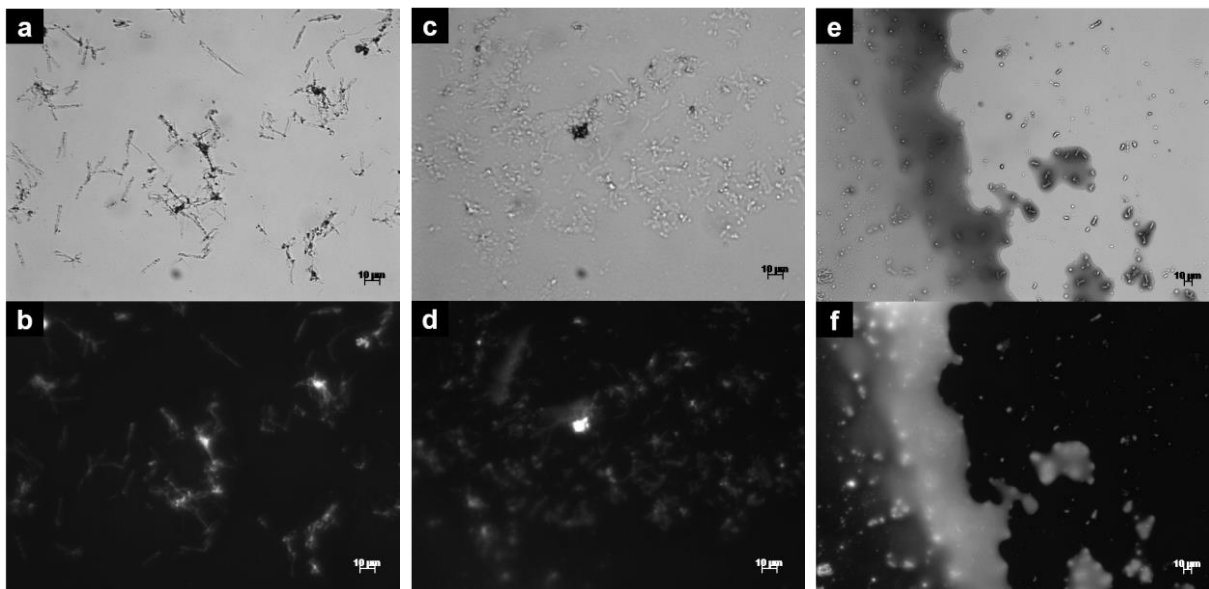
Figure 27 – Light microscopy and fluorescence images of cylindrical alginate-lactose particles, labelled with fluorescein-Na, after purification from PC template and after exposure to humidity.

(a), (b) Fibre diameter is 1 µm; (b) fluorescence image of the identical position. (c), (d) Fibre diameter is 2 µm; (d) fluorescence image of the identical position. (e), (f) Cylinder diameter is 5 µm; (f) fluorescence image of the identical position.

The composition did not change through the infiltration in the pores. This was assessed by the comparison of the fluorescein-Na concentration in the base layer and the fibres; the concentration only revealed negligible deviations. The variations laid within the scattering of the single experiments. The diameter of the pores (minimal size 0.6 µm) is orders of magnitude bigger than the molecular dimension of all chemical entities that were used for the preparation. Thus the infiltration is in no respect hindered and no separation of the compounds can be observed.

Most relevant for the assessment of the aerodynamic behaviour at the chosen experimental conditions (60 l/min) is the deposition of the fibres on stages 2, 3 and 4, representing the stages with a higher than 50 % deposition for objects with an aerodynamic diameter between 5 and 1 µm (Figure 28) [161], the target value for particles in this study.
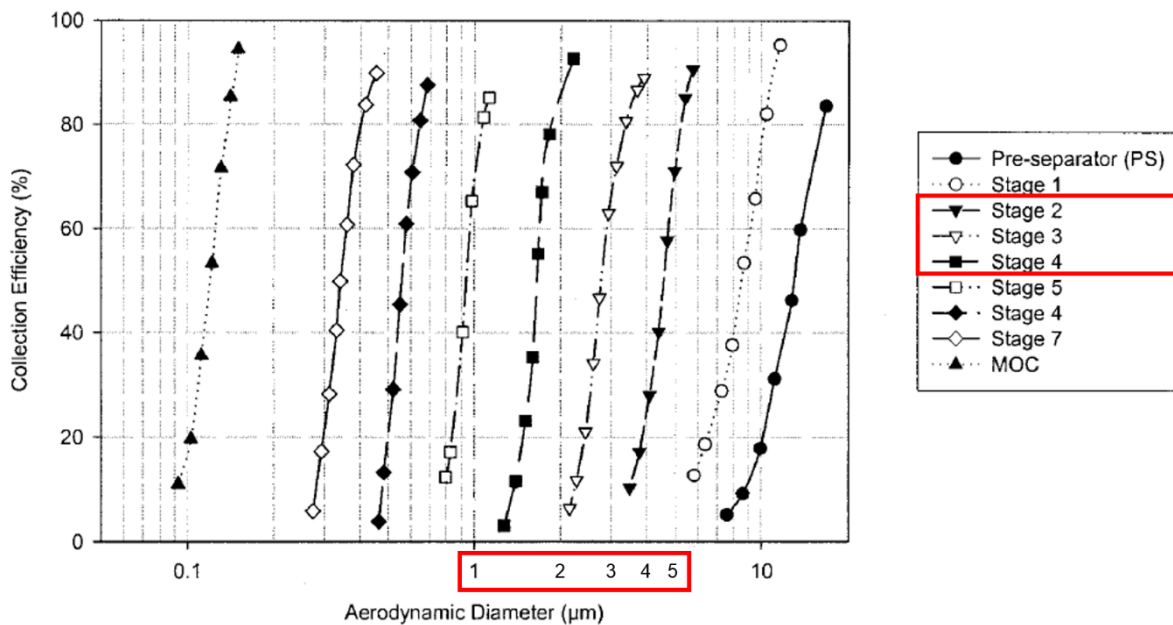
Figure 28 – Deposition on the stages on the NGI as a function of the aerodynamic diameter. Flow rate for the graph is 60 l/min. Stages with high deposition (> 50 %) for the aerodynamic diameter of choice (1 – 5 µm) are highlighted in red. Figure was adapted from [161].

Results and Discussion

The pronounced hygroscopy of the fibres became evident during the first preparations. The fibres clotted after few minutes under ambient conditions (Figure 29). The higher humidity was, the faster this could be observed. For single preparations wetting of filaments was observed within seconds.

Yet another reason for the observed tendency to form aggregates are geometrical considerations. Spheres represent the geometrical objects with maximal volume per surface. All other geometries exhibit an elevated surface, which can be responsible for cohesion, or aggregation. Fibres lying parallel, exhibit a large contact area, which can be responsible for aggregation.

L-leucine has been reported to reduce hygroscopy for pulmonary formulations [208]. The proteinogenic amino acid accumulates at surfaces [209], thus more hygroscopic compounds are less exposed. In addition, the roughness of the surface is increased, which leads to a reduction of the potential contact area, reducing the adherence or adjacent particles (Figure 30 b). The utilization of leucine is an established means in order to increase dispersibility for spray dried powders [208-211]. Common solute concentrations for spray drying are 5 to 10-fold lower than the chosen concentrations for this template-assisted approach [210, 211]. Seville *et al.* used spray drying for the generation of a respirable powder, consisting of salbutamol, lactose and leucine with a total solute concentration of 2 % (m/V) in the spray drying solution. The mass fraction of leucine usually ranges between 0.05 and 0.2 of this solute content [208, 210, 211], representing a maximum content of leucine of 0.4 % (m/V) in the dispersion media, being spray dried. Various leucine concentrations, including a solution close to the solubility limit (24.3 mg/ml [192]) were tested with the template technique. For concentrations of more than 0.6 % (m/V) leucine changes of the morphology of the cylindrical particles have been observed, more truncated and deformed cylinders were found than for

preparations below a concentration of 0.6 % leucine (Figure 30). The surface exhibits a wrinkled and uneven structure, in contrast to cylinders not containing leucine (Figure 30 a). The increase of irregular cylindrical particles implies alterations of the solidification process, restricting the increase of concentration. Being surface active the leucine accumulates at the interface between the template and the gel. The surface to volume ratio for the spray dried microparticles and the cylindrical particles generated with the template technique is completely different. Consequently, the surface of particles for both approaches differs substantially. Supposing a volume of 250 µl for both techniques, the surface of the droplets formed from spray drying is 1.5×10^4 cm² for a diameter of 1 µm and 3.0×10^3 cm² for a diameter of 5 µm respectively. Whereas the interface of the gel with the template membrane is 40.0 cm² for the 1.0 µm membrane and 13.2 cm² for the 5.0 µm membrane respectively for the identical volume of 250 µl; the surface is calculate with the respective values for porosity (Table 1). The surface of the 250 µl drop is 1.9 cm², on the contrary. Even though the leucine concentration of 0.6 % corresponds to a mass fraction of only 3.3×10^{-2} in the formulation, because of the higher solute content of ~ 18 % (m/V)) in the alginate sol (4.2.2.1.2), the interface on which the leucine accumulates is much lower in the template approach. These conditions explain for the increase of deformed particles for concentrations higher than 0.6 % leucine; the excess solidifies on the interface, interfering with the other substances and decreasing the integrity of the cylinders.
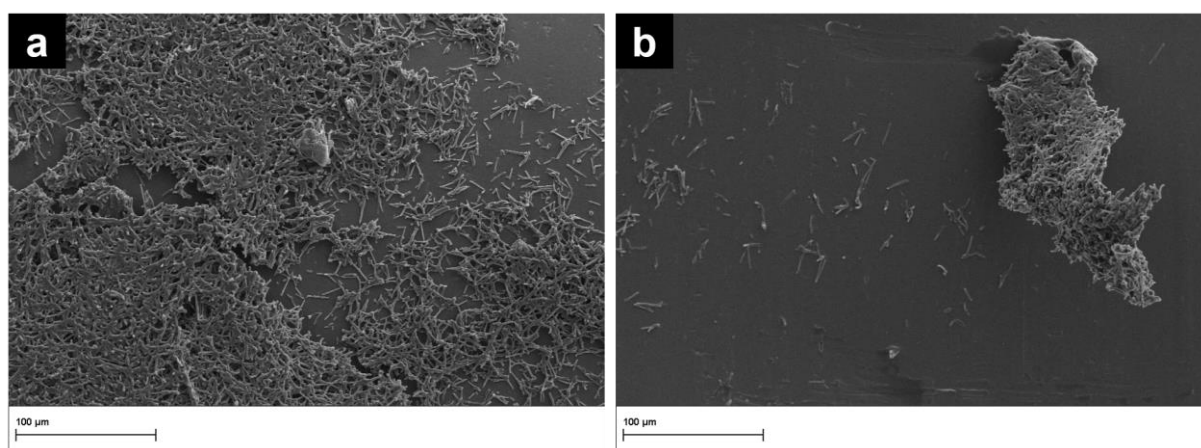
Figure 29 – SEM micrograph of alginate-lactose fibres, containing fluorescein-Na, after exposure to humidity.

The fibres have aggregated due to humidity. (a) Almost no separate fibre can be found, the majority is fused with adjacent particles. (b) The image shows a large aggregate consisting of thousands of filaments. Composition is according to chapter (4.2.2.1.2), 0.6 µm template, the scale bar corresponds to 10 µm
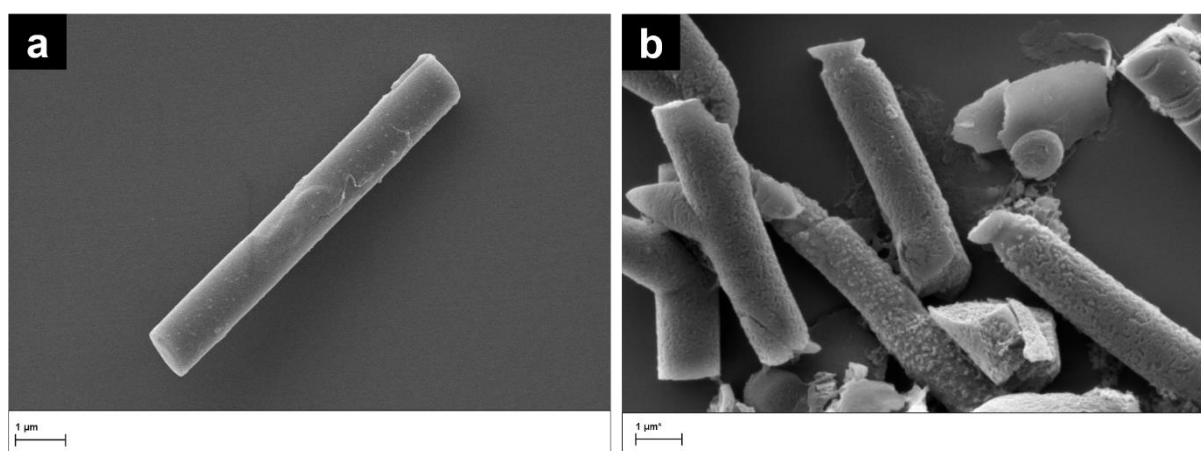
Figure 30 – SEM micrograph of alginate-lactose fibres with and without leucine.

(a) Cylindrical particle with smooth surface, no leucine was present. (b) The surface shows a wrinkled, uneven texture for particles, containing leucine with a mass fraction of 5.4×10^{-2}. This corresponds to a concentration of 1 % (m/V) in the dispersion used for the generation of the fibres. Fibres were formed with 1.0 µm templates, composition is according to chapter (4.2.2.1.2), with exception of the leucine concentration.

Before the collection of the particles in buffer for quantification, the deposition pattern of the deposition in the collection cups, which is caused through the holes of the respective stage, could be seen by naked eye (Figure 31 a). The morphology was verified with SEM. Silicon wafers were placed underneath the holes prior to the experiment and imaged immediately after aerosolisation (Figure 31). The micrographs show that a multitude of intact particles proceeded to the respective stages; aggregates could not be found. Yet, only 24.1 ± 10.9 % (n = 14) of the cylinders could be detected on the stages. Aggregation has a substantial influence on the aerodynamic properties of the cylindrical particles and thus quantification. Most aggregates do not align in the air steam and additionally deposit in earlier stages of the NGI than single fibres. Fluorometric quantification was used in order to detect the concentration in the compartments of the NGI (4.2.2.1.2.1). A single aggregate contains multiple times more label than a single cylindrical particle, shifting the outcome of the NGI experiment in comparison to a number weighted quantification completely (Figure 29 b).
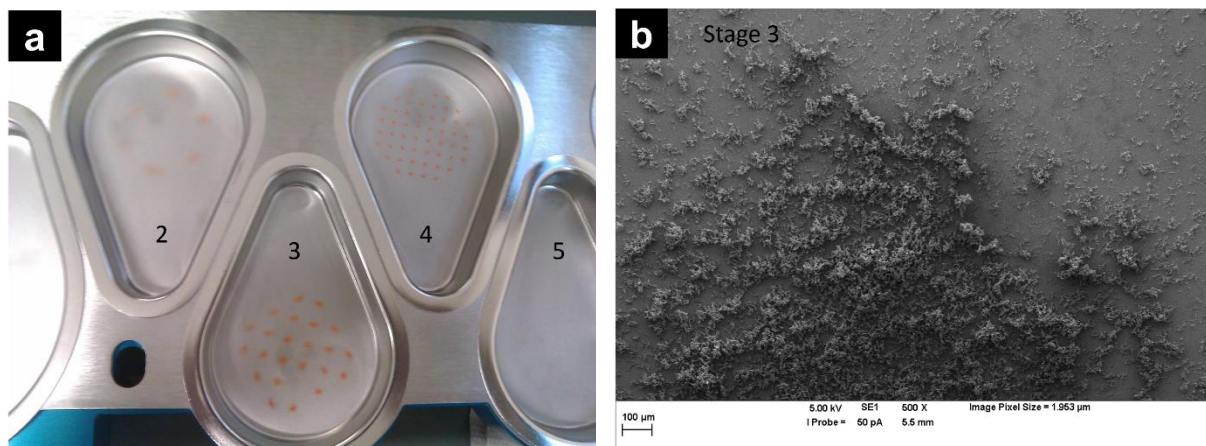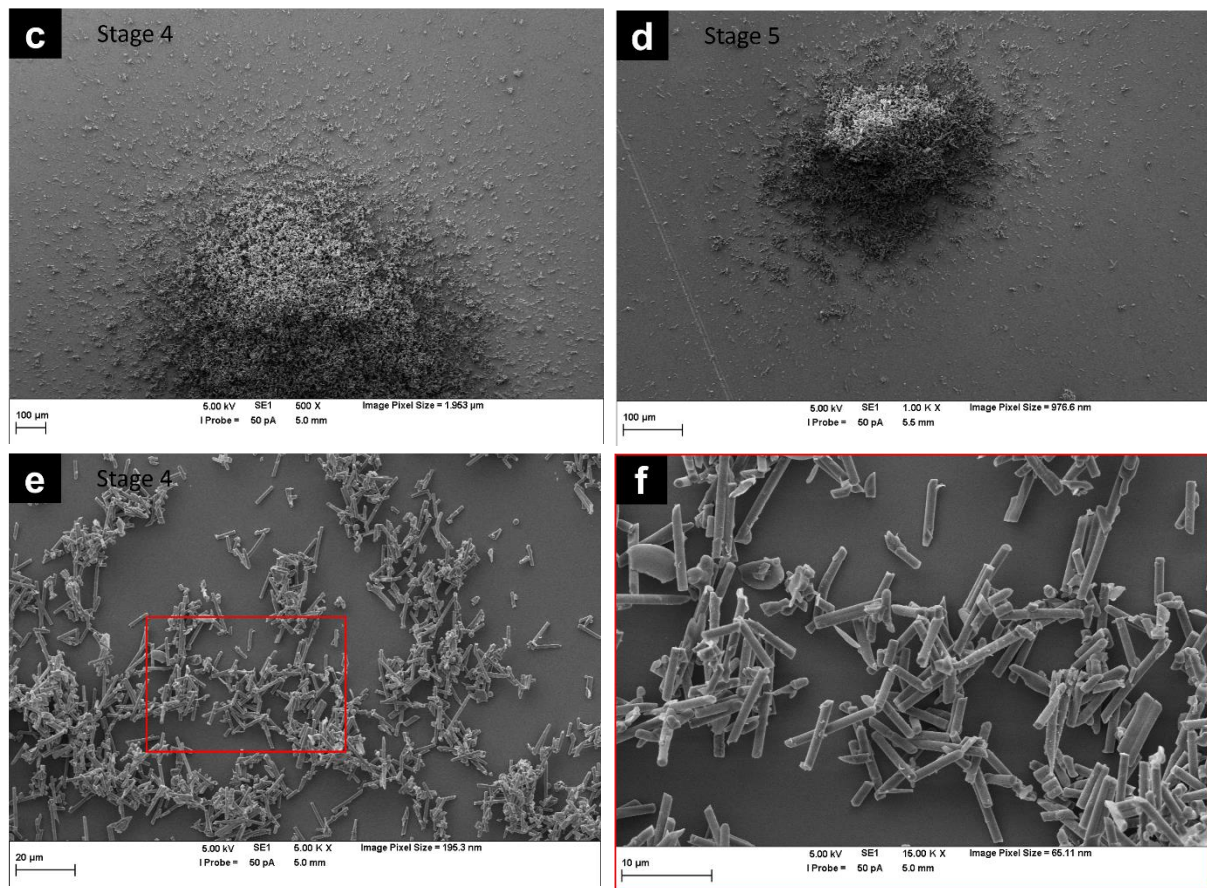
Figure 31 – Photograph and SEM micrographs of the deposition of alginate-lactose fibres after aerosolisation within the NGI.

(a) Photograph of the deposition pattern on the collection cups of the NGI. (b - f) SEM micrographs were captured of silicone waver pieces that had been placed in the NGI underneath the apertures prior to the aerosolisation experiment. (b) SEM image of stage 3; (c) stage 4; (d) stage 5; (e) SEM image of stage 4 with higher magnification; (f) zoom in on the marked frame in image (e). Template dimension was 1.0 µm, the composition is according to chapter (4.2.2.1.2).

Aggregation was reduced through different means. The preparation protocol was optimized in order to reduce the formation of the interlinking layer, bridging multiple single particles. Furthermore, sedimentation was used in order to separate the single particles from the substantially larger aggregates, including the interlinking layer (4.2.2.1.2). Leucine was utilized in order to reduce the hygroscopy of the fibres.

The blending of API particles, in particular for highly active compounds, with lactose particles serving as carrier is another common approach to improve pulmonary administration. α-lactose monohydrate with strict specifications regarding the particle size and distribution (< 100 μm: ≤ 10 %, < 250 μm: 40 - 70 %, < 400 μm: ≥ 90 % [212]) is mixed with the API. The blending is reported to decreases the fine particle fraction (FPF), because during the inhalation process not all particles desagglomerate from the excipient [213]. The excipient particles are pharmacologically inactive and improve the dispersibility and flow of the drug product. This is required in particular for drugs which tend to aggregate if they are micronized [214].

The blending with the cylindrical particles did not improve the deviations between the aerosolisation experiments. The aggregation is caused by the inherent hygroscopy of the hydrophilic compounds and not predominately caused by electrostatic or van-der-Waals forces. In general, hydrophilicity goes along with hygroscopy, which represents a general problem of the protocol for the formation of cylindrical particles from track-etched template membranes (4.2.2.1).

After optimization of the preparation conditions, still 75.9 ± 10.9 % (n = 14) of the aerosol did not reach the relevant stages. The powder either deposited in the induction port and the pre-separator, or was not released from the DPI, including the capsule, under the experimental conditions. The cylinders that reached the stages mainly deposited on the early stages. However, differences were found for particles with varying geometry.

Aerosols are separated in the NGI as a function of the aerodynamic properties; Figure 28 depicts the dominant deposition on the stages depending on the aerodynamic diameter. This dependency can be observed in the deposition pattern of the cylindrical particles after the aerosolisation experiment in Figure 32.

Deposition in NGI
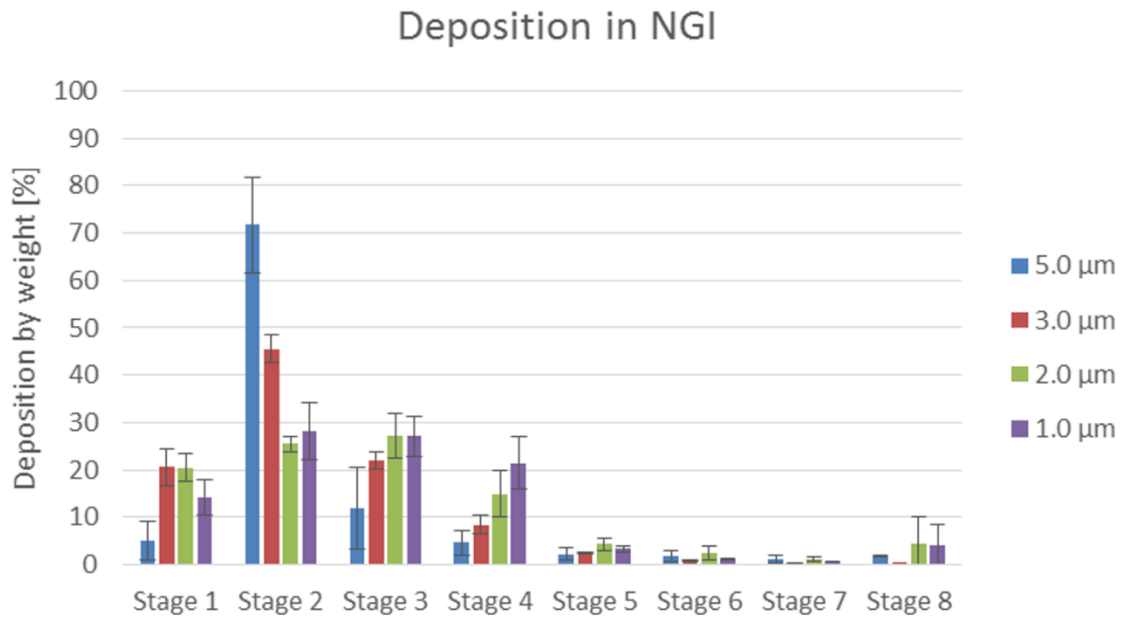
Figure 32 – Deposition of cylindrical alginate-lactose particles with variable diameters on stages of the NGI.

Cylindrical particles were formed with 5.0, 3.0, 2.0 and 1.0 µm template membranes, ventilation flow was 60 l/min. The fraction deposited in the other compartments are not displayed; values for the stages are normalized to 100 %; n ≥ 3; composition is according to chapter (4.2.2.1.2).

The cylinders with a diameter of 5 µm predominately (74.4 %) deposited on stage 2, almost no deposition was observed on stage 1. The cylinders are too small for deposition on this stage and proceed to the next stage, where they are collected to a high extend. The fibres with diameters 3, 2 and 1 µm are deposited to a higher extend on stage 1. This can be attributed to small aggregates that still are able to pass the pre-separator but do not reach the stages of deposition of the single fibres. The highest degree of deposition has also been detected on the second stage for fibres with a diameter of 3 µm. 2 and 1 µm have a similar degree of deposition on stage 3. These results show the expected diameter dependant transition of deposition towards later stages for particles with smaller diameters. On stage 3 predominately fibres with diameters of 2 and 1 µm are deposited. On stage 4, filaments with a diameter of

1 µm are the most abundant, whereas cylinders with diameters 2, 3 and 5 µm were detected with decreasing amount in this order. On stages 5 and later stages less than 5 % of the cylinders were collected per stage, no distinct size dependant pattern could be observed. The signal that was detected on these stages can be attributed to fragmented cylinders, exhibiting a low aerodynamic diameter, and experimental scattering. Fine fragments are responsible for the mildly higher signal that was detected for the last stage. The quantification is concentration based, which means that the correlation between the count of cylinders of the various diameters is not linear; the fluorescence signal given by a 5 µm cylinder is not 5-fold higher than for the cylinder with a diameter of 1 µm, the factor is 25.

Nonetheless, trends for the deposition pattern can be derived from the data. The deposition on stage 2 is dominated by the particles with larger diameters, on stage 3, the deposition is comparable for all observed dimensions (with exception of the largest 5 µm particles) and on stage 4 the cylinders with low diameter display high deposition. Deviations of these trends can be explained with experimental scattering. In fact, both the values of the 2 and 1 µm fibres for stage 2 and 3 lay within the standard deviation of the experiments.

Besides the aggregation through humidity, high porosity of the membrane is another reason for the formation of interlinked particles, exhibiting a larger d_{aer} and consequently a transition towards deposition on earlier stages in NGI experiments. The highest porosity of the 1.0 µm template among the used templates (Table 1) not only increases the yield per membrane, it also raises the likelihood of convergent pores. The interlinked filaments still can pass the pre-separator, but deposit on earlier stages than the single fibres. This is yet another reason for the mildly higher deposition of fibres with 1 µm diameter in comparison to fibres with 2 µm diameter on stage 2.

5.2.3 Cylindrical Particles Made of Agarose, Blended with Lactose

The protocol for the generation of cylindrical particles (4.2.2.1) can be adapted to form cylindrical particles, consisting of a matrix of agarose in concentrations of up to 2.5 % (m/V) and containing lactose in variable concentrations (4.2.2.1.3) (Figure 33 a). Particles could be formed from 5.0, 2.0, and 1.0 μm template membranes. After exposure to humidity the gel backbone is exposed due to diffusion of the small molecule lactose from the fibres (Figure 33 b).
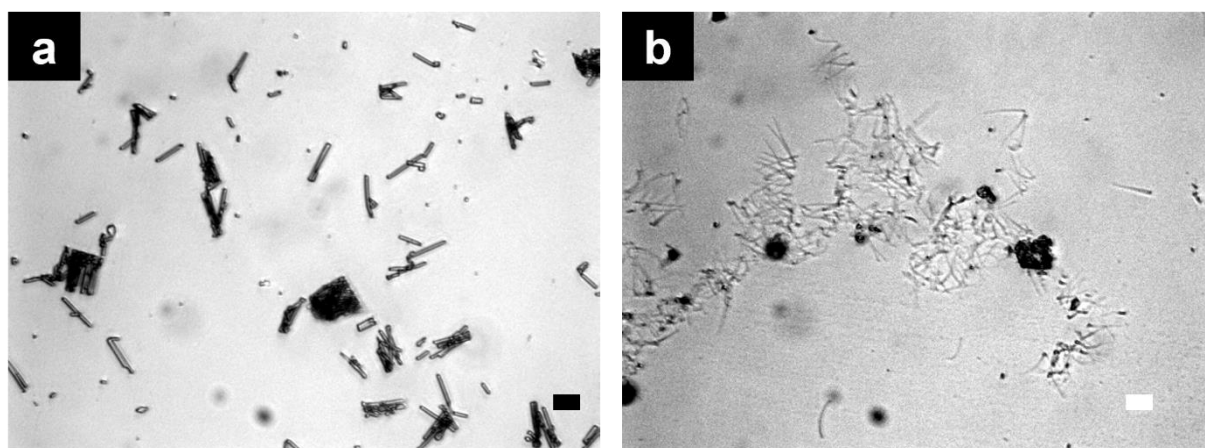
Figure 33 – Light microscopic images of cylindrical particles, composed of agarose and lactose. (a) Fibres after evaporation of the organic dispersion media. (b) Remainder of the agarose-lactose fibres after exposure to humidity. The agarose gel backbone is exposed after removal of the water through drying, the lactose has diffused out of the filaments. Fibre diameter is 1 μm; composition is according to chapter (4.2.2.1.3), the agarose mass faction is 6.3×10^{-2} and 0.94 for lactose, corresponding a concentration of 1 % (m/V) for agarose and 15 % (m/V) for lactose in the dispersion used for the generation of the fibres. Scale bar corresponds to 10 μm.

Pure agarose hydrogel filaments with a concentration of 5 % (m/V) at maximum could also be formed from membranes with a minimum pore diameter of 0.1 μm (Figure 34 and Figure 35). Less fractured cylinders were found, in contrast to cylinders containing high concentrations of

lactose (15 % (m/V)) in the fluid precursor for the preparation protocol "Cylindrical Particles Made of Pure Agarose and Blends with Lactose", (4.2.2.1.3)), because of the flexibility in dry, as well as in wet state. The agarose filaments are stable in aqueous dispersion (Figure 34 a) and were labelled with fluorescein-Na. The small molecule fluorescein was retained by the gel; sufficient concentrations could still be found 6 h after preparation in aqueous dispersion with agarose concentration of 1.5 % (m/V) (Figure 34 a). The pore size of the agarose gel depends on the concentration, which is of particular importance for the separation of fragments of nucleic acids during gel electrophoresis [147]. Filaments from 0.1 µm templates could still be sufficiently visualized (Figure 34 b). Due to the high vacuum of electron microscopes the hydrogel filaments have shrunk (Figure 35); this shrinkage is more pronounced the lower the concentration of the agarose is chosen.
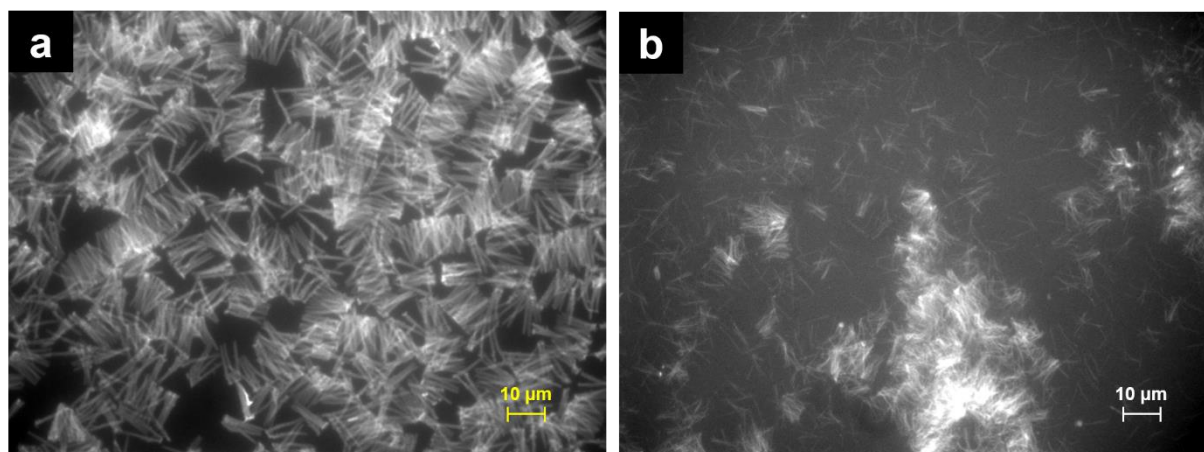
Figure 34 – Fluorescence light microscopic images of agarose filaments containing the marker substance fluorescein-Na.

(a) Agarose filaments formed from 1.0 µm template membrane in aqueous dispersion (6 h), agarose concentration 1.5 % (m/V). (b) Agarose fibres formed with 0.1 µm template, agarose concentration 2.5 % (m/V); the template membrane containing the fibres was dissolved with a few droplets of CH_2Cl_2 prior to imaging. The concentration of fluorescein-Na was approximately 0.01 % (m/V).
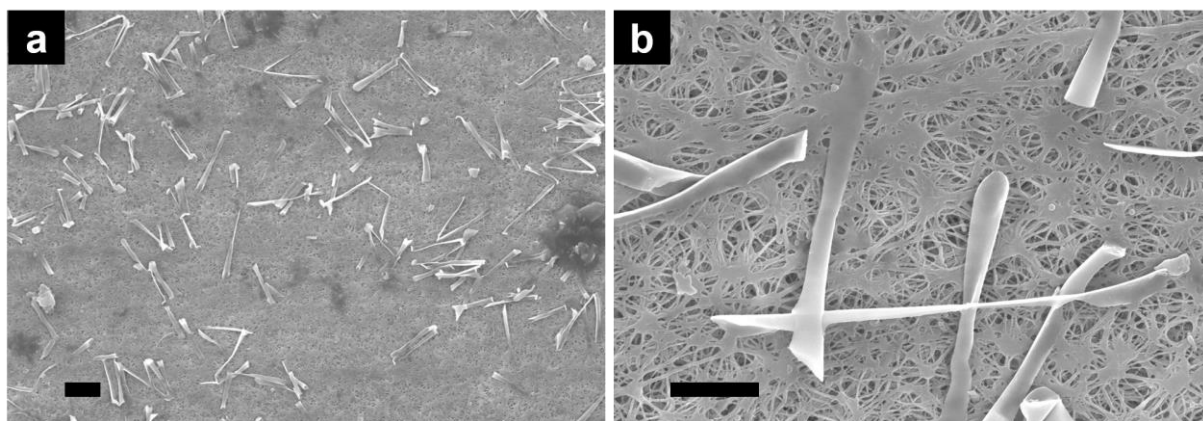
Figure 35 – SEM micrograph of agarose filaments collected on the surface of a Teflon (PTFE) filter at different magnifications.

Agarose concentration 2.5 % (m/V), 2.0 µm template membrane. The higher magnification (b) allows for the visualization of the spider web like structure of the polytetrafluoroethylene (PTFE) filter, which was used for the collection of the agarose fibres. Scale bar corresponds to 10 µm (a) and 5 µm (b).

5.2.4   Cylindrical Particles Made of Gelatin

Filamentous particles made from gelatin in a broad concentration range (1 – 10 %, (m/V)) could be formed with template membranes with 5.0, 2.0 and 1.0 µm pore diameter (Figure 36) according to the protocol described in chapter "Cylindrical Particles Made of Gelatin", (4.2.2.1.4). Because of the elastic nature of the hydrogel, no truncated particles were found, representing the pore geometry of the template membranes in high fidelity. The gelatin particles were crosslinked with GTA, impeding dissolution in aqueous media [215]. Likewise, the crosslinking extend is expected to alter the stability of the filaments. The fibres with the chosen crosslinking method were stable in aqueous media for minimum one day, no structural differences could be detected with the light microscope. The filaments can be labelled in a straightforward fashion. The label is added to the aqueous solution of gelatin before infiltration into the template, the distribution of the labels within the cylinders is homogenous.

After one day of exposure to aqueous media, fluorescence could still be detected, meaning that sufficient dye has been retained and did not diffuse from the filaments.
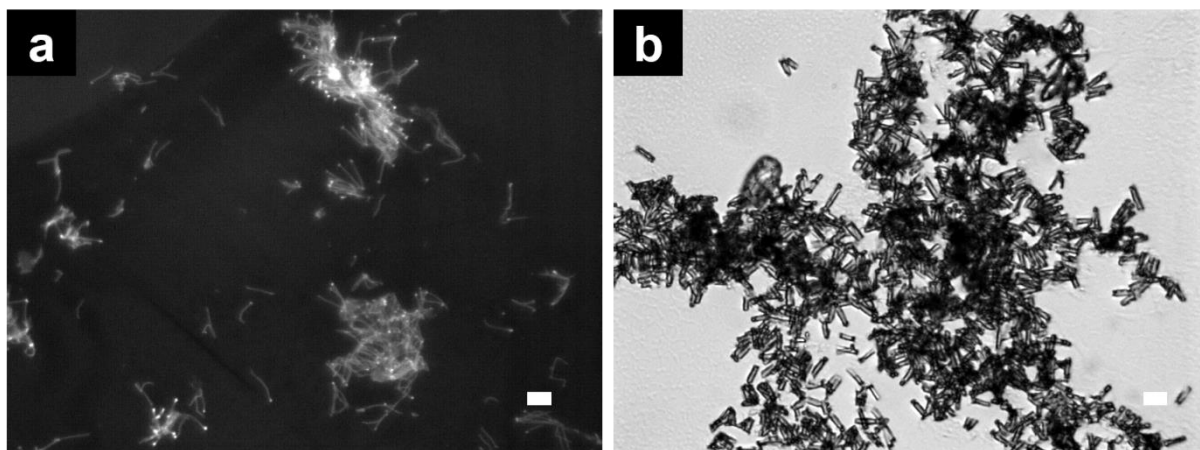
Figure 36 – Fluorescence and light microscopy images of gelatin filaments.

(a) Fluorescence image of gelatin fibres formed with 1.0 µm template membrane, the concentration was 1 % (m/V) gelatin, the fluorescein-Na concentration was approximately 0.01 % (m/V). (b) Light microscopic image of gelatin filaments formed from a 2.0 µm template, the concentration was 10 % (m/V) gelatin. Images were captured after purification from PC. The scale bar corresponds to 10 µm.

Results and Discussion

5.3 Microcylinders Composed of Nanoparticles

5.3.1 Microcylinders Composed of Nanoparticles, Interconnected with Hydrogels

Preparations of particles using membranes with different pore sizes showed the following tendencies regarding relevant criteria. These values can be explained with basic properties of the template membrane (Table 1).

The yield (count of particles) rises with smaller pore diameter.

The tendency to form aggregates rises with smaller pore diameter.

The homogeneity decreases with smaller pore diameter.

As a consequence of these tendencies cylinders formed within template membranes with 2.0 µm pore diameter were used for most experiments and characterized in detail, representing the best compromise of all properties.

5.3.1.1 Microcylinders Composed of NPs, Interconnected with Agarose

The protocol for the formation of cylindrical microparticles composed of NPs, interconnected with agarose (4.2.2.2.1) was successfully used with silica beads having diameters of 841, 500 and 200 nm according to manufacturer specifications (Figure 37) for template membranes with 5.0, 2.0 and 1.0 µm pore diameter.
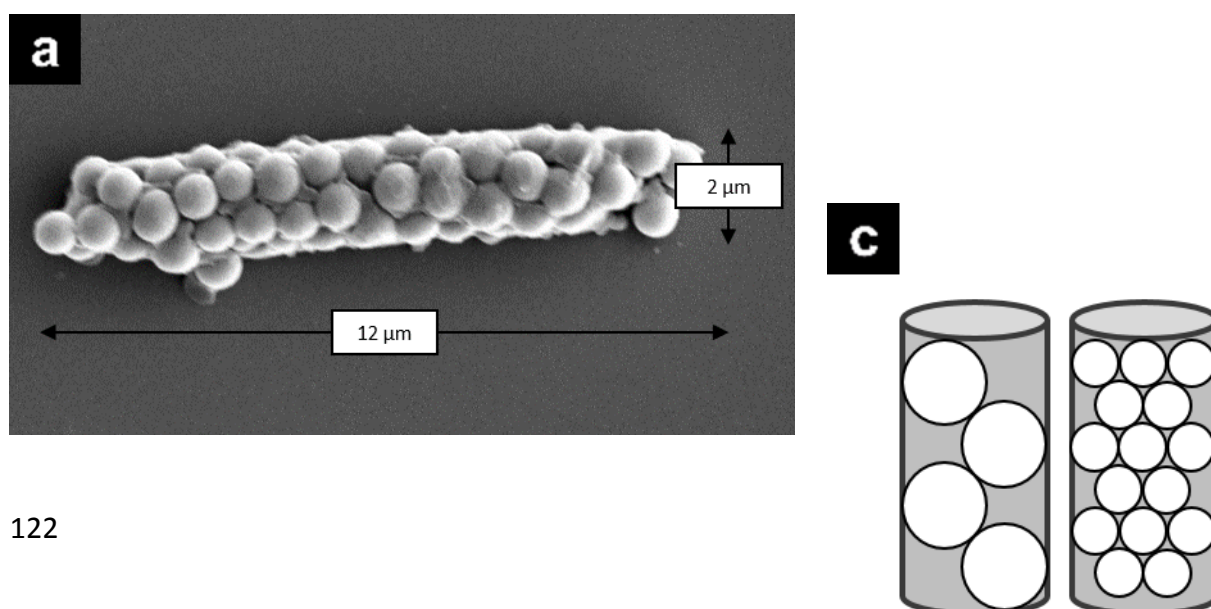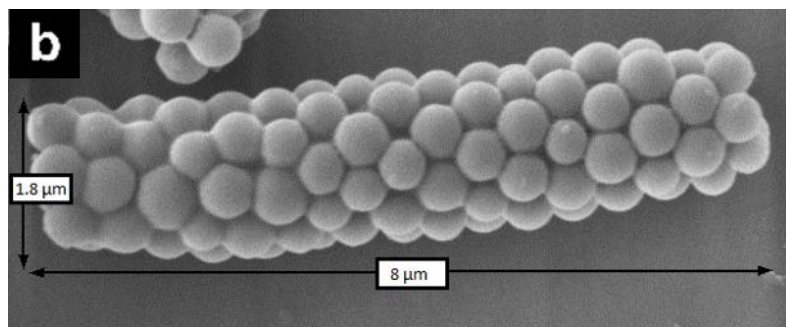
Figure 37 – SEM images of cylindrical particles formed from NPs, interconnected with agarose. The substructured cylindrical particle is composed of either 841 nm (a), or 500 nm (b) silica beads. (c) Schematic depicting the arrangement of the beads in identical pores as a function of the particles size. The arrangement of the silica particles is according to the close-packing of equal spheres. The beads were interconnected with agarose (1.5 % (m/V)) within the pores of a template membrane with 2.0 μm diameter.
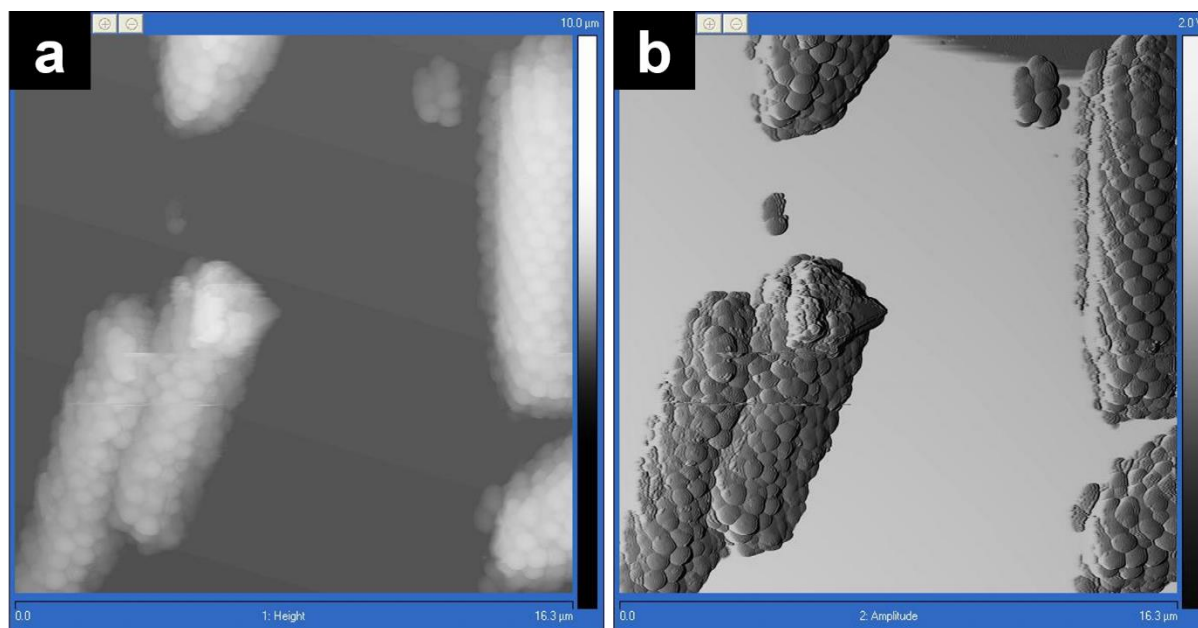
Figure 38 – AFM images of cylindrical particles formed from NPs, interconnected with agarose. The cylindrical particles are composed of 500 nm silica particles, the agarose concentration was 1.5 % (m/V), a template membrane with 2.0 μm pore diameter was used. Image (a) shows the height, (b) shows the amplitude visualized with AFM.
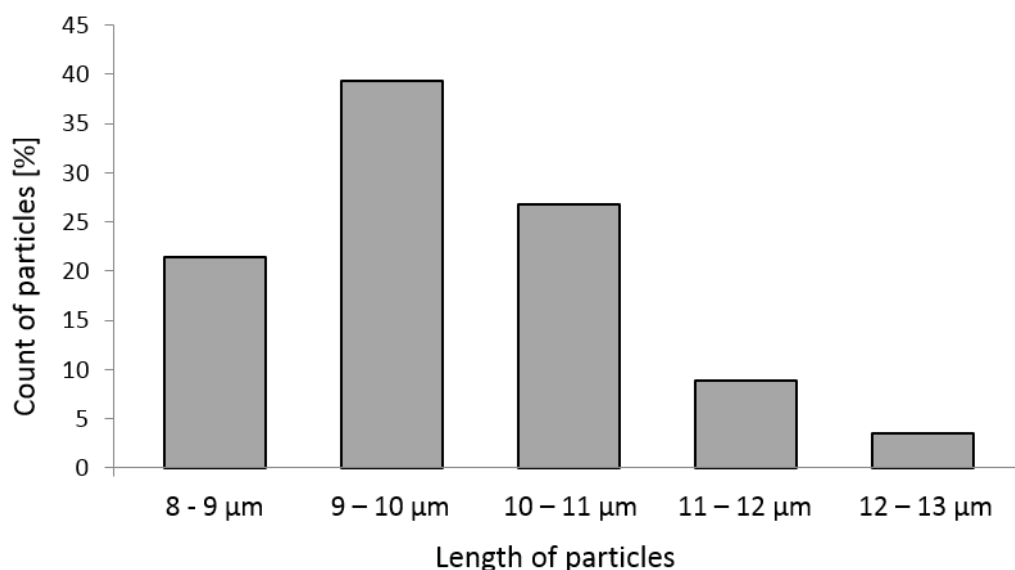
Figure 39 – Length distribution of microcylinders formed from NPs, interconnected with agarose.

The cylinders were composed of 500 nm silica beads, the template dimension was 2.0 µm and the agarose concentration was 1.5 % (m/V) (n = 56).

The cylindrical particles were well-dispersed (Figure 41 a and b), both in THF and in buffer and did not agglomerate, or change in other relevant respects. This could be seen during counting in the Neubauer chamber and the SEM analysis, respectively. Because of the non-spherical nature, the aggregation cannot be assessed with laser diffraction or dynamic light scattering (DLS)/photon correlation spectroscopy (PCS) in a straightforward fashion. The cylinders, composed of 500 nm silica beads, were highly uniform, resembling the inverse features of the template (2.0 × 10 ± 1 µm) in high fidelity, with a length of 10.24 ± 1.47 µm (RSD 14.4 %) (n = 56) (Figure 39) and a width of 1.99 ± 0.08 µm (RSD 3.91 %) (n = 27). The length distribution of the cylinders (Figure 39) shows that some pores are tilted and are therefore longer. Since the template geometry governs the dimension of the cylinders and the thickness can be regarded constant over the entire template (10 ± 1 µm, Figure 23 c), the particles formed within tilted pores become longer (11 - 12 and 12 - 13 µm). Most cylinders have a length between 9 - 10 µm. Ruptured or deformed particles were rare. Deformed cylinders can be

explained with incomplete filling of the template pores. The construction of the filter holder causes the beads to distribute over the entire surface but a complete homogenous distribution is not reached. It was worked with an excess of particles in order to compensate for this effect (4.2.2.2). SEM analysis also reveals the highly ordered arrangement of the silica nanoparticles in a close-packing of spheres fashion that has been preserved by the interconnecting agent agarose (Figure 37 and Figure 38). The hydrogel agarose with its plentiful hydroxyl moieties and the hydrophilic silica beads render the surface of the cylinders hydrophilic, contributing for the stable suspension observed. The preparation strategy is derived from the template-assisted interconnection with polyelectrolytes [66] in which the core particles are completely covered. This suggests that the agarose fully envelops the beads. The preparation allows for a blending of the particles (Figure 40). This was assessed with silica particles having a diameter of 841 and 500 nm. Only the 500 nm beads were fluorescently labelled. The blending of particles did not change the ordered arrangement of the beads with its structure of close-packing of equal spheres. The distribution of the two species of beads within this arrangement was erratic, no demixing or segregation according to size could be observed. In addition, the hydrogel used for the interconnection (in this case agarose) can be loaded with active agents, such as the model compound fluorescein-Na, which can be seen by the fluorescence signal (green) at one end of the particle (Figure 40 b). The signal is more pronounced at one end of the rod. This can be attributed either to the filling procedure, because the template containing the beads is infiltrated from one side of the membrane in order to prevent the formation of bridges (interlinking layer) between the cylinders on both sides (4.2.2.2). Or the rupture of the filaments close to the basis during the cleavage from the base layer during the production protocol (4.2.2.2).

Results and Discussion

The blending of nanoparticles with various properties may allow for a tailoring of the delivery system for the intended use. It is conceivable that the release can be customized, combing fast and slow releasing beads, or the combination of particles loaded with different APIs. In addition, the matrix may also serve as a reservoir for active agents. In these first experiments, the model substance Fluorescein-Na was loaded (green signal Figure 40).
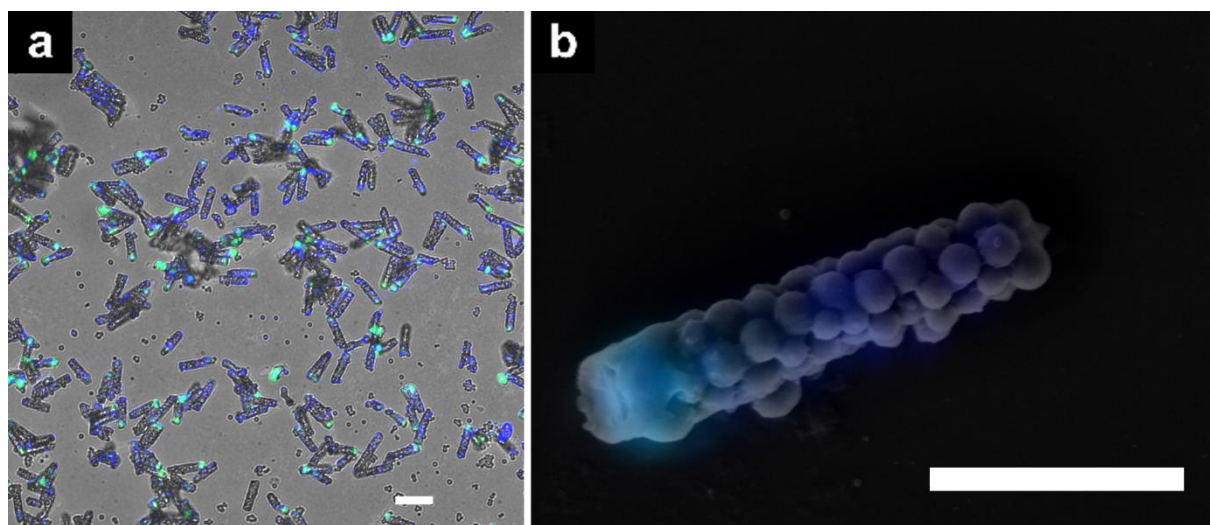
Figure 40 – Light microscopy image and SEM micrograph of microcylinders, composed of two species of beads.

(a) CLSM image and (b) SEM micrograph. 841 and 500 nm silica particles were connected within a template with a pore diameter of 2.0 µm. The 500 nm silica particles were labelled, showing fluorescence in the blue spectrum (blue signal), the agarose gel (1.5 % (m/V)) used for the interconnection of the beads was labelled with fluorescein-Na (green signal, concentration approximately 0.01 % (m/V)).

The long-term stability of the rods in aqueous dispersion is high. No alteration or disintegration of the cylinders could be observed for the dispersion in PBS after storage at 6°C under exclusion of light for 6 months (Figure 41 (c) and (d)). The redispersibility was not altered through the storage, particles could easily be redispersed.

The nature of the used particles dictates the conditions of release, either within the phagocyte or before internalization.
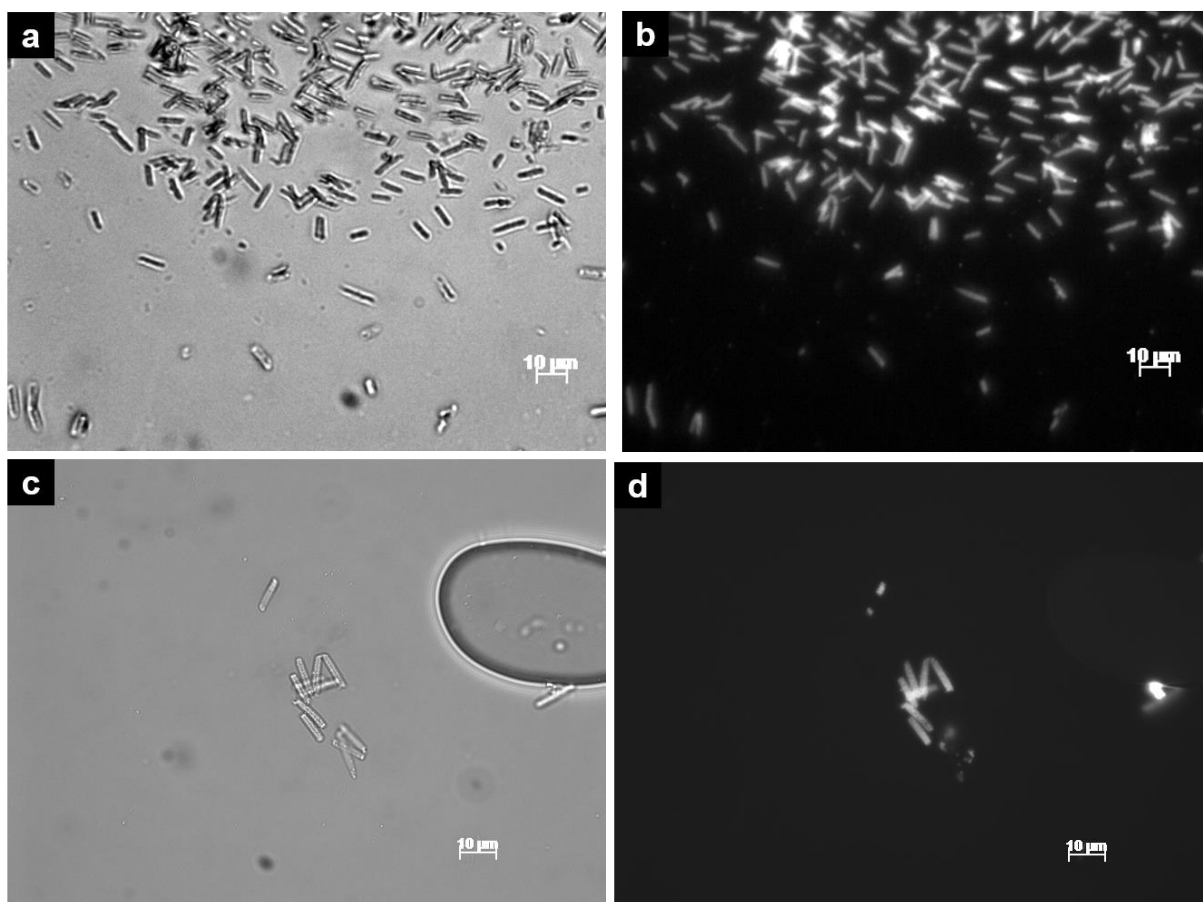
Figure 41 – Light microscopy and fluorescence images of microcylinders formed with NPs.

(a) The image shows the cylinders right after the release from the template. (b) Fluorescence image of the particles after release from the template. (c) Light microscopic image of the particles after storage in aqueous dispersion for 6 months. (d) Fluorescence image of the particles after storage in aqueous dispersion for 6 months. The cylindrical particles were composed of 500 nm silica beads (fluorescence labelled) and were formed within a template with a pore diameter of 2.0 µm. The cylinders were interconnected with agarose (1.5 % (m/V)) according to the protocol (4.2.2.2.1.1).

5.3.1.2 Microcylinders Composed of NPs, Interconnected with Alginate

The protocol is derived from the method for the generation of microcylinders interconnected with the hydrogel agarose (4.2.2.2.1), which was replace by alginate (4.2.2.2.2). Cylinders with a diameter of 5 and 2 μm could be formed with beads having a diameter of 500 nm. The cylinders have a strong tendency to form aggregates over the course of the purification process and over time, in contrast to the microcylinders interconnected with agarose, not showing any agglomeration. Vortexing and sonication helped to reduce the big agglomerates of the cylinders interconnected with alginate, but did not allow for a complete redispersion of single fibres; the integrity of filaments is not affected by the sonication. In order to reduce the tendency build up the aggregates, the purification method was adapted. After purification with THF, the cylinders were no longer directly transferred to the aqueous media, representing a big transition in the polarity, which was observed to cause severe aggregation. After the refinement of the protocol, the purification was performed with solvents with increasing polarity in the order CH_2Cl_2, THF, ethanol, aqueous media. This measure helped to reduce the formation of large aggregates. Nevertheless, smaller aggregates could not be avoided (Figure 42). During storage of the cylinders without agitation, bigger aggregates were formed within hours. The pronounced tendency of the cylinders, interconnected with alginate, to form aggregates can be explained with the gelation mechanism and the presence of excess Ca^{2+} in the gel. The alginate gel, covering the filaments, forms bridges between adjacent cylinders, being in contact with each other. This can be attributed to the same electrostatic forces, responsible for the formation of the gel (4.1.5), in this context causing aggregation.
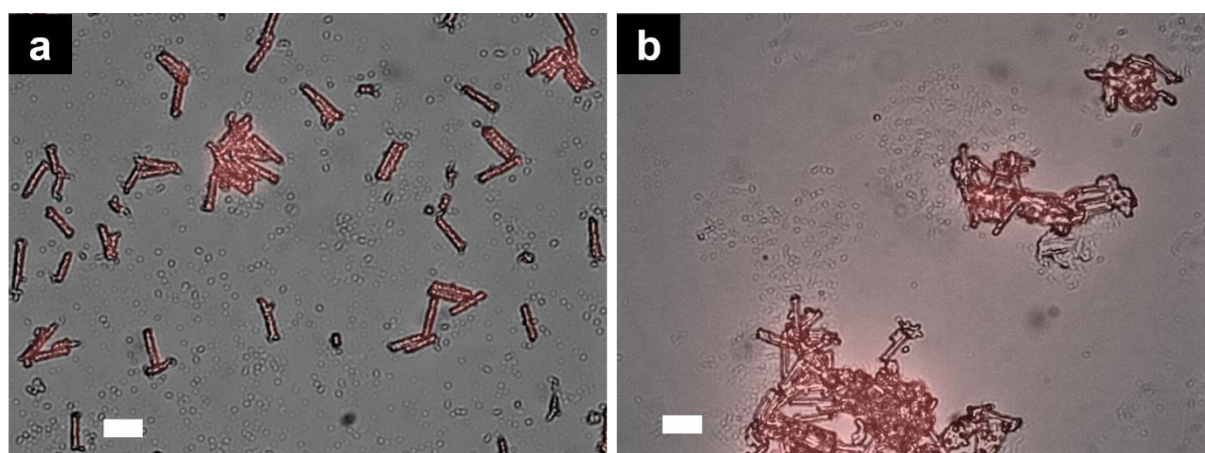
Figure 42 – Light microscopic image with overlaid fluorescence signal of microcylinders formed from silica NPs, interconnected with alginate.

(a) Image taken after the second cycle of centrifugation of the cylinders. Aggregation was limited; most single cylinders adhered to adjacent cylinders, but did not form bigger aggregates. (b) The image shows more severe aggregation of the cylinders after three centrifugation cycles. Cylinders were composed of 500 nm silica beads (fluorescence labelled) and were formed within a template with a pore diameter of 2.0 µm. The alginate concentration was 0.7 % (m/V). Scale bar corresponds to 10 µm.

5.3.2   Phagocytosis of Microcylinders Composed of Nanoparticles

5.3.2.1   Macrophage Uptake of Microcylinders Composed of Silica NPs

Foreign particulate materials, as well as drug carriers, might reach the deep lung by inhalation intentionally, or accidentally. All these particulate objects will presumably be cleared by macrophages, which is the most important clearance mechanism in the deep lung [22]. Shape, orientation of particles and chemical surface composition influence the mechanism of uptake itself and the uptake-kinetics [1, 15]. Phagocytosis has been discovered to be highly shape- and orientation-dependent [15, 22, 23, 216, 217]. In their seminal publication, Mitragotri and co-workers found that the geometry at the point of first contact between the phagocyte and the particle governs the initiation of phagocytosis [22]. After initiation of internalization, the completion of uptake is dictated by the size of the particle. The limit for internalization is given by the volume of the phagocyte [22]. A macrophage uptake experiment with substructured microcylinders was chosen for the verification of the uptake behaviour of cylindrical microparticles prepared with the template technique. The template membrane with a pore diameter of 2.0 µm was chosen, because this template represents the best balance between low tendency for aggregation, good yield and high homogeneity of particles (5.3). As interconnecting agent the biocompatible hydrogel agarose was selected. Fibres, being generated with this template (2.0 × 10 ± 1 µm), exhibit a dimension that can be internalized by macrophages [22, 140, 218]. The cylindrical particles were prepared following the protocol for the formation of microcylinders composed of nanoparticles (4.2.2.2).
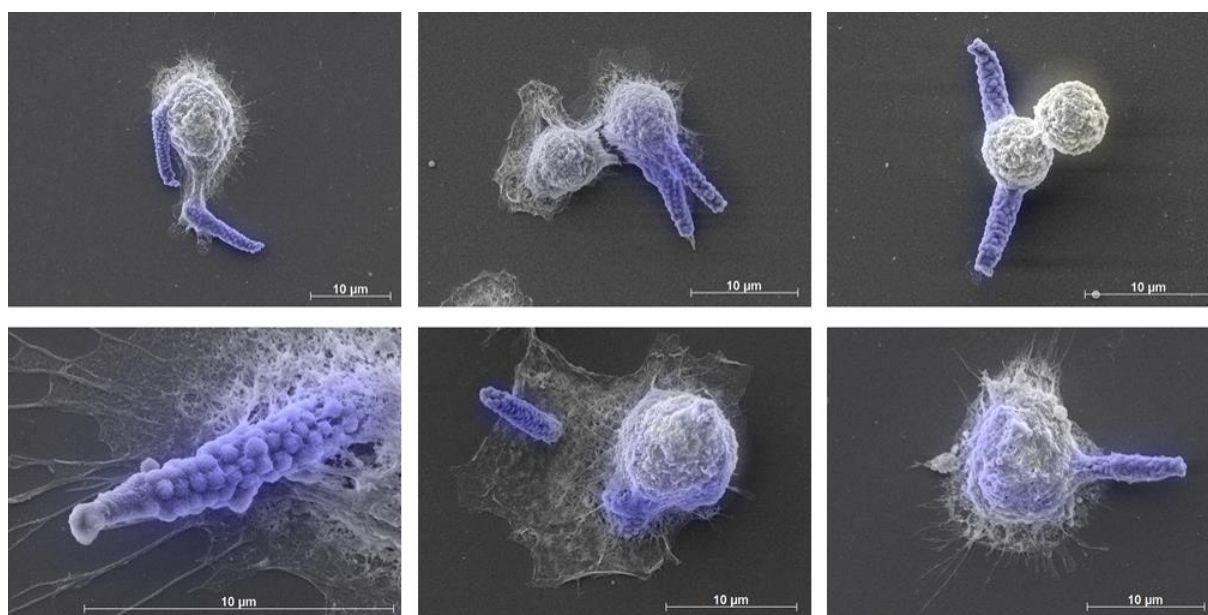
Figure 43 – Shape and orientation dependency of phagocytosis.

Correlated FLM and SEM images (CLEM) displaying the selective invagination of cylindrical microparticles composed of NPs (blue), exclusively from the ends by murine alveolar macrophages. The CLEM images consist of the SEM micrograph on which the fluorescence signal of the FLM image is superimposed. The auto fluorescence of the macrophages is displayed in bright yellow, the fluorescence signal of the cylindrical particles given by the labelled silica beads is shown in blue.

A concise analysis of the uptake behaviour could be undertaken based on SEM. The engulfment of cylindrical particles was observed to take place from the pointy side of the particle without exception (Figure 43). Considering the texturing of the cylindrical particles, composed of spherical submicron particles (500 nm), the observed behaviour is surprising at first glance. The local shape the macrophage encounters is the morphology of spheres embedded into the matrix in a close-packed fashion. Nonetheless, no engulfment could be observed from the flat side, most likely due to the fact that the substructure is too little. Furthermore, the swelling of the agarose gel in aqueous media, which is responsible for the interconnection of the spheres, can mask the underlying structure of the sphere, rendering it too minute to still be sensed by the macrophages.

The paradigm of shape- and orientation-dependent uptake [22] could be confirmed for cylindrical particles formed with the template technique. Therefore, geometry represents a new design parameter for novel sustained release systems.

5.3.2.2 The Advantage of Correlative Light and Electron Microscopy for Uptake Experiments

Correlative microscopy is the synergistic utilization of different microscopic techniques on the very same position and sample (4.2.1.2.3) [176, 177]. For the analysis of uptake experiments with macrophages, fluorescence light microscopy (FLM) and scanning electron microscopy (SEM) were combined (4.2.1.2.3.1).

Fluorescence was used in order to quickly identify regions of interests, harnessing the high biochemical specificity. The labelled cylindrical particles were detected through blue fluorescence, whereas the cells were detected using their auto fluorescence. Bleaching is a common problem of fluorescence dyes and can be drastically reduced through the fast relocation of any ROI. Subsequently, the ROIs were usually scrutinized with SEM. The order of experiments, at least for correlation of FLM with SEM analysis, is not necessarily required to be FLM analysis prior to SEM analysis. However, it is known that the electron beam can corrupt the fluorophores [188], but this effect could not be observed during the experiments. SEM visualizes the surface structure and electrons do not penetrate the entire sample under the chosen measuring conditions. Sputtering prevents accumulation of electrons and helps to dissipate excess electrons, preventing degradation of the fluorophores. This coating with a thickness of approximately 15 nm did not substantially reduce the translucence of the specimen (Figure 44 a). For more sophisticated experiments, that require the detection of faint signals, this order is not appropriate; sputtering can also be performed after the light microscopic observation [187].

In a second step, possible uptake events were identified and verified with the complementary method (SEM). The expansion and position of the cell membrane can be assessed (Figure 45 b, c and d), rendering it possible to judge the state of the uptake process in detail. Two scenarios of misleading quantification based on FLM were observed. Either particles were found that did not seem to have contact with the cell (Figure 45 a), or fluorescing particles were found that seemed to have been internalized (Figure 44 a). Verification with SEM solves this ambiguity. Choosing exemplary images, in the first case SEM analysis revealed that the cell membrane of the macrophage progressed over most of the respective particle, in contrast the impression gained by FLM. In the second case, it became evident that the particle was adhering to the macrophage, rather than having been internalized (Figure 44). Consequently, it could be securely discriminated between contact of particles with cells with no invagination by the cell membrane (Figure 44 b and c, cylinder adhering to the right side of one of the macrophages) and successful engulfment (Figure 44 b and c, left macrophage). SEM analysis alone is not sufficient either. Completely invaginated rods can be fully covered and thereby camouflaged for the recognition with the electron microscope (Figure 44 b, left macrophage) which is yet another reason for wrong quantification.
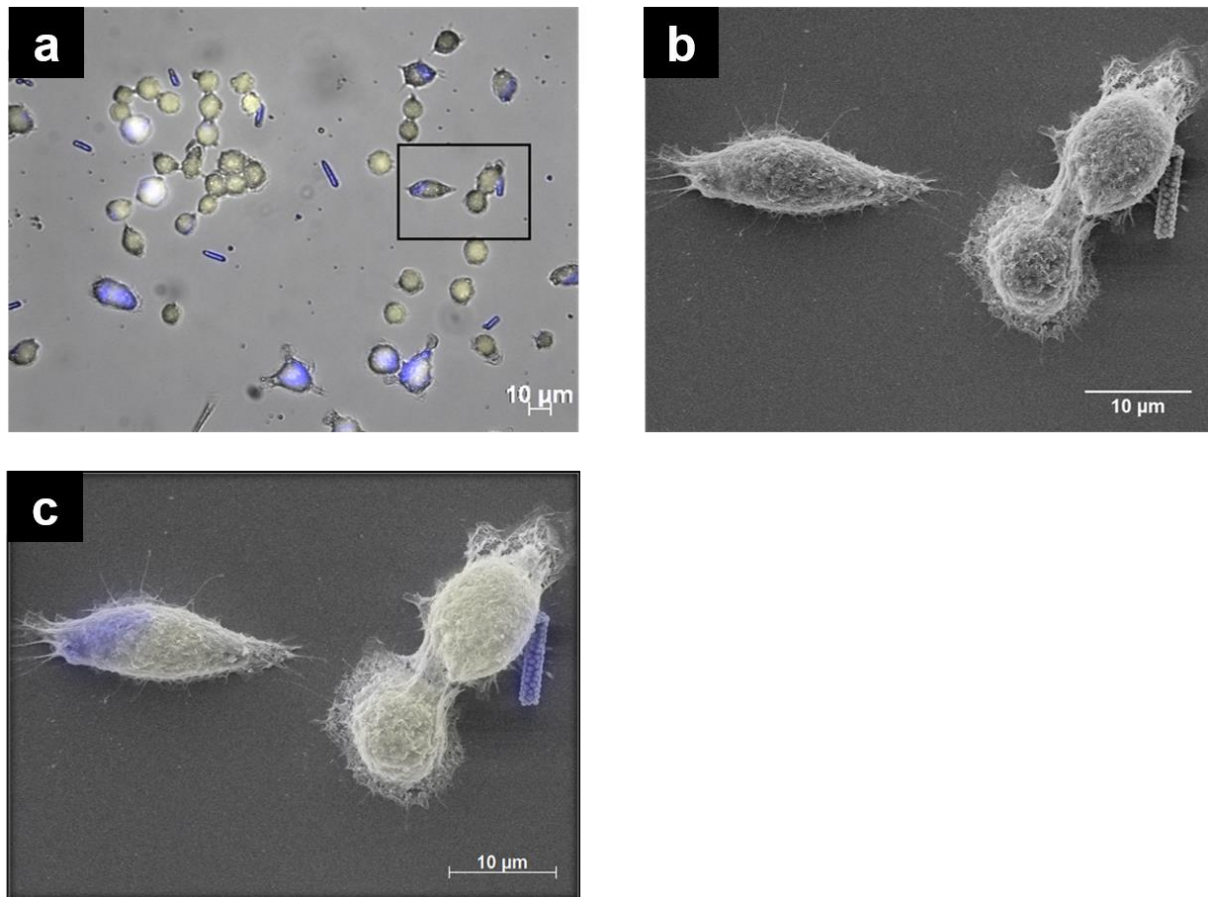
Figure 44 – Steps to identify particle uptake with CLEM.

The routine starts with a typical FLM image (400 × magnification) on which the quantification of uptake events is based and regions of interests can be identified (a). Macrophages are shown by auto fluorescence (bright yellow) and particles were fluorescently labelled (blue). The FLM image indicates two uptakes in the selected region. This position was relocated in the SEM in order to capture the image with the complementary technique. Solely judging from the electron microscopic image, no particle uptake could be observed (b). Only the correlated image (c) allows to distinguish between engulfed particles (macrophage seen on the left) and those which are only in contact with cells (particle on the right).
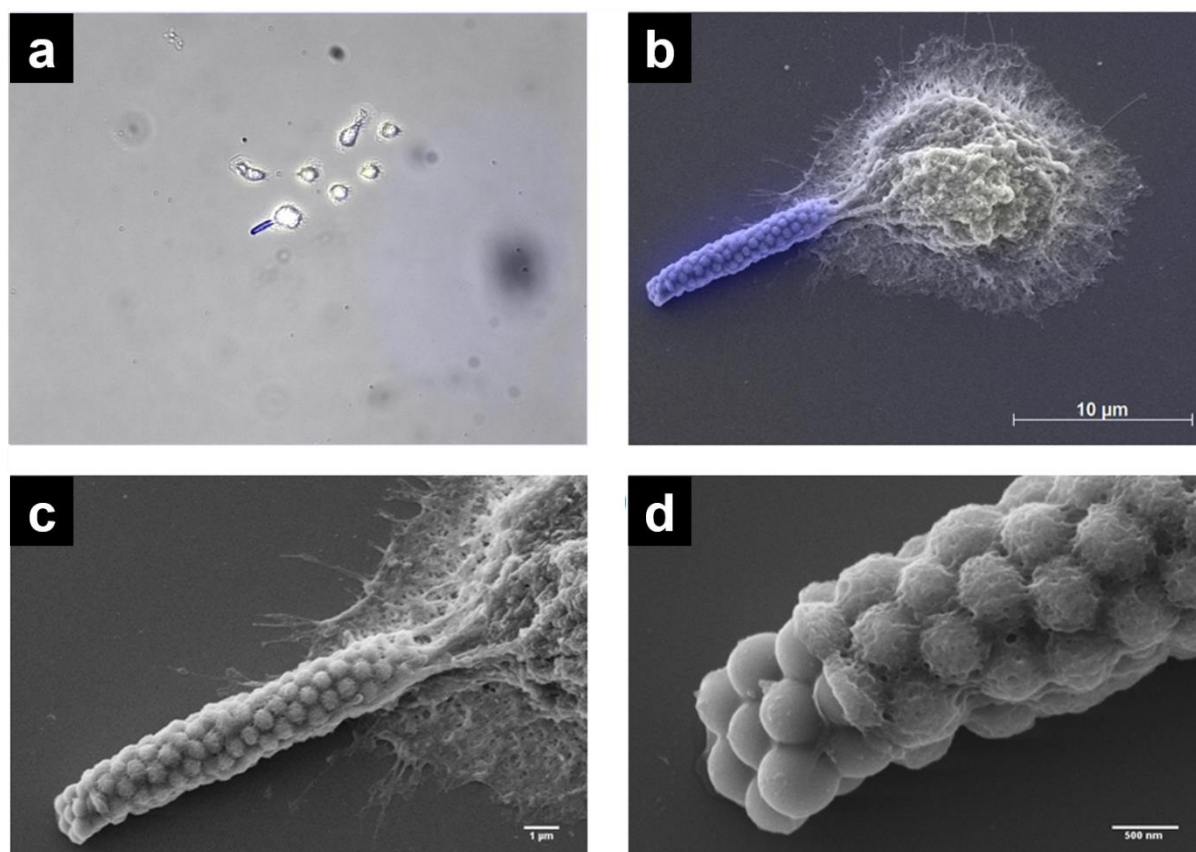
Figure 45 – Uptake process of a cylindrical particle in detail.

(a) In the FLM image (400 × magnification) possible interactions between particle (blue) and macrophage can be identified. (b) The overlay of SEM and FLM images shows an ongoing uptake process. (c, d) Further SEM images allow for a clear examination of the process of internalization of particles, revealing that the particle was nearly completely engulfed here. The plasmalemma has progressed over most of the particle, only approximately 1 µm of the cylinder in length is not yet invaginated.

5.3.2.3 Macrophage Uptake Kinetics of Microcylinders Composed of NPs, Assessed with CLEM

It could be demonstrated that correlative microscopy allows for a clear and secure assessment of uptake events, in contrast to sole quantification with FLM or SEM. Figure 46 illustrates that the uptake kinetics considerably differ between the techniques. The correlative approach shows a steady and gradual increase of the uptake of the particles, cumulating in approximately 19 % of cells having invaginated at least one particle. The quantification with

135

Results and Discussion

FLM exhibits an entirely different trend. Sole analysis with FLM results in a higher uptake count than correlative quantification for the entire incubation time (Figure 46). The FLM graph describes all particles in contact, or close vicinity with the macrophages, including both true and misinterpreted events. This uncertainty for uptake experiments is a known pitfall of light microscopic techniques [23]. The highest discrepancies can be observed for the first time points and only minimal differences at the last time point (Figure 47). This is also displayed by the convergence of the two graphs (Figure 46) with a relative discrepancy of only 7 % after 24 hours, in comparison to the difference of more than 3-fold after 1.5 hours (Figure 47). Considering the shape dependency of the invagination this observation can be explained. Macrophages require several hours in order to reach the adequate orientation (engulfment solely from the tips, not for tangential contact - Figure 43). Over the course of the incubation more and more macrophages align appropriately, displayed by a gradual increase of the overall uptake. After 24 hours of incubation, approximately 94 % of the particles being in contact with the cells (FLM) have been phagocytosed (correlative microscopy). It should be noted that the mentioned ~ 94 % particles uptake is derived only from those macrophages that are either in direct contact with a cylindrical particle, or in close vicinity. This subgroup only constitutes approximately 20 % of the entire macrophages examined for the quantification; Figure 46 is normalized to the count of all macrophages present in the images and not the subgroup of cells, being in contact to particles. The uptake based on the SEM images is comparable to the correlated image for the first time points, but over time the value differs more and more from the value, obtained by correlative microscopy. The largest difference was found after 24 hours.

The particles used in this experiment are fairly large and therefore can be easily identified in early engulfment stages with the SEM. The smaller the particles are, the faster the process of

internalization is likely to be, leading to more particles that are concealed by the membrane and hence cannot be identified with the electron microscope. Consequently, the discrepancy between SEM and CLEM will even be higher than for large particles.

The standard deviations for the three quantification approaches based on three independent experiments are lower for early (1.5 h) and late time points (24 h) of the incubation (Figure 46). Variations of experimental conditions alter the activity of cells and therefore the internalization velocity, which translates into discrepancies between the experiments, in particular for intermediate time points. After long incubation, all objects in the patrolled area are taken up, diminishing the difference.
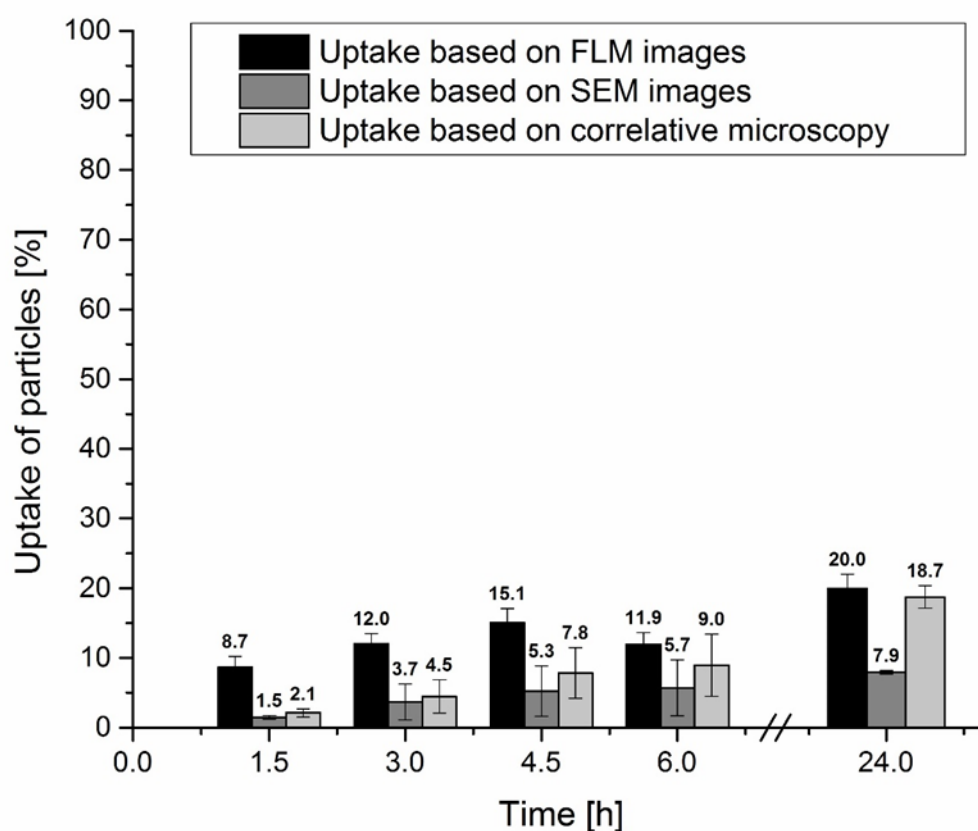
Figure 46 – Uptake kinetics of cylindrical particles by murine alveolar macrophages.

The graph illustrates the difference of the uptake kinetics utilizing FLM, SEM and correlative microscopy (CLEM) determined on the same macrophages. The values are given in percent and represent the number of cells that have partially, or completely invaginated at least one particle, over the total count of cells in the images, captured for the study (n = 300 ± 20 macrophages for three independent experiments). The exact value [%] is given over the respective bar. The black bar shows the uptake based on FLM, the grey bar the uptake based on SEM and the dark grey bar the correction by CLEM. (n = 300 ± 20 macrophages for three independent experiments). The error bars indicate the standard deviation between the three experiments.
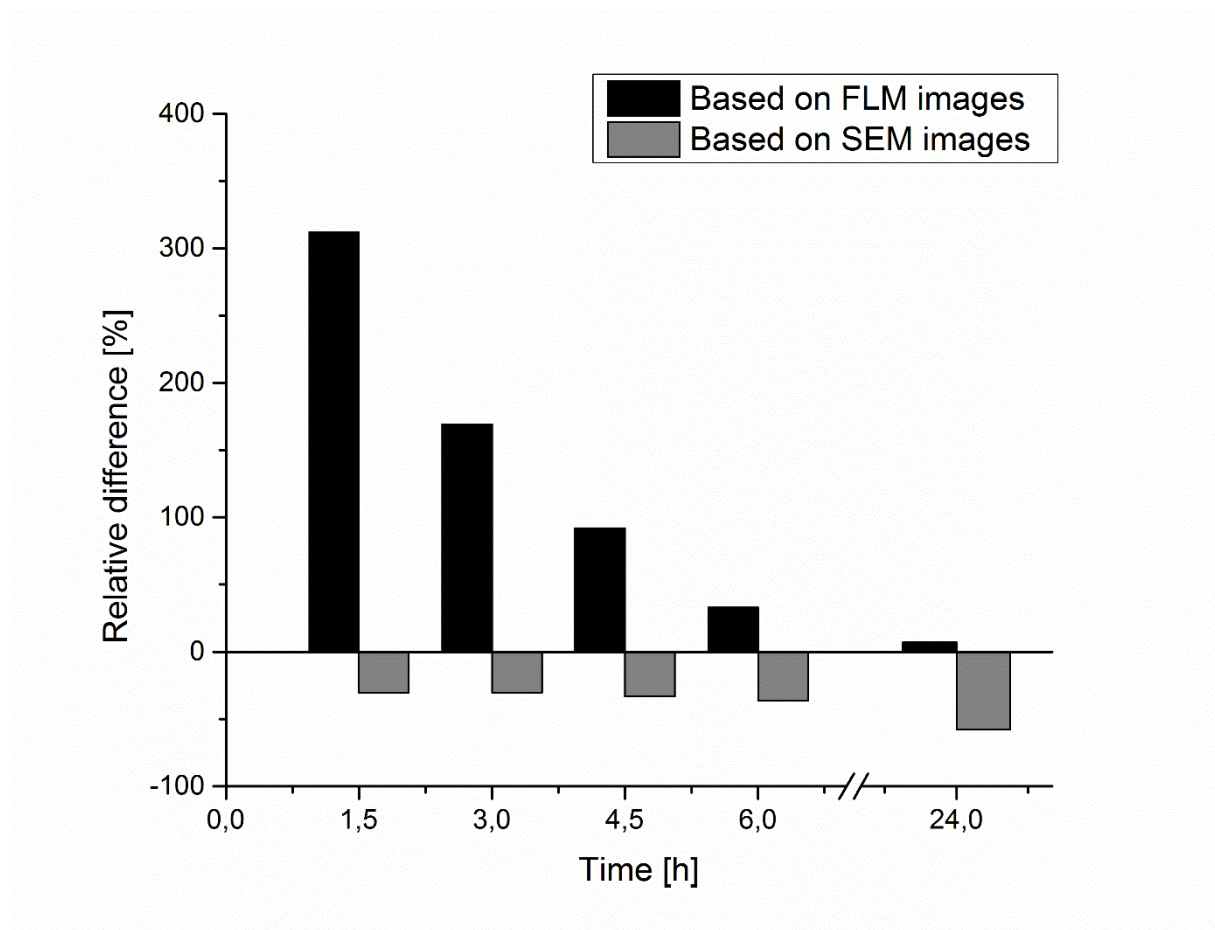
Figure 47 – Discrepancy between FLM or SEM and CLEM over time.

The figure depicts the mean relative discrepancy between the quantification based on FLM (black bar) or SEM (grey bar) and the overlay based on Figure 46. The quotient is given by the equation: Difference in uptake of particles [%] of FLM, or SEM and the correlated image, divided by the overlay times 100. This quotient decreases over time for FLM based analysis and increases for SEM based analysis at time point 24 hours.

In conclusion, the overlay avoids a misinterpretation of possible internalization events and behaviour. The number of uptake events was corrected most substantially for FLM for the first time points and for SEM for all time points, including the time point at 24 h, for which FLM and correlative microscopy yielded similar data. This highlights that it is of importance to correlate the uptake processes for the same macrophages with the identical particles. Otherwise an additional insecurity is added that might bias the absolute values.

5.4   Surfaces with Fibrous Texture

5.4.1   Hydrogels with Hairy Surface

Observations during the preparation of fibres, have led to the development of the protocol for the formation of hydrogels with hairy surfaces (4.2.3). For all examined hydrogels (alginate, agarose, gelatin, chitosan) a cleavage from the base layer was examined after the hydrogel had dried. If parts of the gel were still soaked with water, cleavage was only observed in the dried areas (Figure 48). This behaviour can be attributed firstly to the completely different elasticity of the hydrogel in dried and soaked state. Under dry conditions the hydrogel becomes brittle. Secondly, the adhesion to the pores differs significantly in dried, or soaked state. The mechanical force that is required to peel off the membrane from a dried hydrogel is substantially increased. If the hydrogel is fully soaked in water, only a fraction of the force is needed in order to lift up the filter from the hydrogel. Most likely the different behaviour for the adhesion between dried and soaked state can be attributed to the attachment of the dried hydrogel to the nanoscopic imperfection and indentations, being a result of the etching process of the pores of the track-etched membranes (Figure 23).

Figure 48 – Light microscopy images of the borderline between dried areas and the wet areas of the hydrogel base layer.

Agarose concentration was 1.5 % (m/V), a 2.0 µm template membrane was utilized. Circular areas indicate the regions in which cleavage has occurred between the fibres trapped in the template membrane and the base layer; the areas still soaked with water during peel-off are covered with fibres, next to no cleavage has occurred there. The borderline diagonally separates the cleaved part from the hairy surface in both images. Scale bar corresponds to 10 µm.

5.4.1.1   Hairy Surface Made from Alginate

Many modern therapeutics, in particular biologicals, require mild loading conditions that do not harm these fragile active agents [219, 220]. Alginate gels upon addition of divalent ions and does not require harsh changes of the milieu. Alginate is a widely used, characterized and accepted biopolymer for the encapsulation of viable cells [221, 222]. The protocol for the formation of the hairy surfaces uses comparable gentle conditions and therefore should allow the incorporation of cells into the hydrogel.
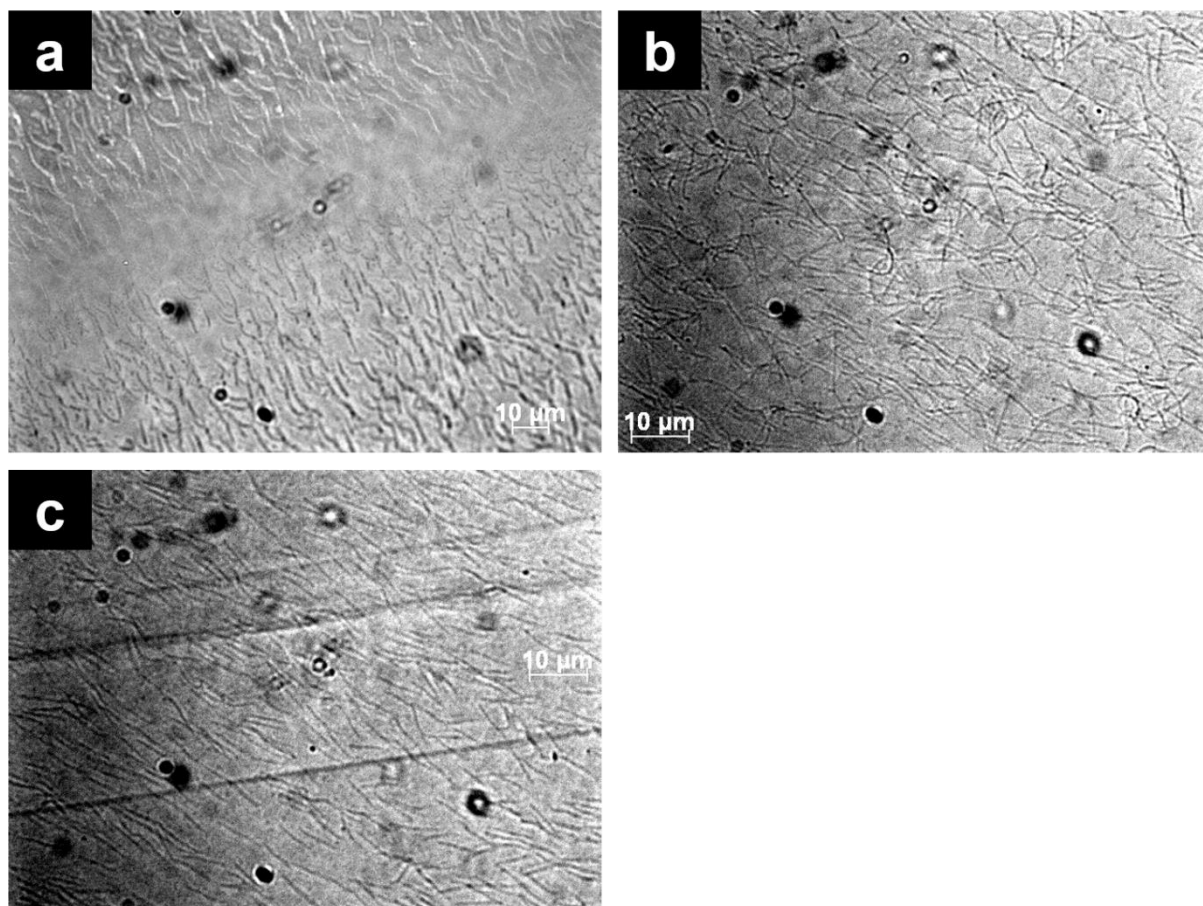
Figure 49 – Light microscopic images of hairy alginate surfaces formed from various template membranes.

(a) 2.0 µm, (b) 1.0 µm and (c) 0.6 µm template. The alginate concentration was 0.7 % (m/V).
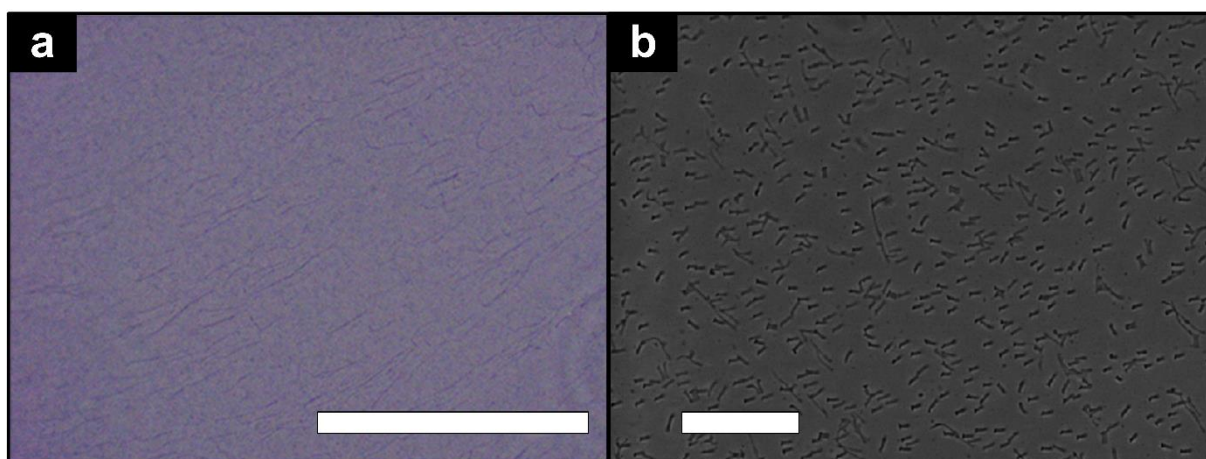
Figure 50 – Visualization of hairy alginate surfaces formed with 0.4 and 5.0 μm templates.

(a) Alginate fibres (0.7 % (m/V)) formed with a 0.4 μm template, captured with phase contrast microscopy, after image processing with the software ZEN. (b) Fibres formed with a 5.0 μm template, captured with phase contrast microscopy. The fibres are visible as darker lines in the images, documenting the homogeneous abundance. The directed orientation of the fibres is due to the peel-off direction, introducing a high organization of the fibre arrangement. Scale bars correspond to 50 μm (a) and 100 μm (b).
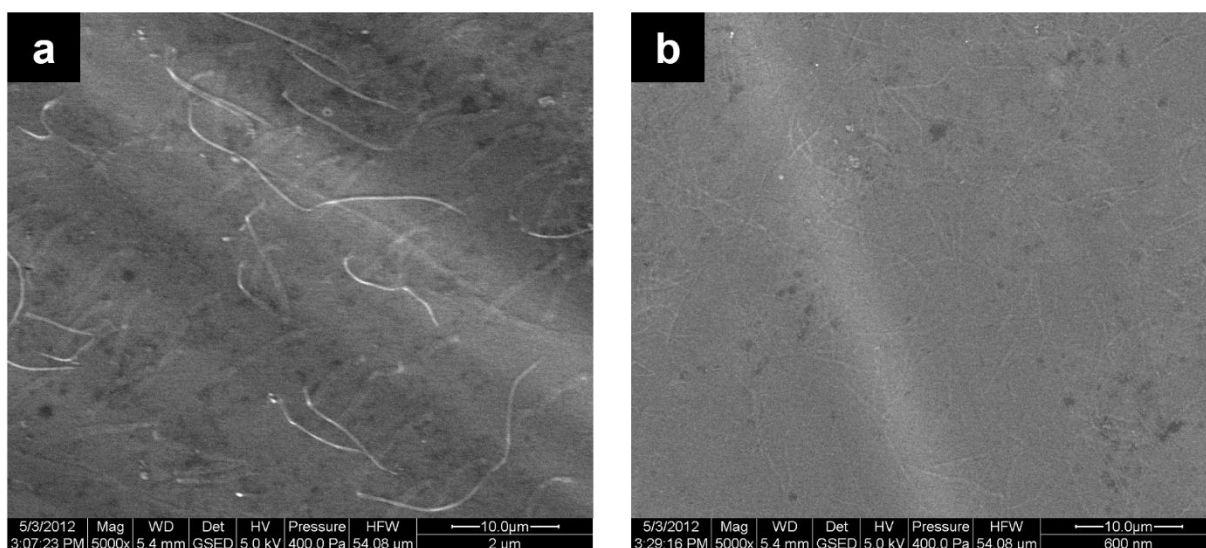
Figure 51 – The fibrous surface of textured alginate sheets visualized with an environmental SEM (ESEM).

The imaging conditions are adjusted in order to image the gel in wet state. (a) Surface of a hairy sheet formed from a 2.0 μm template, (b) surface formed from a 0.6 μm template; alginate concentration 0.7 % (m/V).
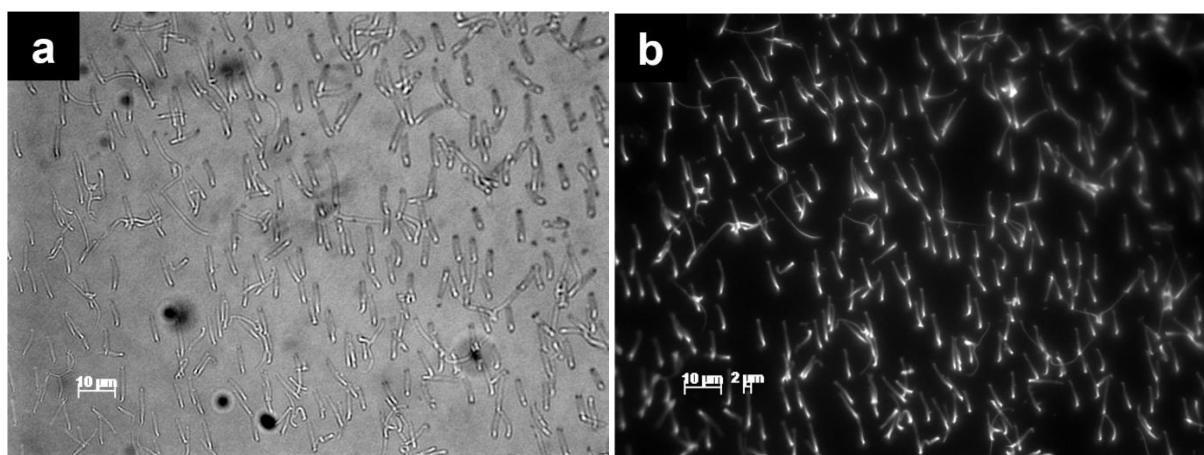
Figure 52 – Light microscopic images of hairy alginate surfaces with selective labelling of fibres. The filaments were formed from a 2.0 µm template. Conventional light microscopy (a) and fluorescence microscopy (b) of the identical position, alginate 0.7 % (m/V), FITC-pLL for labelling.

Filamentous sheets from alginate could be generated with template membranes ranging from 5.0 to 0.4 µm with a concentration of 0.7 % (m/V) alginate (Figure 49, Figure 50 and Figure 51). However, the fibres do not exactly represent the inverse features of the template. Upon gelation, the L-guluronic acid moieties bind the divalent Ca^{2+} ions. Thereby the gel network condenses with a release of water, which leads to shrinkage (so-called syneresis) of the fibres. This behaviour depends on the chemical composition of the alginate polymers [223]. Fibres are finer (precise values could be not determined because of limited resolution) and mildly shorter (8.33 ± 0.74 µm, RSD 8.87 %, n = 46, see Figure 52 a and b), deviating from the template geometry (2.0 × (10 ± 1) µm). A minimal number of fibres was observed to be stretched, likely due to adhesion forces during peeling off. In contrast, no truncated or ruptured fibres were observed; cleavage exclusively occurred on the basis of the sheet for all tested diameters.

Pore size of template [µm]	2.0	1.0	0.6
Pore density of template/100 µm²	2.55	18.44	34.75
Template porosity [%]	8.0 ± 0.3	14.5 ± 0.6	9.8 ± 0.4
Fibre density of structured sheet/100 µm²	2.26	7.38	6.27
Fibre density of structured sheet/cm²	2.26E+06	7.38E+06	6.27E+06
RSD of fibre density of structured sheet [%]	4.6	7.4	4.7
Moulding efficiency [%]	88.7	40.0	18.0

Table 2 – Specifications of template and resulting structured/hairy sheets after moulding. Pore density of template/100 µm² represent the abundance of pores in the template membrane per given area. The template porosity is given by the area of the pores over the filter surface. Fibre density of structured sheet/100 µm² and fibre density of structured sheet/cm² represent the abundance of fibres on the alginate sheet after moulding per given area. RSD of fibre density of structured sheet represents the relative standard deviation (RSD) of the abundance of fibres in light microscopic frames (n ≥ 3). The difference in fibre density between 2.0 and 1.0 (and 2.0 and 0.6) is significant, between 1.0 and 0.6 µm insignificant. The moulding efficiency is the quotient of the fibre density of structured sheet over the pore density of the template, given in percent for the respective pore dimension.

For template membranes with 2.0 µm pores, the count of fibres per given area (fibre density of structured sheet) is not much lower than the count of template pores per given area (pore density of template) (Table 2). The sheets patterned with 1.0 µm and 0.6 µm templates show an increasing discrepancy between the pore count and the number of fibres, bound to the hydrogel surface. This decrease of the moulding efficiency can be attributed to the rupture of the fibres from the hydrogel base layer. The more delicate the features, the more fibres are ripped off during peel-off. The highest porosity (14.5 ± 0.6 %) of the 1.0 µm template, among the used membranes, and the higher moulding efficiency (40.0 %) compared to the 0.6 µm membrane (18.0 %) are the reason for the comparable fibre density values of both, the 1.0

and 0.6 µm hydrogel sheets. In fact, the highest density of the fibres, among the analysed hairy alginate sheets with 7.38×10^6 fibres per cm² made with the 1.0 µm template, is not significantly different from the count for the hydrogel prepared with the 0.6 µm template. The discrepancy of the densities with respect to the hydrogel prepared with the 2.0 µm template is significant for both, the 1.0 and the 0.6 µm membrane. The values are in accordance with the observations made by Hsu *et al.*, having used track-etched membranes for the structuring of the thermoplastic polymer polypropylene (PP) [142]. The absolute values for the moulding efficiency differ between the two different systems; ~ 77 % for the 3.0 µm template, ~ 76 % (1.2 µm) and ~ 2 % (0.6 µm), based on calculations derived from [142] for PP, in contrast to the data in Table 2 for alginate 88.7 % (2.0 µm), 40.0 % (1.0 µm) and 18.0 % (0.6 µm). However, these findings are not surprising considering the different nature of the polymers. Even though the physico-chemical properties, including mechanical and wetting behaviour, are fundamentally different between the plastic PP and the hydrogel, the same trend can be observed: the stability of the fibres with bigger diameter is higher and fewer hairs are ripped off.

Since the porosity of the templates differs and the fibre density between the sheets, structured with 1.0 µm and 0.6 µm templates is comparable (Table 2), the differences in the fibre density can be attributed mainly to the cleavage of the fibres during peel-off. Discrepancies regarding the capillary filling of the templates can be largely ruled out (5.1). More filaments are removed from the surface for smaller feature sizes, which is expected to increase the roughness, introduced through the ruptures, in the order 0.6 µm > 1.0 µm > 2.0 µm. The detection of the increase of roughness is not straightforward. On the one hand, the low contrast and minute feature size does not permit verification with the light microscope. On the other hand, detection in the conventional SEM is hindered through the

high vacuum, causing shrinkage of the features, which disguises faint differences of the surface roughness. Environmental SEMs (ESEMs) operate with lower vacuum and vapour atmosphere, preserving the hydrated state of aqueous specimen, such as the fibrous alginate surfaces. Nevertheless, more delicate features than surfaces formed from the 0.6 µm template could not be detected (Figure 51). In principle, the contrast of the hydrogel features is low, hindering straightforward visualization. Since the efficiency of the moulding process deteriorates with decreasing structure size (Table 2), the hairy sheets were prepared with template membranes, not exhibiting a smaller pore diameter than 0.6 µm.
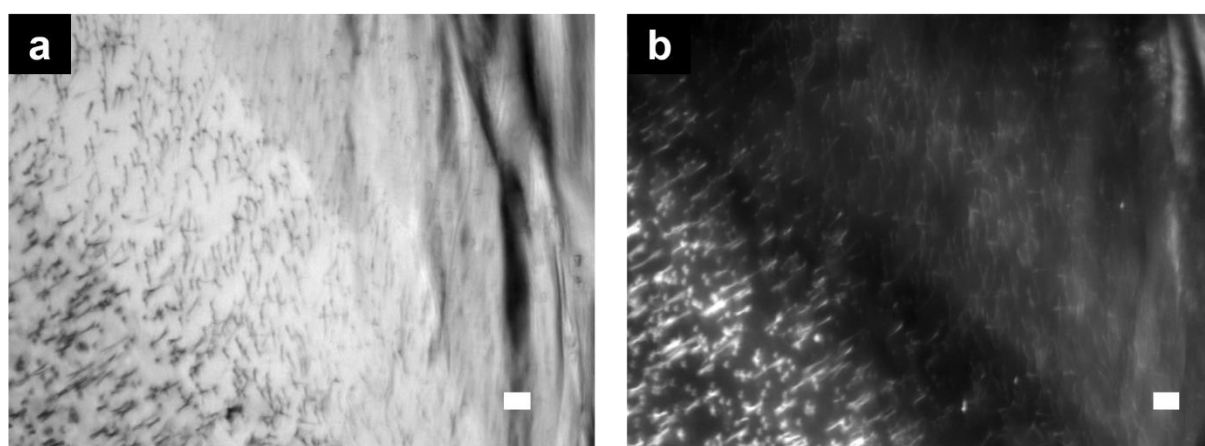
Figure 53 – Light microscopy and fluorescence images of the dissolved template membrane, exposing the hairy surface without peel-off.

The images show a part of the template, being partially dissolved by CH_2Cl_2. (a) Light microscopic image of exposed alginate fibres. In the left corner of the image the pores of the membrane can be seen, in the central segment of the image, the exposed fibres can be seen, in the right corner of the image the fibres are covered by PC that solidified after the dissolution with CH_2Cl_2. (b) Fluorescence image of the same partially dissolved area. The pores of the membrane can be seen in the left corner, the fluorescence is emitted from the filaments and the base layer and can be seen in the pores. In the centre of the image the fluorescence of the exposed fibres can be seen, in the right corner, the signal from the fibres is disguised by the PC cover. The template pore diameter was 2.0 µm, the alginate concentration was 0.7 % (m/V), ~ 0.01 % fluorescein-Na was used for labelling. The scale bar corresponds to 10 µm.

The area of the filamentous surface can be readily increased, in comparison to other (mainly lithographic) approaches; the mere exchange of the easily available membranes with a bigger diameter and adaptation of the volumes is sufficient. The largest membrane utilized for the experiments exhibited a diameter of 47 mm, representing an area of 17 cm².

5.4.1.1.1 Selective Modification of the Filaments and the Tips of the Filaments

Template methods exhibit the advantage to selectively modify the product; being embedded in the template only parts are exposed to the surrounding [224]. Before peeling off the template, only the tips of the fibres are accessible. The base layer below the template is shielded from the modification agents, added on top of the membrane. In order to demonstrate the modification of the negatively charged alginate, the positively charged polymer poly(L-lysine) was used. For straightforward detection a fluorescein isothiocyanate (FITC)-labelled pLL was used and detected by fluorescence microscopy (Figure 54 a). Fluorescence as a marker for modification could be observed along the entire fibre and was most intense on the tips of the fibres, decaying along the filament (Figure 54 b). The minimal increase at the end of the fibre is an artefact that can be attributed to the perpendicular origin of the filaments from the base layer and the bending to the side. A higher signal is detected in top view because a longer fraction of the fibre, including the labels, is emitting fluorescence per pixel. Due to the condensation of the gel matrix during gelation the pores of the template are not entirely filled and the pLL can diffuse into the pores of the membrane through the gaps along the fibres. Consequently, the label binds to the alginate over the entire fibre. The charged nature of the pLL electrostatically hinders the diffusion into the gel matrix of the alginate, modifying predominantly the surface of the fibres, as it was analogously reported in literature for alginate-pLL-alginate beads [225].
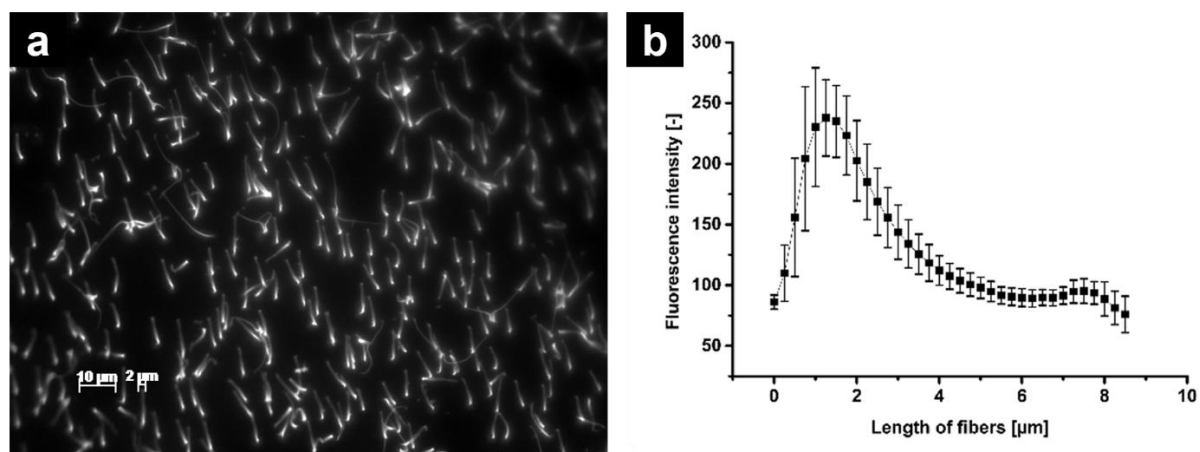
Figure 54 – Fluorescence light microscopy image of hairy alginate surface and intensity gradient of the fluorescence of its labelled alginate fibres.

(a) Fluorescence image of FITC-pLL fluorescence labelled hairy surface. (b) Intensity gradient along fibres in image (a). The alginate concentration was 0.7 % (m/V), the template dimension was 2.0 µm. The grey scale values along the fibre were plotted. Intensity is highest at the tip of the fibres and decreases along the fibre. The minimal increase at the end of the fibre can be attributed to the higher thickness of the hydrogel and thus more signal at the origin of the structure, caused by the bending of the filament. Data points as means ± SD (n = 10).

In addition to the selective chemical modification of the fibres, it has been reported for the template technique that particles could be specifically bound to the tips of tubes because the template membrane protects the rest of the substrate from modification [224]. The experiments, using a completely different setup, indicate that selective labelling of the tips of the filaments with particulate labels is feasible (Figure 55). 200 nm polystyrene beads were coated with the cationic polyelectrolyte PAH (15.0 kDa) in a layer-by-layer approach in order to render the surface positively charged, permitting ionic interactions with the negatively charged alginate. After coating, the beads were characterized using DLS, giving a size of 430.6 ± 30.6 nm with a PDI of 0.309 ± 0.052 and a positive zeta potential of 52.0 ± 2.8 mV, in comparison to - 47.0 ± 0.8 mV prior to coating and a size according to manufacturer specifications (205.6 ± 1.6 nm, PDI of 0.025 ± 0.003). The observed aggregation was of minor

interest for this setup, because the size was still well below the diameter of the template pores (template dimension 2.0 µm pore diameter).
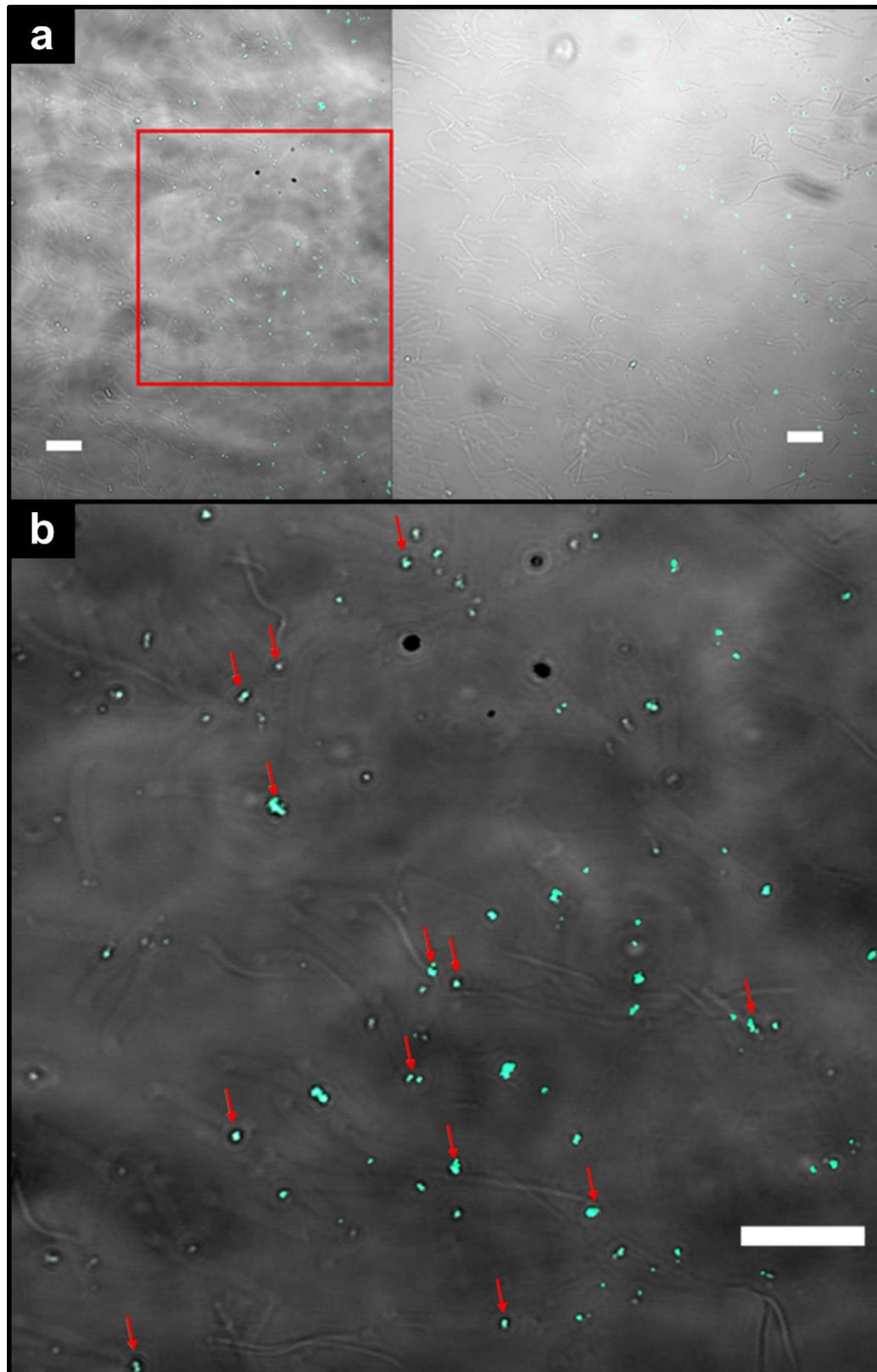
Figure 55 – Selective labelling of the tips of alginate filaments.

Alginate filaments (0.7 % (m/V)) formed with a 2.0 µm template have bound positively charged, fluorescing latex beads at the ends of the filaments. (a) The two images give an overview of the fibres with the fluorescing particles with CLSM. (b) The red frame in image (a) indicates the area that was scrutinized with CLSM in image (b). The arrows mark exemplary positions on which labelling of the tips was observed. Scale bars corresponds to 10 µm.

5.4.1.1.2 Drug Loading and Release from Hairy Alginate Surfaces

Alginate gels upon addition of divalent ions, no reactive agent is required. It has been shown that even sensitive cells can be encapsulated under physiological conditions [221, 222]. Various classes of compounds can be incorporated into the alginate matrix, including enzymes, growth factors, or APIs, allowing for a tailoring for the intended use in a straightforward fashion. The capability of the protocol for loading and release is demonstrated with the hydrophilic small molecule methylene blue and the hydrophilic macromolecule dextran labelled with FITC (Figure 56), serving as model compounds. Aqueous solutions of both model substances in the alginate sol form a hydrogel through the addition of $CaCl_2$.

The rate determining process for non-degrading delivery systems is diffusion [226]. For delivery systems made from hydrogels, the release rate is governed by both the mesh size of the gel backbone and the hydrodynamic radius of the loaded molecule [215, 227]. The mesh size of a hydrogel depends on the concentration, it has been reported to be approximately 4 nm for the alginate used in the study [144]. Small chemical entities, comprising small molecules and small biologicals, such as the peptide insulin (5.8 kDa) [144], can almost freely diffuse. In contrast, large molecules exceeding the threshold pore size are hindered [228], such as the large macromolecule dextran in this case [215, 227]. The dextran used shows a certain conformational flexibility in solution and has a molecular mass of 2000 kDa (Stokes radius/hydrodynamic radius of 27 nm in a coiled state [229]), which impedes free diffusion through the gel network. For most experimental conditions (Dulbecco's phosphate buffered

saline (DPBS) buffer, 2.0 and 0.6 µm), the small molecule methylene was completely released within 3 h (exception: deionized water, 2.0 µm template, release 88 %). The macromolecule dextran on the other hand, was released at a significantly slower rate in all experiments. For complete release, phosphate was added after 3 h in order to decompose the gel, thus increasing the slope of the curve and reaching the maximum after approximately 9 h.

The texture and the feature size of the surface did not impact the release of the small molecule methylene blue, explaining the identical release as expected. The load was completely released in less than 1 h for sheets with both 2.0 µm and 0.6 µm feature size of the hairs.
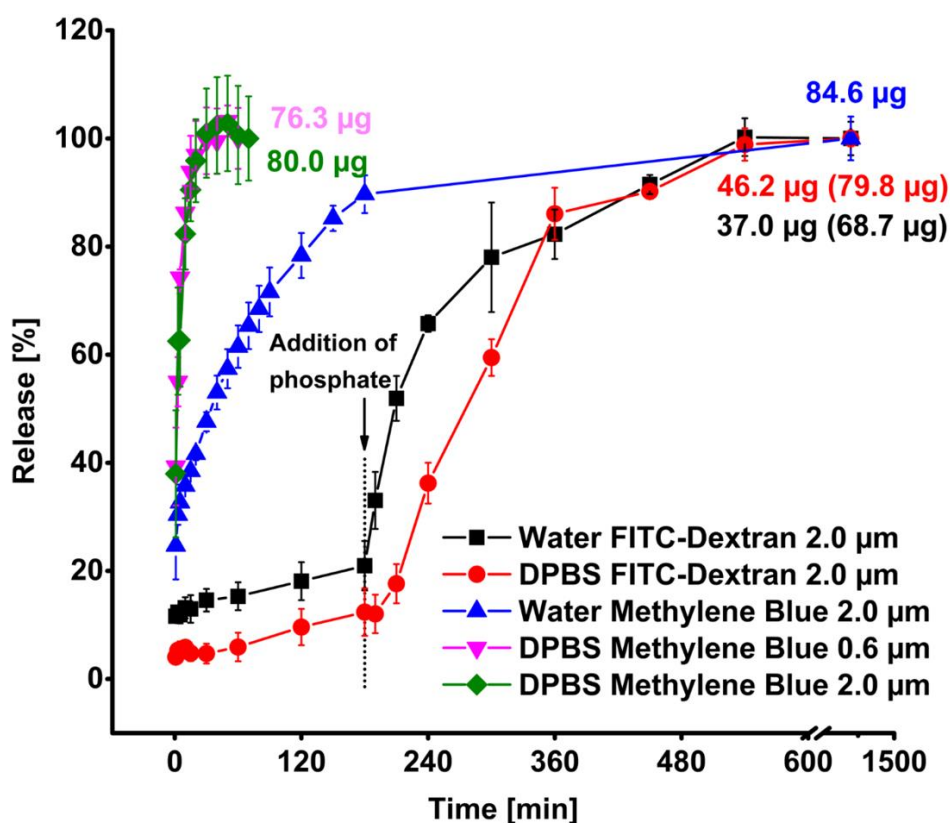
Figure 56 – Release kinetics of methylene blue and FITC-dextran from alginate with different surface structure and varying release media.

After 180 min of incubation, phosphate was added to the dextran-loaded sheets, releasing the remaining FITC-dextran from the gel completely. Values in brackets include the loss of load during the process of cross-linking due to diffusion into the cross-linking solution. The alginate concentration was 0.7 % (m/V) (n ≥ 3 experiments).

In contrast, the medium has a pronounced influence on the release kinetics. The release of methylene blue in deionized water was significantly slower than in phosphate buffered saline, additionally containing Mg^{2+} and Ca^{2+} (DPBS). This can be explained by the low solubility of calcium phosphate ($CaHPO_4$ solubility 100 mg/l [230]; H_3PO_4 pK_{a2} 7.21 [231]) in water at the chosen pH. The Ca^{2+} ions form complexes with phosphate anions, weakening the alginate gel backbone and facilitating the release of the small molecule. This effect did not suffice to speed up the release of the macromolecule dextran under the chosen conditions, exhibiting analogue slopes for the release curves (Figure 56). Light microscopic verification did not reveal structural alterations of the surface for both media after 3 h (Figure 57 a, b), despite complete release. However, extended exposure of the alginate sheet in this buffer (5 days) led to complete disintegration of the gel, because of the extraction of the Ca^{2+} ions through the phosphate anions and precipitation of $Ca_3(PO_4)_2$. Moreover, incubation for 5 days in deionized water did not change the texture of the sheets (Figure 57 c). In order to accelerate the release of the loaded dextran, the concentration of phosphate was strongly increased (by 20 mM); instantaneously more dextran is released with a complete release of the load after approximately 6 h (total 9 h) after addition. The delay for the release of dextran in DPBS is contradictory at first sight, considering the faster release for methylene blue in DPBS. The excess Ca^{2+}, which was still present from the gelation step, diffuses from the gel along the concentration gradient and distributes within the release media, either water (pH 7.4), or DPBS. The gradient is bigger for deionized water in comparison to the physiological buffer DPBS, already containing Ca^{2+}. Upon addition of phosphate, in order to entirely release the macromolecule, the solubility limit of calcium phosphate ($CaHPO_4$), which is almost insoluble in water, is reached and it precipitates within the gel sheet. Precipitates predominately form in DPBS since it contains more ions. This is supported by the observation that over the course

of the experiment the turbidity rises, in particular after addition of phosphate after 3 h, within the sheets immersed in DPBS release media. Visible precipitation was not observed for release in pure water, neither after addition of phosphate. The precipitates were trapped in the alginate gel, initially decreasing the rate of release for the macromolecule dextran, intertwined in the alginate backbone. In both release media, water and DPBS, the entire load was released after 9 h (total incubation time). Discrepancies regarding the mass that is release, ranging from 84.6 to 37.0 µg (including the loss from cross-linking = 68.7 µg), are caused by conditions and concentrations chosen for the gelation. In fact, FITC-dextran diffuses already from the alginate during cross-linking.
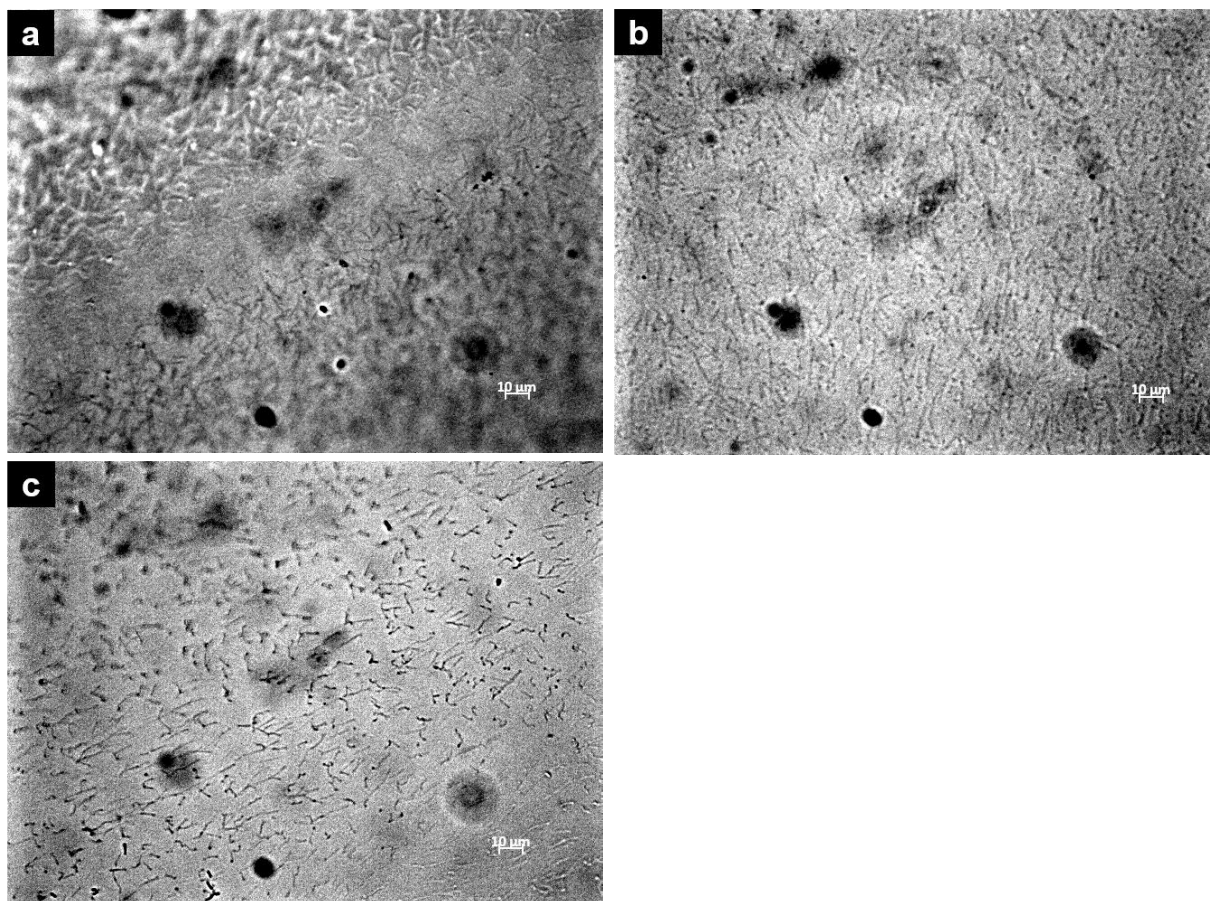
Figure 57 – Light microscopic images of hairy alginate sheets after release of methylene blue in different release media.

Hairy surfaces were formed with 0.6 µm (a) and 2.0 templates (b) and (c). (a) 0.6 µm, 3 hours release in DPBS. (b) 2.0 µm, 3 hours release in DPBS. (c) 2.0 µm, 5 days release in deionized water. The alginate concentration was 0.7 % (m/V).

5.4.1.2   Hairy Surfaces Made from Agarose, Gelatin and Chitosan

Various hydrogels are suitable for the formation of fibrous sheets with membranes serving as templates. The hydrogels were all infiltrated into the pores of the template in sol state, driven by capillary forces. The mode of solidification is different for each hydrogel, agarose forms a gel due to cooling down after heating (4.2.3.2), gelatin was heated and chemically crosslinked (4.2.3.3) and chitosan forms a gel after exposure to basic agents (4.2.3.4).

Applying the standard protocol for the formation of fibrous surfaces (4.2.3), it was possible to generate fibrous surfaces with membranes exhibiting pore diameters between 5.0 – 1.0 µm (Table 3, Figure 58). The concentration range, which was used for the experiments, was individual for each hydrogel. In accordance with the results of the hydrogel alginate, the dimension of the filaments largely is dictated by the internal geometry of the pores of the template membranes. Therefore, the length of the fibres has been observed to be 10 µm and the diameters depends on the chosen membrane.

Hydrogel	Agarose	Gelatin	Chitosan
Filamentous surfaces formed from template membranes (pore diameter)	5.0, 2.0, 1.0 µm	5.0, 2.0, 1.0 µm	5.0, 2.0, 1.0 µm
Concentration of gel (m/V)	5.0 – 0.5 %	10.0 – 1.0 %	2.0 %

Table 3 – Filamentous/Hairy sheets made from the hydrogels agarose, gelatin and chitosan.
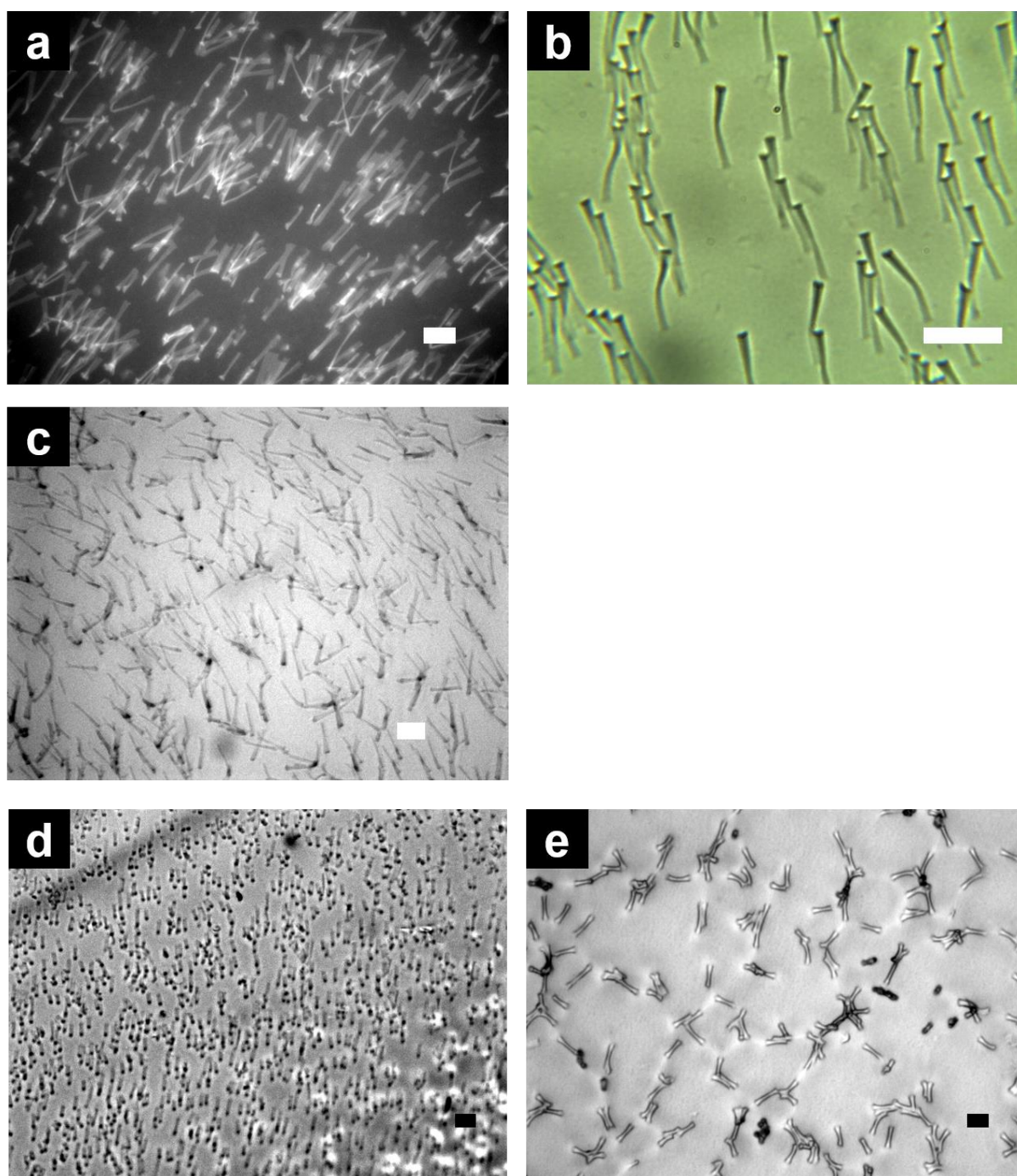
Figure 58 – Light microscopy images of fibrous sheets made from the hydrogels agarose, gelatin and chitosan.

(a) Fluorescence microscopic and (b), (c) light microscopic images of the different specimen made from agarose. (c) The surface was imaged after 1 h of immersion into CH_2Cl_2, without peel-off of the template. Template dimension 2.0 µm diameter, concentrations: (a) 0.5 % (m/V) agarose labelled with fluorescein-Na (~ 0.01 % (m/V)), (b) 1.5 % (m/V) and (c) 3 % (m/V) agarose. (d) Light microscopic image of a fibrous surface made from gelatin. The pore diameter of the template was 2.0 µm, the gelatin concentration was 10 % (m/V).

(e) Light microscopic image of a chitosan sheet formed from a template with pore size 5.0 µm, the chitosan concentration was 2 % (m/V). The scale bar corresponds to 10 µm.

An alternative to the peel-off of the template, is the dissolution of the template with an adequate solvent, such as THF, or CH_2Cl_2 (Figure 58 c). Through dissolution of the template membrane after the infiltration of the liquid precursor and after solidification the feature size could be vastly reduced. It was possible to generate agarose fibres with a template having a diameter of 0.1 µm (Figure 59). The feature size of the single hairs lies below the resolution limit of the conventional light microscope, with which the measurements were performed. Nonetheless, the picture unambiguously shows the presence of a multitude of fibres, regardless the fact that their precise dimension cannot be assessed with the chosen technique. The membrane was still partially covered by PC matrix from the membrane. Complete removal can hinder the visualization, because the PC matrix spatially separates the single filaments. With this setup the resolution of conventional fluorescence light microscopy is sufficient for the detection.
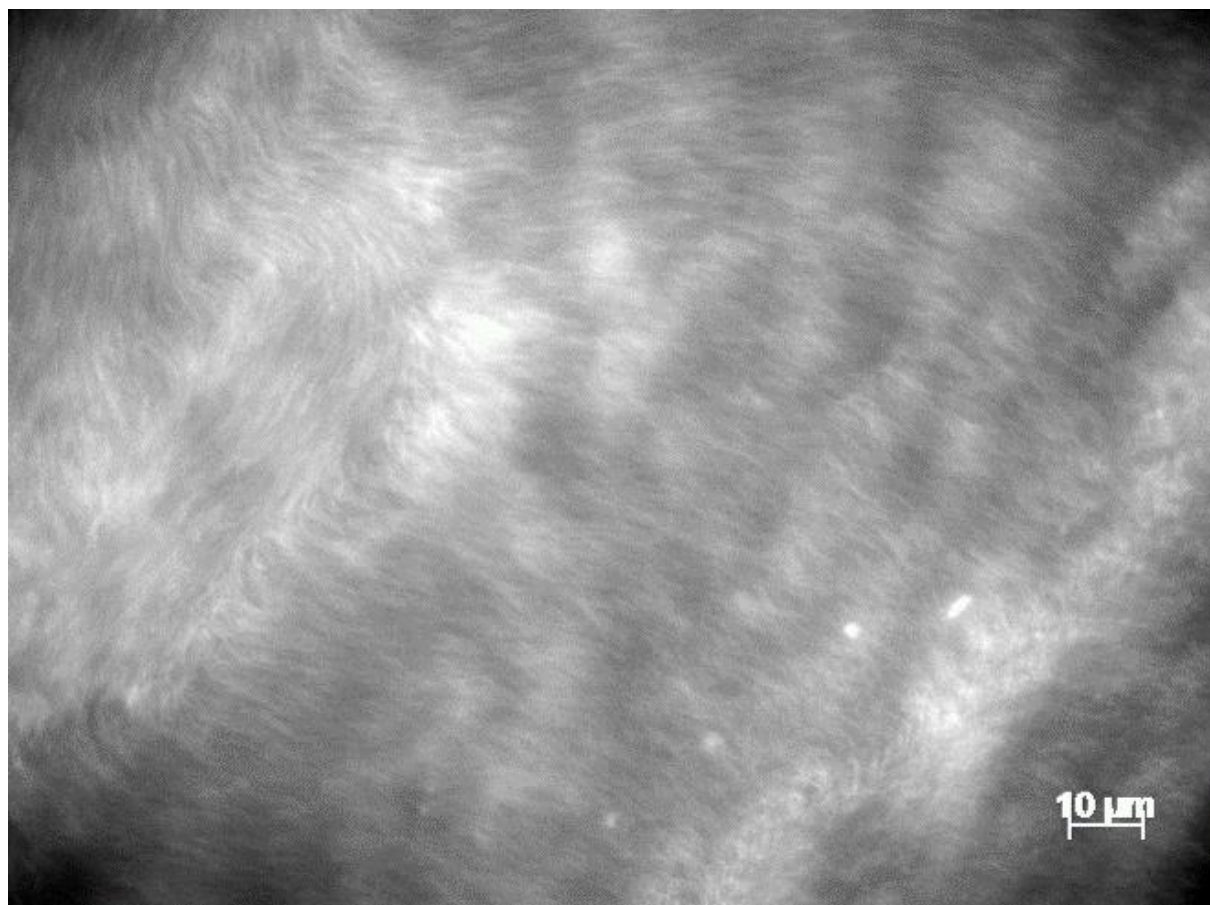
Figure 59 – Fluorescence light microscopic image of fibrous agarose surface formed with a 0.1 µm template membrane.

Agarose concentration was 5 % (m/V), approximately 0.01 % fluorescein-Na was used for labelling. The membrane was not peeled off, it was dissolved with CH_2Cl_2. Not all filaments can be discriminated, because of the diameter of the filaments in combination with the distance between the fibres, which is below the resolution of the microscope.

In accordance with results from the loading of hairy alginate sheets with model drugs (5.4.1.1.2), the hydrogel agarose can also be loaded. Fluorescein-Na (Figure 58 a) and methylene blue were loaded to agarose sheets. The release profile depends on the concentration of agarose, a precise quantification of the release profile remains to be scrutinized.

The hairy alginate sheets are stable over extended time, regardless of the feature size. After one month of incubation in aqueous immersion, no visual alteration could be observed.

5.4.1.3 Hairy Hybrid Sheet – Differences in the Composition of Hairs and Base Layer

Experiments confirmed the option to generate sheets, composed of hairs and a base layer, having different compositions. Fibres are generated in a first step and are bound to a new base layer consecutively (4.2.3.5). First results indicate that this can be extended towards other materials, not only differences of labelling or concentration of the same material of the hairs and the base layer.

5.4.1.3.1 Hairy Hybrid Sheet – Differences in Labelling and Concentration between Fibres and Base Layer – Agarose

The adaptation of the protocol for the generation of hairy surfaces in a consecutive process (4.2.3.5) allows for a generation of hairy sheets exhibiting hairs with a different composition in comparison to the base layer (4.2.3.5.1). First experiments have been performed with the hydrogel agarose, containing the particulate labels (fluorescing 200 nm silica particles) in high concentration (Figure 60, Figure 61, Figure 62). The particulate labels were chosen, because the tendency for diffusion after gelation is strongly decreased in comparison to a low molecular dye which can diffuse to a much higher extend, following the water exchange in the gel. In addition, the particulate labels allow for a visualization in the SEM, the particles do not shrink in the high vacuum and can be seen as protrusions in the hydrogel (Figure 60).
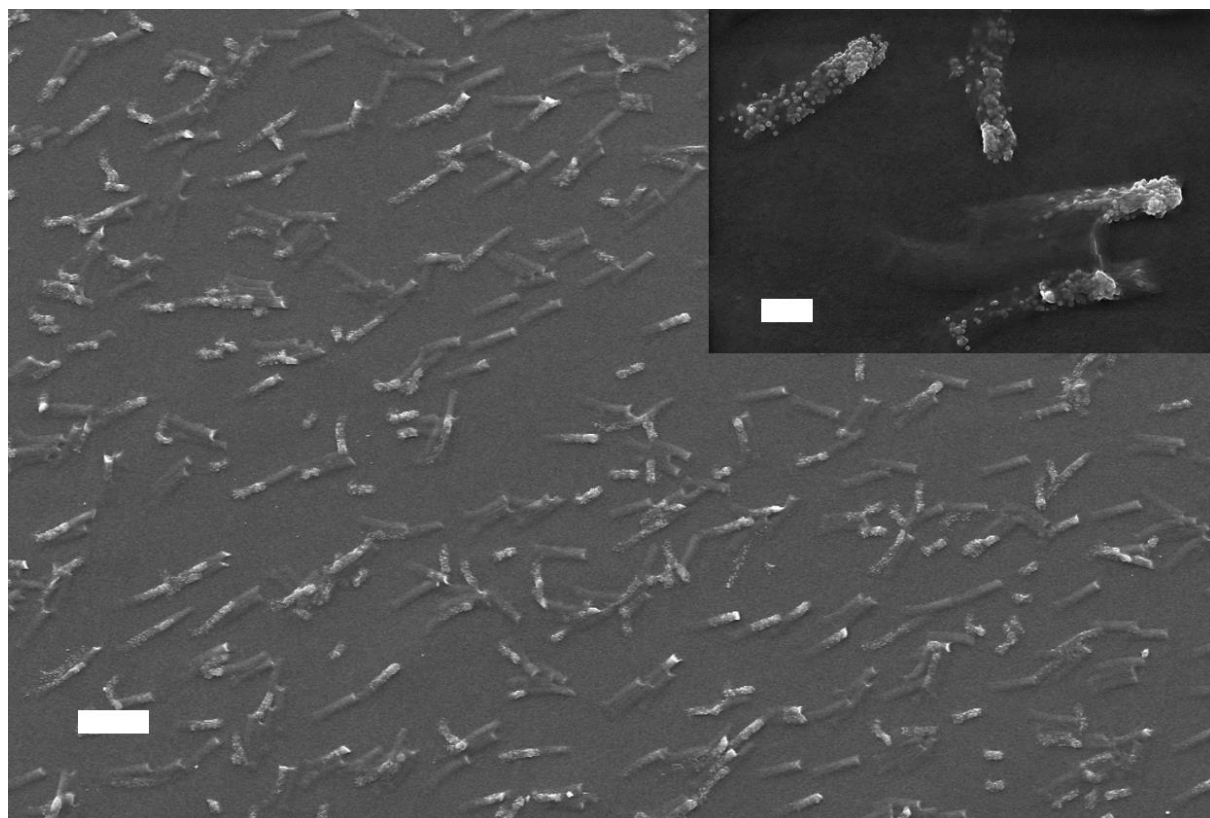
Figure 60 – SEM micrographs of hairy hybrid sheets, exhibiting differences in the composition between the fibres and the base layer.

The fibres contain silica beads with a diameter of 200 nm (0.8 % (m/V)), the agarose concentration used for the fibres was 1 % (m/V). The agarose concentration of the base layer was 2 % (m/V). The pore diameter of the template was 2.0 µm. The scale bar represents 10 µm in the main frame, 2 µm in the inset, displaying the filaments in higher magnification.

The experiments reveal that the silica beads, used as labels, are present to a different extend in most of the fibres for the mainly tested membrane pore diameter of 2.0 µm (Figure 60, Figure 61). The silica particles with a feature size of 200 nm can clearly be seen in the SEM micrographs (Figure 60), protruding from the collapsed hydrogel structure in the high vacuum of the electron microscope. The fluorescence signal, given by the silica beads, can be seen in strongly varying intensity, indicating differences regarding the extend of filling for most of the fibres. The observed differences for the content of particles per fibre can firstly be explained with the inhomogeneous distribution of the labels in the sol during the infiltration. Secondly,

with a certain demixing during the entry into the pores. For low molecular compounds, no segregation was observed between the base layer and the filaments (5.2.2). Thirdly, the incomplete pull-out of the labelled fibres after the second infiltration explains the fact that not all fibres are labelled. The fluorescence of the template membrane (Figure 62) shows that a substantial fraction of the label remained in the template membrane. Fluorescence light microscopy does not allow to precisely reveal the pores in which more label has been trapped. The plentiful pores of the translucent filter membrane deflect the fluorescence light, giving a signal in pores having very little or no intrinsic fluorescence. The vast difference between the two examined pore diameters 2.0 µm and 5.0 µm remains subject to further scrutiny.
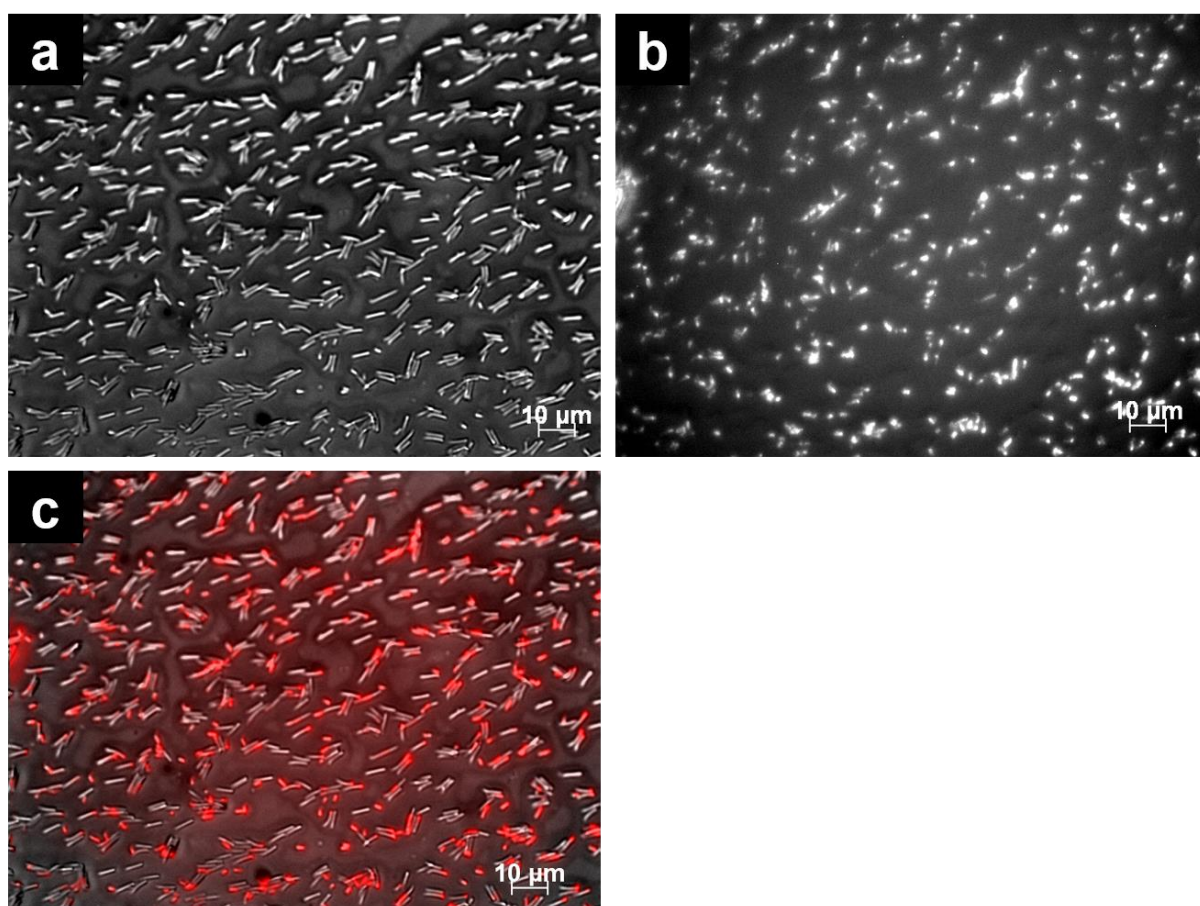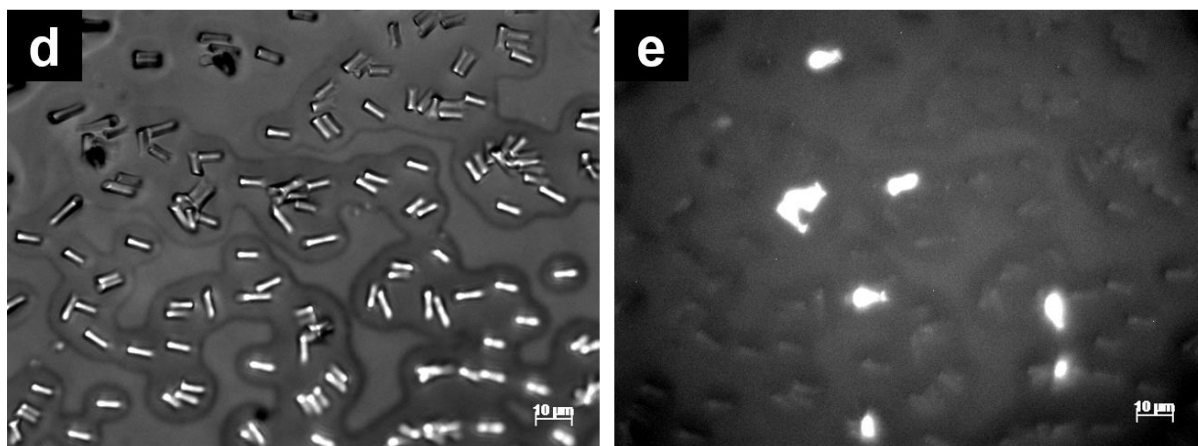
Figure 61 – Light microscopy and fluorescence images of hairy hybrid sheets, exhibiting differences in the composition between the fibres and the base layer.

(a) Light transmission image and (b) fluorescence image of the identical position of the sheet carrying filaments (2.0 μm pore diameter). (c) The fluorescence signal from image (b) (coloured in red) is overlaid onto the transmission light microscopic image from (a). (d) Light transmission image and (e) fluorescence image of the identical position of the sheet carrying filaments (5.0 μm pore diameter). The fibres contain silica beads with a diameter of 200 nm (0.8 % (m/V)), the agarose concentration of the fibres was 1 % (m/V) and 2 % (m/V) for the base layer.
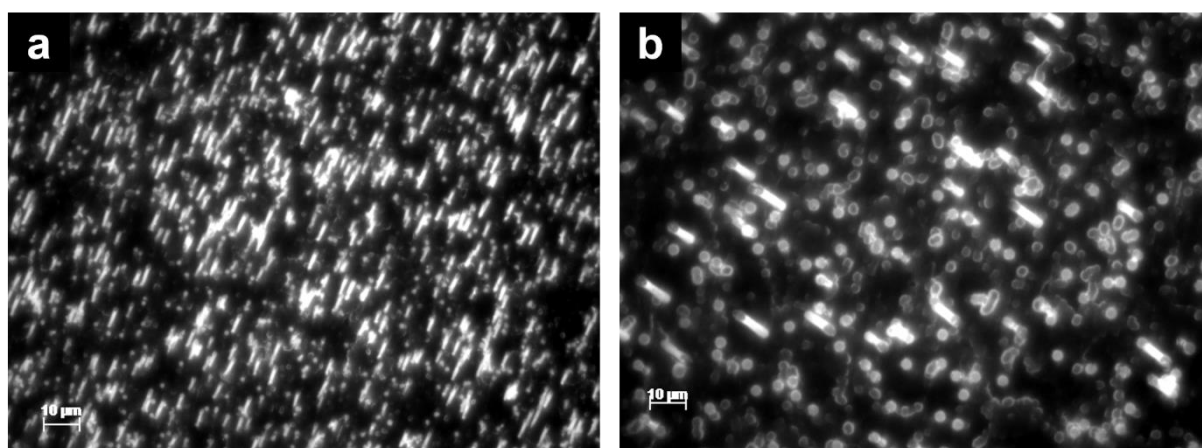
Figure 62 – Fluorescence of template membrane after transfer to a new base layer - agarose with particulate label.

The images show the fluorescence of the 2.0 μm (a) and 5.0 μm (b) template membrane after pull-out after solidification of agarose. Agarose concentration of the fibres was 1 % (m/V), 0.8 % (m/V) SiO_2 particles (200 nm) were used for labelling; agarose base layer concentration was 2 % (m/V).

5.4.1.3.2   Hairy Hybrid Sheet – Differences in Type of Hydrogel

As the next step, the transfer of fibres, differing in the material from the base layer, was examined and the protocol adapted accordingly (4.2.3.5.2). Fluorescently labelled fibres made from gelatin (5 % (m/V)) contained in the pores of the template bound to a base layer made from agarose (2 % (m/V)) to a low degree (Figure 63). The fraction of fibres that could be transferred and bound to another base layer was limited under the chosen conditions. The majority of the fibres remained trapped in the pores (Figure 64) and consequently the fluorescence signal could only be detected inhomogeneously on the surface of the hairy sheet (Figure 63 b and c). Optimization of preparation conditions may allow generating hybrid surfaces with a higher degree of patterning efficiency. Such a protocol would permit to bind hydrogel fibres made from protein (e.g. collagen or gelatin) to hydrogel base sheets. In addition to the right composition this configuration exhibits high structural similarity with the ECM (2.2.1); the main component of the ECM is the fibrous protein collagen. So far, no surrogate for the ECM has been found.
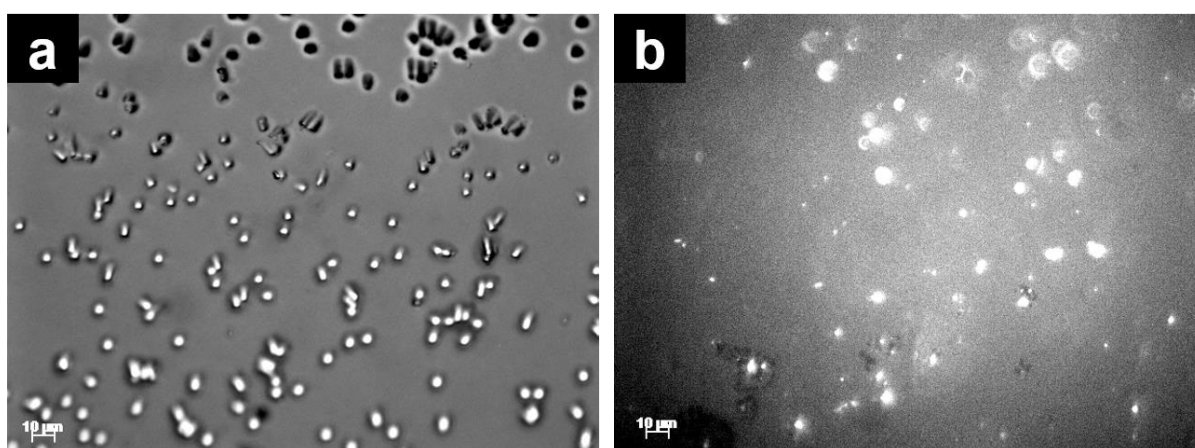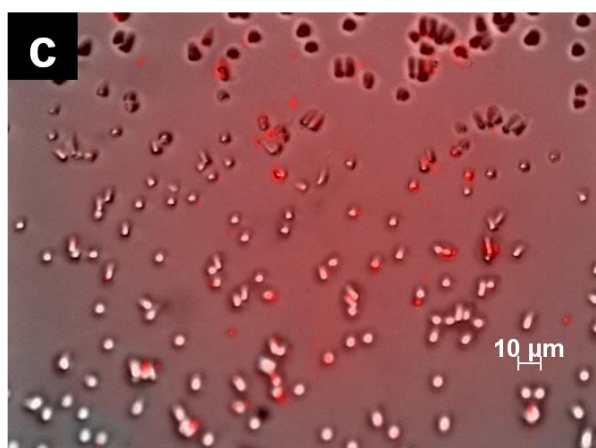
Figure 63 – Light microscopy and fluorescence images of hairy hybrid sheets, consisting of gelatin filaments and agarose as the base layer.

(a) Light transmission image and (b) fluorescence image of the identical position of the sheet carrying filaments. (a) The cylinders appear black in the upper third of the image and white in the lower part of the image; the lower third of the image is not well focused. This optical effect is caused by the orientation of the sheet. The surface of the sheet is tilted and not perfectly horizontal, therefore not all parts of the image are focussed. (c) The fluorescence signal from image (b) (coloured in red) is overlaid onto the transmission light microscopic image from (a). The filaments consist of 5 % (m/V) gelatin, containing 0.6 % (m/V) labelled PS particles (50 nm); the base layer consists of 2 % (m/V) agarose; a template with 5.0 µm pore diameter was used.
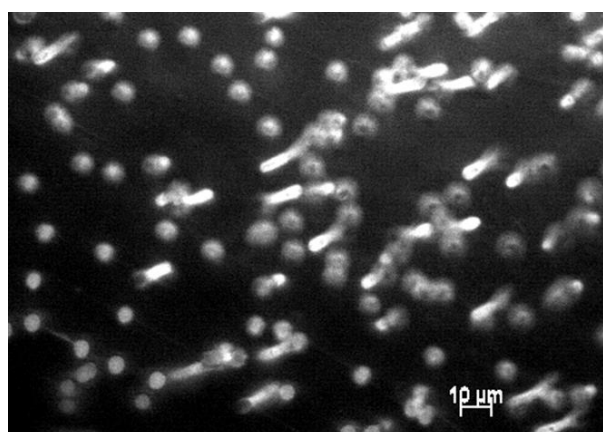
Figure 64 – Fluorescence of template membrane after transfer to a new base layer - gelatin with particulate label.

The template membrane contained filaments, consisting of gelatin 5 % (m/V), labelled with 0.6 % (m/V) fluorescing PS particles (50 nm). The pull-out of the filaments was performed with agarose 2 % (m/V). The pore dimension of the template membrane was 5.0 µm.

5.4.2 Cell Interactions with Hairy Surfaces

The interactions between filamentous alginate surfaces, formed from template membranes with various pore diameters, and fibroblasts have been assessed. The surfaces exhibit substantial differences regarding the count of filaments and the dimension (Table 2). Extensive testing and quantification of the interaction between the fibroblasts and the surfaces was performed for surfaces derived from template membranes with 2.0, 1.0 and 0.6 µm pore diameters, excluding templates with the dimension 5.0 and 0.4. The filaments generated within 5.0 µm pores were regarded as too large, in addition to their low abundance. Likewise, cell adhesion experiments were not carried out with more delicate structures than 0.6 µm, due to the insufficient resolution of the respective microscope (5.4.1.1, Figure 50 a). As in-process control, the presence of the fibres was verified during the experiment, thereby restricting the minimum feature size.

Three classes of cell-surface interaction were defined: Attached, round (not attached) and spheroid (agglomerated). The formation of spheroids reduces the number of single cells on the substrate and indicates preferred cell-cell contacts. The fraction of attached cells was highest on tissue culture treated surface (TC) being larger than 90 % and at the same time the fraction of round cells represented less than 8 %. On native alginate surfaces, the fraction of attached cells was less than 4 % and the fraction of round cells was larger than 85 %. It has to be noted, that the formation of spheroids influences the result on native alginates due to agglomeration and thus reduction of single cells.
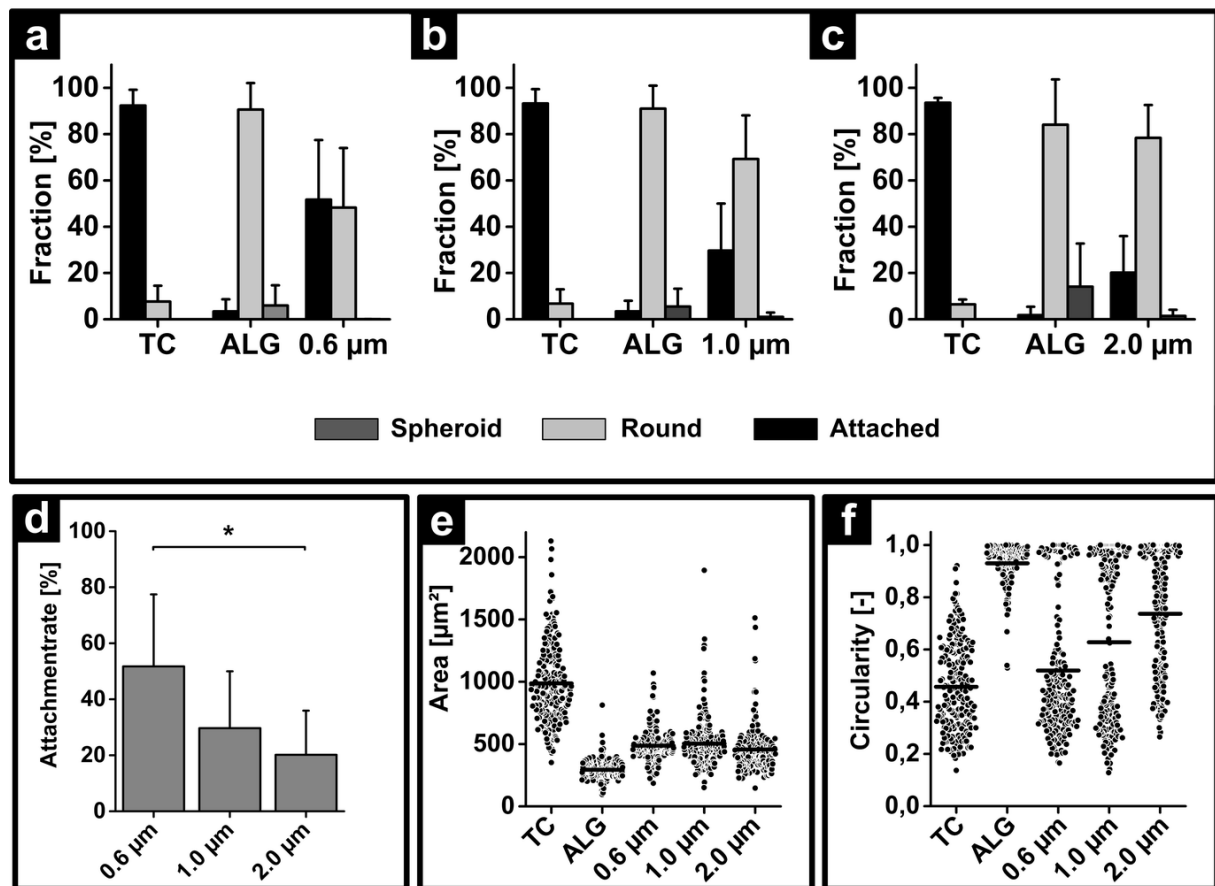
Figure 65 – Interaction of fibroblasts on structured/hairy surfaces.

(a) Interaction of fibroblast on alginate hydrogels structured from 0.6 µm template pores.

(b) Interaction of fibroblast on alginate hydrogels structured from 1.0 µm template pores.

(c) Interaction of fibroblast on alginate hydrogels structured from 2.0 µm template pores.

(a) - (c) For all experiments also the behaviour on TC and pure alginate was investigated.

(d) Comparison of attachment rates of structured alginate hydrogels. (n ≥ 3 experiments). * represents statistical significance (p < 0.05) (e) Quantification of cell area on studied surfaces. (f) Quantification of circularity of cells as morphological parameter. (e) and (f): n = 3 experiments with N > 200, black bars indicate mean value of measurements. Abbreviations: TC: tissue culture treated polystyrene, ALG: unstructured alginate, 0.6 µm, 1.0 µm and 2.0 µm: hairy alginate surfaces and structure dimensions.

The highest fraction of attached fibroblast was observed on 0.6 µm hairy alginate.

51.7 ± 25.7 % fibroblasts were attached to the surface against 48.3 ± 25.8 % fibroblasts with no interaction (Figure 65 a). On 1.0 µm hairy alginate, a fraction of 29.7 ± 20.3 % fibroblasts were attached against 69.3 ± 18.8 % fibroblasts with no interaction (Figure 65 b). The lowest

interaction count was observed on 2.0 µm hairy alginate with 20.2 ± 15.8 % attached and 78.4 ± 14.2 % non-attached fibroblasts (Figure 65 c). Overall, the attachment count could be increased by textured hairy alginate surfaces in comparison to a native alginate surface in the order 0.6 µm > 1.0 µm > 2.0 µm (Figure 65 d).

The morphological analysis of fibroblasts by area and circularity (perfect circle if 1.0, $4 \times \pi \times$ area/perimeter, values between 0 and 1) gives more information on attachment (Figure 65 e and f). On stiff tissue culture treated polystyrene fibroblasts are extremely spread (987 ± 324 µm²) and irregular in shape (circularity of 0.46 ± 0.17). In contrast, on plain alginate surfaces, fibroblasts are not attached and rounded (area of 294 ± 76 µm² and circularity of 0.93 ± 0.07). On structured surfaces the area of fibroblast is increased but only half as large as fibroblasts growing on tissue culture treated polystyrene (0.6 µm: 487 ± 128 µm², 1.0 µm: 504 ±198 µm² and 2.0 µm: 456 ± 176 µm²). The circularity of fibroblasts on structured alginate surfaces lies in between circularity of unstructured alginate surfaces and tissue culture treated polystyrene (0.6 µm: 0.52 ± 0.26, 1.0 µm: 0.63 ± 0.3 and 2.0 µm: 0.74 ± 0.23). The overall smaller cell areas on structured alginate surfaces in comparison to tissue culture treated polystyrene surface can be explained by differences in surface stiffness. It is known that cells do not only react on the chemical composition but also on the mechanical properties of the cultivation surface resulting in morphological changes [232]. The circularity of cell shapes was therefore taken into account, illustrating the irregular morphology of attached cells (Figure 65 f). With respect to the bimodal distribution, the results correlate with the quantification of overall attachment rate shown in Figure 65 a - d.

Native Alginate Surface **Hairy Alginate Surface** **Standard TCPS Surface**
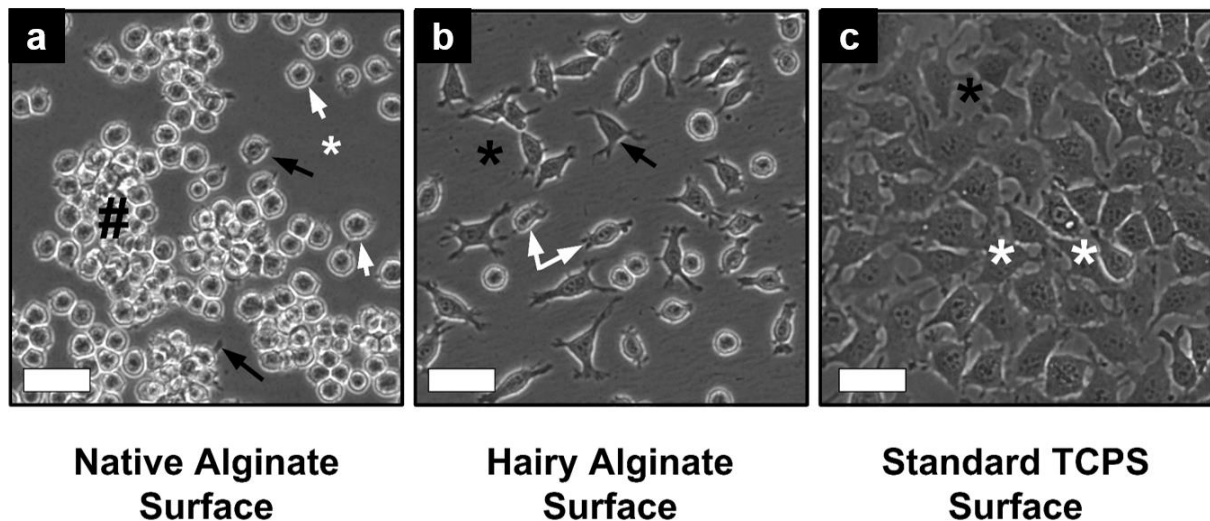
Figure 66 – Phase contrast images of *in vitro* cell study of fibroblasts on filamentous alginate surfaces.

(a) Cellular response on native flat alginate hydrogel surfaces (white asterisk). The cells are predominantly not attached and show only low (black arrows), or no reaction to the surface (white arrows). Cells tend to form large agglomerates (black hash key) due to the lack of adhesion sites. (b) Hairy alginate surface (black asterisk) with partially (white arrows) and complete attached cells with filopodia (black arrows). (c) Cellular response on tissue culture treated polystyrene surfaces (black asterisk). The scale bar corresponds to 50 µm.
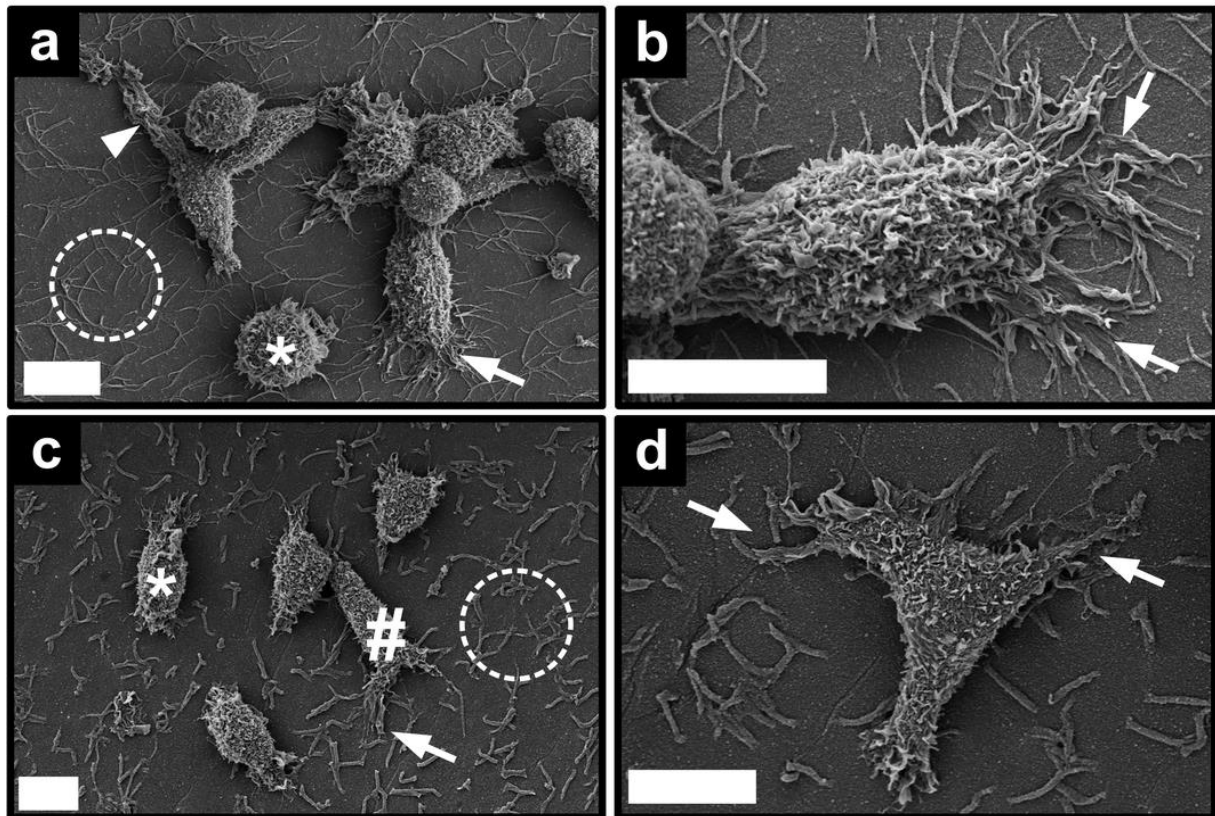
Figure 67 – Interaction of fibroblasts with filamentous alginate sheets visualized with SEM. (a), (b) Interaction on 0.6 µm hairy alginate. (a) Hairy alginate (dashed circle). Interaction of lamellipodia of spread fibroblast with alginate hairs (arrow), attached but not spread fibroblast (asterisk). Large membrane extensions by interaction with hairy alginate (arrow tip). (b) Closer view on interaction of lamellipodia with hairy alginate. (c), (d) Interaction on 2.0 µm hairy alginate. (c) Hairy alginate (dashed circle), attached and slightly spread fibroblast (asterisk) and spread fibroblast (hash) with interaction lamellipodia with hairy alginate (arrow). (d) Closer view on interaction of lamellipodia (arrows) with hairy alginate. The scale bars indicate 10 µm.

A detailed view on interacting fibroblasts by both, phase contrast (Figure 66) as well as SEM (Figure 67), reveals direct interaction of fibroblasts with the hairy alginate surface and textural features, helping to explain the summarized results in Figure 65. Our experiments show both, attached as well as spread fibroblasts. On native alginate hydrogels, attachment of cells is rarely observed (Figure 66 a) due to the physico-chemical properties. It is known that physico-chemical properties, such as negative charge and high hydrophilicity of alginate hydrogels,

forming a gel with calcium ions, inhibit adsorption of serum proteins and in consequence cell attachment and spreading [207]. The observed interactions of the fibroblasts can be explained with the filamentous nature of the surfaces. The hairs of the alginate sheets greatly increase the surface, which is shown to promote cellular interactions [83, 233]. Similarly, electrospun nanofibres made from polycaprolactone (PCL) significantly increased the adhesion of primary rat astrocytes, in comparison to a plain PCL surface [234]. Nonetheless, the filamentous shape does not in all cases increase adhesion. No differences were observed for electrospun meshes and non-fibrous surfaces for alginate [83], or PLA-based diblock copolymers with variable hydrophilic moieties [85].

Not only the geometry of the filament varies, also their abundance on the surface (fibre density) is different for each template dimension (5.4.1.1, Table 2) and contributes to the cellular response. The fibre density between the sheets structured with the 0.6 μm and 1.0 μm template is comparable, which is confirmed by statistical analysis; the differences in the fibre counts are insignificant (Table 2). On the contrary, the discrepancies with fibres from the 2.0 μm template are significant.

The assessment of the surface roughness is not simple. It is expected to be most pronounced for the delicate filaments formed from 0.6 μm templates, exhibiting the lowest moulding efficiency, because many filaments are cleaved during the peel-off (5.4.1.1, Table 2). The introduction of roughness through the rupture of the filaments may in parts also contribute to the observed trend. It has been reported that cellular adhesion of L929 fibroblasts could be increased due to plasma treatment (ionized gas) of the hydrogel alginate, destroying the molecular structure, as well as increasing the roughness [235]. The smaller the feature size in combination with the higher abundance of the filaments was (Table 2), the more adhesion

was observed in our study. These conditions lead to the observed trend of adhesion of fibroblasts to the hairy alginate sheets in the order 0.6 μm > 1.0 μm > 2.0 μm (Figure 65).

No study on elastic hydrogels, exhibiting a plain surface, carrying hairs in micron and submicron size range and implications on adhesion behaviour, has been performed so far. Grimm *et al.* [115] used the template technique for the structuring of elastic polymers forming surfaces, carrying highly homogenous pillars on which fibroblasts were seeded. The study cannot be directly compared because of the much higher abundance of the pillars and the difference in the composition of the pillars (structural core material poly(DL-lactide) (PDLLA), coated with the elastic hydrogels heparin and gelatin). The pillars in the study had a diameter of approximately 200 nm (lattice constant of ~ 500 nm) or bigger pillars in the micron size range (~ 1.3 μm diameter, 2 μm matrix arrangement), both exhibiting a high abundance of its posts. In fact, the tight spacing of the posts did not allow for interactions with the base layer; the cells spread and elongated on top of the pillars, no comparison with a plain surface was performed. In accordance with the results for the hairy alginate surfaces presented here, the bigger micron sized rods showed significantly less elongation and proliferation.

The feature size has been identified to be a major factor [236]. Ordered textures with nanopits (diameters 35 – 120 nm with a pitch between the features ranging from 100 – 300 nm) made from PCL, or polymethylmethacrylate (PMMA) showed the contrary effect. Adhesion of fibroblasts decreased, in contrast to less regular texture, or even the planar surface [237]. This observation shows that the arrangement, in addition to the geometry, impacts the cell-interface interactions.

Lehnert *et al.* studied the influence of the spatial distribution of biochemical patterns on surfaces and the corresponding cellular reaction. They found that cell spreading is limited if the distance of adjacent features is larger than 20 μm [238]. The results presented herein

imply a similar correlation between attachment and spreading of fibroblasts and the spatial feature distribution of filaments on hairy alginate surfaces. Most pronounced attachment of fibroblast was observed on surfaces with the highest feature densities (0.6 µm and 1.0 µm hairy surfaces) and thus shortest distances between adjacent structural features. The minimization of the distance between adjacent structural features, using tailored template membranes could be a valuable step towards improving the cellular response.

Numerous studies with fibroblasts have been performed on predominately stiff textured surface, exhibiting various geometries (grooves, wells, pits and pillars), down to the nanoscale [237, 239-242], mainly generated with photolithographic fabrication techniques derived from microsystems technology [114, 237, 239, 242]. Besides the size of the structure the shape has a vital influence, considering the so-called lotus effect [243]. Despite the increase of area for interaction through the introduction of the micro- and nanoscopic features in comparison to flat surfaces, cellular adhesion of fibroblasts was impeded [244]. Likewise, the decoding of trends holding true in general has been shown to be challenging [114].

Substrate elasticity is a key factor for cellular interactions, in particular for cell spreading [232, 245, 246]. The exerted forces by the cells can deform the substrate, depending on the rigidity of the material [118, 247]. This holds true for the hydrogel filaments; the deformation of single fibres has been observed during live cell imaging through the probing of the fibroblasts with their lamellipodia. The filaments are perceived as more elastic by the cell than the planar surface. The deformability of the fibres is expected to increase in the order 2.0 µm < 1.0 µm < 0.6 µm, describing yet another parameter for the enhancement of adhesion through hairy surfaces in the observed order. Elastic posts made from PDMS in a similar size range and abundance with our study (0.75 to 1.5 µm diameter, spacing between the pillars ranging from

1.5 to 4.5 µm) did not alter the fibroblast spreading, or adhesion in comparison to a flat, continuous surface; cells analogously interacted both with textured and plain surfaces [118]. In addition to the quantitative differences of the interaction of the fibroblasts with the surfaces with varying feature size, a correlation in orientation of fibroblast attachment as a function of orientation of the alginate filaments was observed in single experiments. Fibroblasts preferentially spread in direction of the main alignment of the filaments (Figure 66 b). This alignment of the fibres is caused by the direction of manual peel-off, as the last step of the hydrogel structuring. Cell orientation in response to micro- and nano-scaled texture has already been reported for fibroblasts. In these studies mainly stiff substrates in various geometries of the cavities, including grooves, wells, holes, have been scrutinized [114, 248]. Nonetheless, no study utilizing a filamentous surface, exhibiting a preferential orientation of the fibres, has been performed so far.

Results and Discussion

6   Summary

6.1   Summary

The template technique was selected for the generation of monodisperse fibres, intended for pulmonary administration. The deposition site in the inhalation tract is strongly governed by the geometry (size and shape) of the particle, whereas the precision of targeting is linked to their homogeneity. Since conventional carrier systems are not formed within precisely defined templates, such as the track-etched membranes with cylindrical pores used herein, the geometry is less defined. Despite their largely irregular shape, conventional carriers are described as spherical. Two major benefits of fibrous shape have been identified for pulmonary administration, promising advantages over conventional drug carriers. Firstly, the residence time of the therapeutic in the target region, the deep lung, is extended because of the shape and orientation dependent delay of cellular uptake. Secondly, the load of peripheral delivery is increased through fibrous shape; more material is transported per filament in comparison a spherical particle with identical diameter due to alignment in the airstream.

Experiments confirm that the engulfment exclusively occurred from the tips of the cylindrical particles, delaying the uptake until this orientation was reached by the phagocyte. The aerodynamic properties of the cylindrical particles depend on the diameter of the filaments and not on the length, which was constant for all tested filaments. Cylinders with lower diameter proceed to deeper stages in the impactor, implying alignment with the airstream.

The physiological conditions in the peripheral lung with scarce lining fluid, acting as the solvent, and low enzymatic activity of the fragile tissue largely restrict the selection of compounds for the design of pulmonary carriers. Only a few substances have been approved for this route of administration. Filamentous particles were formed from the FDA-approved excipient lactose, APIs and blends of various ratios. These cylinders dissolved instantaneously upon contact with aqueous media. In contrast, longer residence time is desired for prolonged

Summary

release systems. This can be achieved by the incorporation of hydrogels into the matrix of the cylindrical particles. The biocompatible hydrogel alginate, degrading as a function of the phosphate concentration, was utilized in order to form the backbone of the carrier system. This mode of degradation reduces the likelihood of detrimental long-term accumulation in the peripheral lung because phosphate is ubiquitous in the body.

The template technique allows for the embedding of NPs into the cylinders, too. These hierarchical microfibres were formed from silica NPs and were interconnected with biocompatible hydrogels (alginate and agarose). As a proof of concept, macrophage uptake experiments were performed in order to verify the paradigm of shape and orientation dependent uptake; this could be confirmed for fibres formed with the template technique.

Uptake was quantified using the novel correlative light and electron microscopy (CLEM). Through the combination of high resolution of EM and specificity of fluorescence, misleading quantification based upon the single techniques SEM and FLM could be corrected.

Additionally, the adaptation of the preparation protocol allows for a straightforward generation of hydrogel surfaces carrying fibres in high abundance and fidelity in various diameters and compositions. Literature reports about implications of surface structure on fundamental cell behaviour and functions. Consequently, the adhesion of murine alveolar fibroblasts was scrutinized on hairy alginate sheets with various dimensions and quantities of the filaments. The more abundant and more delicate the filaments were, the more adhesion was observed; in addition to a preferential alignment along the filaments. Without these fibres fibroblasts did not adhere to the alginate hydrogel surface.

Furthermore, the hairy sheets could be loaded with small molecules, as well as macromolecules; a fact that might proof beneficial for potential applications as a surrogate for the ECM, loading growth factors for instance. The release of these model compounds was quantified. It was depending on the molecular size and the phosphate concentration.

6.2 Zusammenfassung

Die sogenannte *template technique* (Templattechnik) wurde gewählt, um monodisperse Fasern zu erzeugen, die als Hilfsstoffsystem für die Lungenanwendung geeignet sind. Die Region der Abscheidung in der Lunge hängt in hohem Maße von der Geometrie der Partikel (Größe und Form) ab, wobei die Präzision des Targetings von deren Homogenität vorgegeben wird. Konventionelle Trägerstoffe für die Lungenanwendung werden nicht mit Hilfe von präzise definierten Templaten, wie die hier verwendeten *track-etched membranes* (Kernspurfilter) mit zylinderförmigen Poren, erzeugt, wodurch deren Geometrie weniger genau vorgegeben ist. Trotz deren größtenteils unregelmäßigen Form werden konventionelle Trägerstoffe als kugelförmig bezeichnet. Die faserförmigen Träger lassen in zwei wesentlichen Punkten auf Verbesserungen im Gegensatz zu konventionellen Trägern hoffen. Die Verweilzeit in der tiefen Lunge, der Zielregion für viele Inhalanda, kann durch die form- und orientierungsabhängige Aufnahme verlängert werden. Des Weiteren kann der Transport in die distalen Bereiche der Lunge durch die Faserform gesteigert werden. Bezogen auf ein faserförmiges Partikel wird im Vergleich zu kugelförmigen Partikeln gleichen Durchmessers mehr Substanz transportiert, weil sich die Fasern im Luftstrom ausrichten.

Die Experimente bestätigen, dass die Aufnahme der Zylinder lediglich von den Enden her erfolgt. Dies führt zu einer Verzögerung der Aufnahme, da die Phagozyten zunächst die korrekte Orientierung einnehmen müssen. Das aerodynamische Verhalten der zylinderförmigen Partikel hängt vom Durchmesser und nicht von deren Länge ab, welche konstant bei allen getesteten zylinderförmigen Partikeln war. Zylinder mit geringerem Durchmesser zeigen eine Verschiebung der Abscheidung hin zu geringeren aerodynamischen Durchmessern, was auf eine Ausrichtung der Fasern im Luftstrom schließen lässt.

Summary

Die physiologischen Gegebenheiten in der Region der Alveolen erschweren die Auswahl der Substanzen für das Design von Inhalanda-Trägersystemen. Es ist nur wenig Flüssigkeit vorhanden, die als Lösungsmittel dienen kann. Außerdem ist das empfindliche Gewebe enzymatisch nur in geringem Umfang aktiv. Aus diesen Gründen sind nur wenige Substanzen für die Lungenanwendung zugelassen. Faserförmige Partikel wurden aus Laktose, welche von der FDA für diese Anwendung zugelassen wurde, sowie Wirkstoffen und verschiedenen Mischungen hergestellt. Diese Zylinder lösten sich sofort nach Kontakt mit dem wässrigen Medium auf. Bei einem Trägersystem mit verlängerter Wirkstofffreigabe ist hingegen eine längere Verweilzeit erwünscht. Dies kann durch die Verwendung von Hydrogelen bei der Erzeugung der Zylinder erreicht werden; diese durchwirken die Zylinder und verändern so das Auflöseverhalten. Das biokompatible Alginatgel löst sich in Abhängigkeit der Phosphatkonzentration auf, wodurch die Gefahr einer schädlichen Anhäufung in der Lunge vermindert werden kann, weil Phosphat überall im Körper vorkommt. Darüber hinaus können die Zylinder auch aus Nanopartikeln hergestellt werden. Die Fasern wurden aus SiO_2-Partikeln geformt und mit biokompatiblen Hydrogelen (Alginat und Agarose) verknüpft. Als *proof of concept* wurden Aufnahmeexperimente mit Makrophagen durchgeführt, um zu überprüfen, ob auch bei den mit der Templattechnik erzeugten Fasern die Aufnahme form- und orientierungsabhängig verläuft. Dies konnte erfolgreich gezeigt werden.

Zur Quantifizierung der Zellaufnahme wurde eine Kombination aus Licht- und Elektronenmikroskopie (*correlative light and electron microscopy* (CLEM)) verwendet. Durch Kombination der hohen Auflösung der Elektronenmikroskopie und der Spezifizität von Fluoreszenztechniken konnten die fehlerbehafteten Ergebnisse der Einzeltechniken (SEM und Fluoreszenzlichtmikroskopie) korrigiert werden.

Darüber hinaus kann mit der Templattechnik auf einfache Art und Weise Oberflächen aus Hydrogelen erzeugt werden, die eine Vielzahl von Fasern hoher Homogenität tragen. Die Durchmesser der Fasern, sowie die Zusammensetzung können angepasst werden. Die Oberflächenbeschaffenheit hat laut Literatur einen entscheidenden Einfluss auf grundlegendes Verhalten und Funktionen von Zellen. Deshalb wurde das Adhäsionsverhalten von alveolaren Mausfibroblasten sowohl in Abhängigkeit vom Faserdurchmesser als auch von deren Häufigkeit untersucht. Je feiner und häufiger die Fasern vorkommen, desto mehr Adhäsion konnte beobachtet werden; zusätzlich zeigten die Fibroblasten eine bevorzugte Ausrichtung entlang der Fasern. Ohne Fasern auf der Oberfläche findet keine Adhäsion statt.

Die fasertragenden Oberflächen können zusätzlich mit Wirkstoffen beladen werden, sowohl niedermolekulare Verbindungen als auch Makromoleküle können verwendet werden. Diese Tatsache könnte sich bei der möglichen Anwendung der Oberflächen als Ersatz für die Extrazelluläre Matrix als vorteilhaft erweisen, etwa die Beladung mit Wachstumsfaktoren. Die Freisetzung der Modelsubstanzen wurde quantifiziert und hing sowohl vom Molekulargewicht als auch von der Phosphatkonzentration des Mediums ab.

Summary

7 References

1. Herd, H. et al., *Nanoparticle Geometry and Surface Orientation Influence Mode of Cellular Uptake.* Acs Nano, 2013. **7**(3): p. 1961-1973.

2. Yoo, J. W.; Doshi, N. and Mitragotri, S., *Endocytosis and Intracellular Distribution of PLGA Particles in Endothelial Cells: Effect of Particle Geometry.* Macromolecular Rapid Communications, 2010. **31**(2): p. 142-148.

3. Alemdaroglu, F. E.; Alemdaroglu, N. C.; Langguth, P. and Herrmann, A., *Cellular Uptake of DNA Block Copolymer Micelles with Different Shapes.* Macromolecular Rapid Communications, 2008. **29**(4): p. 326-329.

4. Park, J. H. et al., *Systematic Surface Engineering of Magnetic Nanoworms for in Vivo Tumor Targeting.* Small, 2009. **5**(6): p. 694-700.

5. Chithrani, B. D.; Ghazani, A. A. and Chan, W. C. W., *Determining the Size and Shape Dependence of Gold Nanoparticle Uptake into Mammalian Cells.* Nano Letters, 2006. **6**(4): p. 662-668.

6. Harris, L. G.; Mead, L.; Müller-Oberländer, E. and Richards, R. G., *Bacteria and Cell Cytocompatibility Studies on Coated Medical Grade Titanium Surfaces.* Journal of Biomedical Materials Research Part A, 2006. **78A**(1): p. 50-58.

7. Muro, S. et al., *Control of Endothelial Targeting and Intracellular Delivery of Therapeutic Enzymes by Modulating the Size and Shape of ICAM-1-Targeted Carriers.* Molecular Therapy, 2008. **16**(8): p. 1450-1458.

8. Park, J. H. et al., *Magnetic Iron Oxide Nanoworms for Tumor Targeting and Imaging.* Advanced Materials, 2008. **20**(9): p. 1630-+.

9. Arnida; Malugin, A. and Ghandehari, H., *Cellular Uptake and Toxicity of Gold Nanoparticles in Prostate Cancer Cells: A Comparative Study of Rods and Spheres.* Journal of Applied Toxicology, 2010. **30**(3): p. 212-217.

10. Chithrani, B. D. and Chan, W. C. W., *Elucidating the Mechanism of Cellular Uptake and Removal of Protein-Coated Gold Nanoparticles of Different Sizes and Shapes.* Nano Letters, 2007. **7**(6): p. 1542-1550.

11. Martin, C. R. and Kohli, P., *The Emerging Field of Nanotube Biotechnology.* Nature Reviews Drug Discovery, 2003. **2**(1): p. 29-37.

References

12.   Mitragotri, S. and Lahann, J., *Physical Approaches to Biomaterial Design.* Nature Materials, 2009. **8**(1): p. 15-23.

13.   Doshi, N. and Mitragotri, S., *Designer Biomaterials for Nanomedicine.* Advanced Functional Materials, 2009. **19**(24): p. 3843-3854.

14.   Mathaes, R.; Winter, G.; Engert, J. and Besheer, A., *Application of Different Analytical Methods for the Characterization of Non-Spherical Micro- and Nanoparticles.* Int J Pharm, 2013. **453**(2): p. 620-9.

15.   Daum, N.; Tscheka, C.; Neumeyer, A. and Schneider, M., *Novel Approaches for Drug Delivery Systems in Nanomedicine: Effects of Particle Design and Shape.* Wiley Interdisciplinary Reviews-Nanomedicine and Nanobiotechnology, 2012. **4**(1): p. 52-65.

16.   (WHO) World Health Organization, *Determination of Airborne Fibre Number Concentrations: A Recommended Method by Phase Contrast Optical Microscopy.* World Health Organization, Geneva, 1997.

17.   Oberdorster, G.; Oberdorster, E. and Oberdorster, J., *Nanotoxicology: An Emerging Discipline Evolving from Studies of Ultrafine Particles.* Environ Health Perspect, 2005. **113**(7): p. 823-39.

18.   Sturm, R. and Hofmann, W., *A Theoretical Approach to the Deposition and Clearance of Fibers with Variable Size in the Human Respiratory Tract.* Journal of Hazardous Materials, 2009. **170**(1): p. 210-218.

19.   Geng, Y. et al., *Shape Effects of Filaments Versus Spherical Particles in Flow and Drug Delivery.* Nature Nanotechnology, 2007. **2**(4): p. 249-255.

20.   Su, W. C. and Cheng, Y. S., *Deposition of Fiber in a Human Airway Replica.* Journal of Aerosol Science, 2006. **37**(11): p. 1429-1441.

21.   Castellanos, A.; Valverde, J. M.; Perez, A. T.; Ramos, A. and Watson, P. K., *Flow Regimes in Fine Cohesive Powders.* Physical Review Letters, 1999. **82**(6): p. 1156-1159.

22.   Champion, J. A. and Mitragotri, S., *Role of Target Geometry in Phagocytosis.* Proceedings of the National Academy of Sciences of the United States of America, 2006. **103**(13): p. 4930-4934.

23.   Champion, J. A. and Mitragotri, S., *Shape Induced Inhibition of Phagocytosis of Polymer Particles.* Pharmaceutical Research, 2009. **26**(1): p. 244-249.

24. Donaldson, K. et al., *Carbon Nanotubes: A Review of Their Properties in Relation to Pulmonary Toxicology and Workplace Safety.* Toxicological Sciences, 2006. **92**(1): p. 5-22.

25. Davis, J. M. G. and Jones, A. D., *Comparisons of the Pathogenicity of Long and Short Fibers of Chrysotile Asbestos in Rats.* British Journal of Experimental Pathology, 1988. **69**(5): p. 717-737.

26. Coin, P. G.; Roggli, V. L. and Brody, A. R., *Persistence of Long, Thin Chrysotile Asbestos Fibers in the Lungs of Rats.* Environmental Health Perspectives, 1994. **102**: p. 197-199.

27. Ozin, G. A., *Nanochemistry - Synthesis in Diminishing Dimensions.* Advanced Materials, 1992. **4**(10): p. 612-649.

28. Merkel, T. J. et al., *Scalable, Shape-Specific, Top-Down Fabrication Methods for the Synthesis of Engineered Colloidal Particles.* Langmuir, 2010. **26**(16): p. 13086-13096.

29. Decuzzi, P.; Pasqualini, R.; Arap, W. and Ferrari, M., *Intravascular Delivery of Particulate Systems: Does Geometry Really Matter?* Pharmaceutical Research, 2009. **26**(1): p. 235-243.

30. Simone, E. A.; Dziubla, T. D. and Muzykantov, V. R., *Polymeric Carriers: Role of Geometry in Drug Delivery.* Expert Opinion on Drug Delivery, 2008. **5**(12): p. 1283-1300.

31. Sau, T. K. and Murphy, C. J., *Seeded High Yield Synthesis of Short Au Nanorods in Aqueous Solution.* Langmuir, 2004. **20**(15): p. 6414-6420.

32. Hutter, E. et al., *Microglial Response to Gold Nanoparticles.* Acs Nano, 2010. **4**(5): p. 2595-2606.

33. Decuzzi, P. et al., *Size and Shape Effects in the Biodistribution of Intravascularly Injected Particles.* Journal of Controlled Release, 2010. **141**(3): p. 320-327.

34. Spector, M. S. et al., *Controlling the Morphology of Chiral Lipid Tubules.* Langmuir, 1998. **14**(13): p. 3493-3500.

35. Reum, N. et al., *Multilayer Coating of Gold Nanoparticles with Drug-Polymer Coadsorbates.* Langmuir, 2010. **26**(22): p. 16901-16908.

36. Labouta, H. I. and Schneider, M., *Tailor-Made Biofunctionalized Nanoparticles Using Layer-by-Layer Technology.* International Journal of Pharmaceutics, 2010. **395**(1-2): p. 236-242.

References

37. Nikoobakht, B. and El-Sayed, M. A., *Preparation and Growth Mechanism of Gold Nanorods (NRs) Using Seed-Mediated Growth Method.* Chemistry of Materials, 2003. **15**(10): p. 1957-1962.

38. Barbosa, S. et al., *Tuning Size and Sensing Properties in Colloidal Gold Nanostars.* Langmuir, 2010. **26**(18): p. 14943-14950.

39. Stober, W.; Fink, A. and Bohn, E., *Controlled Growth of Monodisperse Silica Spheres in Micron Size Range.* Journal of Colloid and Interface Science, 1968. **26**(1): p. 62-&.

40. Arriagada, F. J. and Osseo-Asare, K., *Synthesis of Nanosize Silica in a Nonionic Water-in-Oil Microemulsion: Effects of the Water/Surfactant Molar Ratio and Ammonia Concentration.* Journal of Colloid and Interface Science, 1999. **211**(2): p. 210-220.

41. Galarneau, A.; Desplantier, D.; Dutartre, R. and Di Renzo, F., *Micelle-Templated Silicates as a Test Bed for Methods of Mesopore Size Evaluation.* Microporous and Mesoporous Materials, 1999. **27**(2-3): p. 297-308.

42. Wang, W.; Gu, B. H.; Liang, L. Y. and Hamilton, W., *Fabrication of Two- and Three-Dimensional Silica Nanocolloidal Particle Arrays.* Journal of Physical Chemistry B, 2003. **107**(15): p. 3400-3404.

43. Huh, S.; Wiench, J. W.; Yoo, J. C.; Pruski, M. and Lin, V. S. Y., *Organic Functionalization and Morphology Control of Mesoporous Silicas via a Co-Condensation Synthesis Method.* Chemistry of Materials, 2003. **15**(22): p. 4247-4256.

44. van Dillen, T.; Polman, A.; van Kats, C. M. and van Blaaderen, A., *Ion Beam-Induced Anisotropic Plastic Deformation at 300 keV.* Applied Physics Letters, 2003. **83**(21): p. 4315-4317.

45. Son, S. J.; Bai, X.; Nan, A.; Ghandehari, H. and Lee, S. B., *Template Synthesis of Multifunctional Nanotubes for Controlled Release.* Journal of Controlled Release, 2006. **114**(2): p. 143-152.

46. Mitchell, D. T. et al., *Smart Nanotubes for Bioseparations and Biocatalysis.* Journal of the American Chemical Society, 2002. **124**(40): p. 11864-11865.

47. Schnur, J. M. et al., *Diacetylenic Lipid Tubules - Experimental-Evidence for a Chiral Molecular Architecture.* Science, 1994. **264**(5161): p. 945-947.

48. Discher, D. E. and Eisenberg, A., *Polymer Vesicles.* Science, 2002. **297**(5583): p. 967-973.

49.   Walther, A. et al., *Self-Assembly of Janus Cylinders into Hierarchical Superstructures.* Journal of the American Chemical Society, 2009. **131**(13): p. 4720-4728.

50.   Cecutti, C.; Focher, B.; Perly, B. and Zemb, T., *Glycolipid Self-Assembly - Micellar Structure.* Langmuir, 1991. **7**(11): p. 2580-2585.

51.   Almgren, M., *Mixed Micelles and Other Structures in the Solubilization of Bilayer Lipid Membranes by Surfactants.* Biochimica Et Biophysica Acta-Biomembranes, 2000. **1508**(1-2): p. 146-163.

52.   Walsh, D.; Arcelli, L.; Ikoma, T.; Tanaka, J. and Mann, S., *Dextran Templating for the Synthesis of Metallic and Metal Oxide Sponges.* Nature Materials, 2003. **2**(6): p. 386-U5.

53.   DeVries, G. A. et al., *Divalent Metal Nanoparticles.* Science, 2007. **315**(5810): p. 358-361.

54.   Sukhorukov, G. B. et al., *Stepwise Polyelectrolyte Assembly on Particle Surfaces: A Novel Approach to Colloid Design.* Polymers for Advanced Technologies, 1998. **9**(10-11): p. 759-767.

55.   Doshi, N.; Zahr, A. S.; Bhaskar, S.; Lahann, J. and Mitragotri, S., *Red Blood Cell-Mimicking Synthetic Biomaterial Particles.* Proceedings of the National Academy of Sciences of the United States of America, 2009. **106**(51): p. 21495-21499.

56.   Lee, W.; Ji, R.; Gosele, U. and Nielsch, K., *Fast Fabrication of Long-Range Ordered Porous Alumina Membranes by Hard Anodization.* Nature Materials, 2006. **5**(9): p. 741-747.

57.   Hulteen, J. C. and Martin, C. R., *A General Template-Based Method for the Preparation of Nanomaterials.* Journal of Materials Chemistry, 1997. **7**(7): p. 1075-1087.

58.   Acharya, G. et al., *The Hydrogel Template Method for Fabrication of Homogeneous Nano/Microparticles.* Journal of Controlled Release, 2010. **141**(3): p. 314-319.

59.   Rolland, J. P. et al., *Direct Fabrication and Harvesting of Monodisperse, Shape-Specific Nanobiomaterials.* Journal of the American Chemical Society, 2005. **127**(28): p. 10096-10100.

60.   Dendukuri, D.; Pregibon, D. C.; Collins, J.; Hatton, T. A. and Doyle, P. S., *Continuous-Flow Lithography for High-Throughput Microparticle Synthesis.* Nature Materials, 2006. **5**(5): p. 365-369.

References

61. Martin, C. R., *Nanomaterials - a Membrane-Based Synthetic Approach.* Science, 1994. **266**(5193): p. 1961-1966.

62. Cepak, V. M. and Martin, C. R., *Preparation of Polymeric Micro- and Nanostructures Using a Template-Based Deposition Method.* Chemistry of Materials, 1999. **11**(5): p. 1363-1367.

63. Apel, P., *Track Etching Technique in Membrane Technology.* Radiation Measurements, 2001. **34**(1-6): p. 559-566.

64. Foss, C. A.; Hornyak, G. L.; Stockert, J. A. and Martin, C. R., *Template-Synthesized Nanoscopic Gold Particles - Optical-Spectra and the Effects of Particle-Size and Shape.* Journal of Physical Chemistry, 1994. **98**(11): p. 2963-2971.

65. Kohli, P. et al., *DNA-Functionalized Nanotube Membranes with Single-Base Mismatch Selectivity.* Science, 2004. **305**(5686): p. 984-986.

66. Kohler, D. et al., *Template-Assisted Polyelectrolyte Encapsulation of Nanoparticles into Dispersible, Hierarchically Nanostructured Microfibers.* Advanced Materials, 2011. **23**(11): p. 1376-1379.

67. Xia, Y. N. and Whitesides, G. M., *Soft Lithography.* Annual Review of Materials Science, 1998. **28**: p. 153-184.

68. Perry, J. L.; Herlihy, K. P.; Napier, M. E. and Desimone, J. M., *Print: A Novel Platform toward Shape and Size Specific Nanoparticle Theranostics.* Acc Chem Res, 2011. **44**(10): p. 990-8.

69. Kelly, J. Y. and DeSimone, J. M., *Shape-Specific, Monodisperse Nano-Molding of Protein Particles.* Journal of the American Chemical Society, 2008. **130**(16): p. 5438-+.

70. Gratton, S. E. A. et al., *The Effect of Particle Design on Cellular Internalization Pathways.* Proceedings of the National Academy of Sciences of the United States of America, 2008. **105**(33): p. 11613-11618.

71. Williams, S. S. et al., *High-Resolution PFPE-Based Molding Techniques for Nanofabrication of High-Pattern Density, Sub-20 nm Features: A Fundamental Materials Approach.* Nano Letters, 2010. **10**(4): p. 1421-1428.

72. Wang, Y. P. et al., *Generation of a Library of Particles Having Controlled Sizes and Shapes via the Mechanical Elongation of Master Templates.* Langmuir, 2011. **27**(2): p. 524-528.

73. Glangchai, L. C.; Caldorera-Moore, M.; Shi, L. and Roy, K., *Nanoimprint Lithography Based Fabrication of Shape-Specific, Enzymatically-Triggered Smart Nanoparticles.* Journal of Controlled Release, 2008. **125**(3): p. 263-272.

74. Iijima, S., *Helical Microtubules of Graphitic Carbon.* Nature, 1991. **354**(6348): p. 56-58.

75. Liu, Z. et al., *In Vivo Biodistribution and Highly Efficient Tumour Targeting of Carbon Nanotubes in Mice.* Nature Nanotechnology, 2007. **2**(1): p. 47-52.

76. Nafee, N.; Bhardwaj, V. and Schneider, M., *Transport across Biological Barriers* in *Nanotherapeutics - Drug Delivery Concepts in Nanosciences*, A. Lamprecht, Editor. 2008, WSPC: Singapore.

77. Zheng, L. X. et al., *Ultralong Single-Wall Carbon Nanotubes.* Nature Materials, 2004. **3**(10): p. 673-676.

78. Singh, R. et al., *Tissue Biodistribution and Blood Clearance Rates of Intravenously Administered Carbon Nanotube Radiotracers.* Proceedings of the National Academy of Sciences of the United States of America, 2006. **103**(9): p. 3357-3362.

79. Ho, C. C.; Keller, A.; Odell, J. A. and Ottewill, R. H., *Preparation of Monodisperse Ellipsoidal Polystyrene Particles.* Colloid and Polymer Science, 1993. **271**(5): p. 469-479.

80. Champion, J. A.; Katare, Y. K. and Mitragotri, S., *Making Polymeric Micro- and Nanoparticles of Complex Shapes.* Proceedings of the National Academy of Sciences of the United States of America, 2007. **104**(29): p. 11901-11904.

81. Yoo, J. W. and Mitragotri, S., *Polymer Particles that Switch Shape in Response to a Stimulus.* Proceedings of the National Academy of Sciences of the United States of America, 2010. **107**(25): p. 11205-11210.

82. Greiner, A. and Wendorff, J. H., *Electrospinning: A Fascinating Method for the Preparation of Ultrathin Fibres.* Angewandte Chemie-International Edition, 2007. **46**(30): p. 5670-5703.

83. Jeong, S. I.; Krebs, M. D.; Bonino, C. A.; Khan, S. A. and Alsberg, E., *Electrospun Alginate Nanofibers with Controlled Cell Adhesion for Tissue Engineering.* Macromolecular Bioscience, 2010. **10**(8): p. 934-943.

84. Bhattarai, N.; Li, Z.; Edmondson, D. and Zhang, M., *Alginate-Based Nanofibrous Scaffolds: Structural, Mechanical, and Biological Properties.* Advanced Materials, 2006. **18**(11): p. 1463-1467.

References

85.   Viswanathan, P. et al., *Controlling Surface Topology and Functionality of Electrospun Fibers Using Amphiphilic Block Copolymers to Direct Mesenchymal Progenitor Cell Adhesion.* Biomacromolecules, 2014.

86.   Herd, H. L.; Malugin, A. and Ghandehari, H., *Silica Nanoconstruct Cellular Toleration Threshold in Vitro.* Journal of Controlled Release, 2011. **153**(1): p. 40-48.

87.   Rejman, J.; Oberle, V.; Zuhorn, I. S. and Hoekstra, D., *Size-Dependent Internalization of Particles via the Pathways of Clathrin-and Caveolae-Mediated Endocytosis.* Biochemical Journal, 2004. **377**: p. 159-169.

88.   Hillaireau, H. and Couvreur, P., *Nanocarriers' Entry into the Cell: Relevance to Drug Delivery.* Cellular and Molecular Life Sciences, 2009. **66**(17): p. 2873-2896.

89.   Marsh, M., *Endocytosis*. Frontiers in Molecular Biology, ed. D.M.G. B. D. Hames. 2001: Oxford University Press.

90.   May, R. C. and Machesky, L. M., *Phagocytosis and the Actin Cytoskeleton.* J Cell Sci, 2001. **114**(Pt 6): p. 1061-77.

91.   Cossart, P., *Subversion of the Mammalian Cell Cytoskeleton by Invasive Bacteria.* Journal of Clinical Investigation, 1997. **100**(12): p. S33-S37.

92.   Merril, C. R. et al., *Long-Circulating Bacteriophage as Antibacterial Agents.* Proceedings of the National Academy of Sciences of the United States of America, 1996. **93**(8): p. 3188-3192.

93.   Albanese, A.; Sykes, E. A. and Chan, W. C. W., *Rough around the Edges: The Inflammatory Response of Microglial Cells to Spiky Nanoparticles.* Acs Nano, 2010. **4**(5): p. 2490-2493.

94.   Meng, H. et al., *Aspect Ratio Determines the Quantity of Mesoporous Silica Nanoparticle Uptake by a Small GTPase-Dependent Macropinocytosis Mechanism.* Acs Nano, 2011. **5**(6): p. 4434-4447.

95.   Decuzzi, P. and Ferrari, M., *The Receptor-Mediated Endocytosis of Nonspherical Particles.* Biophysical Journal, 2008. **94**(10): p. 3790-3797.

96.   Mo, Y. Q.; Zhu, X. Q.; Hu, X.; Tollerud, D. J. and Zhang, Q. W., *Cytokine and NO Release from Peripheral Blood Neutrophils after Exposure to Metal Nanoparticles: In Vitro and Ex Vivo Studies.* Nanotoxicology, 2008. **2**(2): p. 79-87.

97. Moghimi, S. M. and Szebeni, J., *Stealth Liposomes and Long Circulating Nanoparticles: Critical Issues in Pharmacokinetics, Opsonization and Protein-Binding Properties.* Progress in Lipid Research, 2003. **42**(6): p. 463-478.

98. Klibanov, A. L.; Maruyama, K.; Torchilin, V. P. and Huang, L., *Amphipathic Polyethyleneglycols Effectively Prolong the Circulation Time of Liposomes.* Febs Letters, 1990. **268**(1): p. 235-237.

99. Slowing, I.; Trewyn, B. G. and Lin, V. S. Y., *Effect of Surface Functionalization of MCM-41-Type Mesoporous Silica Nanoparticleson the Endocytosis by Human Cancer Cells.* Journal of the American Chemical Society, 2006. **128**(46): p. 14792-14793.

100. Hauck, T. S.; Ghazani, A. A. and Chan, W. C. W., *Assessing the Effect of Surface Chemistry on Gold Nanorod Uptake, Toxicity, and Gene Expression in Mammalian Cells.* Small, 2008. **4**(1): p. 153-159.

101. Decuzzi, P. and Ferrari, M., *The Adhesive Strength of Non-Spherical Particles Mediated by Specific Interactions.* Biomaterials, 2006. **27**(30): p. 5307-5314.

102. Mammen, M.; Choi, S. K. and Whitesides, G. M., *Polyvalent Interactions in Biological Systems: Implications for Design and Use of Multivalent Ligands and Inhibitors.* Angewandte Chemie-International Edition, 1998. **37**(20): p. 2755-2794.

103. Doshi, N. et al., *Flow and Adhesion of Drug Carriers in Blood Vessels Depend on Their Shape: A Study Using Model Synthetic Microvascular Networks.* Journal of Controlled Release, 2010. **146**(2): p. 196-200.

104. Gavze, E. and Shapiro, M., *Motion of Inertial Spheroidal Particles in a Shear Flow near a Solid Wall with Special Application to Aerosol Transport in Microgravity.* Journal of Fluid Mechanics, 1998. **371**: p. 59-79.

105. Gentile, F. et al., *The Effect of Shape on the Margination Dynamics of Non-Neutrally Buoyant Particles in Two-Dimensional Shear Flows.* Journal of Biomechanics, 2008. **41**(10): p. 2312-2318.

106. Moghimi, S. M.; Hunter, A. C. and Murray, J. C., *Long-Circulating and Target-Specific Nanoparticles: Theory to Practice.* Pharmacological Reviews, 2001. **53**(2): p. 283-318.

107. Li, S. L.; Nickels, J. and Palmer, A. F., *Liposome-Encapsulated Actin-Hemoglobin (LEAcHb) Artificial Blood Substitutes.* Biomaterials, 2005. **26**(17): p. 3759-3769.

108. Chien, S., *Red-Cell Deformability and Its Relevance to Blood-Flow.* Annual Review of Physiology, 1987. **49**: p. 177-192.

109. Harris, A. et al., *Influenza Virus Pleiomorphy Characterized by Cryoelectron Tomography.* Proceedings of the National Academy of Sciences of the United States of America, 2006. **103**(50): p. 19123-19127.

110. Nan, A. J.; Bai, X.; Son, S. J.; Lee, S. B. and Ghandehari, H., *Cellular Uptake and Cytotoxicity of Silica Nanotubes.* Nano Letters, 2008. **8**(8): p. 2150-2154.

111. Karp, G., in *Cell Biology International Student Version*. 2010, Wiley. p. 411-443.

112. Théry, M. et al., *Anisotropy of Cell Adhesive Microenvironment Governs Cell Internal Organization and Orientation of Polarity.* Proceedings of the National Academy of Sciences, 2006. **103**(52): p. 19771-19776.

113. Kim, D. H.; Provenzano, P. P.; Smith, C. L. and Levchenko, A., *Matrix Nanotopography as a Regulator of Cell Function.* Journal of Cell Biology, 2012. **197**(3): p. 351-360.

114. Martinez, E.; Engel, E.; Planell, J. A. and Samitier, J., *Effects of Artificial Micro- and Nano-Structured Surfaces on Cell Behaviour.* Annals of Anatomy-Anatomischer Anzeiger, 2009. **191**(1): p. 126-135.

115. Grimm, S. et al., *Cellular Interactions of Biodegradable Nanorod Arrays Prepared by Nondestructive Extraction from Nanoporous Alumina.* Journal of Materials Chemistry, 2010. **20**(16): p. 3171-3177.

116. McUsic, A. C.; Lamba, D. A. and Reh, T. A., *Guiding the Morphogenesis of Dissociated Newborn Mouse Retinal Cells and hES Cell-Derived Retinal Cells by Soft Lithography-Patterned Microchannel PLGA Scaffolds.* Biomaterials, 2012. **33**(5): p. 1396-1405.

117. Rice, J. M. et al., *Quantitative Assessment of the Response of Primary Derived Human Osteoblasts and Macrophages to a Range of Nanotopography Surfaces in a Single Culture Model in Vitro.* Biomaterials, 2003. **24**(26): p. 4799-4818.

118. Yang, M. T.; Sniadecki, N. J. and Chen, C. S., *Geometric Considerations of Micro- to Nanoscale Elastomeric Post Arrays to Study Cellular Traction Forces.* Advanced Materials, 2007. **19**(20): p. 3119-+.

119. Geim, A. K. et al., *Microfabricated Adhesive Mimicking Gecko Foot-Hair.* Nature Materials, 2003. **2**(7): p. 461-463.

120. Whitesides, G. M.; Ostuni, E.; Takayama, S.; Jiang, X. Y. and Ingber, D. E., *Soft Lithography in Biology and Biochemistry.* Annual Review of Biomedical Engineering, 2001. **3**: p. 335-373.

121. del Campo, A.; Greiner, C. and Arzt, E., *Contact Shape Controls Adhesion of Bioinspired Fibrillar Surfaces.* Langmuir, 2007. **23**(20): p. 10235-10243.

122. Greiner, C.; del Campo, A. and Arzt, E., *Adhesion of Bioinspired Micropatterned Surfaces: Effects of Pillar Radius, Aspect Ratio, and Preload.* Langmuir, 2007. **23**(7): p. 3495-3502.

123. Vozzi, G.; Flaim, C.; Ahluwalia, A. and Bhatia, S., *Fabrication of PLGA Scaffolds Using Soft Lithography and Microsyringe Deposition.* Biomaterials, 2003. **24**(14): p. 2533-2540.

124. Lemons, B. D.; Ratner, A. S.; Hoffman, F. J. and E., S. J., *A History of Biomaterials*, in *Biomaterials Science (Third Edition)*. 2013, Academic Press. p. xli-liii.

125. Yeom, J.; Wu, Y.; Selby, J. C. and Shannon, M. A., *Maximum Achievable Aspect Ratio in Deep Reactive Ion Etching of Silicon Due to Aspect Ratio Dependent Transport and the Microloading Effect.* Journal of Vacuum Science & Technology B, 2005. **23**(6): p. 2319-2329.

126. Thews, M., Vaupel, *Respirationstrakt und Atmung*, in *Anatomie, Physiologie, Pathophysiologie des Menschen*. 1999. p. 265-311.

127. *Gray's Anatomy : The Anatomical Basis of Clinical Practice / Editor-in-Chief, Susan Standring*, ed. S. Standring and H.A. Gray. 2008, Edinburgh: Churchill Livingstone.

128. Klinke R., P. H. C., Silbernagel S., *Physiologie*. 2005: Georg Thieme Verlag, Stuttgart.

129. G., T., *Anatomie, Physiologie, Pathophysiologie des Menschen*. 2007: Wissenschaftliche Verlagsgesellschaft Stuttgart, Stuttgart.

130. Ruge, C. A.; Kirch, J. and Lehr, C.-M., *Pulmonary Drug Delivery: from Generating Aerosols to Overcoming Biological Barriers-Therapeutic Possibilities and Technological Challenges.* The Lancet. Respiratory medicine, 2013. **1**(5).

131. Patton, J. S. and Byron, P. R., *Inhaling Medicines: Delivering Drugs to the Body through the Lungs.* Nat Rev Drug Discov, 2007. **6**(1): p. 67-74.

132. Patton, J. S.; Fishburn, C. S. and Weers, J. G., *The Lungs as a Portal of Entry for Systemic Drug Delivery.* Proceedings of the American Thoracic Society, 2004. **1**(4).

133. Gehr, P. and Heyder, J., *Particle-Lung Interactions*. 2000, New York, Basel: Marcel Dekker Inc.

134. Hinds, W. C., *Aerosol Technology - Properties, Behavior, and Measurement of Airborne Particles*. Vol. 2nd Edition. 1999, Toronto: John Wiley & Sons.

135. Dolovich, M. A. et al., *Consensus Statement: Aerosols and Delivery Devices. American Association for Respiratory Care.* Respiratory care, 2000. **45**(6).

136. Heyder, J., *Deposition of Inhaled Particles in the Human Respiratory Tract and Consequences for Regional Targeting in Respiratory Drug Delivery.* Proceedings of the American Thoracic Society, 2004. **1**(4).

137. Shekunov, B. Y.; Chattopadhyay, P.; Tong, H. H. Y. and Chow, A. H. L., *Particle Size Analysis in Pharmaceutics: Principles, Methods and Applications.* Pharmaceutical Research, 2007. **24**(2): p. 203-227.

138. Mitchell, J.; Newman, S. and Chan, H.-K., *In Vitro and in Vivo Aspects of Cascade Impactor Tests and Inhaler Performance: A Review.* AAPS PharmSciTech, 2007. **8**(4).

139. Andersen, A. A., *New Sampler for the Collection, Sizing, and Enumeration of Viable Airborne Particles.* Journal of Bacteriology, 1958. **76**(5): p. 471-484.

140. Kohler, D. A. L., *Asymmetric Particles for Pulmonary Drug Delivery*, in *Naturwissenschaftlich-Technischen Fakultaet III Chemie, Pharmazie, Bio- und Werkstoffwissenschaften*. 2010, Universitaet des Saarlandes: Saarbruecken.

141. May, S., *Dissolution Testing of Powders for Inhalation*, in *Naturwissenschaftlich-Technischen Fakultaet III Chemie, Pharmazie, Bio- und Werkstoffwissenschaften*. 2013, Universitaet des Saarlandes: Saarbruecken.

142. Hsu, S. H. and Sigmund, W. M., *Artificial Hairy Surfaces with a Nearly Perfect Hydrophobic Response.* Langmuir, 2010. **26**(3): p. 1504-1506.

143. Zimmermann, H. et al., *Physical and Biological Properties of Barium Cross-Linked Alginate Membranes.* Biomaterials, 2007. **28**(7): p. 1327-1345.

144. Zimmermann, H. et al., *Towards a Medically Approved Technology for Alginate-Based Microcapsules Allowing Long-Term Immunoisolated Transplantation.* J. Mater. Sci.: Mater. Med., 2005. **16**(6): p. 491-501.

145. Rodríguez, M. C.; Matulewicz, M. C.; Noseda, M. D.; Ducatti, D. R. B. and Leonardi, P. I., *Agar from Gracilaria Gracilis (Gracilariales, Rhodophyta) of the Patagonic Coast of Argentina – Content, Structure and Physical Properties.* Bioresource Technology, 2009. **100**(3): p. 1435-1441.

146. Pluen, A.; Netti, P. A.; Jain, R. K. and Berk, D. A., *Diffusion of Macromolecules in Agarose Gels: Comparison of Linear and Globular Configurations.* Biophysical Journal, 1999. **77**(1): p. 542-552.

147. Stellwagen, N. C. and Stellwagen, E., *Effect of the Matrix on DNA Electrophoretic Mobility.* Journal of Chromatography A, 2009. **1216**(10): p. 1917-1929.

148. Schwartz, D. C. and Cantor, C. R., *Separation of Yeast Chromosome-Sized DNAs by Pulsed Field Gradient Gel-Electrophoresis.* Cell, 1984. **37**(1): p. 67-75.

149. Zimmermann, H.; Shirley, S. G.; Zimmermann, U. and others, *Alginate-Based Encapsulation of Cells: Past, Present, and Future.* Curr. Diab. Rep., 2007. **7**(4): p. 314-314.

150. Rowley, J. A.; Madlambayan, G. and Mooney, D. J., *Alginate Hydrogels as Synthetic Extracellular Matrix Materials.* Biomaterials, 1999. **20**(1): p. 45-53.

151. Gacesa, P., *Alginates.* Carbohydrate Polymers, 1988. **8**(3): p. 161-182.

152. Gunday Tureli, N.; Tureli, A. E. and Schneider, M., *Inhalable Antibiotic Nanoformulations for the Treatment of Pseudomonas Aeruginosa Infection in Cystic Fibrosis – a Review.* Drug Delivery Letters, 2013. **4**(3): p. 193-207.

153. Augst, A. D.; Kong, H. J. and Mooney, D. J., *Alginate Hydrogels as Biomaterials.* Macromolecular Bioscience, 2006. **6**(8): p. 623-633.

154. Li, L.; Fang, Y.; Vreeker, R.; Appelqvist, I. and Mendes, E., *Reexamining the Egg-Box Model in Calcium-Alginate Gels with X-Ray Diffraction.* Biomacromolecules, 2007. **8**(2): p. 464-8.

155. Smidsrod, O., *Molecular Basis for Some Physical Properties of Alginates in the Gel State.* Faraday Discussions of the Chemical Society, 1974. **57**(0): p. 263-274.

156. Zimmermann, U. et al., *A Novel Class of Amitogenic Alginate Microcapsules for Long-Term Immunoisolated Transplantation.* Ann. N. Y. Acad. Sci., 2001. **944**(1): p. 199-215.

157. Töpel, A., *Chemie und Physik der Milch: Naturstoff, Rohstoff, Lebensmittel*. 2007: Behr's Verlag.

158. Machado, J. J. B.; Coutinho, J. A. and Macedo, E. A., *Solid–Liquid Equilibrium of A-Lactose in Ethanol/Water.* Fluid Phase Equilibria, 2000. **173**(1): p. 121-134.

159. Haase, G. and Nickerson, T. A., *Kinetic Reactions of Alpha and Beta Lactose. I. Mutarotation1.* Journal of Dairy Science. **49**(2): p. 127-132.

160. Marple, V. A. et al., *Next Generation Pharmaceutical Impactor (a New Impactor for Pharmaceutical Inhaler Testing). Part I: Design.* Journal of Aerosol Medicine-Deposition Clearance and Effects in the Lung, 2003. **16**(3): p. 283-299.

References

161. Marple, V. A. et al., *Next Generation Pharmaceutical Impactor (a New Impactor for Pharmaceutical Inhaler Testing). Part II: Archival Calibration.* Journal of Aerosol Medicine-Deposition Clearance and Effects in the Lung, 2003. **16**(3): p. 301-324.

162. Marple, V. A. et al., *Next Generation Pharmaceutical Impactor: A New Impactor for Pharmaceutical Inhaler Testing. Part III. Extension of Archival Calibration to 15 l/min.* Journal of Aerosol Medicine-Deposition Clearance and Effects in the Lung, 2004. **17**(4): p. 335-343.

163. *Preparations for Inhalation: Aerodynamic Assessment of Fine Particles*, in *European Pharmacopoeia 8th Edition, Supplement 8.7*. 2016.

164. *Inhalation and Nasal Drug Products: Aerosols, Sprays, and Powders—Performance Quality Tests*, in *United States Pharmacopoeia and the National Formulary (USP 39– NF 34)*.

165. Leichner, C., *Etablierung des Next Generation Impactor (NGI) und Untersuchung neuer pulmonaler Formulierungen*, in *Naturwissenschaftlich-Technischen Fakultät III Chemie, Pharmazie, Bio- und Werkstoffwissenschaften*. 2013, Universität des Saarlandes: Saarbrücken.

166. Klingler, C., *Insulin Mikro- Und Nanopartikel zur pulmonalen Applikation*, in *Mathematisch-Naturwissenschaftliche Fakultaet*. 2009, Christian-Albrechts-Universitaet: Kiel.

167. Michalet, X. et al., *Quantum Dots for Live Cells, in Vivo Imaging, and Diagnostics.* Science, 2005. **307**(5709): p. 538-544.

168. Fernandez, T. D. et al., *Intracellular Accumulation and Immunological Properties of Fluorescent Gold Nanoclusters in Human Dendritic Cells.* Biomaterials, 2015. **43**.

169. Le Guevel, X. et al., *Ligand Effect on the Size, Valence State and Red/Near Infrared Photoluminescence of Bidentate Thiol Gold Nanoclusters.* Nanoscale, 2014. **6**(14): p. 8091-8099.

170. Le Guevel, X.; Daum, N. and Schneider, M., *Synthesis and Characterization of Human Transferrin-Stabilized Gold Nanoclusters.* Nanotechnology, 2011. **22**(27).

171. Patel, H.; Tscheka, C. and Heerklotz, H., *Characterizing Vesicle Leakage by Fluorescence Lifetime Measurements.* Soft Matter, 2009. **5**(15): p. 2849-2851.

172. Kopelman, R. and Tan, W. H., *Near-Field Optics - Imaging Single Molecules.* Science, 1993. **262**(5138): p. 1382-1384.

173. Hell, S. W. and Wichmann, J., *Breaking the Diffraction Resolution Limit by Stimulated Emission: Stimulated-Emission-Depletion Fluorescence Microscopy.* Optics Letters, 1994. **19**(11): p. 780-782.

174. Rust, M. J.; Bates, M. and Zhuang, X. W., *Sub-Diffraction-Limit Imaging by Stochastic Optical Reconstruction Microscopy (Storm).* Nature Methods, 2006. **3**(10): p. 793-795.

175. Haider, M. et al., *Electron Microscopy Image Enhanced.* Nature, 1998. **392**(6678): p. 768-769.

176. Jahn, K. A. et al., *Correlative Microscopy: Providing New Understanding in the Biomedical and Plant Sciences.* Micron, 2012. **43**(5): p. 565-582.

177. Sjollema, K. A.; Schnell, U.; Kuipers, J.; Kalicharan, R. and Giepmans, B. N. G., *Correlated Light Microscopy and Electron Microscopy*, in *Correlative Light and Electron Microscopy*, T. Muller-Reichert and P. Verkade, Editors. 2012, Elsevier Academic Press Inc: San Diego. p. 157-173.

178. Hermsdörfer, A.; Madl, J. and Römer, W., *Combination of High-Resolution AFM with Super-Resolution Stochastic Optical Reconstruction Microscopy (Storm)*. 2013, JPK Instuments AG. p. 1-9.

179. Stukalov, O.; Korenevsky, A.; Beveridge, T. J. and Dutcher, J. R., *Use of Atomic Force Microscopy and Transmission Electron Microscopy for Correlative Studies of Bacterial Capsules.* Applied and Environmental Microbiology, 2008. **74**(17): p. 5457-5465.

180. Labernadie, A.; Thibault, C.; Vieu, C.; Maridonneau-Parini, I. and Charriere, G. M., *Dynamics of Podosome Stiffness Revealed by Atomic Force Microscopy.* Proceedings of the National Academy of Sciences of the United States of America, 2010. **107**(49): p. 21016-21021.

181. *Combining AFM with Super-Resolution STED (Stimulated Emission Depletion) Microscopy System - Technical Note*. JPK Instruments AG. p. 1-4.

182. Nisman, R.; Dellaire, G.; Ren, Y.; Li, R. and Bazett-Jones, D. P., *Application of Quantum Dots as Probes for Correlative Fluorescence, Conventional, and Energy-Filtered Transmission Electron Microscopy.* Journal of Histochemistry & Cytochemistry, 2004. **52**(1): p. 13-18.

183. Grabenbauer, M. et al., *Correlative Microscopy and Electron Tomography of GFP through Photooxidation.* Nature Methods, 2005. **2**(11): p. 857-862.

References

184. Valentijn, K. M. et al., *Multigranular Exocytosis of Weibel-Palade Bodies in Vascular Endothelial Cells.* Blood, 2010. **116**(10): p. 1807-1816.

185. Schellenberger, P. et al., *High-Precision Correlative Fluorescence and Electron Cryo Microscopy Using Two Independent Alignment Markers.* Ultramicroscopy, 2014(0).

186. *Shuttle & Find for Life Sciences*. Carl Zeiss Microscopy 2013; Available from: http://www.zeiss.com/microscopy/en_de/products/correlative-microscopy/shuttle-find-life-sciences.html#downloads.

187. Czymmek, K. Z., *Zeiss Webinar: Strategies for Correlative Microscopy in Bioscience Research*. 2013.

188. Smith, C., *Two Microscopes Are Better Than One.* Nature, 2012. **492**(7428): p. 293-297.

189. Wade, W. L.; Mammone, R. J. and Binder, M., *Surface Properties of Commercial Polymer Films Following Various Gas Plasma Treatments.* Journal of Applied Polymer Science, 1991. **43**(9): p. 1589-1591.

190. Ali, H. S. M. et al., *Solubility of Salbutamol and Salbutamol Sulphate in Ethanol + water mixtures at 25 °C.* Journal of Molecular Liquids, 2012. **173**(0): p. 62-65.

191. Dehn, W. M., Journal of the American Chemical Society, 1917. **39**: p. 1399-1404.

192. L-Leucine - CAS Number: 61-90-5, E., *The Merck Index*. 12th Edition ed.

193. Martin, M. M. and Lindqvist, L., *The pH Dependence of Fluorescein Fluorescence.* Journal of Luminescence, 1975. **10**(6): p. 381-390.

194. Applichem GmbH, D., Germany, *Methylene Blue - Cas Number 61-73-4 - Material Safety Data Sheet*. 2014.

195. Whatman International Ltd., S. M., James Whatman Way, Maidstone, Kent ME14 2LE, England, *Whatman Nuclepore(R) Membranes - Microfiltration Membrane Characteristics*.

196. GESTIS-Substance-Database, *A-Lactose (Monohydrate), Cas Nr. 64044-51-5*. 2015.

197. Tompkins, B. D.; Dennison, J. M. and Fisher, E. R., *H_2O Plasma Modification of Track-Etched Polymer Membranes for Increased Wettability and Improved Performance.* Journal of Membrane Science, 2013. **428**(0): p. 576-588.

198. Tunney, M. M. and Gorman, S. P., *Evaluation of a Poly(Vinyl Pyrollidone)-Coated Biomaterial for Urological Use.* Biomaterials, 2002. **23**(23): p. 4601-4608.

199. Tas, N. R.; Haneveld, J.; Jansen, H. V.; Elwenspoek, M. and van den Berg, A., *Capillary Filling Speed of Water in Nanochannels.* Applied Physics Letters, 2004. **85**(15): p. 3274-3276.

200. Hibara, A. et al., *Nanochannels on a Fused-Silica Microchip and Liquid Properties Investigation by Time-Resolved Fluorescence Measurements.* Analytical Chemistry, 2002. **74**(24): p. 6170-6176.

201. Poland, C. A. et al., *Carbon Nanotubes Introduced into the Abdominal Cavity of Mice Show Asbestos-Like Pathogenicity in a Pilot Study.* Nature Nanotechnology, 2008. **3**(7): p. 423-428.

202. Donaldson, K.; Murphy, F. A.; Duffin, R. and Poland, C. A., *Asbestos, Carbon Nanotubes and the Pleural Mesothelium: A Review of the Hypothesis Regarding the Role of Long Fibre Retention in the Parietal Pleura, Inflammation and Mesothelioma.* Particle and Fibre Toxicology, 2010. **7**.

203. *Poly(Ethylene Glycol) Chemistry Biotechnical and Biomedical Applications*. Topics in Applied Chemistry, ed. J.M. Harris. Vol. 1. 1992: Springer US. 385.

204. Allen, T. M.; Hansen, C.; Martin, F.; Redemann, C. and Yauyoung, A., *Liposomes Containing Synthetic Lipid Derivatives of Poly(Ethylene Glycol) Show Prolonged Circulation Half-Lives Invivo.* Biochimica Et Biophysica Acta, 1991. **1066**(1): p. 29-36.

205. Prime, K. L. and Whitesides, G. M., *Self-Assembled Organic Monolayers - Model Systems for Studying Adsorption of Proteins at Surfaces.* Science, 1991. **252**(5009): p. 1164-1167.

206. Schulte, V. A.; Diez, M.; Moller, M. and Lensen, M. C., *Surface Topography Induces Fibroblast Adhesion on Intrinsically Nonadhesive Poly(Ethylene Glycol) Substrates.* Biomacromolecules, 2009. **10**(10): p. 2795-2801.

207. Machida-Sano, I. et al., *Surface Characteristics Determining the Cell Compatibility of Ionically Cross-Linked Alginate Gels.* Biomed Mater, 2014. **9**(2): p. 025007.

208. Aquino, R. P. et al., *Dry Powder Inhalers of Gentamicin and Leucine: Formulation Parameters, Aerosol Performance and in Vitro Toxicity on Cufi1 Cells.* International Journal of Pharmaceutics, 2012. **426**(1–2): p. 100-107.

209. Vehring, R., *Pharmaceutical Particle Engineering via Spray Drying.* Pharmaceutical Research, 2008. **25**(5): p. 999-1022.

References

210. Seville, P. C.; Learoyd, T. P.; Li, H. Y.; Williamson, I. J. and Birchall, J. C., *Amino Acid-Modified Spray-Dried Powders with Enhanced Aerosolisation Properties for Pulmonary Drug Delivery.* Powder Technology, 2007. **178**(1): p. 40-50.

211. Feng, A. L. et al., *Mechanistic Models Facilitate Efficient Development of Leucine Containing Microparticles for Pulmonary Drug Delivery.* International Journal of Pharmaceutics, 2011. **409**(1–2): p. 156-163.

212. CapsuLac 60, M. E. T., Wasserburg, Germany, *Technical Brochure, Milled and Sieved Lactose*. 2014.

213. French, D. L.; Edwards, D. A. and Niven, R. W., *The Influence of Formulation on Emission, Deaggregation and Deposition of Dry Powders for Inhalation.* Journal of Aerosol Science, 1996. **27**(5): p. 769-783.

214. Telko, M. J. and Hickey, A. J., *Dry Powder Inhaler Formulation.* Respiratory care, 2005. **50**(9).

215. Khan, S. A. and Schneider, M., *Improvement of Nanoprecipitation Technique for Preparation of Gelatin Nanoparticles and Potential Macromolecular Drug Loading.* Macromolecular Bioscience, 2013. **13**(4): p. 455-463.

216. Clarke, M. et al., *Curvature Recognition and Force Generation in Phagocytosis.* Bmc Biology, 2010. **8**.

217. Gerisch, G., *Actin Switches in Phagocytosis.* Communicative & integrative biology, 2011. **4**(3).

218. Hittinger, M.; Tscheka, C.; Lehr, C. M.; Schneider, M. and Daum, N., *Utilization of "Shuttle & Find" for Uptake Analysis of Substructured, Rodshaped Microparticles by Alveolar Macrophages*, in *Advances in Imaging and Electron Physics, Vol 179*, P.W. Hawkes, Editor. 2013, Elsevier Academic Press Inc: San Diego. p. 187-188.

219. van de Weert, M.; Hennink, W. and Jiskoot, W., *Protein Instability in Poly(Lactic-Co-Glycolic Acid) Microparticles.* Pharmaceutical Research, 2000. **17**(10): p. 1159-1167.

220. Ye, M.; Kim, S. and Park, K., *Issues in Long-Term Protein Delivery Using Biodegradable Microparticles.* Journal of Controlled Release, 2010. **146**(2): p. 241-260.

221. Smidsrod, O. and Skjakbraek, G., *Alginate as Immobilization Matrix for Cells.* Trends in Biotechnology, 1990. **8**(3): p. 71-78.

222. Ehrhart, F. et al., *Biocompatible Coating of Encapsulated Cells Using Ionotropic Gelation.* Plos One, 2013. **8**(9).

223. Rehm, B., *Alginates: Biology and Applications*. Vol. 13. 2009: Springer.

224. Hillebrenner, H. et al., *Corking Nano Test Tubes by Chemical Self-Assembly.* Journal of the American Chemical Society, 2006. **128**(13): p. 4236-4237.

225. Ma, X.; Vacek, I. and Sun, A., *Generation of Alginate-Poly-L-Lysine-Alginate (APA) Biomicrocapsules: The Relationship between the Membrane Strength and the Reaction Conditions.* Artificial Cells, Blood Substitutes and Biotechnology, 1994. **22**(1): p. 43-69.

226. Fu, Y. and Kao, W. J., *Drug Release Kinetics and Transport Mechanisms of Non-Degradable and Degradable Polymeric Delivery Systems.* Expert Opin Drug Deliv, 2010. **7**(4): p. 429-44.

227. Khan, S. A. and Schneider, M., *Stabilization of Gelatin Nanoparticles without Crosslinking.* Macromolecular Bioscience, 2014. **14**(11): p. 1627-1638.

228. Brandl, F. et al., *Hydrogel-Based Drug Delivery Systems: Comparison of Drug Diffusivity and Release Kinetics.* Journal of Controlled Release, 2010. **142**(2): p. 221-228.

229. *FITC-Dextran, Product Information Sheet*, V.A.S.-U. TdB Consultancy AB, Editor. 2010.

230. Smola, T.; Cramer, J.; Veloso, A.; Giese, K. and Mosel, J., *$CaHPO_4$*, in *CAS number 7757-93-9*. 2014.

231. *H_3PO_4, Cas Number 7664-38-2*, in *Roempp*. 2014, Thieme Verlag.

232. Engler, A. J.; Sen, S.; Sweeney, H. L. and Discher, D. E., *Matrix Elasticity Directs Stem Cell Lineage Specification.* Cell, 2006. **126**(4): p. 677-689.

233. Zhang, Y.; Lim, C.; Ramakrishna, S. and Huang, Z.-M., *Recent Development of Polymer Nanofibers for Biomedical and Biotechnological Applications.* Journal of Materials Science: Materials in Medicine, 2005. **16**(10): p. 933-946.

234. Min, S. K.; Kim, C. R.; Jung, S. M. and Shin, H. S., *Astrocyte Behavior and GFAP Expression on Spirulina Extract-Incorporated PCL Nanofiber.* Journal of Biomedical Materials Research Part A, 2013. **101**(12): p. 3467-3473.

235. Morra, M. and Cassinelli, C., *Cell Adhesion Micropatterning by Plasma Treatment of Alginate Coated Surfaces.* Plasmas and Polymers, 2002. **7**(2): p. 89-101.

236. Jeon, H.; Simon, C. G. and Kim, G., *A Mini-Review: Cell Response to Microscale, Nanoscale, and Hierarchical Patterning of Surface Structure.* Journal of Biomedical Materials Research Part B-Applied Biomaterials, 2014. **102**(7): p. 1580-1594.

237. Curtis, A. S. G. et al., *Cells React to Nanoscale Order and Symmetry in Their Surroundings.* Ieee Transactions on Nanobioscience, 2004. **3**(1): p. 61-65.

References

238. Lehnert, D. et al., *Cell Behaviour on Micropatterned Substrata: Limits of Extracellular Matrix Geometry for Spreading and Adhesion.* Journal of Cell Science, 2004. **117**(1): p. 41-52.

239. Gallagher, J. O.; McGhee, K. F.; Wilkinson, C. D. W. and Riehle, M. O., *Interaction of Animal Cells with Ordered Nanotopography.* Ieee Transactions on Nanobioscience, 2002. **1**(1): p. 24-28.

240. Dalby, M. J. et al., *Fibroblast Reaction to Island Topography: Changes in Cytoskeleton and Morphology with Time.* Biomaterials, 2003. **24**(6): p. 927-935.

241. Dalby, M. J.; Riehle, M. O.; Sutherland, D. S.; Agheli, H. and Curtis, A. S. G., *Changes in Fibroblast Morphology in Response to Nano-Columns Produced by Colloidal Lithography.* Biomaterials, 2004. **25**(23): p. 5415-5422.

242. Loesberg, W. A. et al., *The Threshold at Which Substrate Nanogroove Dimensions May Influence Fibroblast Alignment and Adhesion.* Biomaterials, 2007. **28**(27): p. 3944-3951.

243. Barthlott, W. and Neinhuis, C., *Purity of the Sacred Lotus, or Escape from Contamination in Biological Surfaces.* Planta, 1997. **202**(1): p. 1-8.

244. Zheng, J.; Li, D.; Yuan, L.; Liu, X. L. and Chen, H., *Lotus-Leaf-Like Topography Predominates over Adsorbed ECM Proteins in Poly(3-Hydroxybutyrate-Co-3-Hydroxyhexanoate) Surface/Cell Interactions.* Acs Applied Materials & Interfaces, 2013. **5**(12): p. 5882-5887.

245. Lo, C. M.; Wang, H. B.; Dembo, M. and Wang, Y. L., *Cell Movement Is Guided by the Rigidity of the Substrate.* Biophysical Journal, 2000. **79**(1): p. 144-152.

246. Discher, D. E.; Janmey, P. and Wang, Y. L., *Tissue Cells Feel and Respond to the Stiffness of Their Substrate.* Science, 2005. **310**(5751): p. 1139-1143.

247. Tan, J. L. et al., *Cells Lying on a Bed of Microneedles: An Approach to Isolate Mechanical Force.* Proceedings of the National Academy of Sciences of the United States of America, 2003. **100**(4): p. 1484-1489.

248. Walboomers, X. F.; Croes, H. J. E.; Ginsel, L. A. and Jansen, J. A., *Growth Behavior of Fibroblasts on Microgrooved Polystyrene.* Biomaterials, 1998. **19**(20): p. 1861-1868.

8 Scientific Output

8.1 Journal Articles

Excerpts of this thesis have either been published in the following peer reviewed scientific journals, or are drafted for submission:

Biomimetic Alginate Hydrogel with Hairy Texture Alters the Cell-Surface Interaction of Fibroblasts

Tscheka, Clemens; Gepp, Michael; Zimmermann, Heiko; Schneider, Marc

Macrophage Uptake of Cylindrical Microparticles Investigated with Correlative Microscopy

Tscheka, Clemens; Hittinger, Marius; Lehr, Claus-Michael; Daum, Nicole; Schneider, Marc

European Journal of Pharmaceutics and Biopharmaceutics

Volume: **95**, Issue: Pt A, Pages: 151-155, DOI:10.1016/j.ejpb.2015.03.010, Published: September 2015 (Epub - March 14th 2015)

Utilization of `Shuttle & Find´ for Uptake Analysis of Substructured, Rodshaped Microparticles by Alveolar Macrophages

Hittinger, Marius; Tscheka, Clemens; Lehr, Claus-Michael; Schneider, Marc; Daum, Nicole

Published abstract in:

Advances in Imaging and Electron Physics

Volume: **179**, Pages: 137-202, Published: 2013, Chapter Two - In-Situ and Correlative Electron Microscopy: Proceedings of the Conference on In-Situ and Correlative Electron Microscopy (CISCEM), Niels DeJonge

Novel Approaches for Drug Delivery Systems in Nanomedicine: Effects of Particle Design and Shape

Daum, Nicole; Tscheka, Clemens; Neumeyer, Andrea; Schneider, Marc

Wiley Interdisciplinary Reviews-Nanomedicine and Nanobiotechnology

Volume: **4**, Issue: 1, Pages: 52-65, Published: January-February 2012

8.2 Poster Presentations

The Advantage of Correlative Microscopy for Macrophage Uptake Studies with Non-Spherical Particles

Tscheka, Clemens; Hittinger, Marius; Lehr, Claus-Michael; Daum, Nicole; Schneider, Marc

GPEN 2014, Helsinki, Finland, August 2014

Analysis of Macrophage Uptake of Cylindrical Particles by Means of Correlative Microscopy

Tscheka, Clemens; Hittinger, Marius; Daum, Nicole; Lehr, Claus-Michael; Schneider, Marc

10th International Conference and Workshop on Biological Barriers 2014, Saarbrücken, February 2014

Novel Filamentous Carrier Systems Made from Hydrogels of Bacterial Origin

Tscheka, Clemens; Tawfik, Mohamed; Khan, Saeed Ahmad; Schneider, Marc

3rd HIPS Symposium, Saarbrücken, July 2013

Novel Filamentous Carrier Systems Based on Biodegradable Hydrogels

Tscheka, Clemens; Khan, Saeed Ahmad; Hittinger, Marius; Haimour, Eman; Tawfik, Mohamed; Schneider, Marc

CRS 2013 Local Chapter, Ludwigshafen, March 2013

Nano- and Microfibers Utilised as Carrier Systems for pulmonary Administration

Tscheka, Clemens; Schneider, Marc

INASCON 2012, Saarbrücken, August 2012

Photoacoustic Microscopy Imaging of Model Hair Shafts Containing Magnetite-PLGA Nanoparticles

Mardiyanto; Tscheka, Clemens; Fournelle, Marc; Schneider, Marc

INASCON 2012, Saarbrücken, August 2012

Novel Filamentous Carrier Systems for Drug Delivery to Bio-Films

Tscheka, Clemens; Haimour, Eman; Khan, Saeed Ahmad; Schneider, Marc

2nd HIPS Symposium, Saarbrücken, June 2012

Novel Filamentous Carrier Systems for Pulmonary Administration

Tscheka, Clemens; Schneider, Marc

CRS 2012 Local Chapter, Würzburg, March 2012

Template-Assisted Generation of Fiberous Drug Carriers for Pulmonary Administration

Tscheka, Clemens; Schneider, Marc

9th International Conference and Workshop on Biological Barriers 2012, Saarbrücken, February 2012

Non-Spherical Drug Carriers for Pulmonary Administration Formed with a Template-Assisted Approach

Tscheka, Clemens; Schneider, Marc

CRS 2011 Local Chapter, Jena, March 2011

Novel Drug-Carriers for Pulmonary Administration Utilizing a Template-Assisted Approach

Tscheka, Clemens; Kohler, Dorothee; Schneider Marc

DPhG 2010, Braunschweig, October 2010

9 Acknowledgments

I would like to express my sincere gratitude to all those who contributed to the successful completion of this work.

First and foremost, I would like to thank Prof. Dr. Marc Schneider for giving me the opportunity to join his working group and to prepare my PhD thesis. Scientific discussion and his support more often than once helped to pass the plentiful obstacles along the way. Prof. Schneider spurred the idea for the participation in the national scientific photo competition "Nano-Momente" in which we participated successfully, winning once and once receiving the 2nd prize.

In particular, he supported and advocated for interdisciplinary work. The very first months of the thesis, I was given the opportunity to work at the Max-Planck-Institut für Kolloid- und Grenzflächenforschung (MPIKG) in Postdam-Golm. During that time, I learned the essentials for my PhD work in the working group of Prof. Dr. Dr. Helmuth Möhwald, to whom I am very grateful.

Prof. Dr. Claus-Michael Lehr, Abteilung Wirkstoff-Transport, Helmholtz-Institut für Pharmazeutische Forschung Saarland (HIPS), is thanked for the kind provision of state-of-the-art equipment, which was placed at my disposal during the time in Saarbrücken. Prof. (apl.) Dr. Ulrich Schäfer is particularly thanked for his assistance regarding administrative questions. Most of all, I am thankful for their scientific input that helped to solve more than one problem and for their supervision of my qualification as a specialist pharmacist in Pharmaceutical Technology.

Furthermore, I would like to thank Prof. Dr. Heiko Zimmermann, Fraunhofer-Institut für Biomedizinische Technik (IBMT), St. Ingbert, and Prof. Dr. Udo Bakowsky, Pharmazeutische Technologie und Biopharmazie, Philipps-Universität Marburg, for their help and cooperation.